Energy Dissipation in Metal Matrix Composites

Submitted by

Narasimalu Srikanth
(B. Engg., M. Tech., M. Sc)
(Matric No. HT006481H)

A Thesis Submitted
For the Degree of Doctor of Philosophy

Department of Mechanical Engineering
National University of Singapore

2005

Summary

Passive damping is a critically important material property from the viewpoint of vibration suppression in aerospace, semiconductor and automotive industries. The ultimate goal is to design and produce materials with high damping. Metals are chosen for such applications since they possess many mechanisms which contribute to the total damping e.g. point defect relaxation, dislocation motion, grain boundary sliding, inclusion-matrix friction, magnetoelastic effects, and elasto-thermodynamic effects. In the present study, effect of the addition of stiff particulates to the metallic matrix's overall damping capacity was studied. Such particulates were varied in type of material (ceramic versus metal), morphology (discontinuous versus interconnected) and size (micro size to nano size).

Additionally, in the present research, a new methodology of using free-free beam method coupled with circle-fit approach is used to determine damping of ceramic reinforced metal matrix materials. This technique is based on classical vibration theory, by which the geometry and material properties of the metal matrix composites are related to resonant frequency and structural damping of the test specimen. Using the fact that the ratio of the vibration response to the applied force fits to a circle in the Argand plane for each resonant frequency of the test specimen, the damping factor and elastic modulus are predicted accurately for the test specimens.

Results confirmed that the presence of stiff reinforcement enhanced the damping characteristics of the ductile matrix. This increase in damping capability of the MMC when compared against the monolithic specimen can be attributed to the increase in

dislocation density and presence of plastic zone at the matrix-particulate interface due to thermal mismatch.

A novel finite element based numerical model has been formulated that is capable to predict the damping caused due to the micro-plasticity and elasto-thermodynamic damping mechanisms which may help material scientists to formulate new composite formulations in future.

Damping results of the nanomaterials containing critical dimensions in nano-regime (viz., nano-grain, nano-particle) were also studied which showed enhanced and interesting results which are in tune with other peculiar properties exhibited by nanomaterials.

Acknowledgements

I would like to acknowledge with gratitude and appreciation, the guidance rendered by my supervisor, Prof. Manoj Gupta, Department of Mechanical Engineering, whose valuable suggestions, constructive criticisms and continuous encouragement led to the fruition of my efforts in the form of this thesis and other publication works.

I would also like to thank my employer, ASM Technology Singapore, for providing me the financial support and the opportunity to work in this research topic and implement these research outcomes in the design of high throughput semiconductor machinery such as wire bonders.

I wish to thank all my fellow researchers, especially Eugene Wong, S.F. Hassan, L.M. Tham, S. Ugandher, and Calvin Ho for their kind support during the research.

I also wish to convey my deep gratitude to my parents and brothers who had invested their life in bringing me up. My special thanks to my wife and little daughter whose moral support and patience helps me to concentrate in my studies.

Contents

Summary i

Acknowledgements iii

Contents iv

List of Figures ix

List of Tables xxi

List of Papers Published xxiv

Chapter 1 Introduction 1

Chapter 2 Literature Review

2.0 Motivation for Damping Studies 7

2.1 Damping capacity of common engineering materials 8

2.2 The Metal Matrix Composite Concept 13

2.3 The meaning of anelasticity 16

2.4 Measures of damping 17

2.5 Mathematical model of Damping Behavior 19

2.6 Material Property Measurements 20

2.7 Damping in Monolithic Metals 22

2.7.1 Point defect relaxations 23

2.7.2 Grain Boundary Viscosity: 25

2.7.3 Macro-Thermoelasticity: 27

2.7.4 Micro-thermoelasticity 29

2.7.5 Magneto-mechanical damping 29

2.7.6 Dislocation Based Damping Mechanisms: 30

2.8 Interfaces in Metallic Matrix 33

2.8.1 Interface types 34

2.8.1.1 Homophase Interface 36

2.8.1.2 Heterophase interface 41

2.8.3 Metal-Ceramic Interface 46

2.8.3.1 Atomic Model 47

2.8.3.2 Ion Exchange 49

2.8.3.3 Reaction at metal-ceramic interface 51

2.8.3.4 Wetting of Ceramics by Liquid Metals 54

2.9 Effect of particulate reinforcement in metals 57

Chapter 3 New Free-Free Beam Method Coupled With Circle Fit Approach

3.1 Introduction 65

3.2 Free-Free beam type method 68

3.3 Presence of End Mass at Ends 69

3.4 The circle-fit method 72

3.5 Damping Interpretation 75

Chapter 4 Experimental Procedures

4.1 Materials and Processes 83

4.1.1 Solid state processing 83

4.1.2 Liquid Spray Processing 84

4.2 Microstructure Characterization 86

4.3 Density and Porosity Measurement 86

	4.4	Thermo-Mechanical Testing	87
	4.5	Tensile Testing and Fractography	87
	4.6	Hardness measurement	87
	4.7	Suspended Beam Dynamic Testing	88
Chapter 5	**Ceramic Particulate Reinforced Metal Matrix Composites**		
	5.0	Introduction	92
	5.1	Materials and Processes	93
	5.2	Results	93
	5.3	Discussion	99
	5.4	Summary	108
Chapter 6	**Metal Particulates Reinforced Metal Matrix Composites**		
	6.0	Introduction	111
	6.1	Materials and Processes	112
	6.2	Results	112
	6.3	Discussion	116
	6.4	Summary	122
Chapter 7	**Inter-Connected Metal Reinforced Metal Matrix Composites**		
	7.0	Introduction	125
	7.1	Materials and Processes	125
	7.2	Results	127
	7.3	Discussion	131
	7.4	Summary	138
Chapter 8	**Hybrid Composites**		

8.0 Introduction 140

8.1 Materials and Processes 140

8.2 Results 142

8.3 Discussion 153

8.4 Summary 162

Chapter 9 Numerical Modeling of Plastic Zone Induced Damping in PRMMCs

9.0 Introduction 165

9.1 Finite Element Method 166

9.2 Unit Cell Model 167

9.3 Constitutive Behaviour of Viscoplastic Metallic Matrix 168

9.4 Numerical Implementation 171

9.5 Results From Numerical Predictions

9.5.1 Al-SiC System 172

9.5.2 Al-Ti System 180

9.5.3 Al-SiC-Ge System 184

9.6 Discussion 185

9.7 Summary 188

Chapter 10 Numerical Modeling of ETD in Metal Based Composites

10.0 Introduction 191

10.1 Theoretical Consideration 193

10.2 Macro thermo elasticity: Flexural vibrations of beams 197

10.3 Micro Thermoelastic Damping: PRMMCs 199

10.4 Finite element implementation of Micro-thermoelasticity 202

10.5 UCM for Micro-thermoelasticity 211

10.6 Discussion of UCM Predicted Micro-ETD Effects 215

10.7 Summary 222

Chapter 11 Effects of Nano Particle Reinforcement on MMC Damping

11.0 Introduction 225

11.1 Materials and Processes 225

11.2 Results 228

11.3 Discussion 229

11.5 Summary 234

Chapter 12 Effect of Nano Grain Size on Damping Capacity of Metallic Materials

12.0 Introduction 237

12.1 Materials and Processes 238

12.2 Results 239

12.3 Discussion 242

12.4 Summary 248

Overall Conclusions 250

Future Recommended Work 254

References 256

Appendix

List of Figures

Fig. 2.1 Various forces acting in a typical single degree of freedom and the associated free body diagram [1]. 7

Fig. 2.2 (a) Influence zone of mass, spring and damping in a SDOF (b) vector diagram showing how the various forces varies with frequency in terms of magnitude and direction (c) effect of damping on the amplification factor (d) effect of damping on phase lag between applied force and induced displacement [1]. 8

Fig. 2.3 Various vibration modes of an orthotropic plate predicted and confirmed using experiments. 10

Fig. 2.4 Wind induced failure of Tacoma Narrows bridge: (a) torsional vibration (b) vortex shedding and swinging of the structure (c) and (d) final collapse [6]. 11

Fig. 2.5 (a) Canadram arm under assembly and (b) arm under operation [7]. 12

Fig. 2.6 Variation of various engineering materials: (a) specific modulus versus specific strength (b) loss coefficient versus Young's modulus. 12

Fig. 2.7 Matrix reinforced with (a) discontinuous particles (b) whiskers and (c) continuous fibers. 13

Fig. 2.8 (a) Dynamic mechanical analyzer with a cantilever type sample holder used by Zhang [21] and (b) Torsion test setup used by Ke [22]. 21

Fig. 2.9 Internal friction or damping peaks for hypothetical material compared against several metals due to different microstructural mechanisms such 22

as Cu-Mn alloy (movement of twin interfaces), German silver (thermal currents in transverse vibration), Alpha brass (stress induced by preferential orientation of axis joining pairs of solute atoms) and Polycrystalline brass (intercrystalline thermal currents) [2].

Fig.2.10 Positions of the distribution of interstitial atoms in the cubic body centered lattice: (a) octahedral positions (b) tetrahedral positions (c) variation of snoek damping in Fe matrix with 20 ppm of carbon [4]. 23

Fig. 2.11 Effect of temperature and frequency on internal friction associated with grain boundary shear: (a) hypothetical stress-strain loops of case 1 which correspond to high frequency or low temperature, case 2 which correspond to optimum combination to cause relaxation peak and case 3 which correspond to low frequency or high temperature [18] and (b) experimental results of grain boundary induced damping results of aluminium [22]. 26

Fig. 2.12 Damping caused by transverse thermal currents in a beam of German Silver [24]. 28

Fig. 2.13 Dislocation motion behavior: from stages (a) to (c) the dislocation provides amplitude-independent damping behavior and after overcoming the barrier, from stages (d) to (g) the dislocation provides a strong strain amplitude dependent damping behavior [30]. 33

Fig. 2.14 Types of interfaces (a) coherent (b) semicoherent (c) incoherent [31]. 35

Fig. 2.15 (a) HRTEM image of a $\sum$=3 {111} twin in Cu imaged along a <110> zone axis [34] (b) typical grain boundary in aluminium [36]. 36

Fig. 2.16 (a) High angle and low angle tilt boundary explained using soap bubble experiment. (b) Comparison of measured energies (dashed line) against populations for symmetric [110] tilt boundaries in Al [35]. 39

Fig. 2.17 HRTEM image of: (a) silver-rich G.P.zone in an aluminium –silver alloy which shows a coherent interface [37] and (b) Co-Ni interface which is a FCC-HCP interface [40]. 41

Fig. 2.18 HRTEM image of a {111} copper-silver interface in a Cu-Ag alloy aged to grow silver precipitates in the copper matrix is example of semicoherent interface [42]. Arrow indicate the periodic misfit dislocation. 43

Fig. 2.19 HRTEM image of a aluminium –germanium interface showing a typical incoherent interface [36, 47]. 44

Fig. 2.20 Typical Metal-Ceramic Interface in MMCs and how damage arises [49]. 46

Fig. 2.21 Al-TiC interface showing: (a) dislocation structure and (b) interface showing the lattice misfit [53]. 49

Fig. 2.22 Diffusion profile of Al and Si at the Al-SiC interface [58] (b) Calculated istothermal quaternary phase diagram for Al-Si-C-O system (Temp 600 to 1000 ^{o}C) [59]. 51

Fig. 2.23 SEM micrographs showing (a) clean interface of a SiC particle just after addition in Al melt and (b) reacted interface with Al_4C_3 interface after 15 minutes holding time. [63]. 52

Fig. 2.24 SEM micrographs showing: (a) as received SiC particles (b) Oxide coated SiC particles (c) the thickness of oxidized layer (HRTEM image) 53

of the composite reinforced with SiC particles at 1100^{o}C for 2 hours [65].

Fig. 2.25 (a) Typical spreading of molten Al on ceramic substrate [69], (b) definition of contact angle and (c) incomplete coating of Au on alumina surface [70]. 54

Fig. 2.26 (a) Orowan loops around alumina particles in Cu30%Zn due to higher shear strength of the particle and (b) dislocation cuts a relatively soft precipitate in Ni 19%Cr6%Al [24]. 59

Fig. 2.27 Work hardening behavior of Al-SiC MMC systems [101]. 60

Fig. 2.28 Variation of damping loss factor and stiffness of: (a) pure Al6061-T6 matrix and (b) Al6061-T6 with 5 vol. % SiC_p [21]. 61

Fig. 2.29 (a) Variation of damping loss factor with strain amplitude for 6061/SiC_p, (b) same data in terms of strain amplitude against product of strain amplitude over damping loss factor shows a linear behavior using which the coefficients are determined [101]. 61

Fig. 2.30Variation of internal friction in Al matrix (a) under increasing temperature and with and without the presence of 13 vol. % of SiC_p [102] (b) with different vol. % of saffil fibers and under heating and cooling part of a thermal cycle [103]. 62

Fig. 3.1 (a) to (d) Dynamic mechanical analysis equipment built using a rotary to reciprocating conversion mechanism to measure the energy dissipated within each cycle (e) phase lag measured between stress and strain (f) actual result for pure al sample and (g) Calculation of energy spent and maximum strain energy from the hysterisis loop. 66

Fig. 3.2 Time domain damping measurement: (a) sample mounting and using laser to measure, (b) actual measurement result, (c) & (d) idealizing the decay as a SDOF with single frequency and (f) calculation procedure. 67

Fig. 3.3 Schematic diagram showing experimental setup of suspended beam technique. 68

Fig. 3.4 (a) Schematic diagram showing experimental setup of suspended beam technique, (b) enlarged sketch showing the fastening method of end mass shown as detail 'A' (c) actual load and sensor placement direction and (d) sketch explaining the sensor placement location. 70

Fig. 3.5 Typical real part of receptance frequency response function (FRF) of a metallic sample which shows the resonance peak is so sharp that damping calculation is difficult to derive the damping factor. 72

Fig. 3.6 Typical receptance frequency response function (FRF) showing the use of the natural frequency and two data points to derive the damping factor. 73

Fig. 5.1 (a) SEM micrograph showing the particulate/matrix interface in Mg/20μm SiC sample. (b) SEM micrograph showing the distribution of SiC particulate in Mg/20μm SiC sample. (e) Optical micrograph showing equiaxed grain morphology of pure magnesium sample. (f) Optical micrograph showing equiaxed grain morphology of Mg/20μm SiC sample. 94

Fig. 5.2 (a) SEM micrograph showing the distribution of SiC particulate in Al-5.2 wt.% SiC sample. (d) SEM micrograph showing the particulate/matrix interface in Al-5.2 wt.% SiC sample. (e) Optical micrograph showing 95

equiaxed grain morphology of pure aluminium sample. (f) Optical micrograph showing equiaxed grain morphology Al-17.7 wt.% SiC sample.

Fig. 5.3 SEM micrograph of tensile fractured specimens of: (a) Al/17.7 wt. % SiC sample and (b) Mg/14.9 wt. % SiC sample, which is denoted with (1) interfacial debonding of SiC particulate and the metallic matrix and (2) SiC particulate breakage. 96

Fig. 5.4 Typical receptance frequency response function (FRF) showing actual FRF data of: (a) pure magenisium (b) Mg/7.6 wt.% SiC (c) Mg/14.9 wt.% SiC (d) Mg/26.0 wt.% SiC. 97

Fig. 5.5 Typical receptance frequency response function (FRF) showing actual FRF data of: (a) pure aluminium (b) Al/5.2 wt.% SiC (c) Al/13.9 wt.% SiC (d) Al/17.7 wt.% SiC. 98

Fig. 5.6 Predicted variation of ETD damping with SiC volume fraction in Al-SiC and Mg-SiC type particulate MMC samples using closed form analytical prediction (at 1000Hz and 23^{o}C). 107

Fig. 6.1 SEM micrographs showing: (a) pure Ti particulates, (b) reinforcement distribution in Al-3.3%Ti, (c) good interfacial integrity of the reinforcement exhibited in Al-3.3%Ti, (d) typical clustering of particles in Al-6%Ti, (e) fractograph exhibiting particulate debonding in Al-3.3% Ti and (f) fractograph exhibiting particulate breakage in Al-7.5% Ti. 113

Fig. 6.2 Circle-fit plot of FRF data of: (a) the pure Al sample, (b) the Al-3.3%Ti sample, (c) the Al-6%Ti sample and (d) the Al-7.5%Ti sample. 116

Fig. 7.1 Schematic diagram of the inter-connected reinforcement preforms with: (a) 2 lobes, (b) 4 lobes, and (c) 6 lobes geometries. 126

Fig. 7.2 Representative SEM micrographs showing: (a) the interfacial integrity between the matrix and reinforcement wire of Sample B, (b) tensile fracture surface of monolithic aluminium, (c) magnified image of dimpled fracture surface of monolithic aluminium, (d) typical tensile fractured surface of Sample B, (e) magnified image of dimpled fracture surface of Sample B and (f) interfacial debonding of matrix and the reinforcement wire and wire breakage in the tensile fracture surface of Sample B. 129

Fig. 7.3 Representative EDX graphs showing the composition at: (a) interfacial reaction zone and (b) the matrix of the composite materials. 130

Fig. 7.4 Actual FRF data of sample corresponding to: (a) pure Al (b) Al with 1.6 vol.% iron mesh reinforcement (c) Al with 3.1 vol. % iron mesh reinforcement (d) Al with 4.7 vol. % iron mesh reinforcement. 132

Fig. 8.1 Schematic diagram of the inter-connected reinforcement performs used in the ingot. 141

Fig. 8.2 SEM micrographs of case A samples showing: (a) the distribution of SiC particulate in Mg/ 9 vol. % SiC sample, (b) the distribution of Ti particulate in Mg/ 8.8 vol. % SiC/1.1 vol. % Ti sample and (c) the particulate/matrix interface of Ti in Mg/ 5.7 vol. % SiC/1.1 vol. % Ti sample. 144

Fig. 8.3 Representative SEM micrographs of case B samples showing: (a) & (b) 145

the interfacial integrity between the matrix and reinforcement wire of sample BC1 at low and high magnification, respectively, (c) typical SiC distribution in the sample BC2 (d) typical interfacial integrity of the SiC particulate with the matrix in the sample BC2 (e) typical interfacial debonding of matrix and the reinforcement wire and wire breakage in the tensile fracture surface of Sample BC1 (f) typical SiC failure in sample BC3 exhibiting interfacial debonding and particulate breakage.

Fig. 8.4 SEM micrographs of case C samples showing: (a) the distribution of Ge and SiC particulate in Al-1.8Ge/2.9SiC sample, (b) the particulate/matrix interface of Ge in Al-1.8Ge/2.9SiC sample and (c) the particulate/matrix interface of SiC in Al-1.8Ge/2.9SiC sample. 146

Fig. 8.5 Representative XRD graph performed on: (a) monolithic Al sample-BM (b) sample-BC1 (c) sample-BC2 (d) sample-BC3. 148

Fig. 8.6 Ashby's map showing variation of damping loss factor against the thermal expansion for various engineering materials [8]. 160

Fig. 9.1 Methodology for deducing a simplified FEM model for the PRMMC: (a) hexagonal representation of a particulate reinforced MMC, (b) unit hexagonal cell, (c) approximated cylindrical unit cell, (d) axisymmetric FEM model of the cylindrical unit cell, (e) equivalent stress contour plot and (f) hysterisis curve. 166

Fig. 9.2 Equivalent plastic strain plot in the unit cell model containing particulates with: (a) Al- 5.2 wt. % SiC (b) Al- 13.9 wt. % SiC and (c) Al- 17.7 wt. % SiC. 173

Fig. 9.3 UCM predicted results: (a) Variation of equivalent plastic strain plot along the radial direction for different volume percentage of SiC in the Al matrix, viz., 4.4 %, 12.0% and 15.4% (b) Variation of plastic zone induced damping loss factor with the number of the loading cycle in the Al- 13.9 wt. % SiC (c) Variation of equivalent plastic strain plot along the radial direction for different loading cycle in the Al- 13.9 wt. % SiC. 174

Fig. 9.4 (a) Variation of FEM predicted damping loss factor with respect to volume fraction of SiC in Al matrix. (b) Comparison of FEM predicted damping loss factor for different particulate shapes. (c) Comparison of FEM predicted damping loss factor for different process induced defects. 177

Fig. 9.5 (a) Particulates of similar volume but with different shape morphologies. (b) Process-induced defects assumed to study their effects on the overall energy dissipation. 178

Fig. 9.6 Equivalent plastic strain plot in the unit cell model containing particulates with: (a) spherical shape (b) double cone shape (c) cylindrical shape and (d) ellipsoidal shape with an aspect ratio of 2. 179

Fig. 9.7 Equivalent plastic strain plot in the unit cell model under the presence of: (a) debonded metal-particulate interface, (b) a broken particulate along the central half plane (at y=0), and (c) void of 0.77 volume percentage. 179

Fig. 9.8 Variation of plastic zone induced damping coefficient with strain amplitude. 180

Fig. 9.9 Variation of aluminium and titanium properties with temperature: (a) coefficient of thermal expansion and (b) elastic modulus. 181

Fig. 9.10 Equivalent plastic strain plot in the unit cell model containing particulates with: (a) Al- 3.3 wt. % Ti, (b) Al- 6 wt. % Ti and (c) Al- 7.5 wt. % Ti. 182

Fig. 9.11 Plots showing variation of: (a) equivalent plastic strain in the unit cell model along the radial direction and (b) computed damping loss factor for different weight percentage of Ti in the Al matrix, viz., 3.3 %, 6% and 7.5%. 183

Fig. 9.12 Equivalent plastic strain contour plot in the unit cell model containing composition equivalent to: (a) Al- 1.9 vol. % Ge (b) Al-1.8 vol. % Ge /2.9 vol. % SiC. 184

Fig 10.1 Effect of normalized frequency of the vibration on the damping capacity for Al reinforced with 20 vol. % of SiC with different particle size (a) ranging from 5 μm to 50 μm. 204

Fig. 10.2 (a) FEM based axisymmetric model similar to that of Kinra et al. [7] having a spherical matrix and particle (b) Corresponding damping characteristics result of Al-10 vol.% SiC for different spherical particle radius ranging from 0.1 to 20 micron. 205

Fig. 10.3 Particulates of similar volume but with different shape morphologies. 206

Fig. 10.4 (a) Typical SiC particle distribution and shape in an Al containing 5 volume percentage of SiC (b) Typical particle cracking and debond. 206

Fig. 10.5 UCM models with different defects (a) broken particle (b) particle matrix debonding (c) presence of voids in matrix (d) presence of cracks in matrix. 206

Fig. 10.6 Damping characteristics of Aluminium with cylindrical SiC particle and volume fraction ranging from 5 to 50 percentage. 207

Fig. 10.7 Variation of damping characteristics of Al containing 10 vol. % of SiC with particle shapes of cylinder, sphere and truncated cone. 207

Fig. 10.8 Material deformation under (a) tensile part (b) compressive part of the cyclic load at a non-dimensional frequency of Ω~10. Corresponding temperature flux pattern in the unit cell under the same instance of (c) tensile direction (d) compressive direction of the cyclic load. 206

Fig. 10.9 Typical hydrostatic stress distribution under the compressive part of the load at non dimensional frequency of Ω~10 for a particle shape of (a) cylinder (b) sphere (c) truncated cone. 209

Fig. 10.10 Damping characteristics of Al containing 10 vol. % of cylindrical SiC particle with aspect ratio ranging from 0.5 to 2.0 210

Fig. 10.11 Effect of process induced defects on the ETD damping characteristics of an Al matrix containing 10 vol. % of cylinder shape particle. 210

Fig. 10.12 Variation of specific damping capacity with the non-dimensional frequency for different matrix-reinforcement combinations for a similar volume fraction of 0.5. 220

Fig. 10.13 Surface plot of specific damping capacity variation of Al matrix with various vol. fraction of SiC. 221

Fig. 11.1 Representative SEM micrographs showing: grain morphology of: (a) Al-Mg (b) Al-Mg-0.3 μm Al_2O_3 and (c) Al-Mg-10 μm Al_2O_3 and distribution of: (d) $Al_{12}Mg_{17}$ precipitates in Al-Mg matrix and typical 227

clusters in (e) Al-Mg-0.3 Al_2O_3 and (f) Al-Mg-10 Al_2O_3 .

Fig. 11.2 Typical FESEM image showing nano-size Al_2O_3 particulate distribution in a Mg/2.5 vol.%Al_2O_3 sample. 228

Fig. 11.3 Decay of vibration amplitude with time under different damping loss factor in a cantilever when subjected to a unit starting deformation. 234

Fig 12.1. X-ray diffraction spectra of: (a) MMed pure Cu powder and (b) MMed + extruded Cu at different milling durations. 240

Fig. 12.2 Typical receptance frequency response function (FRF) showing: (a) Actual FRF data for the 0-h MMed sample. (b) Actual FRF data for the 10-h MMed sample. (c) Actual FRF data for the micro-grain Cu sample. 241

List of Tables

Table 2.1	Representative values of selected mechanical properties of common reinforcement and matrix materials [11].	15
Table 2.2	Values of intrinsic stacking fault energy γ_{sf}, twin boundary energy γ_{twin}, grain-boundary energy γ_{gb} and crystal vapor surface energy γ_{sv} for various metals [36].	40
Table 2.3	Interface boundary energies (γ^{SS}) for the three types of interface [35].	45
Table 2.4	Bond lengths and binding energies of combinations of Si, C and Al atoms.	47
Table 2.5	Contact angle formed by liquid Al with various ceramic phases.	55
Table 5.1	Results of microstructural studies conducted on Case A monolithic Mg and Mg-SiC composite samples.	95
Table 5.2	Results of microstructural studies conducted on Case B monolithic Al and Al-SiC composite samples.	95
Table 5.3	Theoretical and experimental results of Case A monolithic and MMC samples.	96
Table 5.4	Theoretical and experimental results of Case B monolithic and MMC samples.	98
Table 6.1	Results of the microstructural and thermo-mechanical characterization.	114
Table 6.2	X-ray diffraction results obtained from the preheated Ti powder and the extruded specimens.	114

Table 6.2 Results of theoretical predictions of microstructural characteristics and of experimental damping measurements. 115

Table 7.1 Results of the microstructural, CTE, tensile properties and damping characterization. 127

Table 8.1 Results of acid dissolution, density, porosity, chemical analysis and grain size measurements of the Case A samples. 142

Table 8.2 Results of the microstructural and thermomechanical properties of Case B samples. 143

Table 8.3 Microstructural results of the various composite samples of Case C. 144

Table 8.4 Results of X-ray diffractometry studies conducted on extruded MMC samples of Case A. 147

Table 8.5 X-Ray diffraction results of Case C samples. 147

Table 8.6 Results of hardness and thermal expansion properties of Case A samples. 150

Table 8.7 Experimental values of various thermo-mechanical properties of the various composite samples of Case C. 150

Table 8.8 Results of room temperature tensile properties of Case A samples. 150

Table 8.9. Results of theoretical predictions and damping measurement of Case A samples. 151

Table 8.10 Results of theoretical predictions and damping measurement of the various composite samples of Case C. 152

Table 11.1 Results of the case A monolithic and composite samples. 226

Table 11.2 Results of density, CTE and hardness measurement of Mg and 226

Mg/Al_2O_3 composites.

Table 11.3 Results of damping measurement and prediction in the case of Mg and Mg/Al_2O_3 samples. 227

Table 12.1 Results of microstructural and damping studies of nano-Cu samples. 241

List of Publications

Refereed Journal Papers

[1] N. Srikanth, and M. Gupta: *Materials Research Bulletin*, Vol. 37 (2002) 1149-1162.

[2] N. Srikanth, and M. Gupta: *Scripta Materialia*, Vol. 45 (2001) 1031-1037.

[3] N. Srikanth, V. V. Ganesh, and M. Gupta: *Mat. Sci. and Tech.*, Vol. 19 (2003) 1-7.

[4] N. Srikanth, S. C. V. Lim, M. Gupta: *J. of Comp. Mat.*, Vol. 36 (2002) 2339-2355.

[5] N. Srikanth, and M. Gupta: *Physica Status Solidi (a)*, Vol. 193, no. 2, (2002) 236-245.

[6] N. Srikanth, and M. Gupta: *Key Engineering Materials*, Vol. 227 (2002) 211-216.

[7] N. Srikanth, and M. Gupta: *Composite Science & Technology*, Vol. 63 (2003) 559-568.

[8] N. Srikanth, and M. Gupta, *Materials Technology*, Vol. 17, no.4 (2002) 231-234 – Special invited review paper .

[9] N. Srikanth, L. A. Kurniawan, and M. Gupta, *Composites Science and Technology*, Vol. 63 (2003) 839-849.

[10] N. Srikanth, M. A. Thien and M. Gupta: *Mat. Sci. and Engg. A.*, Vol. 366 (2004) 38-44.

[11] N. Srikanth, C. H. Gaofeng, and M. Gupta, *J. of Alloys and Compounds*, vol. 352, (2003) 106-110.

[12] N. Srikanth, K. K. Tun, M.Gupta, *J. of Comp. Mat.*, Vol. 37 (2003) 1385-1410.

[13] N. Srikanth, S. F. Hassan, M. Gupta, *J. of Comp. Mat.,* Vol.38 (2004) 2037-2047.

[14] N. Srikanth, L. K. Hoong and M. Gupta, *J. Materials Science,* 40 (2005) 1-7.

[15] N. Srikanth, M. Gupta, *J. of Alloys and Compounds*, Vol. 394 (2005) 226-234.

[16] N. Srikanth, M. Gupta, J. *of Engineering Materials and Technology*, Vol.127, (2005) 289-294.

[17] N. Srikanth, D. Saravanaranganathan, M. Gupta, *Mat. Sci. and Tech.*, Vol. 20 (2004) 1389-1396.

[18] N. Srikanth, X. L. Zhong, M. Gupta, Materials Letters, accepted, 2005.

[19] N. Srikanth, S. Ugandhar, M. Gupta, T. S. Srivatsan, Advanced Engineering Materials, Vol. 7 (2005) 735-743.

[20] S. Ugandher, N.Srikanth, M. Gupta, S.K.Sinha, Advanced Engineering Materials, Vol. 6 (2004) 957-964.

[21] N. Srikanth, X. L. Zhong, M.Gupta, Materials Science and Technology, accepted, 2006.

[22] N. Srikanth, M. Gupta, Acta Materialia, accepted, 2006.

Conference Papers

[1] N.Srikanth and M.Gupta, Determination of Energy Dissipation in Mg/SiC Formulations Using the Innovative Method of Suspended Beam Coupled with Circle Fit Approach, SEM (Society of Experimental Method) conference in portland, USA [1] on June 3rd 2001, pp.6-8.

[2] N.Srikanth and M.Gupta, Damping Characterization of Aluminium Based Composites Using an Innovative Circle-fit Approach, Symposium L, ICMAT conference held on 3rd July 2001.

[3] N.Srikanth and M.Gupta, FEM Analysis of Energy Dissipation In Particulate Reinforced MMCs, International Modal Analysis Conference – XX held in Los Angeles, California, Feb 4th–7th 2002, organized by Soceity of Experimental Mechanics, pp. 180- 185.

[4] N.Srikanth and M.Gupta, Damping Characterization of Magnesium Based PRMMCs Using a Circle-Fit Approach, International Modal Analysis Conference – XX held in Los Angeles, California, Feb 4th–7th 2002, organized by Soceity of Experimental Mechanics, pp. 1227-1232.

[5] N. Srikanth, V. Ganesh and M. Gupta, Damping Characterization of Aluminium Based Composites Containing Interconnected-Wires Type Reinforcement, International Modal Analysis Conference –XX held in Los Angeles, California, Feb 4th–7th 2002, organized by Soceity of Experimental Mechanics, pp. 241-246.

[6] N. Srikanth, and M. Gupta, FEM Based Damping Studies of Particulate Reinforced Composites, Ansys Conference held in Singapore, Nov 5th – 6th , 2002.

[7] N. Srikanth, S. F. Hassan and M.Gupta, Energy Dissipation Studies of Mg Nanocomposites Using an Innovative Circle-fit Approach, presented in 14th International Conference on Composite Materials (ICCM)(Eds. H. Thomas Hahn, M.J.Martin), held in San Diego during July 14th-18th 2003, California, USA.

[8] N. Srikanth, M. A. Thein and M.Gupta, Effect of Milling on the Damping Behavior of Nano-Structured Copper, presented in 14th International Conference on Composite Materials (ICCM)(Eds. H. Thomas Hahn, M.J.Martin), held in San Diego during July 14th-18th 2003, California, USA.

[9] N. Srikanth, M. A. Thein and M. Gupta, Damping Characterization of Bulk Nanostructured Nickel Using an Innovative Circle-Fit Approach: Effect of Frequency, ICMAT-2004 conference held in Suntec City, 2004.

[10] N. Srikanth, X. L. Zhong, M. Gupta, Effect of the Presence of Nano-Size Alumina Particles on the Damping Property of Elemental Magnesium, The Thirteenth International Conference on Processing and Fabrication of Advanced Materials (PFAM XIII) December 6-8, 2004, Singapore.

[11] N. Srikanth and M. Gupta, Effect of the Presence of Continuous/Discontinuous/ Hybrid Reinforcement on the Damping Characteristics of Pure Aluminium Matrix, Submitted to Symposium S in ICMAT-2005 conference held in singapore on July 3-8, 2005.

[12] N. Srikanth, H. K. Feng Calvin and M. Gupta, Effect of Length Scale of Alumina Particles on the Damping Characteristics of an Al-Mg Alloy, Submitted to Symposium S in ICMAT-2005 conference in singapore on July 3-8, 2005.

[13] N. Srikanth and M. Gupta, Viscoplastic Energy Dissipation Mechanisms in Ti Particulate Reinforced Al Based PRMMCs, The 5th Ansys Asean User's conference, held in singapore, on 31 March 2005.

Chapter 1

Introduction

Introduction

Material damping characteristics are important to physicists, metallurgists, and mechanical engineers. The physicists and metallurgists are primarily interested because of the insight into microstructural characteristics that material damping provides [1-3]. Mechanical and structural engineers, however, are most interested in the effect of damping on the vibration response of structures [3-4].

From engineering perspective, uncontrolled vibrations can lead to fatigue damage, structural failure and excessive noise radiation from the structure. For example, at a resonance condition a mechanical system's response is controlled purely by its inherent damping capacity. In order to improve the service reliability of components under such dynamic vibration conditions, the judicious selection of materials exhibiting good damping apart from high specific stiffness and high specific strength becomes imperative. Intrinsic damping or passive damping reflects the ability of a material to dissipate mechanical energy. Thus a material with high damping capability will be able to reduce the vibration amplitude significantly.

The dissipation of the mechanical energy takes place through the means of different energy transformation such as mechanical energy to caloric energy. In metallic specimens, various factors that contribute to the total damping include, for example, crystalline defects, dislocation motion, grain boundary sliding, elastothermodynamic and magnetoelastic effects [4]. It has been shown in the previous studies that the contributions of the factors that govern the damping of the materials depend on frequency, temperature and strain amplitude [2-3].

Composite materials using high-strength and high-stiffness reinforcement phase in a suitable matrix are finding increasing usage in light weight structures such as in

aerospace, military, semiconductor equipments and sports industries. Among them, metal-matrix composites (MMCs) constitute a new breed of materials that can provide improved mechanical properties in terms of stiffness, strength, hardness and wear resistance [11-20] even at elevated temperature compared to that of polymer based composites. In particular, the damping levels in MMCs are high compared to the inherent damping capacity of the parent materials. Chapter 2 covers: (a) fundamentals behind the vibration damping and its uses in machine and structural design, (b) physical mechanisms that cause damping within metals and (c) types of interfaces and the effect of adding a new phase (ceramic/metal) within a metallic matrix and its influence on the damping capacity.

Generally, damping loss factor η of a material is determined experimentally by deforming a sample through a cycle and thereby determining the ratio between the energy dissipated against the total input energy. Under small deformation amplitude the damping loss factor is independent of the amplitude of the cycle, and if the material is within the elastic limits, the loss factor is related to other measures of damping factors such as logarithmic decrement δ, the half bandwidth at resonance $\Delta\omega$ and the phase angle, ϕ, which is the angle by which the strain lags behind the stress under harmonic vibration condition [14-18]. A variety of testing methods has been developed to measure the damping characteristics of a specimen. Ideally, the testing methods attempt to isolate the material damping from any outside damping sources, which may be present in the system. Chapter 3 introduces the existing damping measurement method and a new method which is based on suspended beam method coupled with a frequency based

circle-fit approach. This method is simple and elegant to determine the damping characteristics of light metal-based composites such as Al and Mg based MMCs.

In the present study, such a method is used to study the effect of the presence of a stiffer reinforcement phase (metal/ceramic) in a ductile metallic phase (Al/Mg) on the overall damping characteristics. The stiff reinforcement includes discontinuous and inter-connected type reinforcement that are either ceramic or metallic in nature. Chapter 5 introduces the effect of discontinuous ceramic particulates in MMC while chapter 6 discusses the effect of discontinuous stiff metallic particulates in a ductile matrix. Further, in chapter 7 the effect of inter-connected reinforcement is discussed. Based on the above results, it was encouraging to investigate the effect of hybrid composites that combines two or more different of reinforcements to investigate its effect on the damping capacity of the metallic matrix, which forms chapter 8. Light weight metallic materials such as Al and Mg, are getting popular in the design of dynamic mechanical systems in semiconductor manufacturing equipments, aerospace and defence related industries. Hence Al and Mg are chosen as the matrix metal for forming the MMCs in all these studies.

Apart from experimental characterization, a numerical model capable to predict the energy dissipation in metallic matrix was also formulated. Among the various damping mechanisms as explained in chapter 2, it is notable that micro-plasticity and elastothermodynamic (ETD) damping are the key mechanisms and are found to be predicable using suitable assumptions. Hence chapter 9 and 10 discusses the formulation of the mathematical model. Such knowledge to predict the properties such as stiffness, damping, strength, etc., helps to tailor a material for given working condition of a

dynamic condition viz., frequency, strain amplitude, temperature, etc. This also paves a way to devise new type of materials and optimize before investing money and time in to direct experimental work.

Published works of various researchers also shows that when the microstuctural features (such as reinforcement dimension, grain size, etc.) approaches less than 100 nm, the material exhibits novel properties, such materials are commonly known as Nanomaterials (NM) and are subject of diverse in-depth studies. Hence the present research in energy dissipation of metal based materials also extends to understand the effect of reducing the characteristic dimensions of a material (viz., grain size, particulate size, etc.) as it approaches from a micron size to a nano size. Chapter 11 and 12 discusses the effect of the including nano particulates in a metallic matrix while chapter 12 discusses the effect of bringing the grain size toward nano-regime.

Chapter 2

Literature Review

2.0 Motivation for Damping Studies

Free vibration is a manifestation of the repetitive interchange of kinetic and potential energies among components in the system. Thus vibration is defined as a periodic motion about some equilibrium point and the rate of vibration cycles is termed frequency. Vibration is commonly expressed using the amplitude, frequency and phase of a series of wave forms that are sinusoidal in nature [1-4].

Vibrations may be excited by forces within a system or may be transmitted through an external source. All mechanical equipment in motion generates a vibration profile, or signature, that reflects its operating condition. This is true regardless of speed or whether the mode of operation is rotation, reciprocation, or linear motion. There are vibrations that are added purposefully in a dynamic system to perform a specific work e.g. ultrasonic transducers, loud speakers, vibratory bowls, magnetic stirrer, etc. while there are unwanted vibrations which may make the system: (1) unpleasant or harmful, (2) susceptible to fatigue, (3) difficult to control, and (4) slow in terms of increasing the machine's settling time.

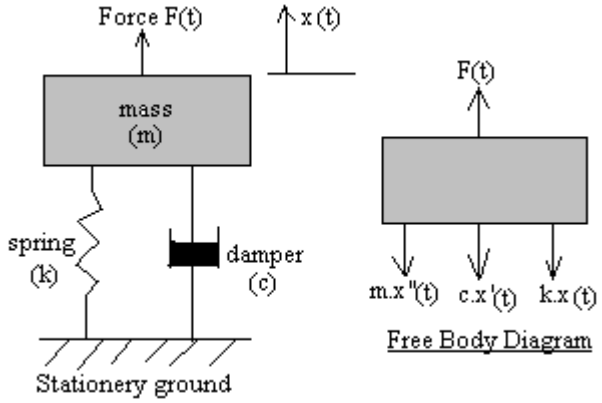

Fig. 2.1 Various forces acting in a typical single degree of freedom and the associated free body diagram [1].

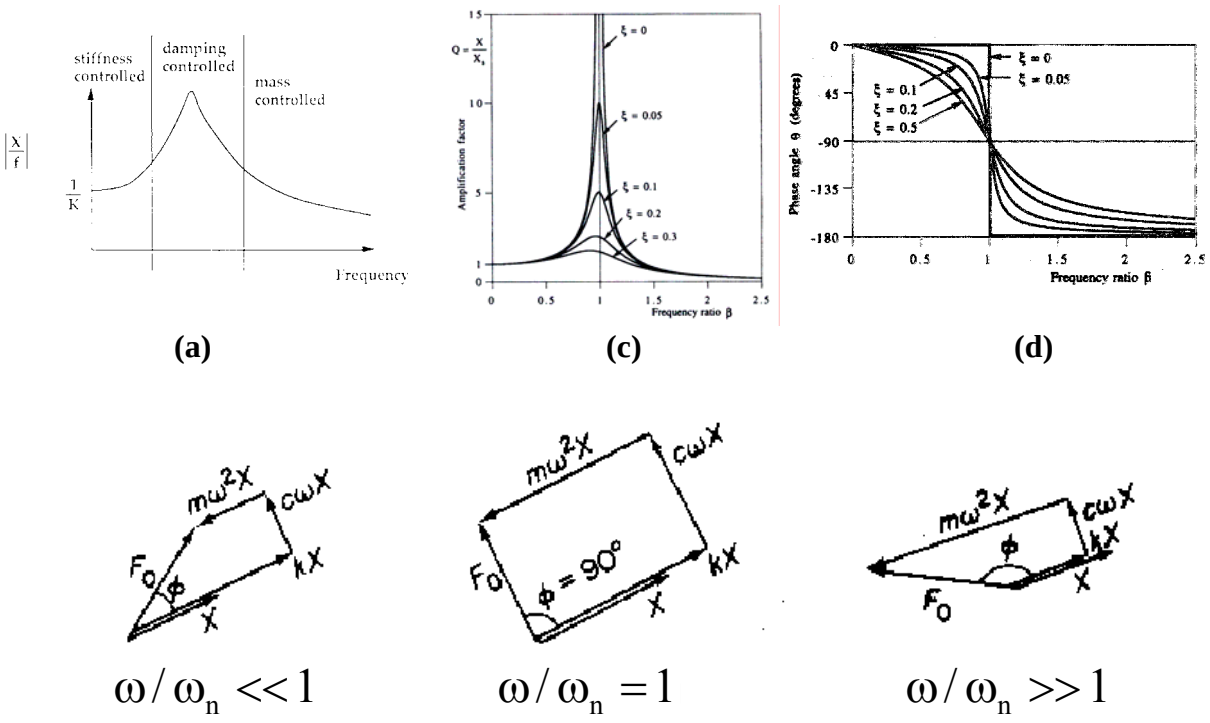

Fig. 2.2 (a) Influence zone of mass, spring and damping in a SDOF (b) vector diagram showing how the various forces varies with frequency in terms of magnitude and direction (c) effect of damping on the amplification factor (d) effect of damping on phase lag between applied force and induced displacement [1].

Design of static structures requires knowledge of elastic properties of materials that are used in predicting deformation and failure of materials. It is required to take into account the rigidity of the materials and the probability that a certain amount of energy will accumulate within the structure during service life of the structure. But in a dynamic system, according to Newton's law of motion the applied force F(t) is equal to the sum of inertial force which is equal to the product of mass and acccelertion ($mx''(t)$), damping force which is equal to the product of velocity and dashpot coefficient ($cx'(t)$) and spring force which is equal to the product of spring stiffness coefficient and the

displacement ($kx(t)$). The notations are described for a typical single degree of freedom (SDOF) in Fig. 2.1. In frequency domain the dynamic equation can be written as follows:

$$m\omega^2 x + c\omega x + kx = F(\omega) \tag{2.1}$$

The undamped resonant frequency is the square-root of stiffness (k) over mass (m) of the system $\left(\omega_n = \sqrt{k/m}\right)$. Thus we see that at resonance, the inertial forces and the spring forces are equal and opposite to each other and hence cancel. The only force that works against the applied dynamic force is the damping force close to resonance. Fig .2.2 (a) and (b) shows the zones of influence of mass, stiffness, damping in a SDOF. Hence in a mechanical system to avert the serious consequences of resonance the damping is varied as shown in Fig. 2.2(c), such as in high speed machines where the bandwidth of the control system is high (>2000Hz), hence all the resonances are excited due to simultaneous provision of energy to the dynamic system for the complete frequency range within the bandwidth. Compared to the present discussion of SDOF, in reality, component or parts are made of millions of atoms that are interconnected by inter-atomic forces which act as multi-degree of freedom system and hence modeling a component such as beam or plate as a rigid mass with few springs is a gross assumption. But this is essentially done by researchers to ascertain the lowest fundamental resonant frequency [1]. Thus even in the case of a simplistic beam or plate for example, the stiffness depends on the deformation pattern such as bending, torsion, axial, etc. and their respective higher modes of deformation or combinations [1]. Finite element method becomes useful to study such mechanical components to predict the innumerable vibration frequencies and the corresponding mode of vibration which is a pattern with which it deforms [5]. For example the various vibration modes are shown in Fig. 2.3 for a epoxy reinforced carbon

fiber plate (with a density of 1.44 g/cc) with a dimension of 50cmx40cmx7.6mm with a orthotropic elastic modulus of 75.69 GPa, 28.37 GPa and 23.32 GPa along fiber direction, perpendicular to fiber and in thickness direction, respectively.

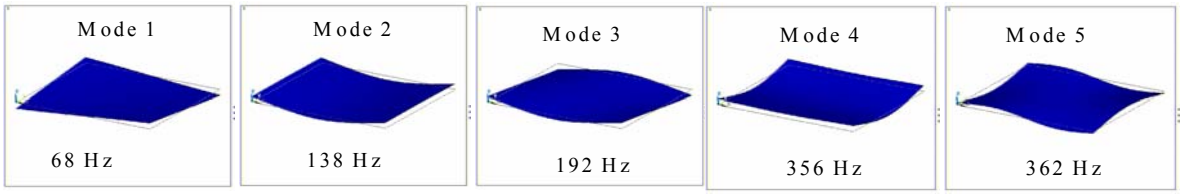

Fig. 2.3 Various vibration modes of an orthotropic plate predicted and confirmed using experiments.

When a structure is excited by a time varying force such that it's frequency of vibration matches the resonant frequency and direction of force is such that it matches that mode of vibration, energy is transferred efficiently to the particular system's resonance and hence the system vibrates violently such that only the damping forces are the saviors. For example, in a single degree of freedom system (SDOF) the damping controls the resonance amplitude, as illustrated in Fig. 2.1. One good example from a practial scenario was the tacoma bridge which was suspected to be excited in torsional resonance by periodic vortex shed by the wind [6]. The additional causes are suspected to be the negative damping effect. Nevertheless, it is confirmed that the bridge had a torsional resonance frequency of 0.2 Hz and hence twists back and forth in a torsional mode, along with the close mathching of the wind's vortex shedding frequency with the bridge's torsional frequency (see Fig. 2.4).

Space applications are known to have no aero-damping atmosphere and hence totally rely on the passive damping capacity of the material and active damping techniques. Since passive damping is the most reliable, designers expect to maximize this in their

design. A good example is the Canadarm (see Fig. 2.5) which played a critical role in retrieving the Hubble telescope, placing it in the shuttle Endeavour's cargo bay for repairs, and releasing it in space afterwards [7]. The final product is a 15.2-meter-long robot arm analogue to the human arm, with copper wires as nerves, carbon fiber reinforced tubing as bones, and electric motors as muscles. For example, when the space shuttle accelerates or decelerates or turns the system exhibits transient vibration and exhibits free vibration during which passive damping ability of the material acts as a savior to minimize the settling time efficiently and thus enhance the useful productive time of the system during each operation.

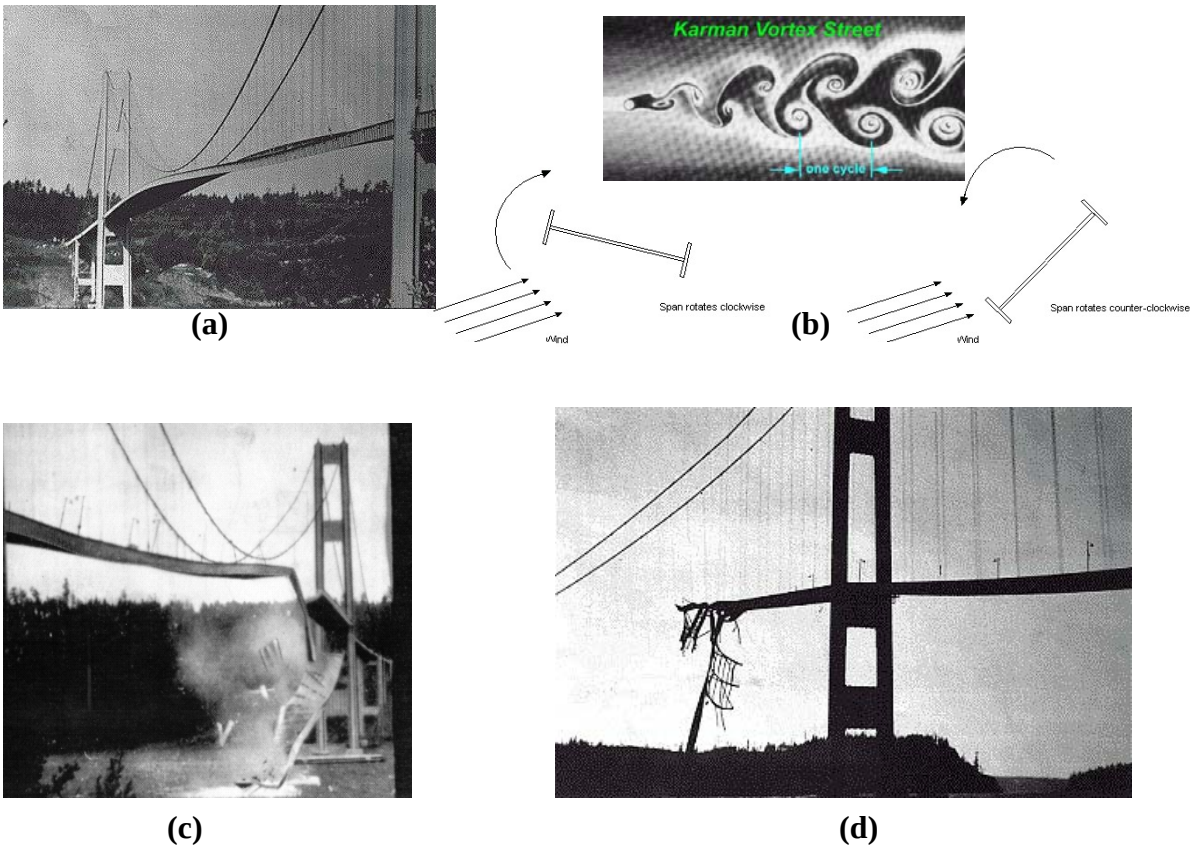

Fig. 2.4 Wind induced failure of Tacoma Narrows bridge: (a) torsional vibration (b) vortex shedding and swinging of the structure, (c) and (d) final collapse [6].

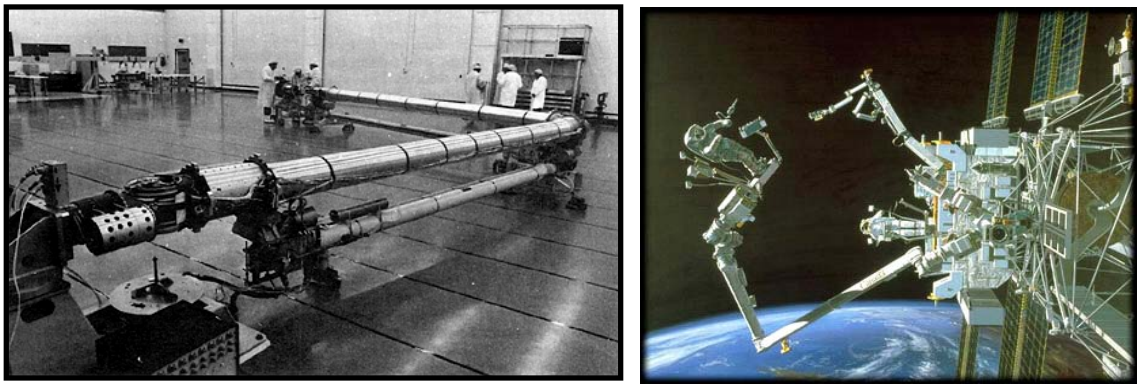

(a) (b)

Fig. 2.5 (a) Canadram arm under assembly and (b) arm under operation [7].

2.1 Damping capacity of common engineering materials

Ashby studies [8] shows that for various monolithic materials in general, the stiffer the material better is its strength, e.g. ceramics are better than polymer, see Fig 2.6 (a). But it can be observed that the stiffer the material, lesser the inherent damping capacity too, refer Fig. 2.6 (b). For example, a silicon carbide ceramic exhibits a elastic modulus of 400GPa while it's damping capacity measured in terms of loss factor is around 0.0001, while in the case of plexiglass plastic the elastic modulus is around 31

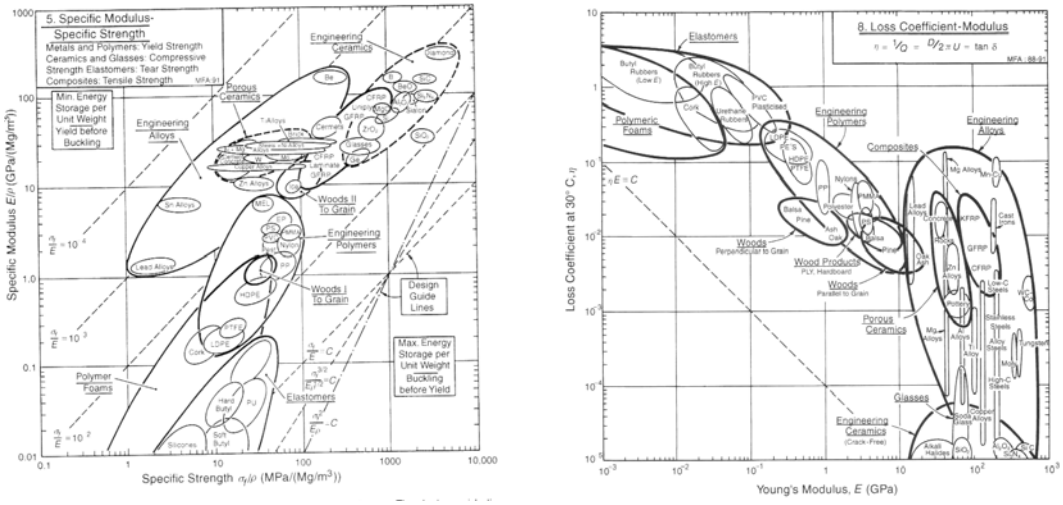

(a) **(b)**

Fig. 2.6 Variation of various engineering materials: (a) specific modulus versus specific strength (b) loss coefficient versus Young's modulus [8].

KPa while the damping loss factor is around 0.02. In between these two extremes of ceramics and polymers, pure metals fall in general. Thus for example, pure magnesium has an elastic modulus of 40GPa and a damping loss factor of 0.005 [4]. Hence design engineers look at the product of stiffness and damping as a measure to compare materials during selection for a design.

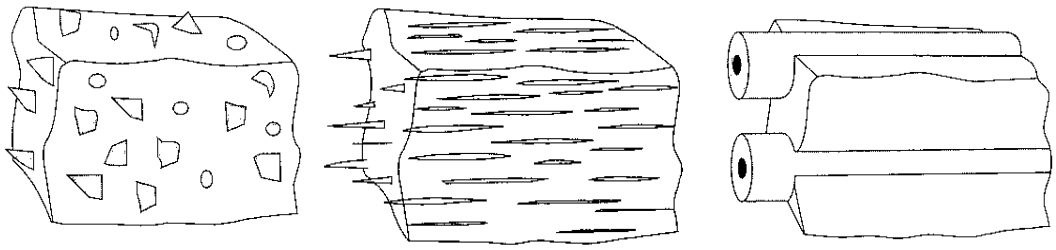

(a) **(b)** **(c)**

Fig. 2.7 Matrix reinforced with: (a) discontinuous particles (b) whiskers and (c) continuous fibers [12].

2.2 The Metal Matrix Composite Concept

The new class of heterogenous materials called composite materials is thus aimed in achieving a better stiffness and damping characteristics. Hence fiber reinforced plastics were designed which had better properties such as carbon fiber reinforced epoxy composite which has an elastic modulus of 100GPa and a damping loss factor of 0.025 [9-10]. But the basic drawback of such materials is their poor performance at high temperature mainly due to their softening at the glass-transition temperature (T_g) during which the elastic modulus drops by about ten times. Hence metal-based composites were designed which aimed in reinforcing a better damping ductile metallic matrix (such as magnesium) with a stiffer phase (such as silicon carbide). A further classification can be made on the basis of the form of the reinforcement material used – such as particulate, whisker or fiber composites (as shown in Fig. 2.7).

MMCs are a broad family of materials aimed at achieving an enhanced combination of properties. While the matrix can be any metal or alloy, most interest has been shown in the lighter structural metals; in which, improvement in mechanical properties has been the primary objective.

Various definitions of MMCs exist [11-13]. In some cases, the definition has been limited to materials where the volume fraction of the added material exceeds 10%. This definition excludes oxide dispersion strengthened metals with volume fractions of added materials of around 5%. On the other hand, an alternative definition considers MMCs to consist of materials whose microstructures are synthesized artificially, to form component phases as opposed to conventional metals whose microstructures are obtained by naturally occurring phase transformation. This definition would include mechanically alloyed oxide dispersed alloys but would not include in situ grown eutectic composites.

Much of the progress in the field of MMCs is closely linked to developments in reinforcements for incorporation in metallic matrices. To date, the attainment of higher strength and stiffness has been the prime motive behind the development of MMCs. Other important improvements in parameters such as damping capacity, component weight, wear resistance, thermal expansion and high temperature capabilities can be achieved by suitable combinations of reinforcement and metallic matrices. At the same time, the desirable properties of metals such as ease of fabrication, ductility, and high thermal and electrical conductivity should preferably be maintained. Furthermore the desired combination of properties needs to be obtained at minimum component cost.

It is possible to develop new materials with a unique combination of properties previously unattainable with conventional materials. In principle, judicious choice of

reinforcement type and reinforcement content, for example, permits the attainment of a desired thermal expansion coefficient. This ability to engineer materials with specific properties for specific applications represents a great potential advantage of composites.

Table 2.1 Representative values of selected mechanical properties of common reinforcement and matrix materials [11].

Reinforcement & Matrix Material	**Modulus (GPa)**	**Density (g/cm^3)**	**Thermal expansion ($10^{-6}/ ^oC$)**	**Melting point (^oC)**	**Tensile strength (MPa)**
SiC platelets	480	3.2	-	-	10000
SiC whisker	840	3.2	-	-	21000
SiC fiber	450	3.2	4.8	-	2300
Al_2O_3 whisker	250	4.0	-	-	15000
Al_2O_3 fiber	470	4.0	6.2	2053	2000
Boron	420	2.6	8.3	-	3500
Borsic (SiC coated B)	400	2.71	5.0	2100	3100
E-Glass fiber	72	2.54	-	-	3400
AlN	345	3.26	3.3	-	-
Si_3N_4	297	3.18	1.5	-	650
W	410	19.4	4.5	3410	1520
Ti	110	4.4	9.5	1650	1170
Zn	70	6.6	27.4	390	280
6061 Al	70	2.8	23.4	580	310
AZ31B Mg	40	1.7	25.2	570	280
Cu	120	8.9	17.6	1080	340

It is also possible to selectively reinforce particular areas of components, thus providing advancement of material properties only in areas where it is truly necessary. The multitude of possible combinations of metal matrices and reinforcements in various forms, however, means that an enormous database of properties will be required for their

full characterization. Table 2.1 lists the various materials with their properties that have been used successfully as reinforcement and matrix.

2.3 The meaning of anelasticity

An ideal elastic material obeys Hooke's law which states that the applied stress is proportional to strain and the constant of proportionality is called modulus of elasticity. To define anelasticity, three postulates are defined [14-18]:

1. For every applied stress state there is a unique equilibrium value of strain and vice versa.
2. The equilibrium response is achieved only after the passage of sufficient time.
3. The stress-strain relationship is linear.

It will be recalled that a thermodynamic substance is one, which can assume a continuous succession of unique equilibrium states in response to a series of infinitesimal changes in an external variable, hence thermodynamic solids satisfy postulate 1 and 3. The second postulate of anelasticity means that in response to a change in the applied mechanical forces, time is required for the equilibration of an anelastic material. In general, the self-adjustment of a thermodynamic system with time toward a new equilibrium state in a response to a change in an external variable is termed relaxation. Specifically, where the external variable is mechanical (a stress or strain) the phenomenon is called anelastic relaxation (or mechanical relaxation). This is possible only when the external manifestation of relaxation occurs with the adjustment of internal variables to a new equilibrium values. Thus anelastic relaxation is a thermodynamic phenomenon, which

arises from a coupling between the stress and strain via certain internal variables that can change to a new equilibrium values only though kinetic processes such as diffusion.

2.4 Measures of damping

Damping mechanism takes part in various physical phenomena due to energy dissipation and researchers tend to use many parameters to measure the effectiveness of the damping. These parameters are generally defined elegantly from a lumped spring-mass-damper type system that has a single degree of freedom in free and forced vibration condition. These common damping quantities are [1-3, 19]:

- Loss factors of a structure made of a particular material (η) are defined as the fraction of a system's vibration energy that is dissipated per radian of the vibratory motion at the structures' resonances.
- Specific damping capacity of the vibration system (ψ) represents the ratio between the vibration energy dissipated per cycle and the maximum elastic energy stored during the cycle.
- Decay rate of free vibrations (D) expressed in decibels per second (dB/sec) represents the rate of reduction of the vibration level during exponential decay.
- Logarithmic decrement of free vibrations of the system (δ) is defined as the natural logarithm of the ratio of the amplitudes of any two successive cycles of the decaying vibration.
- Damping ratio or damping factor (ς) is defined as the fraction of critical damping under a equivalent viscous damping, and is expressed as percent of critical

damping $\left(\varsigma = c/c_c\right)$, where c is viscous damping coefficient and c_c is critical (viscous) damping coefficient.

- The quality factor Q of the dynamic system is the resonant amplification factor which expresses the sharpness at the resonance. For example, sharp tall resonance peak means minimal damping while blunt and wide spread resonance peak means higher damping. Mathematically this is shown as $Q = \left(\omega_n/\left(\omega_2 - \omega_1\right)\right)$, where ω_n is the resonance frequency, ω_1 & ω_2 are the sideband frequencies at 3 dB below the peak amplitude of resonance.
- For materials with low damping such as metals, $\varsigma < 1, \eta < 1, \delta < 1, 2Q < 1, \psi < 4\pi$, all these parameters are inter-related as follows:

$$\delta = 2\pi\varsigma = \frac{\pi}{Q} = \pi\eta \qquad (2.2)$$

In addition, other measures of damping of vibratory systems are also related [19]:

- The reverberation time (T_{60}) is the time within which the vibration level of a system vibrating freely at resonance frequency decreases by 60 dB (i.e. the amplitude decreases to one-thousandth of its initial value).
- Spatial decay, expressed in dB per wavelength, represents the reduction in the steady-state vibration level with distance that occurs along a long beam vibrating in flexure.
- Hysterisis loop, a plot of the amplitude of instantaneous force versus instantaneous displacement x with distance or the applied stress versus induced strain during steady state forced vibration, is equal to the energy dissipated in the vibratory system.

From the above it is noted that loss factor and damping capacity are defined directly in terms of the cyclic energy dissipation. Also, none of the measures of damping discussed above is specific to one form of damping mechanism and is thus universal.

2.5 Mathematical model of Damping Behavior

Literature review shows coulomb was the first to observe damping in 1784 under torsional vibration condition [1]. Since then much investigation have been made and various damping mechanisms were discovered in metallic materials that were first compiled and published by Lazan [18] in 1968. These mechanisms are classified as linear and non-linear. Linear materials can be modeled with classical linear components. For example, in the classical linear damping, the liner dashpot is used to mimic the inner viscous damping force (F_d=c.v) which is proportional to the velocity (v) while the proportionality constant 'c' is the dashpot coefficient. Thus the Kelvin-Voigt model shown in Fig. 2.1 predicts the material behavior like a spring and dashpot in parallel. Under one cycle, the energy dissipated (D) is given by [5]:

$$D = \int_0^{2\pi} c\left(\dot{x}\right)^2 dt = \pi c\omega X_o^2 \tag{2.3}$$

where dot denotes derivative and X_o is the maximum amplitude. The maximum potential energy stored in the system is given by [2]:

$$U = \tfrac{1}{2} k X_o^2 \tag{2.4}$$

The loss factor (η) of the Kelvin-Voigt model is given by equation (2.1) as follows:

$$\eta = \frac{D}{2\pi U} = \frac{c\omega}{k} \tag{2.5}$$

Thus based on this model the damping is proportional to frequency but independent of vibration amplitude (or strain amplitude).

More elaborate models have been developed to mimic the behavior of a material so as to account various relaxation mechanisms. Among them a “standard linear solid" introduced by Zener [15] is a popular one which describes the stress-strain constitutive law for the solid material as:

$$\sigma + \tau_{\varepsilon}\dot{\sigma} = E\left(\varepsilon + \tau_{\sigma}\dot{\varepsilon}\right) \tag{2.6}$$

where σ, ε, E are the stress, strain and elastic modulus, respectively, τ_{σ} and τ_{ε} are the relaxation time under constant stress and strain, respectively, and the dots represent derivative. Such models are capable to model multiple relaxations that occur due to the simultaneous operation of different damping mechanisms which are explained in the forthcoming section.

2.6 Material Property Measurements

To control vibration problems effectively in structures it is essential to know the damping properties of the structural materials used. These properties can be determined by various techniques [19]. Basically there are four major categories of apparatus for the investigation of anelastic phenomena. All these methods put together are capable to provide a frequency range that effectively starts from 10^{-5} to 100GHz. As a broad generalization, relaxations that involve atomic migration are generally investigated at kilohertz frequencies or below, so as to place the relaxation in a convenient (not too high) temperature range. On the other hand, high frequency techniques (>1 MHz) are usually required for dislocation, electron and phonon studies so as to match the applied frequency

to the short relaxation times involved in these cases [20]. Similarly, from engineering applications point of view, civil structures are subjected to low frequencies from 0.1-50 Hz, while mechanical moving systems such as turbo-engines, machinery, pumps, etc experience vibrations at 1-2500 Hz. Generally, damping characteristics are required optimally at 1000 Hz which is not generally available. The most notable methods are the dynamic mechanical analyzer (DMA), resonant beam test and the torsion test [1, 16, 21, 22] (see Fig. 2.8) which can cater to only 50-100 Hz. Other test procedures, such as Rheovibron and the progressive wave technique are also used. The resonant beam technique for determining damping properties of materials is the procedure endorsed by the ASTM (American society for Testing and Materials) and forms the basis of ASTM E756-80. In forthcoming chapter, the new method developed in the present work is described which utilizes a free-free type suspension that exhibits minimal energy dissipation to surrounding due to holding the sample at its vibration nodes.

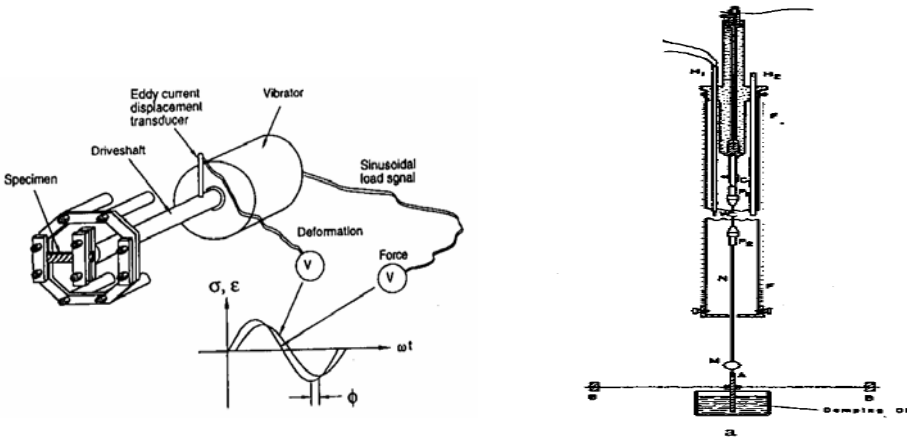

(a) **(b)**

Fig. 2.8 (a) Dynamic mechanical analyzer with a cantilever type sample holder used by Zhang [21] and (b) Torsion test setup used by Ke [22].

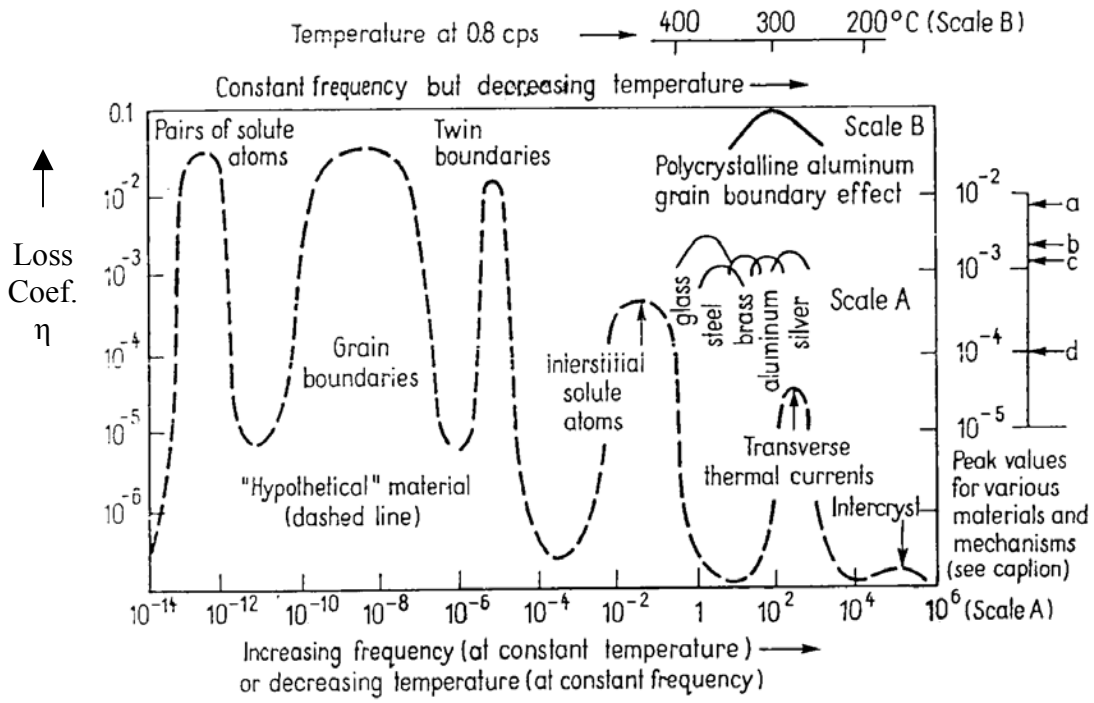

Fig. 2.9 Internal friction or damping peaks for hypothetical material compared against several metals due to different microstructural mechanisms such as Cu-Mn alloy (movement of twin interfaces), German silver (thermal currents in transverse vibration), Alpha brass (stress induced by preferential orientation of axis joining pairs of solute atoms) and Polycrystalline brass (intercrystalline thermal currents) [2].

2.7 Damping in Monolithic Metals

A better understanding of the internal friction mechanisms in metals helps us in the selection of the correct matrix material for the metal matrix composite. During recent years much focus was placed to understand the micromechanisms that cause the damping behavior (also called anelastic behavior) [14-21]. Studies show in general, internal friction of metals varies as a function of temperature, strain amplitude and strain rate (or frequency of vibration) and in various critical ranges of these variables sharply peaked values of the loss coefficient are often observed which can be associated with some physical mechanism operating in the materials under cyclic stress in such a way, so as to dissipate maximum energy under some optimum condition. The physical mechanisms

operative can generally be expressed in terms of the relaxation times such as the τ_s parameter of the spring-dashpot model (as in Fig. 2.1) which is equal to $\sqrt{\eta/k}$ [1].

Many different anelastic mechanisms that produce internal friction peaks are discussed in the following paragraphs. The peaks are commonly known as relaxation peaks and occurs at certain combinations of frequency and temperature in the damping curve (refer Fig. 2.9), and also results in a change in elastic modulus [4, 18].

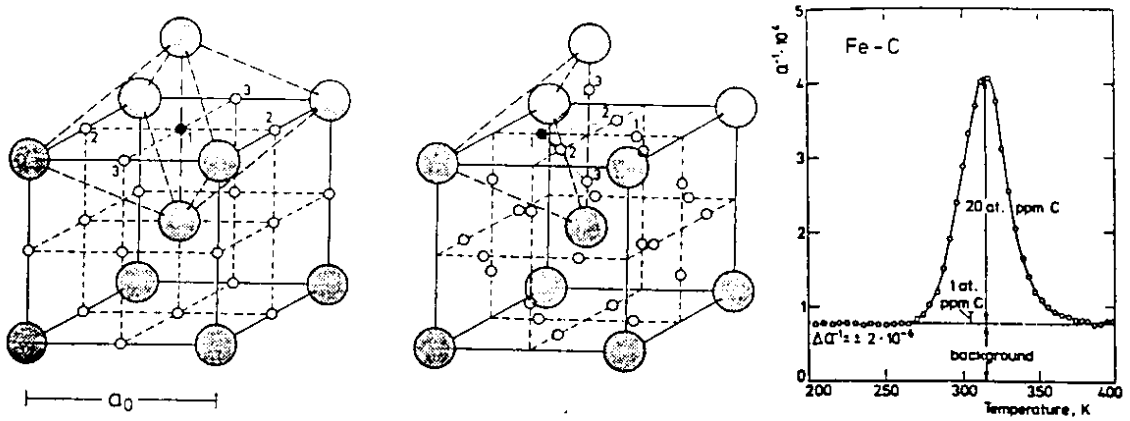

(a) **(b)** **(c)**

Fig. 2.10 Positions of the distribution of interstitial atoms in the cubic body centered lattice: (a) octahedral positions (b) tetrahedral positions (c) variation of snoek damping in Fe matrix with 20 ppm of carbon [4].

2.7.1 Point defect relaxations: Crystalline materials generally include many types of single defects or impurities as well as clusters of several such defects on adjacent or nearby sites. This produces a local non-symmetry in the crystal. As a consequence of this lowering of symmetry, sets of crystallographic equivalent positions or sites exist and the point defects can occupy these in the crystal. This type of imperfection leads to anelastic behavior. Under cyclic stress, such "defective microstructures" produce hysteretic loop or damping effects that include relaxation peaks of the type discussed previously. The Snoek effect [14, 16, 18] is associated with the presence of interstitial carbon or nitrogen

impurity atoms in iron and their motions under cyclic stress have been well studied. Based on the works of Nowick and Berry [14], the operative micromechanisms have been well identified for point defect relaxation and equations defining their characteristics have been well developed.

Based on the research of Snoek [14], in steel under no external load, carbon or nitrogen atoms reside at octahedral position (see Fig. 2.10). But when stress is applied the atoms drift to the stretched interstitial positions from the compressed octahedral positions. The length of the jump in repeated loading is $x = \left(a\sqrt{2}\right)/2$, where 'a' is the lattice spacing. The diffusion process decides the time t required to travel the distance x which is given by the parabolic equation $\left(x^2 = Dt\right)$, where D is the diffusivity coefficient in α-iron. The time τ_1 required for a single diffusion jump is described as follows:

$$\tau_1 = \tau_0 e^{-q/kT} \tag{2.7}$$

where τ_0 is the physical constant, k is the boltzmann constant, T is absolute temperature, and q is the energy barrier which the carbon or nitrogen atom should overcome so as to shift from one interstitial position to the other. Under low frequency, the time provided by the external stress is larger than the time constant τ_1 for that particular temperature, and hence the interstitial atom has time to move without any phase lag between the induced strain and the applied stress. Similarly under higher frequency of applied stress, the time provided for the interstitial atom is very short than the time constant τ_1 and hence the atom remains in their original sites and hence no phase lag between the stress and strain. But when applied stress oscillates at a frequency such that the time provided is equal to the time constant τ_1 for jumping, the phase lag is maximum, which is seen as the

highest internal friction. Such phenomenon is seen in many materials, for example, nitrogen in iron, nitrogen in tantalum, nitrogen in vanadium and niobium, etc [4].

In addition, a pair of defects also contributes to the formation of internal friction due to their orientation and position changes due to external stress variation. The pair can be vacancies, substitutional and interstitial atoms or their combinations. This is because a pair of defect may have a non-uniform deformation which tries to orientate to the external force so as to minimize its energy and thus results in internal friction. For example, a pair of substitutional atoms in a cubic lattice results in tetragonality of the lattice due to inhomogenity in deformation in their vicinity. Under no external stress they are orientated according to the individual crystal orientation. After the external stress, they orient in line with the external stress. This is observed in alloys such as Cu-Zn and Ag-Zn [14].

2.7.2 Grain Boundary Viscosity: Grain boundaries in metals are in a relatively disordered state and thus display viscous-like properties [14, 16, 18, 21]. The unit energy dissipated in grain boundaries under cyclic shear stress or strain is therefore larger, in general, than that dissipated within the grain. The internal friction associated with grain boundary shear depends on the shear and relaxation properties of the grain boundary which is a function of temperature and also on strain rate (or frequency). Fig. 2.11 (a) shows the effect of temperature and frequency on internal friction associated with grain boundary shear, using hypothetical stress-strain loops. Considering only the shear effects, the energy dissipated by grain boundary motion is proportional to the product of shear stress and anelastic shear strain. At high frequencies of vibration (or at low temperature)

the shear stress across a grain boundary can relax only slightly during a strain cycle and the material remains reasonably elastic. Thus, although the shear stress may be large, the anelastic shear strain is small, and the hysteresis loop is narrow. This is illustrated as case (1) in Fig. 2.11 (a) [18] and the loop shown has small damping. By contrast, at low frequency (or at high temperature) large stress relaxation can occur under cyclic strain and the shear stress is correspondingly reduced. Here again the area within the loop is small as shown by curve (3) in Fig. 2.11 (a). At some intermediate condition, however, the rate of stress relaxation is optimum for producing the maximum area within the hysterisis loop as shown in Case (2) of Fig. 2.11 (a).

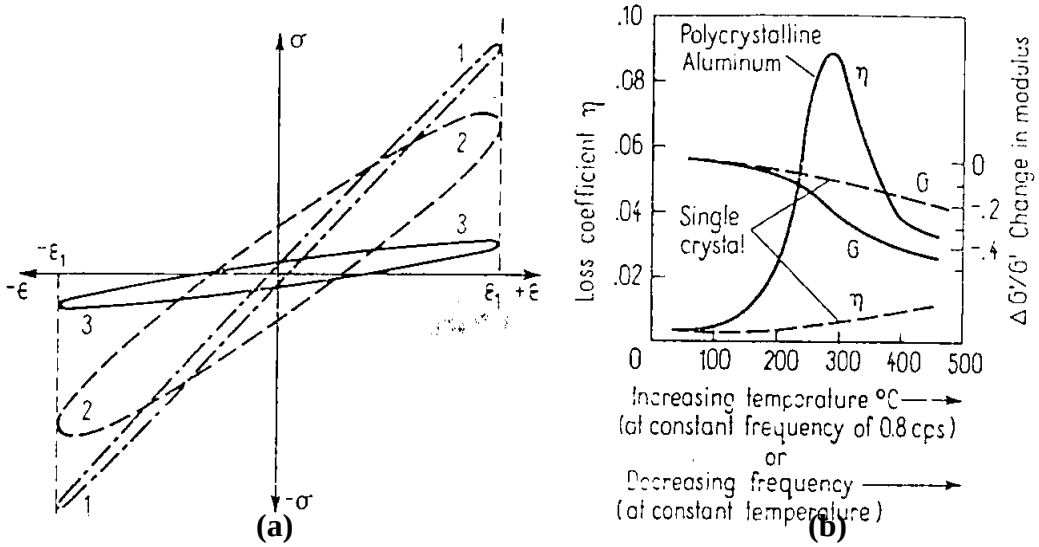

Fig. 2.11 Effect of temperature and frequency on internal friction associated with grain boundary shear: (a) hypothetical stress-strain loops of case 1 which correspond to high frequency or low temperature, case 2 which correspond to optimum combination to cause relaxation peak and case 3 which correspond to low frequency or high temperature [18] and (b) experimental results of grain boundary induced damping results of aluminium [22].

Additionally, the elastic modulus E also changes significantly in the critical regions of temperature and frequency, which produce relaxation effects. This is illustrated in Fig. 2.11 (a) by the decrease in average slope of the loops with increasing

temperature. Based on the studies of K$\hat{e}$ [22] on polycrystalline aluminium as a function of frequency or temperature are shown in Fig. 2.11 (b). The curve for single crystal aluminium displays no such peak (see dashed lines), but relaxation phenomena are very evident in the polycrystalline aluminium. The experimental results shown are consistent with predictions made by a theory based on grain boundary effects.

2.7.3 Macro-Thermoelasticity: If a specimen is stressed non-uniformly and rapidly (i.e., adiabatically), local temperature differences are produced which depends upon the local stress levels and properties in the specimen [15, 18, 21]. The results at temperature gradients within the specimen tend to produce heat flow unless the load is quickly released to remove the temperature gradients. For an isotropic material, it can be shown that:

$$\left(\frac{\partial T}{\partial \sigma_{kk}}\right)_S = -T\frac{\alpha}{C} \tag{2.8}$$

where T is the absolute temperature, σ_{kk} is the hydrostatic stress, the S subscript denotes an isentropic process, α is the linear coefficient of thermal expansion, and C is the specific heat per unit volume. It is important to note that this temperature change is independent of the shear stresses [15]. Under high-frequency vibration (period much shorter than the time required for significant heat flow) the process remains adiabatic and reversible; thus the cyclic heat flow is insignificant and the observed damping is small. By contrast, at very low frequency, the process remains isothermal, but still reversible, and again no significant damping energy is dissipated. If, however the period of the cyclic stress is comparable with the time required for significant heat flow along the temperature gradients produced (from one side of the specimen to the other, for example,

in the case of a vibrating beam), an irreversible conversion of mechanical energy into heat occurs and damping is observed.

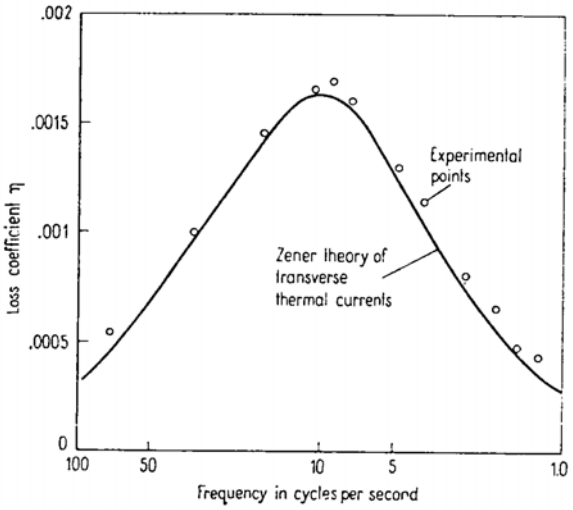

Fig. 2.12 Damping caused by transverse thermal currents in a beam of German Silver [24].

Macro-thermoelastic damping occurs in many types of members and vibrations. An example of such damping under flexural vibrations is illustrated in the data on a German silver beam shown in Fig. 2.12. Both the experimental points and the theoretical curve illustrate the general character of the damping or relaxation peak. Based on the temperature difference between the expanded and compressed sides of the bar and the resulting heat flow across the depth d of the bar, the following theoretical equations can be derived:

$$\eta = \Delta_r \frac{\omega\tau_s}{1+\omega^2\tau_s^2}$$

$$\tau_s = \left(\frac{d}{\pi}\right)^2 \frac{\rho C_p}{K} \qquad (2.9)$$

$$\Delta_r = \frac{\alpha_T^2 E_T T}{\rho C_p}$$

where the (ρC_p) is the specific heat per unit volume, K is thermal conductivity, ω is frequency of vibration, α_T is the temperature expansion coefficient, E_T is the young's modulus at constant temperature, and T is absolute temperature. The frequency dependence of equation (2.9) is such that a resonant type peak is reached at $\omega = 1/\tau_s$.

Similar theromoelastic effects can be demonstrated in bars vibrated longitudinally [15]. Peak values have also been calculated for cold rolled mild steel, for half hard brass and for 2024-T4 aluminium alloy and 6061-T6 aluminium alloy [23].

2.7.4 Micro-thermoelasticity: Thermal currents that lead to internal friction can also exist on a microscopic scale. An example of this is observed in polycrystalline materials. Individual crystals in an aggregate are generally anisotropic with regards to both thermal and mechanical properties. Neighboring grains generally have different orientations and therefore different mechanical thermal properties in the direction of principal stresses in the specimen. Local temperature gradients are therefore produced even under macroscopically uniform axial stress. In materials under cyclic stresses micro-anisotropy can cause cyclic micro-thermal currents across grain boundaries. This process leads to energy dissipation [15, 18]. At certain combinations of temperature and frequency the energy-dissipation effects are maximized and relaxation peaks are observed.

2.7.5 Magneto-mechanical damping: This phenomenon results in ferromagnetic materials due to movement of Bloch walls under time varying external stress. The effect of this damping can be suppressed by applying a strong field to the loaded material. For

example, a magnetic flux with an intensity of $2x10^{-4}$ A/m greatly decreases the contribution in iron and mild steel [18].

2.7.6 Dislocation Based Damping Mechanisms: Dislocation motions, caused by resolved shearing stress along glide planes, can occur even at low stress (local microscopic stress may be large even though macroscopic stress is small) [24-28]. As stress amplitude is increased, rather complex dislocations can be produced and it is usually difficult to determine uniquely what dislocation mechanisms are responsible for the damping properties observed. Under these circumstances it is usually more efficient to use a continuum mechanics point of view for engineering problems. Nevertheless, knowledge of such mechanisms currently accepted as a cause of dislocation damping might be helpful in understanding some of the phenomenology observed in structural metals and is described in the following paragraphs.

Dislocation motions contribute to the total strain produced by a specified stress [25]. Under alternating stress, the dislocation component of the strain may lag behind the applied stress (Bordoni relaxation), thus forming a hysteretic loop and contributing to the dissipation of energy. Estimates of the magnitude of this effect for typical dislocation densities, assuming that the dislocations are perfectly mobile with no restrictions on their motion, yield a much larger value than that observed experimentally. Impediments to the motion of dislocations or other types of interactions might therefore be present. Examples of such impediments are pinning points, network points, jogs, and other dislocations.

To dissipate energy the dislocation motion must lag behind the applied stress. In one model the dislocation is assumed to be viscously damped as it moves through the

electron or phonon gas. In other models impediments such as mentioned above are assumed to produce a jerky motion of the dislocation which leads to a phase lag, both at low stress amplitude and high stresses (catastrophic unpinning) [25].

One generally accepted dislocation model for damping is that proposed and developed by Granato and Lucke [29]. In other models dislocation motions are viewed as being analogous to a vibrating string in a viscous medium, and an equation for the motion can be written considering the effective mass per unit length and the effective tension in the dislocation [29] as follows:

$$Q^{-1} = Q_a^{-1} + Q_f^{-1} \tag{2.10}$$

$$Q_a^{-1} = C_1 \frac{\rho b^2}{\varepsilon_o} \exp\left(-\frac{C_2}{\varepsilon_o}\right) \tag{2.11}$$

$$Q_f^{-1} = \frac{C_3 \rho f^2}{b^2} \tag{2.12}$$

$$C_1 = \frac{\omega \Delta_o L_N^3 K \rho_m \varepsilon'}{\delta \pi \omega_r L_c^2} \tag{2.13}$$

$$C_2 = \frac{K \varepsilon' a}{L_c} \tag{2.14}$$

$$C_3 = \frac{\pi^2 B \Delta_o^2 L_c^4}{2 \delta \omega_r G} \tag{2.15}$$

$$K = \frac{32G}{\pi^2 p^2 RE} \tag{2.16}$$

$$\Delta_o = \frac{4(1-\upsilon)}{\pi^2} \tag{2.17}$$

where Q_f^{-1} is the frequency independent part, Q_a^{-1} is the strain amplitude dependent part, ρ is the dislocation density, b is burgers vector, ε_o is strain amplitude, f is frequency, ω is angular frequency, ω_r is the resonant frequency, L_N is the dislocation network length that depends on the interfiber or interparticle spacing in the cases of MMCs, L_c is the minor pinning length that is 0.02-2μm suggested for MMCs by Wolfenden et al. [30], ρ_m is the

matrix material density, ε' is Cottrell's misfit parameter that is equal to the fractional difference in the size of the solute and solvent atoms and was suggested to be 10^{-2} by Granoto and Lucke [29] a is the lattice parameter, E, G and ν are Young's modulus, shear modulus, and poisson's ratio of the matrix, respectively, P is a constant between 2 and 3, R is the resolved shear stress factor by Schmid's principle, B is a constant of $5x10^{-5}$ to $5x10^{-3}$ [29].

This model is shown schematically in Fig. 2.13. The relative positions of dislocation and pinpoints under zero stress are shown in Fig. 2.13(a). Figs. 2.13(b) and (c) show how the pinned dislocations bow out as the stress is increased. If the dislocation remains anchored to the pinpoints (Figs. 2.13(a), (b) and (c)) then linear damping (proportional to area swept by dislocation) is observed. Non-linear effects are produced when dislocations leave the pinpoints as shown in Figs. 2.13 (d) to (g).

Dislocation damping in the linear region is a function of frequency similar to that observed for anelastic phenomena. At low frequencies, the velocity of the dislocation is small so that viscous force and damping are small. Under these conditions, the displacement is limited by the tension forces in the dislocation and is parabolic in shape as shown by the "LF" arcs in Fig. 2.13 (c). As the frequency increases, the viscous forces become dominant and the displacement of the dislocation cannot achieve its full parabolic values, Under these circumstances it behaves like a rigid rod except for curvature at its ends near the pinning points as shown by the "HF" lines in Fig. 2.13 (c). At very high frequency, the drag forces may be large but the displacement is very small, thus the damping is small. At some intermediate or optimum frequency, the integral of the drag forces and displacement is a maximum and thus the damping is also a maximum.

As a result, the damping versus frequency curve displays a typical relaxation or resonance type peak. This has been well verified for a high purity copper [18].

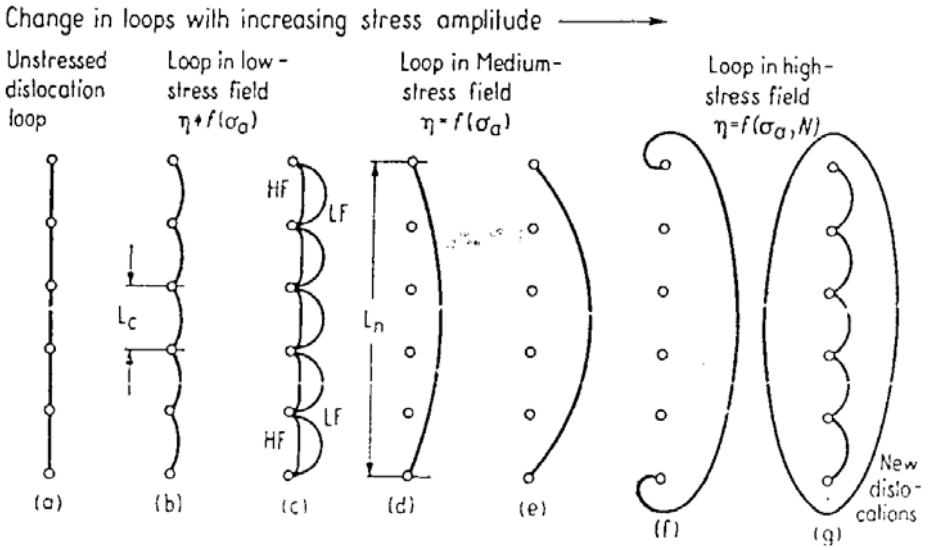

Fig. 2.13 Dislocation motion behavior: from stages (a) to (c) the dislocation provides amplitude-independent damping behavior and after overcoming the barrier, from stages (d) to (g) the dislocation provides a strong strain amplitude dependent damping behavior [30].

2.8 Interfaces in Metallic Matrix

Solid-solid interfaces are complex due to the wide variety of defects that arise and reside at the interfaces and possess elastic strain fields. Some of the most important properties of materials in high technology applications are strongly influenced and or even controlled by the presence of solid interfaces. For example, in electronic industry the success depends on understanding the semiconductor-metal, ceramic-metal and semiconductor-ceramic interfaces [30]. Further examples are in the area of surface modification techniques to achieve corrosion protection and/or in tribological or catalytic applications. Similar situation exists in the success of the metal based composites. Here understanding is required between metal-ceramic, metal-metal and metal-polymer

interfaces. In contrast, Wolf and Yip [31] notes that our understanding of even the simplest interfaces such as free surfaces and grain boundaries are rudimentary at best. It is noted that physical properties at or near an interface differs from the bulk properties. For example, the thermal expansion, electrical resistivity, or elastic response near an interface can be seen to be anisotropic in an otherwise isotropic bulk material [31]. The gradient of variations extends for a few atomic layers and hence requires experiments with atomic-level resolution coordinated with computer-based simulations at atomic and electronic levels.

Damping studies of materials helps to visualize the effect of defects in terms of internal friction and hence becomes a good choice to characterize interface since they contain defects. However a detail understanding on interfaces and their defects is essential, hence in the present section, literature related to solid-solid interface types and their defects in monolithic metals and metal matrix composites are discussed briefly.

2.8.1 Interface types

Generally solid-solid interfaces are classified as homophase and heterophase in nature. Homophase interface refers to orientation difference or a translation between two crystals of same phase across an interface. Examples include grain boundaries and special types of interfaces such as twin boundaries and stacking faults. Heterophase interface includes interfaces of two crystals that differ in composition and or Bravais lattice. They are further divided in terms of atomic matching or coherency as follows (see Fig.2.14):

1. Coherent interface that exhibits continuity of atomic planes and lines at the bi-material interface and possess long range order.

2. Semicoherent where lattice mismatch exists which is accommodated by periodic misfit dislocations.
3. Incoherent interface where there is no correspondence between the two phases in terms of atomic matching.

All these different interfaces seek to minimize the interfacial free energy, and this is achieved by maximizing the atomic matching (i.e. minimizing the number of broken bonds) at the interface. Thus there is a strong tendency for the planes and direction with the highest atomic densities to align across solid-solid interfaces. This is found to hold good even for metal-ceramic [32] and ceramic-polymer systems [33]. Presence of defects, elastic strain and different types of atomic bonds in a interface complicates this fundamental principle.

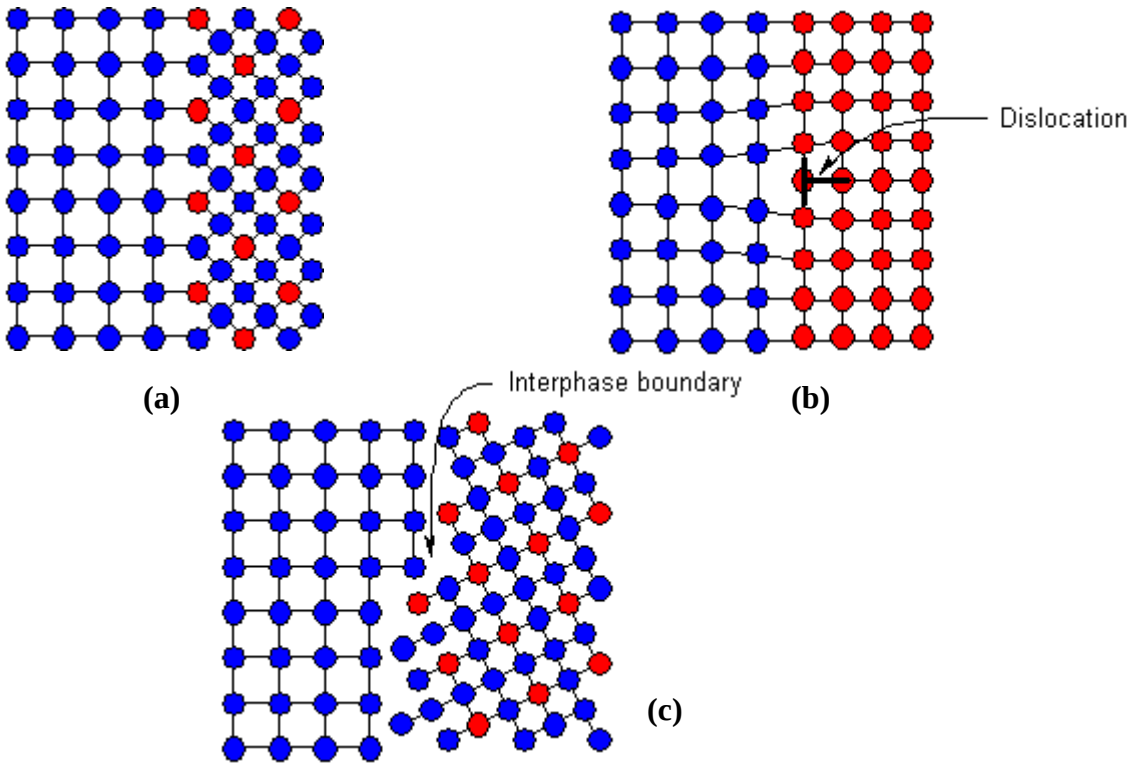

Fig. 2.14 Types of interfaces: (a) coherent, (b) semicoherent, and (c) incoherent [31].

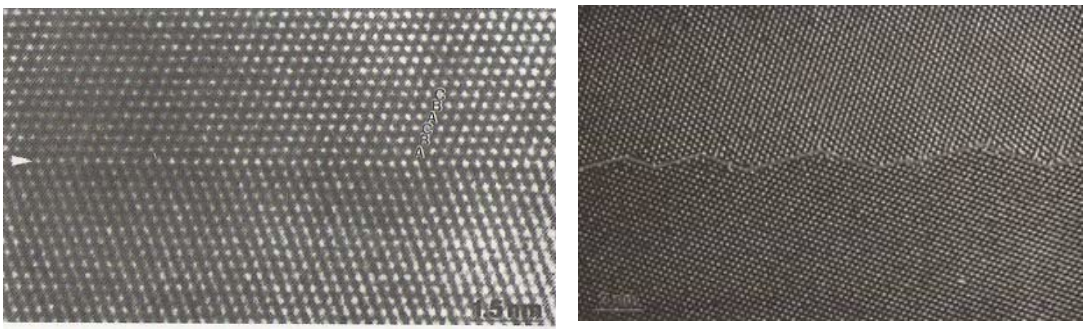

(a) **(b)**

Fig. 2.15 (a) HRTEM image of a ∑=3 {111} twin in Cu imaged along a <110> zone axis [34] (b) typical grain boundary in aluminium [36].

2.8.1.1 Homophase Interface

High resolution TEM has been useful in the study of the atomic structures in homophase and heterophase materials. Fig. 2.15 (a) shows a HRTEM image of a {1,1,1} twin interface in f.c.c copper [34]. The planes are edge on and horizontal in the image so that we can see ABCABC…stacking of the close-packed planes progressing vertically in the image. Note the mirror symmetry across the twin interface indicated by an arrow. The energy can be calculated using a nearest-neighbor bonding model using the position of the atoms. Since there is no missing bonds and their stacking order is changed, these twin interfaces exhibit a relatively low-energy interface and hence a common planar defect.

Grain boundaries are most common planar (two-dimensional) defects in materials. Grain boundaries are the interfacial transition region between two grains, which are in contact but differs in crystallographic orientation (see Fig. 2.15 (b)). These grains may be perfect crystals in a single-phase material or may vary in composition. Hence a grain boundary has no independent existence and exists as an interfacial transition region between two-dimensional imperfections in crystalline materials. Experimental studies show that they are highly disordered (as compared to the adjacent grains) two-

dimensional regions and only a few atomic sizes in thickness (5 to 10 A^o) in an otherwise perfect crystal.

Grain boundaries are non-equilibrium defects of crystals, contrary to vacancies, for example. This is because the energy of the grain boundary cannot be compensated by configuration entropy, which is small for grain boundaries [35]. The potential grain boundary unit area per unit volume is as follows:

$$M = \int_0^\infty \tilde{A} \frac{\sigma_b}{kT\Omega_a} \exp\left(\frac{\sigma_b \tilde{A}}{kT}\right) d\tilde{A} = \frac{kT}{\sigma_b \Omega_a} \approx 10^{-15}\,cm^{-1} \qquad (2.18)$$

where Ω_a is the atomic volume, σ_b is the surface tension, T is the temperature, $\tilde{A}$ is the surface area, k is the number of components.

Small angle grain boundaries

If the misorientation between adjacent grains is small, a set of dislocations can be used to make the grain boundary. This has been confirmed by soap bubble model as well as high-resolution electron microscopy (HREM). Symmetric tilt boundary consists of single set of dislocations as follows [36]:

$$\frac{b}{d} = 2\sin\frac{\varphi}{2} \approx \varphi \qquad (2.19)$$

where b is burgers vector, d is dislocation spacing, φ is the rotation angle. From the above equation, it is clear that dislocation spacing decreases with increasing rotation angle. The free energy of a small angle grain boundary can be calculated using the stress field of dislocation in an infinite periodic arrangement in the order of the dislocation spacing d. The energy of an edge dislocation per unit length, therefore reads as follows [36]:

$$E_d = \frac{\mu b^2}{4\pi(1-\upsilon)} \ln\left(\frac{d}{r_o}\right) + E_c \qquad (2.20)$$

where μ is the shear modulus, υ is poisons ratio, r_o is the radius of the dislocation core radius $(\approx b)$, and E_c is the energy of dislocation core. Thus for a symmetric tilt boundary with tilt angle φ, the number of dislocations per unit length $n = 1/d = \varphi/b$, and thus the grain boundary energy per unit area is given by [36]:

$$\sigma_{stb} = \frac{\varphi}{b}\left(\frac{\mu b^2}{4\pi(1-\upsilon)} \ln\frac{1}{\varphi} + E_c\right) = \varphi(A - B.\ln\varphi) \qquad (2.21)$$

with $A = E_c/b$ and $B = \mu b/4\pi(1-\nu)$. The curve in Fig. 2.16 (b) was calculated using equation (2.21) for Al and agrees for angle $\varphi < 15^o$.

Large angle grain boundaries

For rotation angles greater than 15 degrees, the dislocation model fails, because the dislocation cores tend to overlap. Fig. 2.16 (a) shows the typical low and high angle grain boundaries using a simple soap bubble experiment. Thus the dislocations lose their identity as individual lattice defects so that equation (2.21) does not apply any more. Therefore, grain boundaries with rotation angles in excess of 15 degrees are termed high angle grain boundaries. A fundamental reason for the failure of the above model is the requirement of starting periodic dislocation arrangement to minimize grain boundary energy.

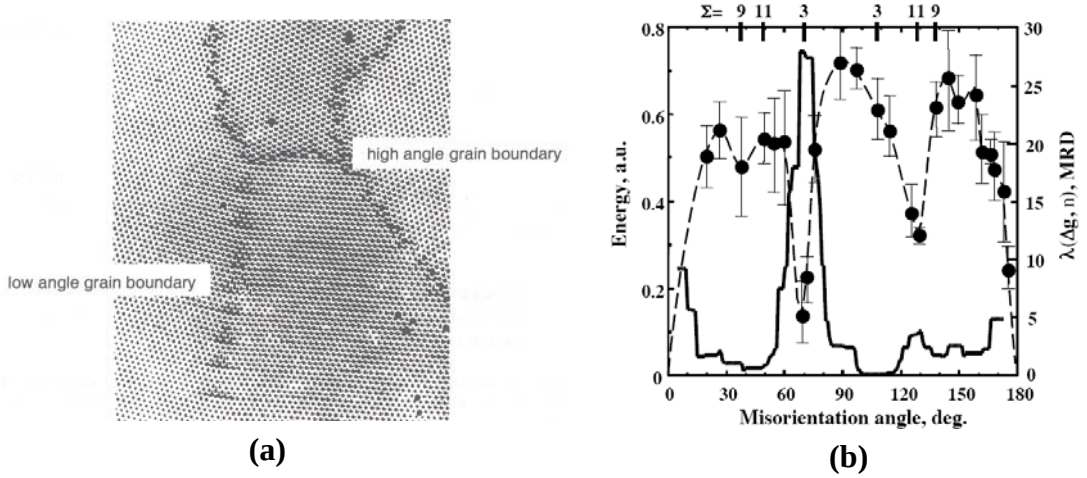

(a) **(b)**

Fig. 2.16 (a) High angle and low angle tilt boundary explained using soap bubble experiment. (b) Comparison of measured energies (dashed line) against populations for symmetric [110] tilt boundaries in Al [35].

In a perfect crystal the atoms have a defined (averaged) position, which is determined by the minimum of the free energy. Any deviation from this position necessarily increases the free energy. Therefore, it can be assumed that the crystal will try to keep the atoms as much as possible in their ideal position and also in the grain boundary. There are orientation relationships, where crystallographic planes continue through the grain boundary from one crystal to the other, i.e. there are atomic positions in the grain boundary, which coincide with ideal positions of both adjacent lattices. Such lattice points are called coincidence sites. Since the orientation relationship between the adjacent crystals is described by a rotation, it can be investigated under what condition coincidence sites will occur. Since both crystal lattices are periodic, the coincidence sites also must be periodic, i.e. they also define a lattice, the coincidence site lattice (CSL). As a measure for the density of the coincidence sites or for the size of the elementary cell of the CSL, researchers define the quantity:

Σ = Vol. of elem. cell of CSL / Vol. of elem. cell of crystal lattice (2.22)

Table 2.2 Values of intrinsic stacking fault energy γ_{sf}, twin boundary energy γ_{twin}, grain-boundary energy γ_{gb} and crystal vapor surface energy γ_{sv} for various metals [36].

Metal	γ_{sf}	γ_{twin}	γ_{gb}	γ_{sv}
Ag	16	8	790	1140
Al	166	75	325	980
Au	32	15	364	1485
Cu	45	24	625	1725
Fe	-	-	780	1950
Ni	125	43	866	2280
Pd	180	-	-	-
Pt	322	161	1000	3000
Mg	125	-	-	-
Zn	140	-	340	-

Good fit of the atoms (coincidence sites represent atoms with ideal fit) is associated with a low energy and hence grain boundary strongly favors running through coincidence sites rather than non-coincidence sites. Grain boundaries between crystallites, which have an orientation relationship corresponding to a high density of coincidence, are called CSL boundaries or special boundaries. The smaller Σ the more ordered is the grain boundary. Small angle grain boundaries can be characterized by $\Sigma = 1$, since almost all lattice points, except for the atoms of the dislocation cores, are coincidence sites. Grain boundaries with twin orientation are defined as $\Sigma = 3$ and in the coherent twin boundary all lattice sites are coincidence sites, thus in a 3-D every third plane parallel to the coherent twin boundary is in perfect coincidence. Thus within a single phase metal energy is accumulated in the form of interface which contain these defects. Table 2.2 lists the energy trapped in the different form of such defects.

2.8.1.2 Heterophase interface

In the case of heterophase interface, a silver-rich GP zone in an aluminium-silver alloy is a good example [37] (see Fig. 2.17 (a)). The Ag and Al atoms are of similar size so that clustering of Ag atoms forms a precipitate, which has a coherent interface mainly due to the similar crystal structure. Similar coherent interface exists between semiconductor materials such as GaAs-AlGaAs multilayer [38]. These interfaces can be mathematically modeled using the Cahn-Hilliard model [39]. In contrast, cobalt-nickel martensite interface has a change in Bravais lattice but no change in composition and still exhibit a perfect coherent interface, see Fig. 2.17 (b) [40].

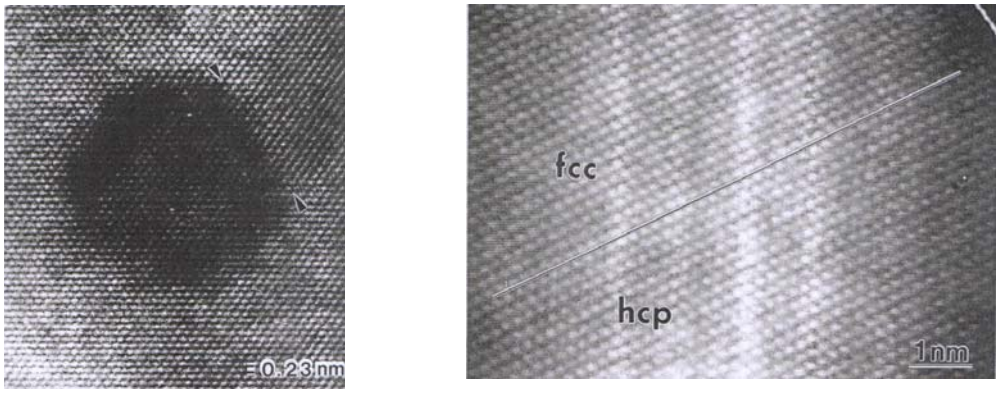

(a) **(b)**

Fig. 2.17 HRTEM image of: (a) silver-rich G.P.zone in an aluminium –silver alloy which shows a coherent interface [37] and (b) Co-Ni interface which is a FCC-HCP interface [40].

Among the various models, the simplest and easiest model to calculate the interfacial energy of a fully coherent interface between two phases α and β that differ in composition was done by Becker [41]. He employed a nearest neighbor broken bond model to derive the coherent solid-solid interphase boundary energy γ_c^{ss} assuming that both phases are homogenous up to the interface. The energy is given as follows:

$$\gamma_c^{ss} = N_{s\{hkl\}} z_j \left(X_\alpha - X_\beta\right)^2 \varepsilon \tag{2.23}$$

where $N_{s\{hkl\}}$ is the number of atoms per unit area on the {hkl} interface plane, z_j is the coordination number across the interface, X_α and X_β are the equilibrium atom fractions of atom B in the α and β phases, respectively, and ε represents the variation in bond energy between the two atoms (A and B) which is calculated as the difference between the A-B bond energy and the average of A-A and B-B bond energies. For example, to compute the energy of Au-Ni system at 400^{o}C, the X_α and X_β are obtained from phase diagram as 0.075 and 0.985 corresponding to that temperature, so that $\left(X_\alpha - X_\beta\right)^2 = 0.828$. The lattice parameter of gold is 0.40nm and hence $N_{s\{111\}} = 4/\sqrt{3}\left(0.4e-9\right)^2 = 1.44x10^{19}$ atoms/m^2 and $z_j = 3$ for the {111} plane. The factor ε can be calculated from the critical temperature T_c (which is equal to 810.3^{o}C) for this alloy ($\varepsilon = 2RT_c/N_A z$). Thus using the above equation $\gamma_{c(Au-Ni)}^{ss}$ was found to be $0.107 J/m^2$. The limitation of the above equation is that the boundary is infinitely sharp and does not include the interface width as a thermodynamic variable. Hence the gradient theory and discrete lattice plane models can be used when this assumption fails. However this equation is appealingly simple and can be used to obtain an estimate of interface boundary energy.

When the lattice parameters are similar a semicoherent interface forms. Copper-silver interface forms a good example for a semicoherent interface (see Fig. 2.18). Here the lattice mismatch is around 12 %, which necessitates a dislocation for every nine planes [42]. Yet the interface is atomically flat and there is excellent atomic matching across the interface between the misfit dislocations, which accommodate the mismatch

locally at the interface. Another example is the interface between cadmium telluride and gallium arsenide [43]. Thus this interface arises for small plate shaped precipitates and lattice matched semiconductors. In many other cases, there is sufficient lattice mismatch that coherent interfaces relax to an unstrained condition with an array of misfit dislocations at the interface.

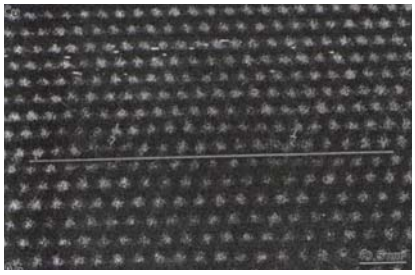

Fig. 2.18 HRTEM image of a {111} copper-silver interface in a Cu-Ag alloy aged to grow silver precipitates in the copper matrix is example of semicoherent interface [42]. Arrow indicate the periodic misfit dislocation.

When an interface takes dislocations to accommodate the mismatch, it is referred to as semicoherent (discommnesurate) interface. Turnball [44] suggested that in a semicoherent interface between two phases $(\alpha \,\&\, \beta)$ that differ in composition, the energy can be calculated as if the total energy consists of a compositional γ_c^{ss} and structural γ_s^{ss} component of the interface boundary energies. Thus the additional structural component compared to coherent interface was first analyzed by Frank and Vander Merwe [45, 46], where the misfit is considered in one direction and the atomic relaxation is permitted in the vicinity of the misfit dislocations. The interaction of the atoms across the interface boundary is assumed to occur according to a sinusoidal force law and the interaction within a given phase is treated on the basis of an elastic continuum, which yields the following expression for the misfit dislocation energy at the $\alpha - \beta$ boundary.

$$\gamma_s^{ss} = \mu\bar{a}/4\pi^2\left(1+\Lambda-\left(1+\Lambda^2\right)^{0.5}-\Lambda\ln\left(\left(2\Lambda\right)\left(1+\Lambda^2\right)^{0.5}-2\Lambda^2\right)\right) \qquad (2.24)$$

where a_α and a_β are the lattice constants, μ_α and μ_β are the shear moduli and ν_α and ν_β are Poisson's ratio in the α and β phases, respectively. The average lattice constant between the two phases is denoted as $\bar{a}\left(=\left(a_\alpha+a_\beta\right)/2\right)$ and the lattice misfit is denoted as $\delta\left(=\left(a_\alpha-a_\beta\right)/a_\alpha\right)$ and the repeat distance between the dislocations is denoted as $D_\delta=\left(a_\alpha+a_\beta\right)^2/4\left(a_\alpha-a_\beta\right)$, thus the misfit δ between the two phases can be shown to be $\delta=\bar{a}/D_\delta$. μ is the shear modulus at the interface and C_8 term accounts for elastic interactions within each crystal where μ accounts for the $\alpha-\beta$ interface.

$$\Lambda = 2\pi\delta\left(C_8/\mu\right)$$
$$C_8=\left(\left(1-\nu_\alpha/\mu_\alpha\right)+\left(1-\nu_\beta/\mu_\beta\right)\right)^{-1} \qquad (2.25)$$

Incoherent interfaces exist between a germanium particle and aluminum matrix in an Al-Ge alloy [47]. In this material, a lattice mismatch of 30% exists and Al & Ge exhibits a twin related interface (see Fig. 2.19). In addition, Ge has covalent bonds that

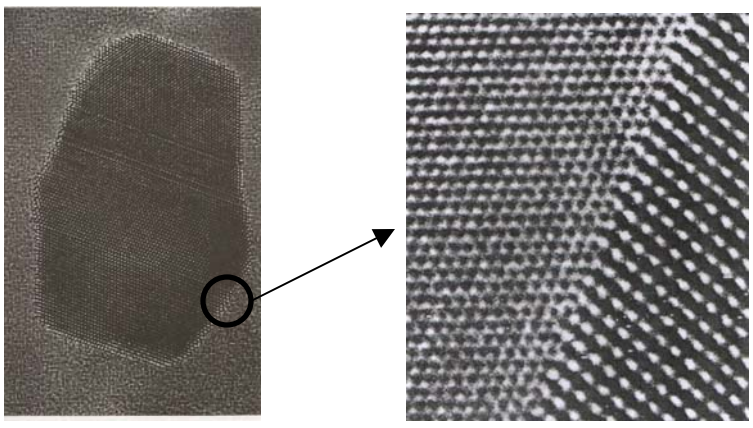

Fig. 2.19 HRTEM image of a aluminium –germanium interface showing a typical incoherent interface [36, 47].

are directional compared to the Al, which has a FCC structure made of metallic bonds. Hence unlike the previous mentioned interfaces, no relaxation takes place at an incoherent interface. Yet in Al-Ge, experiment results show that interface plane parallels the common close packed {1 1 1} planes in the two phases, so as to minimize the interface energy by faceting along common close-packed planes. Similar example is a krypton-graphite interface. These interface differ from semicoherent interface and that there is no local relaxation of the misfit into dislocations at the interface. Instead, the misfit is spread evenly across the entire interface and the two phases retain their bulk structure up to the interfacial plane, where they terminate abruptly. Thus this type of interface possesses high interfacial energy and low strength. An upper limit and a reasonable estimate can be obtained by adding the surface energies of the two crystallographic faces (hkl) of the α and β phases. Thus, in common, the heterophase interfaces also exhibit a interface plane which is generally atomically flat and parallel to the common close-packed planes in the crystals.

Table 2.3 Interface boundary energies (γ^{SS}) for the three types of interface [35].

Interface	$\gamma^{SS}\left(mJ/m^2\right)$
Coherent	5-200
Semi-coherent	200-800
Incoherent	800-2500

In summary, the above examples show that there is a strong tendency for solid-solid interface in materials to lie along close-packed planes so as to minimize their interfacial energy and hence are planar in nature. Dissimilar material phases also wishes to align their close packed directions across the interface to achieve a minimal energy. In conditions where parallel close-packed planes are favored, atomic row matching is

favored. Table 2.3 shows the comparison of the interface energies for the three different interfaces.

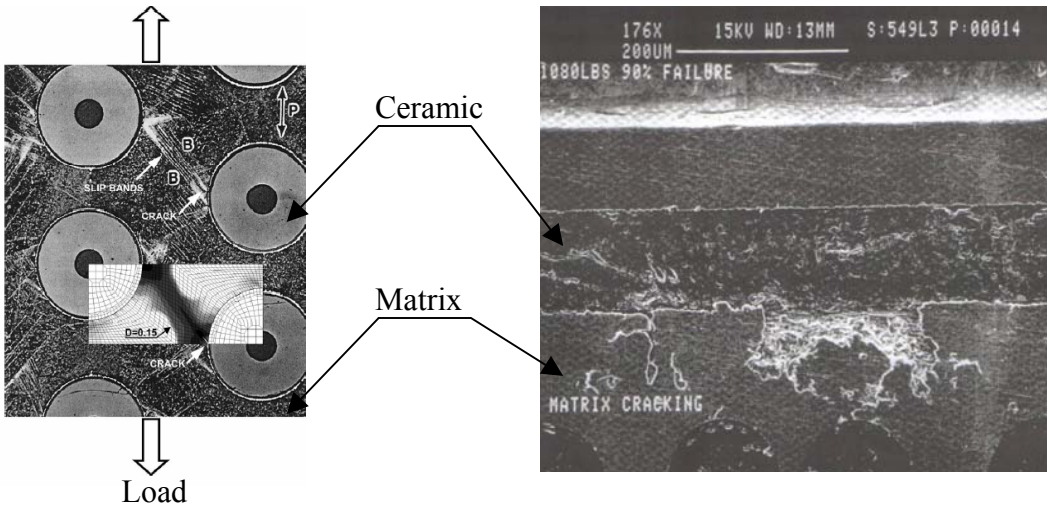

Fig. 2.20 Typical Metal-Ceramic Interface in MMCs and how damage arises [49].

2.8.3 Metal-Ceramic Interface

Metal-ceramic interfaces (MCI) are typically heterophase boundaries and are subject to intense research and of several conferences [48-50]. In a dynamic system the MCIs should transmit forces and heat without failure in a structural application as shown in Fig. 2.20. Hence interfaces determine the overall efficiency. For discontinuously reinforced MMCs, the main mechanism of interfacial bonding has not been fully understood. Here in the following sections, the various ideas of bonding at different levels are being reviewed.

Based on the literature review, Al-SiC composite is a very popular system among material systems in metal matrix composites. Four different models have been proposed for metal-ceramic interfaces: (1) direct electronic bonding between the atoms across the interface, (2) a chemical bond due to the reaction at the interface that forms another

compound, such as Al_4C_3, (3) inter-diffusion at the interface and (4) the presence of SiO_2 film at the interface to which both, the matrix and reinforcement adhere.

2.8.3.1 Atomic Model

Al has a lattice size of a_{sic} = 0.405 nm while SiC has an hcp structure of a_{sic} = 0.307 nm and c_{sic} = 1.503nm. The basal plane of SiC is the natural cleavage plane and this accounts for the platelet shape of SiC particles. It is reasonable to assume that the basal plane controls the overall crystalline orientation relation between the SiC and Al. Calculations using O-lattice theory show that the <111> planes of Al parallel to the (0001) basal plane of SiC are energetically more favorable choice over the <112> of Al parallel to the (0001) basal plane of SiC.

Table 2.4: Bond lengths and binding energies of combinations of Si, C and Al atoms.

System	Bond length (A^o)		Binding energy (eV)	
	Experiment	Theory	Experiment	Theory
Al-Al	2.56	2.71	1.55	1.26
Si-Si	2.25	2.26	3.21	2.83
C-C	1.243	1.26	6.08	5.26
Al-C	1.95	2.00	1.86	3.19
Si-C	1.70	1.71	-	4.28
Al-Si	2.41	2.42	2.60	2.37

Literature review shows only few attempts are made to understand the atomic arrangements at the interface using first principles. A spectroscopic study of Bermudez [49] shows the physical and electronic structure of the interface between the Al and SiC. He found that aluminium deposited at room temperature forms islands randomly distributed over the surface. Al aggregates at C-rich sites and at high temperature reacts with carbon to form carbide (Al_4C_3). He also observed a shift in the 2p level of Al to

higher binding energy while the 2p shell of Si goes to a lower binding energy. Table 2.4 lists the bond lengths and binding energy of the various bonds formed out of combinations of Si, C and Al atoms predicted by Rao and Jena [50] using a self-consistent quantum mechanical calculation method which can be compared against experimental values. From Table 2.4, the binding energy of the Al-Al bond is the weakest, whereas that for C-C is the strongest, but this is understandable since the former is metallic bond while the later has a covalent bond. Results show that the binding energy of Al-C is significantly higher than that of Al-Al and Al-Si. This is because of charge transfer between Al and Si is smaller than that between Al and C, but in both cases charge transfer is from Al. The overall strength of the Al-C bond implies that when an interface is formed between Al and SiC, Al would prefer to bond with a C-terminated SiC matrix. Similar conclusion can be arrived by comparing the ionization potential of C, Al and Si atoms, which are -11.26, -5.99 and –8.15 eV, respectively. Clearly in the case of Al-C bond it would be energetically preferable to transfer electrons from the Al to C. This is in agreement with the annealing studies [4] where Al was found to aggregate to the C-rich sites.

Structural studies by quantitative high-resolution transmission electron microscopy as well as investigations on chemical processes and bonding across the interface by analytical electron microscopy (AEM) have been used by various researchers to study the ceramic-metal interface. Fig. 2.21 shows global and localized image of a Al-TiC interface [51]. Studies of Li et al. [53] showed that bond or adhesion energy enhances when (111) planes of Al bonding parallel to the (0001) planes of SiC, with a dislocation separation distance of 40 nm in Al, along the interface. Thus studies showed

that if the process does not lead to recrystallization of the matrix a random chance exists for an orientation relationship to form, which will have a greatest adhesive energy and conversely the smallest strain energy. On the other hand, if the matrix is in the molten state then it appears more likely that the lowest strain energy orientation relationship will form.

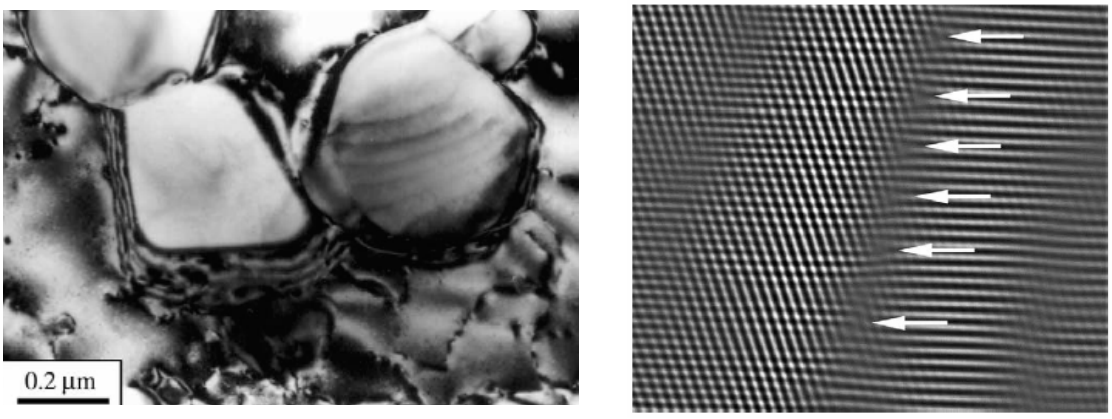

(a) **(b)**

Fig. 2.21 Al-TiC interface showing: (a) dislocation structure and (b) interface showing the lattice misfit [53].

2.8.3.2 Ion Exchange

Ion exchange is a possible mechanism which takes places at the metal-ceramic interface. This is used to induce a compressive stress in the near surface regions of silicate glasses [54]. The principle driving force for the ion-exchange is the entropy of mixing. For example in the studies of Raj et al. [55] they showed the ceramic which was a magnesium aluminium spinel and the metal which was nominally pure aluminium, the exchange reaction can be written as follows:

$$MgO.1.25Al_2O_3 + x.Al \rightarrow Mg_{1-x}O.1.25Al_{2+x/1.25}\,O_3 + xMg_{ss} \qquad (2.26)$$

The spinel contains two cations, Mg^{2+} and Al^{3+}. The ideal spinel structure consists of cubic closed packed arrays of oxygen ions with divalent and trivalent cations distributed in the tetrahedral (A) and octahedral (B) sites, respectively. However, the cations may exchange their position by the following reaction:

$$Mg_A + Al_B = Mg'_B + Al^{\cdot}_A \qquad (2.27)$$

The terms on the left hand side denote the cation locations in the ideal crystal. The inverse cation locations are given on the right. The Mg divalent ion present in the octahedral site embodies an effective negative charge of one unit and the Al trivalent ion in the tetrahedral site carries a positive charge of equal magnitude. The enthalpy for reaction in equation (2.27) becomes comparable to the entropy of mixing at approximately 625^{o}C for the present system [55]. The rate of ion-exchange reaction was found to depend on the particle size. The small particles have larger surface area to volume ratio and hence showed significant progress in the reaction compared to the large particles. Thus the ion exchange mechanism is expected to produce a strong cohesion between aluminum and magnesium aluminate spinel in the form of electrostatic attraction between the charges on either side of the interface. Such an attractive force between charges in the ceramic and image charges in the metal have been proposed to explain a phemenological observation that interfaces between metals and non-stoichiometric ceramics (e.g. spinel) exhibit strong bonding [56]. Similar studies at Nb/Al_2O_3 interface using first principles allow detailed analysis of the bonding [57]. Thus further studies are expected to investigate the charge and electrical field gradient near the interface to validate and compare between different material systems.

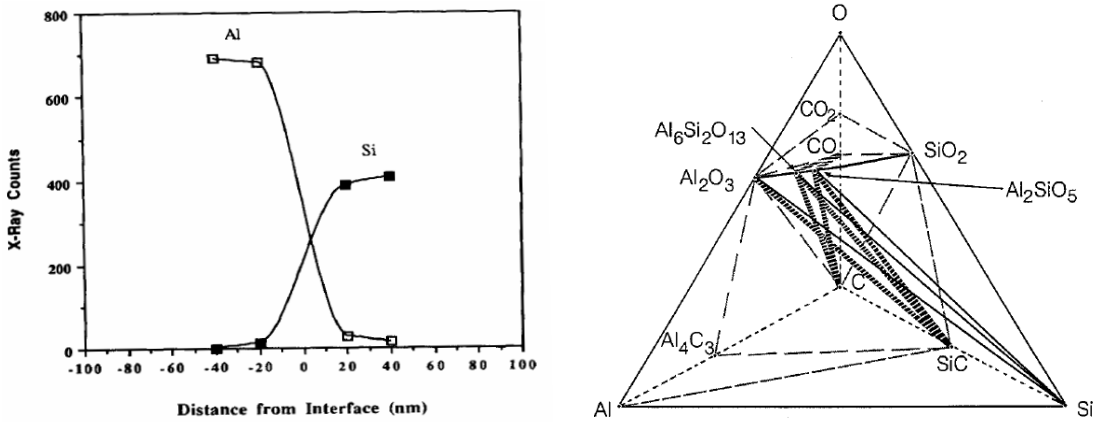

(a) **(b)**

Fig. 2.22 Diffusion profile of Al and Si at the Al-SiC interface [58] (b) Calculated istothermal quaternary phase diagram for Al-Si-C-O system (Temp 600 to 1000 ^{o}C) [59].

2.8.3.3 Reaction at metal-ceramic interface

At the interface of two dissimilar materials segregation of impurities and/or formation of reaction products may occur. These lead to modification of the composite's properties. Therefore it is essential to study the composition and possible reactions at the metal-ceramic interface. The best available data by Romero et al. [58] shows that little penetration of 40 nm exists between the Al and SiC phases. Studies of Singer et al. [59] shows a quaternary phase diagram of Al-Si-C-O (see Fig. 2.22(b)). The composition and phase changes were explained in terms of thermo-chemical reactions expected of the Al-Al_2O_3-SiC-O_2 system. The triangle at its base is the ternary diagram of the Al-Si-C system; the three remaining triangles on the sides are ternary diagrams that depict oxidation of the three binary legs of the Al-Si-C ternary diagram. Solid or dashed lines connecting elements and compounds are tie lines which connect phases in equilibrium. Tie-lines inside tetrahedron join with external tie-lines to define tie-planes that completely divide the interior space into tetrahedral domains. The four vertices of each tetrahedron identify the four "co-existing" phases that are at stable equilibrium products

of any mixture of compounds or elements within it. For example, adding O to the Al-implanted SiC layer moves the composition off the Al-SiC tie line into the Al-SiC-Al_4C_3-Al_2O_3 tetrahedron. The tie-line between Al and SiC indicates that Al does not react with SiC at low temperature. At higher temperature thermodynamic unstability can occur giving rise to the following reaction which affects the final composites' properties:

$$4\ Al + 3\ SiC \Rightarrow Al_4C_3 + 3\ Si \tag{2.28}$$

Studies of Handwerker et al. [60] showed Sritharan et al. [60] reported that Al_4C_3 forms as discrete precipitates parallel to the (0001) direction forming ledges and forms easily identifiable ledges and pits which are visible in optical and SEM microscopes. Studies have shown that Al-SiC is thermally stable up to 650^{o}C although substantial penetration of Al into SiC parallel to the basal planes is seen to occur at temperature above 680^{o}C while at temperature higher than 700^{o}C the formation of Al_4C_3 occurs [60-62]. Fig. 2.23 shows by holding the Al-SiC interface at high temperature the carbide reaction takes place significantly with 15 minutes [63]. Du et al. [64] reported such Al_4C_3 precipitates in Al-implanted SiC formed at 500^{o}C, and a continuous dense $Al_6Si_2O_{13}$ phase formed in Al-implanted SiC oxidized at 1300^{o}C.

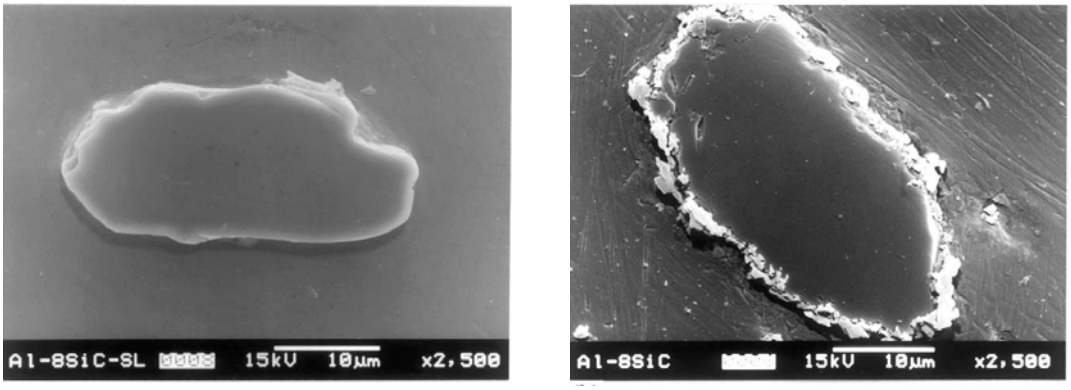

(a) **(b)**

Fig. 2.23 SEM micrographs showing (a) clean interface of a SiC particle just after addition in Al melt and (b) reacted interface with Al_4C_3 interface after 15 minutes holding time. [63].

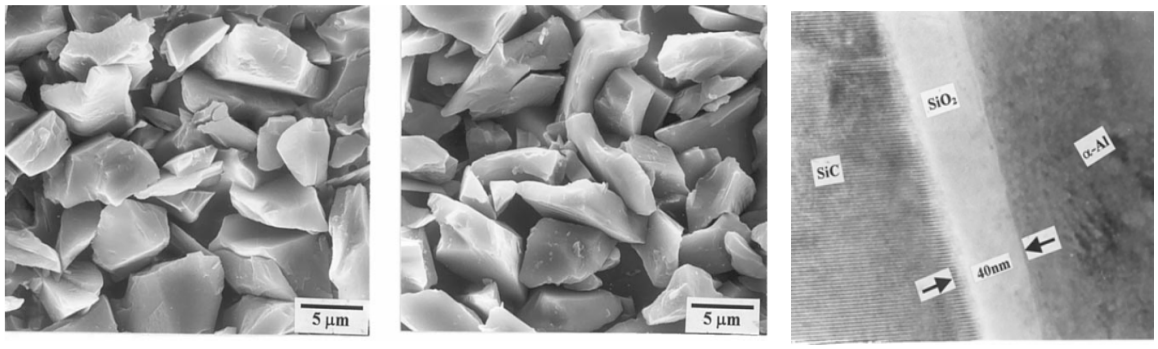

Fig. 2.24 SEM micrographs showing: (a) as received SiC particles (b) Oxide coated SiC particles (c) the thickness of oxidized layer (HRTEM image) of the composite reinforced with SiC particles at 1100^{o}C for 2 hours [65].

Studies of Evans and Boyd [65] showed that a 40 nm thick amorphous interface layer develops during processing of the composite material by diffusion of Al and Mg into the preexisting SiO_2 layer on the 3 μm SiC particles, in which particle-matrix adhesion takes place at this interface. Ratnaparkhi and Howe [66] produced an Al/SiC composite by diffusion bonding surfaces and observed an amorphous interface layer having similar thickness and composition as in the present work. Prior to deformation, stacking faults were observed in the SiC particles. At a plastic strain of 0.7%, perfect dislocations are observed in the SiC and the stacking faults disappear. These dislocations are due to the combination of applied stress and the residual micro stresses present in the SiC particles after cooling. The accumulation of perfect dislocations in the SiC leading to particle cracking was also observed. However the particle matrix decohesion in the MMC studied appears to be associated with an amorphous Si-Mg-Al-O layer at the interface. Using a method based on an interfacial energy criterion [67], the local critical stress for fracture of the interfacial layer is calculated to be 200-300 MPa.

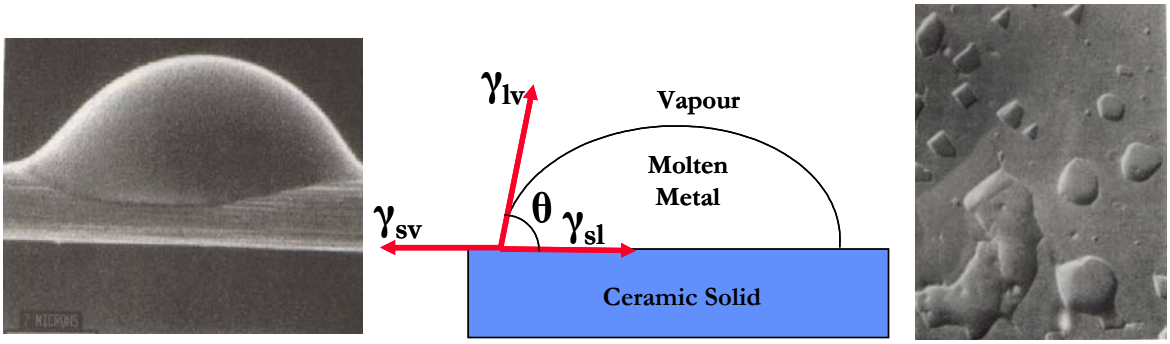

Fig. 2.25 (a) Typical spreading of molten Al on ceramic substrate [69], (b) definition of contact angle and (c) incomplete coating of Au on alumina surface [70].

2.8.3.4 Wetting of Ceramics by Liquid Metals

Even though aggregation of Al to C rich sites at Al-SiC interface can be seen at a molecular level, for a quantitative understanding of the interfacial adhesion in metal-matrix composites, it is however necessary to consider the geometry, composition and atomic relaxations at the interface. Good wetting between the solid ceramic phase and the liquid metal matrix is an essential condition for the generation of a satisfactory bond between metal-reinforcement.

Wettability can be defined as the ability of a liquid to spread over a solid surface and express the extent of intimate contact between the two phases. The fundamental thermodynamic property of an interface is the free energy per unit area γ. It can be determined by measured the contact angle between a drop of the liquid and the solid substrate, as shown in Fig. 2.25. The contact angle θ is related to the surface energy of the vapour-solid interface γ_{sv} and the liquid-solid interface γ_{lv}. When a liquid drop wets a solid surface, it replaces the solid-vapour interface and hence this will occur provided it results in a decrease in free energy of the total system. The bonding force between the liquid and solid phase, i.e. the work of adhesion W_{ad} is defined as:

$$W_{ad} = \gamma_{lv} + \gamma_{sv} - \gamma_{sl} \approx \gamma_{lv}(1 + \cos\theta) \quad (2.29)$$

The magnitude of the contact angle decides the wettability, as follows [68]:

- $\theta = 0$ denotes perfect wetting
- $\theta = 180$ denotes no wetting
- $0 < \theta < 90$ denotes partial wetting and $90 < \theta < 180$ denotes nonwetting.

A liquid is said to wet when $\gamma_{sv} > \gamma_{sl}$ which happens when $\cos\theta > 0$. Table 2.5 lists the contact angles of molten aluminum under different temperature and substrate materials.

Table 2.5 Contact angle formed by liquid Al with various ceramic phases.

Ceramic phase	**Temperature (deg.C)**	**Angle θ (degrees)**	**Vacuum (Torr)**	**Reference**
SiC	900	150	$2.7\text{x}10^{-4}$	[70]
	1100	42	$2.7\text{x}10^{-4}$	[71]
B_4C	900	135	10^{-5} to 10^{-6}	[72]
	1100	120	10^{-5} to 10^{-6}	[72]
Al_2O_3	900	120	10^{-5}	[73]
	1100	80	10^{-4}	[73]

Wetting of a liquid metal on a solid ceramic surface can be promoted by various methods:

1. The addition of alloying elements to the matrix alloy.
2. Coating the ceramic particulates.
3. Treatment of the ceramic particulates.

Addition of reactive elements to the liquid melt promotes wetting. For example, addition of Mg, Ca, Ti or Zr to the liquid melt reduces the surface tension of the melt, decreasing the solid-liquid interfacial energy of the melt or inducing wettability by chemical reaction. In Al based composites, Mg has a greater effect in wetting and promoting distribution than other materials such as Ce, La, Zr and Ti [73], Bi, Pb, Zn,

and Cu [74]. The addition of 3 wt. % Mg to Al reduces its surface tension from 0.760 to 0.620 at 720^{o}C. The reduction is very sharp for the initial 1 wt. % Mg addition, e.g. with 1 wt. % Mg the surface energy of an Al alloy drops from 860 to 650 dyn/cm. This is because, Mg has a lower surface tension of 0.599 N/m compared with that of Al (0.760 N/m) or Al-11.8 wt. % Si alloy (0.817 N/m).

Heat treatment of particles before dispersion in the melt helps in desorption of gases and altering the surface composition for example in heating SiC particle to 900^{o}C due to the formation of an oxide layer on the surface [75] (see Fig. 2.24). The ability of this particle oxide layer to improve the wettability of SiC particles by an alloy melt has been suggested by several investigators [76-77], and its action is distinctly different from that of a melt oxide layer which is a barrier to wetting. The addition of preheated alumina particles in an Al-Mg melt has also been found to improve the wetting of alumina [78, 79].

Pretreatment to achieve a clean surface using ultrasonic techniques, various etching techniques and heating in suitable atmosphere helps to enhance wetting [80]. The silica layer grown naturally or artificially on the surface of SiC particles used in Al based MMCs, helps to resist Al attack on SiC and the formation of Al_4C_3 and to improve wettability by Al which would result from the reaction between Al and the SiO_2 layer [81].

In general surface of non-metallic particles are difficult to wet by liquid metal. Hence wetting by a prior coating of the particles by a wettable metal, is commonly practiced since a liquid metal always almost wets a solid metal [82]. Such coating is possible using chemical vapour deposition (CVD), plasma vapour deposition (PVD),

electroplating, cementation, plasma spraying [83] and sol-gel processes [84]. Ni and Cu are good candidates for coating the particles [85-89].

Other mechanical methods such as stirring in a semi-solid state did help to promote wettability between SiC particles and Al-Si and Al-Mg alloys. Application of ultrasonic vibration in a liquid melt also helps in promoting the wetting of alumina by aluminium [90]. Experimental results show that contact angle varies with time and hence mixing time is one of the important variables. Near linear decrease of wetting angle with time for the SiC/Al system was observed at 900^{o}C by Kohler and Halverson et al. [91]. Similarly, Berman and Pask [92] observed linear dependence with time for Al-Al_2O_3 interface. Hence processing time should be controlled so that the coating does not dissolve completely.

Thus from metallurgical consideration the desired interfacial region in a composite relies on the following factors:

1. A good contact between reinforcement and matrix to establish satisfactory wetting of the reinforcement by the matrix.
2. Minimal variation in lattice spacing and crystal structure between the phases.
3. A very low rate of chemical reaction at the interface and little or no inter-diffusion between the component phases so that the reinforcement is not degraded.

2.9 Effect of particulate reinforcement in metals

In addition to the above damping mechanisms which are encountered in a ductile metallic matrix the contribution of ceramic particulates to the overall MMC damping may

also be related to the increase in dislocation density in the metallic matrix as a result of thermal strain mismatch between the ceramic particulates and metallic matrix during fabrication [93-96]. The residual thermal mismatch strain is proportional to the difference between the CTEs of the reinforcement and matrix, for example, the CTE of SiC and Al alloy is around 4ppm and 23ppm, respectively [23]. Several studies [26, 95] have shown that the dislocation density found in as-quenched, age-hardenable Al alloys is low, typically less than $10^{12}\,m^{-2}$, but the dislocation density in Al matrices containing ceramic particulates is of the order of 10^{13} to 10^{14} m^{-2} with the actual density dependent on the temperature interval of cooling, the difference in CTE ($\Delta\alpha$) between two phases and the shape of the reinforcement. Mathematically it is shown as follows:

$$\Delta\rho = \frac{\Delta\alpha\Delta T N A}{b} \tag{2.30}$$

where b is the burger's vector, N is number of particles, ΔT is the temperature change, and A is the surface area of particles. Studies of Hartman et al. [97] showed that pure Al6061 has a dislocation density of $3x10^{13}$ m^{-2} which increases to $70x10^{13}$ m^{-2} and $80x10^{13}$ m^{-2} under the presence of 5 and 20 vol. % of SiC particles. While the stresses induced by cooling are relieved considerably by dislocation generation, some residual (internal) stresses can locally surround the reinforcement with a magnitude dependent on its shape and spatial distribution [98-99]. These dislocations, generated to accommodate the residual thermal mismatch strains associated with the difference between the CTEs of the matrix and the reinforcements, are located primarily near the reinforcement-matrix interface and decrease with increasing distance from the interface. Fig. 2.21 shows a typical dislocation accumulation scenario in Al-TiC interface. In addition, secondary cold

forming processes such as extrusion, rolling, etc., produces dislocations called geometrically necessary dislocations (ρ_g), which was shown by Ashby [100] as follows:

$$\rho_g = \frac{k\varepsilon f}{rb} \tag{2.31}$$

where k is a constant, f is volume fraction of particles, b is burgers vector, r is the particle radius, and ε is the true plastic strain. Hence the presence of reinforcement may result in a greater dislocation density $(\Delta\rho + \rho_g)$. Consequently, these become a possible source of high internal friction because of the motion of the dislocations under cyclic loading based on the Granato-Lucke Mechanism [29] explained in the previous sections. Fig. 2.26 shows the actual dislocations motion from experimental observation.

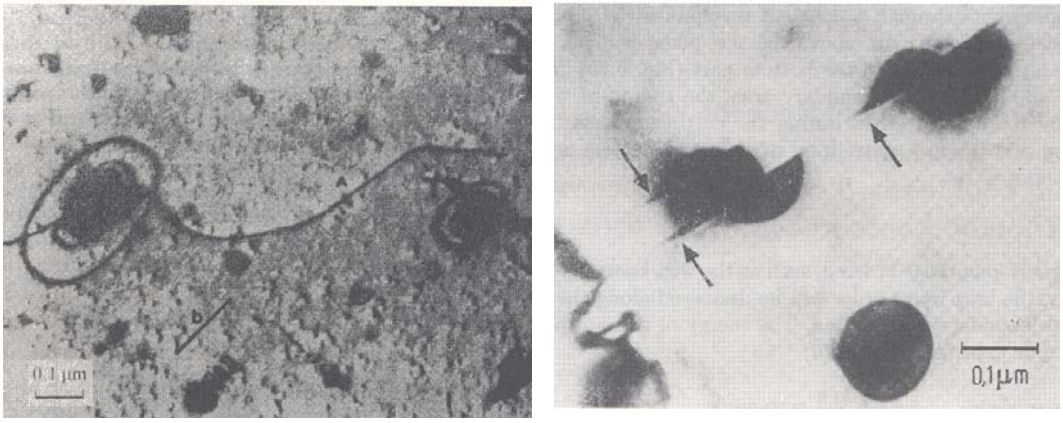

(a) **(b)**

Fig. 2.26 (a) Orowan loops around alumina particles in Cu30%Zn due to higher shear strength of the particle and (b) dislocation cuts a relatively soft precipitate in Ni 19%Cr6%Al [24].

The dislocation motion can be observed in terms of yield stress increase due to the impediment by the particle reinforcements. This increase in strength is related to the stress needed to force a dislocation between two inclusions. The total passage stress can be expressed as [101]:

$$\sigma_{pass} = \left(\frac{\mu b}{\lambda}\right) + \left(\frac{5}{2\pi}\right)\mu f\varepsilon \tag{2.32}$$

where μ is the shear modulus of the matrix, b is the burgers vector, λ is the inter-particle spacing, f is the volume fraction of reinforcement and ε is the plastic strain. Hence the actual strength of the composite that includes the effect of the thermal mismatch induced internal stress is given as:

$$\sigma_{pass} = \sigma_m + \left(\frac{\mu b}{\lambda}\right) + \left(\frac{5}{2\pi}\right)\gamma\left(1 - \frac{\varepsilon}{\varepsilon_f}\right)\mu f\varepsilon \tag{2.33}$$

where γ is a material constant and ε_f is the failure strain. Hence the work hardening rate is given as follows:

$$\frac{d\sigma}{d\varepsilon} = 4.8\mu\gamma f\left(1 - \frac{\varepsilon}{\varepsilon_f}\right) \tag{2.34}$$

Fig. 2.27 shows the variation in working hardening rate vs. plastic strain for Al-SiC MMC samples containing three different weight percentage viz., 6, 8 and 17. Thus the increase in dislocation with strain can be confirmed by studying the hardening behavior.

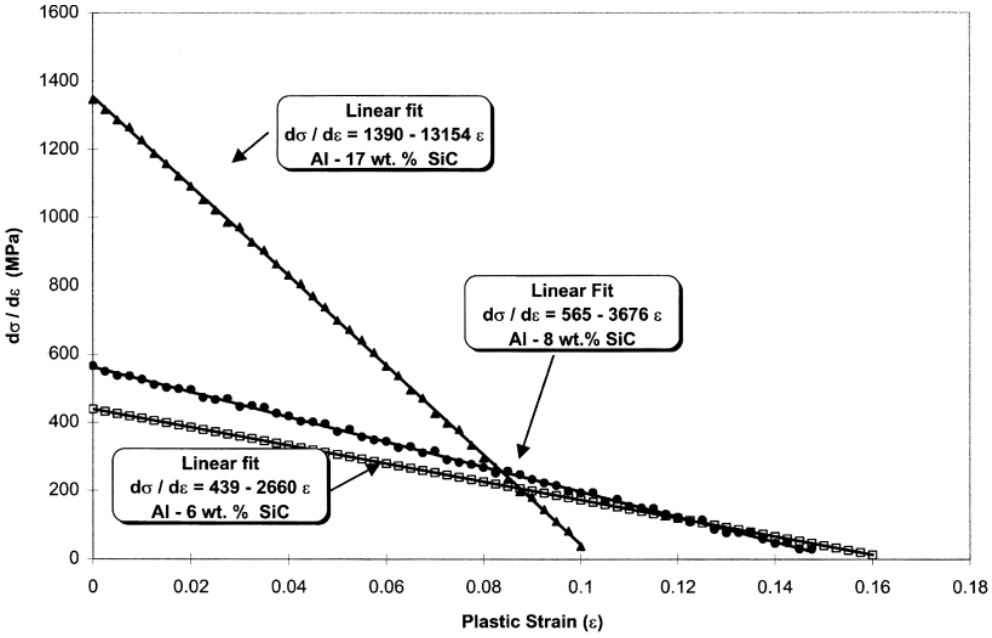

Fig. 2.27 Work hardening behavior of Al-SiC MMC systems [101].

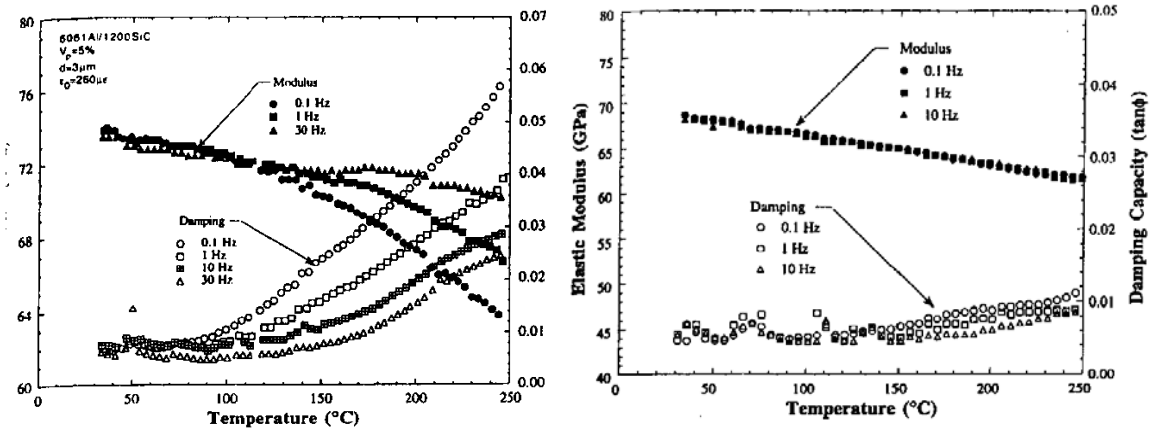

(a) **(b)**

Fig. 2.28 Variation of damping loss factor and stiffness of: (a) pure Al6061-T6 matrix and (b) Al6061-T6 with 5 vol. % SiC_p [21].

Damping studies of Zhang et al. [21, 102] clearly showed that the damping capacity due to presence of SiC particles in the Al6061 matrix exhibits a temperature, frequency (see Fig. 2.28) and strain amplitude dependence of internal friction (see Fig. 2.29). Due to dislocation motion dependence on strain amplitude (equtaion (2.10)), there is a critical strain amplitude (ε_c) of 10^{-5} below which only the frequency dependency is dominant. Above the ε_c the damping loss factor increases drastically as shown in Fig.

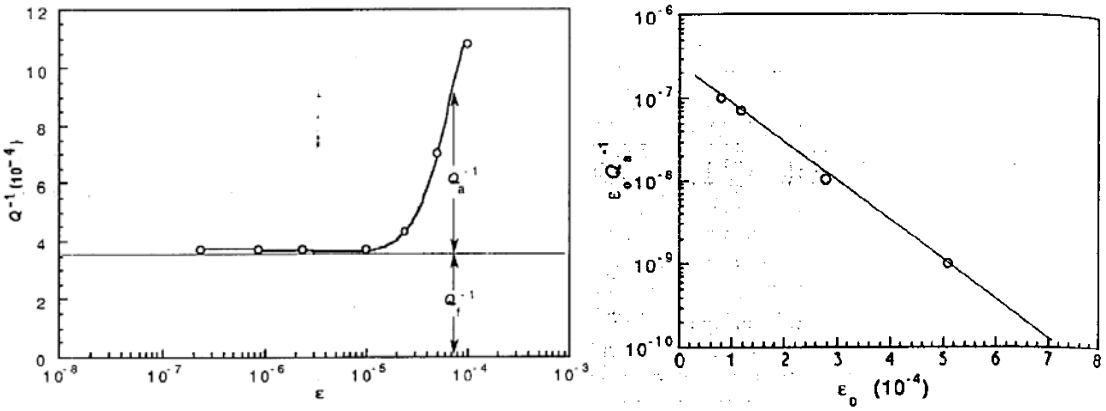

(a) **(b)**

Fig. 2.29 (a) Variation of damping loss factor with strain amplitude for 6061/SiC_p, (b) same data in terms of strain amplitude against product of strain amplitude over damping loss factor shows a linear behavior using which the coefficients are determined [102].

2.29, which can be studied by plotting the variation of strain amplitude and the product of strain amplitude and damping loss factor and thus enabling to determine the material constants and dislocation density [102]. The presence of dislocation can also be studied by varying the temperature and volume fraction of reinforcement. Results of Can Wang et al. [103] showed that the presence of 13 vol. % of SiC_p clearly increases the damping characteristics compared to the monolithic material condition, especially at higher temperature and the effect of grain boundary sliding is also clearly visible at a temperature of 475 ^oK (Fig. 2.30 (a)). Results of Schaller et al. [104] showed (Fig. 2.30 (b)) that under increasing volume fraction of saffil fibers (10 to 30 %) the internal friction of the Al matrix increased proportionally, and the rate of change in the internal friction with heating and cooling were different. Thus the effect of temperature, strain-rate (or frequency) and strain amplitude were clearly observed experimentally (Fig. 2.28 to 2.30) that could be attributed to the dislocation motion behavior and explained using G-L theory that was described in section 2.7.

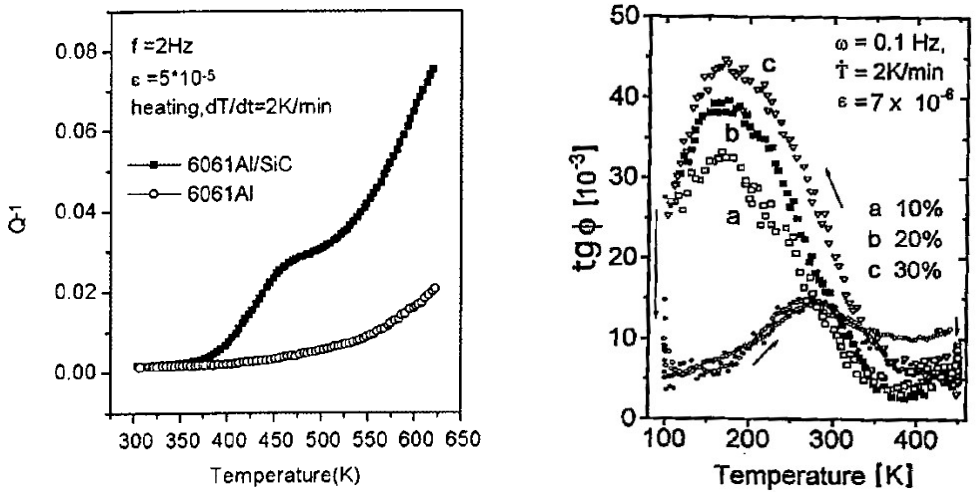

(a) **(b)**

Fig. 2.30 Variation of internal friction in Al matrix (a) under increasing temperature and with and without the presence of 13 vol. % of SiC_p [103] (b) with different vol. % of saffil fibers and under heating and cooling part of a thermal cycle [104].

Addition of discontinuous ceramic particulates results in grain refinement which is described mathematically by Humphreys [105] by assuming each particle nucleates one grain, as follows:

$$D_{gbp} = \frac{d(1-f)^{1/3}}{f^{1/3}} \tag{2.35}$$

where d is the particle size and f is the volume fraction of reinforcement. The above equation is verified for Al-SiC_p composites with d ranging from 3 to 100 μm and f ranging from 0.05 to 0.3. Miller and Humphreys [105] showed the recrystallized grain size by nucleation (as above equation) holds good for particles above 20 μm, but for particles below 3 μm, a grain size corresponding to a grain growth limited grain size, D_{gsp}, Zener's pinning relation holds good [106].

$$D_{gsp} = \frac{2d}{3f} \tag{2.36}$$

As described earlier, grain boundary sliding results in enhanced damping especially at elevated temperature (300^{o}C in Al) and in MMCs the increased presence of grain boundary will definitely result in enhanced damping at elevated temperature. This is confirmed in the damping results of Wang and Zhu [103] (Fig. 2.30 (a)), where the additional hump for Al/SiC sample confirms the enhanced grain boundary sliding.

In addition, based on the research works of Bishop and Kinra [107], addition of ceramic particulate improves the Elasto-ThermoDynamic (ETD) damping capability of the metallic matrix. Moreover, for particle and fiber-reinforced MMCs, it has been established that the ETD can be tailored to develop composite materials with high stiffness, strength and better damping properties [107]. Srivastava et al. [108] have reported a full dynamic solution (including inertia terms) for the calculation of ETD in heterogeneous materials.

Chapter 3

New Free-Free Beam Method Coupled With Circle-Fit Approach

3.1 Introduction

Experimental methods involved in the measurement of damping loss factor vary in the nature of deformation that is applied on the test specimen. The two basic types of deformation are: (a) shear deformation, where the shape of the material changes without volume change, and (b) dilatational deformation, where there are volume changes without any shape change [14, 109]. Most common techniques that are used to determine the damping behaviour of metal-based materials include: (1) time domain based torsion test method in which a cylindrical specimen is deformed in torsion to produce pure shear deformation and (2) time domain based flexural test method in which a suspended beam or a cantilever beam is deformed in bending and the transient vibration's settling time of vibration is recorded [23].

In the present research, a dynamic mechanical analyzer was built for a cantilever type specimen. The method was able to predict damping from 1Hz to 100 Hz at different temperatures and strain amplitudes. Fig.3.1 shows the typical arrangement, methodology, result and calculation procedure. The results matched the works of Lavernia and Zhang [21]. Similarly a simple impact type experimental setup using cantilever arrangement and laser based response measurement was setup. Fig. 3.2 shows the typical arrangement, methodology and results of an aluminium sample. Here again the method was successful only for low frequencies up to 30 Hz. The samples need to be long enough such that they would exhibit bending vibration but if it were too long, the sample vibrates at multi-modes and hence the calculated procedure as explained in Fig. 3.2 (d) is no more applicable. As mentioned, these procedures essentially provide damping only below 100 Hz, but design engineer involved in fast machines have bandwidth upto 2000Hz and

hence interest to develop a measurement close to this frequency is of much interest. Some researchers used ultrasonic methods to study damping [20] but their frequencies cross frequencies above 20 KHz to several MHz and hence not useful from structural and

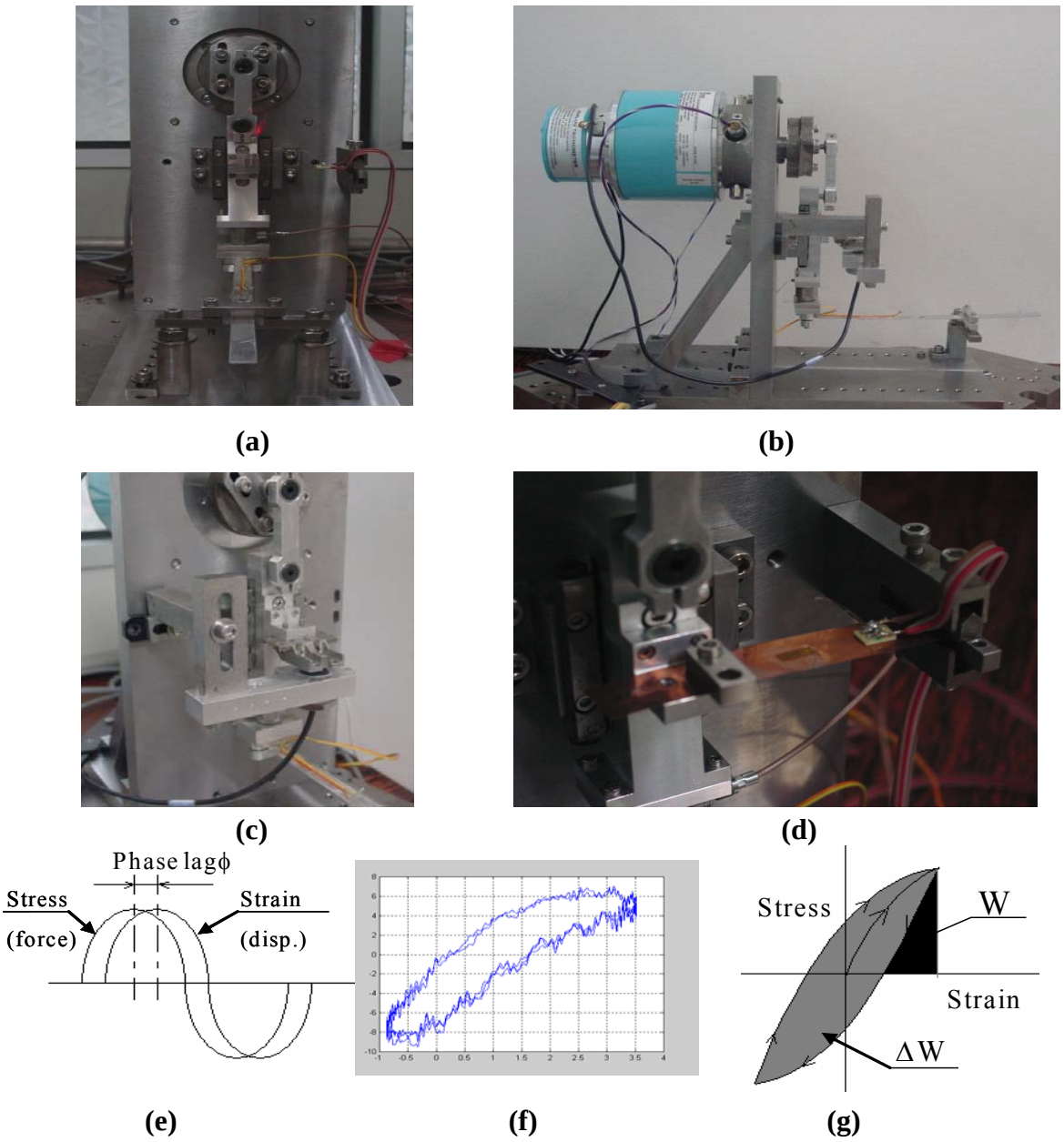

Fig. 3.1 (a) to (d) Dynamic mechanical analysis equipment built using a rotary to reciprocating conversion mechanism to measure the energy dissipated within each cycle (e) phase lag measured between stress and strain (f) actual result for pure Al sample and (g) Calculation of energy spent and maximum strain energy from the hysterisis loop.

mechanical designers' point of view.

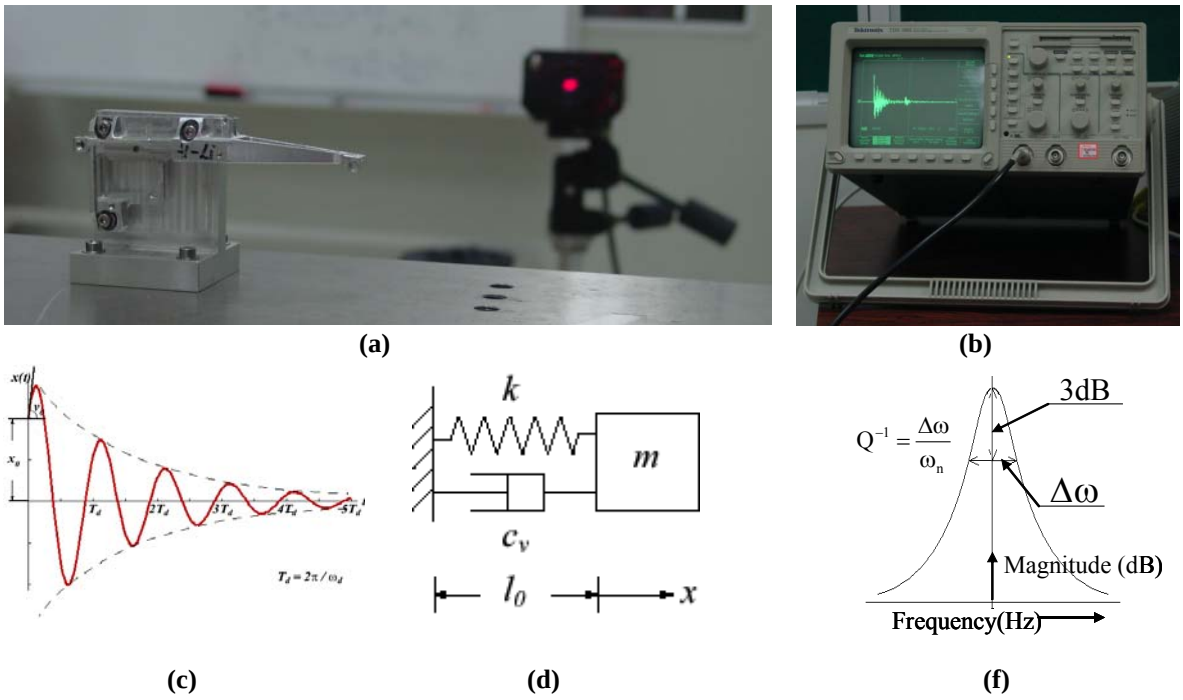

Fig. 3.2 Time domain damping measurement: (a) sample mounting and using laser to measure, (b) actual measurement result, (c) & (d) idealizing the decay as a SDOF with single frequency and (f) calculation procedure.

The results of the literature search revealed that no attempt is made so far to determine the damping behaviour of material using free-free type suspended beam technique utilizing frequency domain based circle-fit approach. Such a method ensures minimum energy dissipation to the support and differentiates each mode of vibration if the sample vibrates at multi-modes. Accordingly, in the present study, the feasibility of free-free type suspended beam approach was devised to determine the damping behaviour of metal based monolithic and composite samples. The damping loss factor, η, corresponding to the resonant frequency was obtained from a form of circle-fit method. In the following sections, the theoretical background for this method is elaborated.

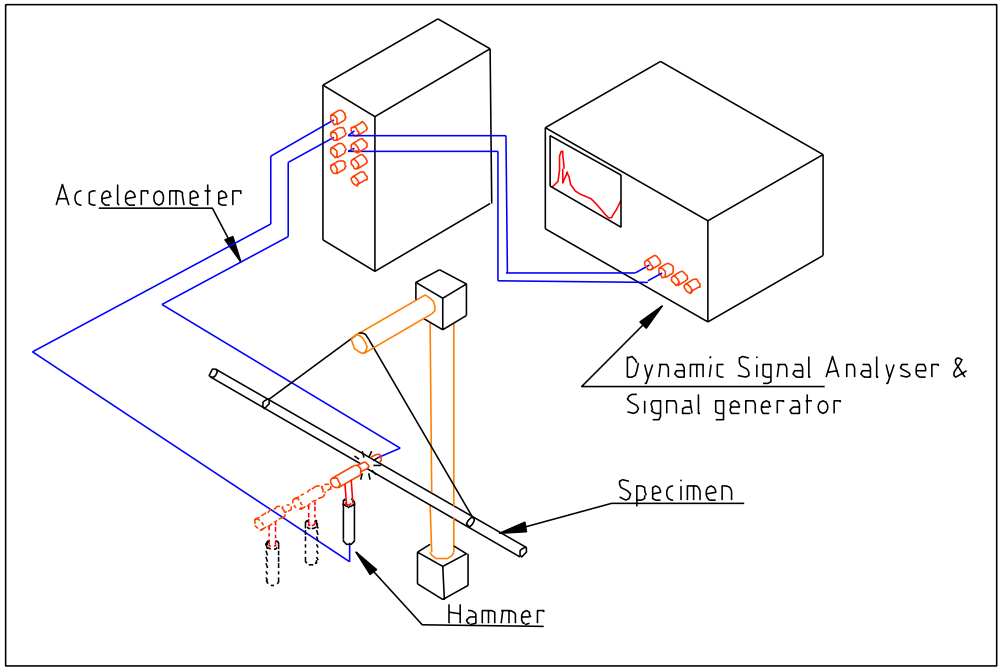

Fig. 3.3 Schematic diagram showing experimental setup of suspended beam technique.

3.2 Free-Free beam type method

The flexural vibration of a long slender specimen in the transverse direction under suspended beam support condition, shown in Fig. 3.3, can be mathematically described by the Bernoulli-Euler equation as follows [111, 112]:

$$\frac{EI}{\gamma A}\frac{\partial^4 y}{\partial x^4}+\frac{\partial^2 y}{\partial t^2}=0 \qquad (3.1)$$

where y is the transverse displacement, t is time, x is the position along the beam, γ is the density, A is the cross-sectional area of the beam, E is the Young's modulus and I is the second moment of the cross-sectional area. Practically the round specimen can be assumed to be slender if the length to diameter ratio is greater than 25.

Equation (3.1) is a fourth order differential equation, which can be solved to arrive at the natural frequency of vibration of the beam for various end support conditions

[36]. The deformation of the specimen under the free-free type condition can be described as [111]:

$$(kl)^2 (1 - \cosh kl \cos kl) = 0 \tag{3.2}$$

where l is the sample length and k is a constant such that $(kl \approx 4.73)$ for the first mode. To achieve the free-free support condition in a practical situation, the beam is suspended at the vibration nodal points by nylon strings. From equation (3.2) the node points can be determined corresponding to the first bending mode which is around 0.224 times the sample length. The natural frequency (ω_n) of the beam under the free-free condition such that it exhibits the bending mode is given by the following equation:

$$\omega_n = 22.4\sqrt{\frac{EI}{A\gamma L^4}} \tag{3.3}$$

3.3 Presence of End Mass at Ends

In the present study, the above method was also extended to alter the resonant frequency of the specimen. This was achieved by attaching end masses at both ends of the beam (see Fig. 3.4 (a)) and the beam was suspended at the vibration nodal points by nylon strings. Under this condition, the boundary conditions at the two ends can be expressed as follows [111, 112]:

$$\begin{pmatrix} \text{at} \quad x = 0 \Rightarrow \quad m_e \dfrac{\partial^2 y(0,t)}{\partial t^2} = -EI \dfrac{\partial^3 y}{\partial x^3} \quad \text{and} \quad \dfrac{\partial^2 y(0,t)}{\partial x^2} = 0 \\ \text{at} \quad x = L \Rightarrow \quad m_e \dfrac{\partial^2 y(L,t)}{\partial t^2} = EI \dfrac{\partial^3 y(L,t)}{\partial x^3} \quad \text{and} \quad \dfrac{\partial^2 y(L,t)}{\partial x^2} = 0 \end{pmatrix} \tag{3.4}$$

Thus solving equation (3.1) and (3.4), the corresponding fundamental natural frequency (ω_n) of the beam with end masses can be expressed by the following equation:

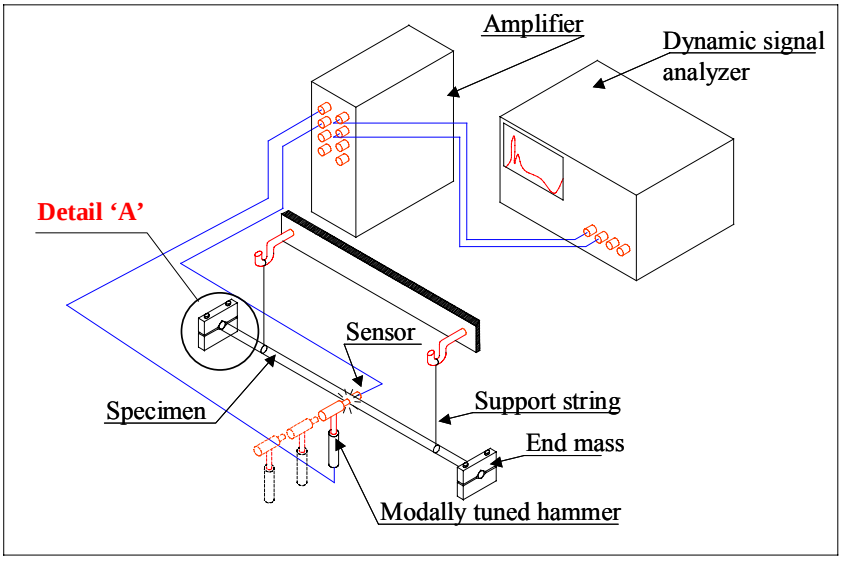

(a)

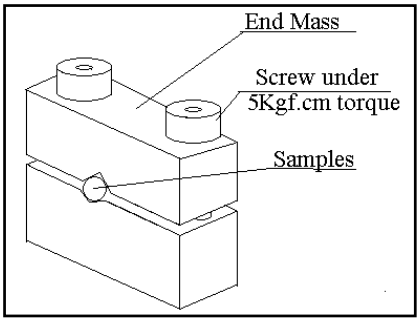

(b)

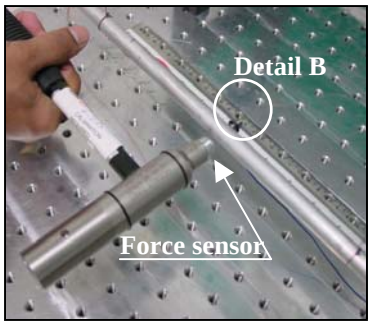

(c)

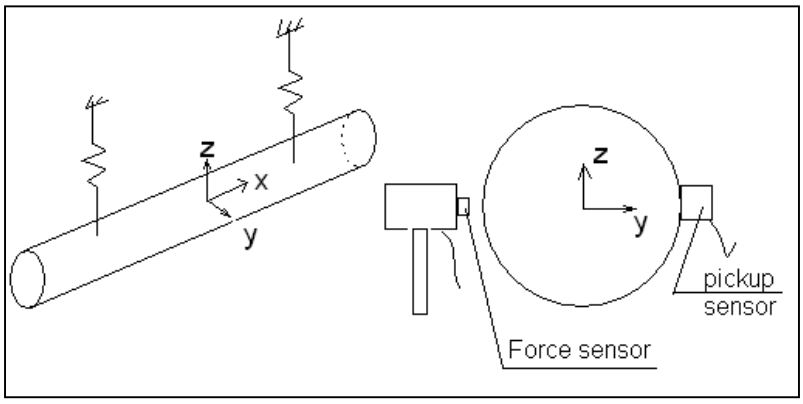

(d)

Fig. 3.4 (a) Schematic diagram showing experimental setup of suspended beam technique, (b) enlarged sketch showing the fastening method of end mass shown as detail 'A', (c) actual load and sensor placement direction and (d) sketch explaining the sensor placement location.

$$\omega_n = \frac{\pi}{2}\left\{\frac{EI}{L^3 m_b}\left[1+\frac{5.45}{1-77.4\left(m_e/m_b\right)^2}\right]\right\}^{0.5} \tag{3.5}$$

where m_e and m_b are the mass of the end mass and beam, respectively. It is observed that if the end mass exceeds five times of the specimen (beam) mass then end mass acts like a hinge location. Thus by varying the end mass size the resonant frequency can be varied and the corresponding frequency can be determined. In the present study, a small impact force is applied using the modally tuned hammer and the vibration response is measured using a small mass type accelerometer. Generally an added mass such as accelerometer should not exceed 3% of the specimen weight. In the present study the accelerometer used less than few grams in weight. Results from the computations are available as plots of amplitude against frequency and are called frequency response function (FRF). The ratio of the displacement response to the applied force is called receptance frequency response function, which is calculated using fast fourier transform (FFT) method [113]. The FRF is mathematically computed by dividing the cross power spectrum $S_{x,f}(j\omega)$ estimate between input and output by the input auto power spectrum estimate $S_{f,f}(j\omega)$ as follows [113]:

$$FRF = H(j\omega) = \frac{S_{x,f}(j\omega)}{S_{f,f}(j\omega)} \tag{3.6}$$

Fig. 3.5 shows a typical receptance FRF for a pure Al sample, which shows the sharp resonance peak and hence using conventional damping calculation which is performed for polymer samples becomes difficult. Further the exact natural frequency and the damping property is measured using the circle-fit method, which is described in the following section.

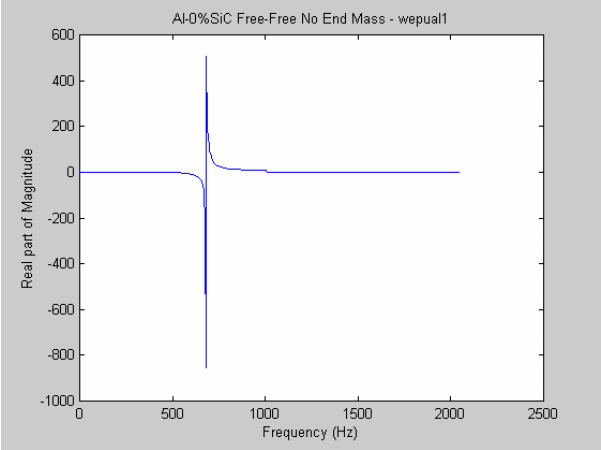

Fig. 3.5 Typical real part of receptance frequency response function (FRF) of a metallic sample which shows the resonance peak is so sharp that damping calculation is difficult to derive the damping factor.

3.4 The circle-fit method

As shown in Fig. 3.5, metallic samples have low damping hence special methods are required to handle measurement data containing low damping signals. The circle-fit method, first introduced by Kennedy and Pancu [114] uses the Argand plane to display the real and the imaginary parts of the receptance frequency response function (FRF). Around each natural frequency, the FRF curve approaches a circle and the natural frequency is located at the point where the rate of change of arc length with frequency attains a maximum. The model assumed that the damping is the hysteretic one and the damping factor is evaluated from a simplified half-power points calculation and the mode shapes are calculated from the ratios of the diameters of the circles, fitted around each natural frequency for the various output responses. A comprehensive study of the circle-fitting method has been presented by Ewins [115]. In the present study, the circle-fitting method was implemented as software, which predicts accurately the natural frequency ω_n and the damping factor η. Based on vibration theory [115], the receptance frequency

response function of an N degree of freedom system with hysteretic damping is given by the following equation:

$$\alpha_{jk} = \sum_{r=1}^{N} \frac{C_{jk}^{r}}{\omega_r^2 - \omega^2 + i\eta_r\omega_r^2} \tag{3.7}$$

where η_r, ω_r and C_{jk}^{r} are the hysteretic damping ratio, natural frequency and complex modal constant, respectively, associated with each mode r.

From experimental results of beam vibration close to a particular mode's frequency range the contribution of the out-of-range modes to the total response is a constant. Therefore, the receptance can be expressed as [115]:

$$\alpha_{jk}(\omega) = \frac{C_{jk}^{r}}{\omega_r^2 - \omega^2 + i\eta_r\omega_r^2} + D_{jk}^{r} \tag{3.8}$$

where D_{jk}^{r} is a complex constant associated with mode r. The nyquist plot of $(\omega_r^2 - \omega^2 + i\eta_r\omega_r^2)^{-1}$ is a circle. Thus, multiplication by the complex constant C_{jk}^{r} means a magnification or reduction of the circle radius, as well as a certain rotation. Addition of

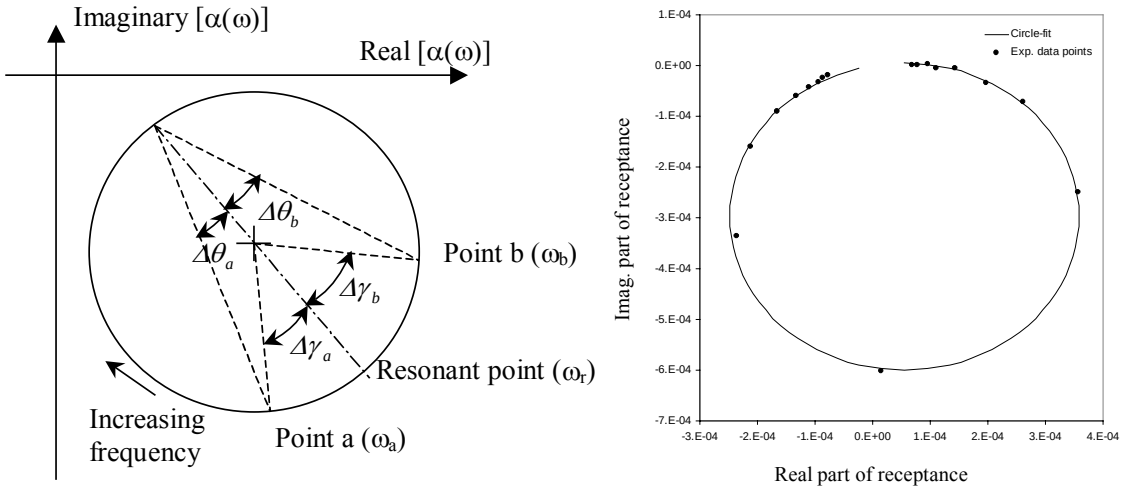

(a) **(b)**

Fig. 3.6 Typical receptance frequency response function (FRF) showing the use of the natural frequency and two data points to derive the damping factor.

D^r_{jk} corresponds to a simple translation of the circle in the argand plane. In practice, the complete curve will not be exactly a circle around each natural frequency, but the curve will have circular arcs around those frequencies especially when close modes exists.

In the present study, the derivation of the damping factor and the natural frequency associated with a particular mode of the beam, relies on the fitting of a circle based on the minimisation of error (e_1) to the M data points of the frequency response curve near the resonant frequency. The error e_1 can be represented as follows:

$$e_1 = \sum_{j=1}^{M} \left[R_o^2 - \left[(x_j - x_o)^2 + (y_j - y_o)^2 \right] \right]^2 \tag{3.9}$$

where x_o and y_o are the coordinates of the circle centre and R_o is the radius of the circle fit.

The location and determination of the natural frequency are usually based on a frequency spacing technique. For a given mode, and apart from the effect of the complex modal constant, the phase angle θ_r associated with the dynamic response is given by equation (3.7) from which the resonant frequency ω_r can be derived when $d\omega^2/d\theta_r$ is a minimum.

$$\theta_r = \tan^{-1}\left[\eta_r \left(1 - \frac{\omega}{\omega_r} \right)^{-2} \right] \tag{3.10}$$

Since angle θ and angle γ are related as shown in Fig. 3.6 (a), it is evident that calculating the minimum of $d\omega^2/d\gamma_r$ is the same as $d\omega^2/d\theta_r$. Fig. 3.6(b) shows a typical circle fit plot for a pure Al sample which shows the frequency spacing variation near resonance. Thus taking two points a and b on the circle, one corresponding to a

frequency below the natural frequency ω_b and another corresponding to a frequency above the natural frequency ω_a, the damping factor η_r can be expressed as follows:

$$\eta_r = \frac{\omega_a^2 - \omega_b^2}{\omega_r^2} \frac{1}{\mathrm{Tan}(\Delta\theta_a) + \mathrm{Tan}(\Delta\theta_b)} \tag{3.11}$$

3.5 Damping Interpretation

It may be noted that under low damping conditions such as in composite specimens, equation (3.12) can be used to relate the loss factor η to the other damping measures, where, ψ is the ratio between the energy dissipated during each loading cycle, ΔW, and the maximum energy stored during the cycle, W, ζ is the damping ratio, δ is the logarithmic decrement, ϕ is the phase angle between the applied stress and the resultant strain, Q^{-1} is the inverse quality factor, $A(t_1)$ and $A(t_2)$ are the displacements at times t_1 and t_2, respectively, and f_r is the resonant frequency [23].

$$\psi = \Delta W / W = 4\pi\zeta = 2\delta = 2\pi \tan\phi = 2\pi\eta = 2\pi Q^{-1} = \frac{2\ln\left(A(t_1)/A(t_2)\right)}{f_r[t_2 - t_1]} \tag{3.12}$$

In the experimental method used in the present study various forms of damping can be expected to influence the specimen vibration other than the material damping, such as support energy dissipation due to strings and aerodynamic drag on the specimen surface. The specimen is hung at its nodal points of the first bending mode, which ensures that the relative displacement of the strings with respect to the beam surface is kept to a minimum. Secondly, as stated by Ewins [115] if the support in a free-free system is kept perpendicular to the direction of motion then the energy dissipated through the strings is expected to be negligible. This is because the strings are of soft material

type (such as nylon) whose stiffness is very low compared to the aluminium-based sample. Secondly the present suspension system is like a pendulum arrangement whose resonant frequency (ω_{sn}) provides a resonant frequency which depends only on the suspension length (L_s) as follows [112]:

$$\omega_{sn} = \sqrt{g / L_s} \tag{3.13}$$

In the present study, the length was maintained at 0.4 m, which provides a resonant frequency of 0.79 Hz that simulates closer to a free-free type condition.

When a beam is supported by two resilient strings that support the beam by a distance that is slightly off from the node point of vibration from beam, it can dissipate a fraction of the vibration energy of the beam. To quantify the energy dissipated by the string support placed at a distance 'a' from the nodal location of the beam, reasonable assumptions were made which are listed in the following paragraphs.

The vibration pattern for any end mass can be predicted by solving the Euler-Bernoulli equation and the boundary conditions described by equation (3.2). For example, in the case of free-free type beam the mode shape gives the characteristics vibration pattern of the specimen under resonance operating condition as follows [1]:

$$y_i = \cosh\left(\frac{\lambda_i x}{L}\right) + \cos\left(\frac{\lambda_i x}{L}\right) - \sigma_i\left(\sinh\left(\frac{\lambda_i x}{L}\right) + \sin\left(\frac{\lambda_i x}{L}\right)\right) \tag{3.14}$$

where λ_i and σ_i depends on the mode number and for first bending mode they are found to be 4.73 and 0.9825, respectively [1]. When the string is held at a distance 'a' from the node location, which is denoted as the distance x_a from the free end of the beam, it is expected to vibrate sinusoidally (as $A_o \sin \omega_n t$, where A is the maximum amplitude at string support and ω_n is the beam resonant frequency). The node location for a free-free

beam can be computed from the equation (3.14) to be 0.224 times the beam length from the free end. The maximum vibration amplitude A_o at the string supports can be computed in terms of beam's amplitude at distance x_a, using the equation (3.14) as follows:

$$A_o = \left(\cosh\left(\frac{\lambda_i x_a}{L}\right) + \cos\left(\frac{\lambda_i x_a}{L}\right)\right) - \sigma_i \left(\sinh\left(\frac{\lambda_i x_a}{L}\right) + \sin\left(\frac{\lambda_i x_a}{L}\right)\right) \quad (3.15)$$

For example, if the string is supported at a distance of 5 mm from the nodal point of dislocation, the vibration amplitude of the string end is expected to be around 0.111 compared to the beam's center vibration amplitude.

Using the string displacement variation with time and the damping capability of the string material, the energy dissipated by the string support in one cycle can be shown as follows:

$$E_{string} = \frac{\eta_{string}}{2} K A_o^2 V_{string} \int_0^T \left(\sin(\omega_n t)\right)^2 dt \quad (3.16)$$

where, V_{string} is the volume of the each string, ω_n is the beam resonant frequency, K is the string stiffness which can be taken to be the axial stiffness of the string (as an upper bound of its maximum stiffness) that is equal to $(E_s.A_s / L_s)$, where E_s, A_s and L_s are the Young's modulus, area of cross-section and length of the string support. In the present study, nylon strings of 1mm diameter and 0.4m long with an elastic modulus of 1GPa [2] was used as the resilient support for the beam. The damping loss factor of nylon string η_{string} is around 0.1 [2]. Further, the energy dissipated by the two strings at the beam resonant frequency can be expressed as an equivalent damping loss factor η_{string} as follows:

$$\eta_{string} = \frac{2E_{string}}{\pi\omega_n^2 m\overline{X}^2} \tag{3.17}$$

where, m is the mass of the beam, $\overline{X}^2$ is the mean square of the vibration amplitude and ω is the resonant frequency of the beam. Thus using the above assumptions it can be shown that for a magnesium beam under free-free support, the strings placed at 5mm distance from the nodal position can provide an equivalent damping loss factor of around $2.7x10^{-13}$, which is significantly less than the damping loss factor of pure magnesium of 0.0038 [18].

In addition, the specimen experiences aerodynamic drag as it vibrates in the open atmosphere. The aerodynamic drag of the specimen is always opposite to the direction of velocity and has a magnitude given by [111]:

$$F_{drag} = C_D(Re)A_p \frac{1}{2}\rho sgn(v)v^2 \tag{3.18}$$

where sgn(v) denotes the sign of the velocity v, A_p is the area of the specimen projected on a plane perpendicular to the direction of motion and ρ is the density of the air. $C_D(Re)$ is the drag coefficient of a cylindrical rod perpendicular to flow which depends on the Reynolds number (Re) and based on the experiment results of Blevins [111] the drag coefficient of the specimen in the present study can experience a drag coefficient of 2.5, based on the specimen dimensions, such as diameter and length, which were maintained to be 300mm and 10mm long, respectively.

Further, the energy dissipated over one cycle of motion due to damping force F_{drag} can be shown as follows:

$$\Delta E = \int_0^{2\pi/\omega} F_{drag} v dt = \int_0^{2\pi/\omega} F_{drag} X\omega\cos(\omega t)dt \tag{3.19}$$

The energy dissipated per cycle ΔE can be expressed as damping ratio ζ by dividing it by the critical damping factor $C_{cr}\left(=2\omega_n m\right)$, where m is the specimen mass and ω_n is the natural frequency. The damping ratio can be further expressed as damping loss factor η_{air} using equation (3.19) as follows:

$$\eta_{air} = \frac{4\rho C_D A_p \omega X}{3\pi\omega_n m} \tag{3.20}$$

where X is the vibration amplitude and ω is the frequency of vibration. Using this approach, the damping loss factor due to aerodynamic forces corresponding to a deformation amplitude which can cause a strain amplitude of 10^{-6} in the specimen was calculated corresponding to resonant frequency of the rods and normal ambient condition. This amounted to be $2x10^{-7}$ which is very low compared to the typical material damping loss factor of the metallic specimen which is around 0.0023 in the present study. Secondly, in the present study the support damping due to strings as well as due to drag forces are expected to be same for all the specimens due to their similar dimensions and since they were subjected to similar loading conditions.

Using equation (3.3), the elastic modulus of the sample can be determined by using the sample dimensions (viz., diameter and length) as well as the density of the sample. Thus with the knowledge of the elastic modulus and damping from the single experiment, the material can be mapped on to a Ashby map explained in Fig. 2.6. To assess materials, internal damping of the beam material can be taken into account by expressing the elastic modulus of the material as a complex quantity E^* for any lightly damped material such as metallic materials [2] which can be written at any given temperature in terms of the loss factor η as follows:

$$E^* = E(1 + i\eta) \tag{3.21}$$

where i denotes the complex number. Thus from the above details the storage modulus and loss modulus can be differentiated as obtained from a typical dynamic mechanical analysis experiment [116]. Thus the testing methodology introduced in this study provides the researchers with yet another tool for measuring the damping behavior of materials.

Material damping is related to the time-dependent elastic behavior of materials. Metallic materials respond to an applied load not only by an instantaneous elastic strain $\varepsilon_{elastic}$ that is time independent, but also by a strain lagging behind the applied load, which is time dependent in nature. Therefore the overall strain ε is the sum of elastic part $\varepsilon_{elastic}$ and the anelastic part $\varepsilon_{anelastic}$ as described in equation (3.22), while the variation in the anelastic part of the strain for the loading and the unloading part can be expressed as $\varepsilon_{anelastic-loading}$ and $\varepsilon_{anelastic-unloading}$ by equation (3.23) and (3.24), respectively, as follows [18]:

$$\varepsilon = \varepsilon_{elastic} + \varepsilon_{anelastic} \tag{3.22}$$

$$\varepsilon_{anelastic-loading} = \varepsilon_{initial}\left[1 - \exp(-t/\tau)\right] \tag{3.23}$$

$$\varepsilon_{anelastic-unloading} = \varepsilon_{initial}\left[\exp(-t/\tau)\right] \tag{3.24}$$

where $\varepsilon_{initial}$ is the initial strain, t is the time and τ is the relaxation constant which signifies the intrinsic energy dissipated within the material. Hence such a strain response under a sinusoidally varying applied stress σ with a frequency ω, results in a hysterisis loop, which represents the energy dissipated in one loading cycle ΔW and can be mathematically represented as follows:

$$\Delta W = \oint \sigma . d\varepsilon \tag{3.25}$$

The maximum strain energy W can be shown to be:

$$W = \int_{\omega t=0}^{\omega t=\pi/2} \sigma.d\varepsilon \tag{3.26}$$

The damping loss factor η, which is the ratio of ΔW versus W, can be shown to be a function of the time constant τ based on the above described equations. Furthermore, the stiffness of the material E^* which is the ratio of stress versus strain at any given time instant can be shown to be a complex number due to the anelastic behavior based on the above equations (i.e. from (3.21) to (3.24)) and hence related to the measured modulus and damping loss factor, as follows:

$$E^* = \frac{\sigma}{\varepsilon} = E' + iE'' = E'\left(1 + i\frac{c\omega\tau}{1+\omega^2\tau^2}\right) = E'(1+i\eta) \tag{3.27}$$

where E' is the storage modulus, E'' is the loss modulus, c is a constant and i is the complex number $\left(\sqrt{-1}\right)$.

Related publications

[1] N. Srikanth, and M. Gupta: *Materials Research Bulletin*, Vol. 37 (2002), pp. 1149-1162.

[2] N. Srikanth, D. Saravanaranganathan, M. Gupta, *Mat. Sci. and Tech.*, Vol. 20 (2004) 1389-1396.

Chapter 4

Experimental Procedures

4.1 Materials and Processes

As noted earlier there are principally two methods of preparing the composites: power metallurgy and solidification method. Processing of MMCs can be done using a number of techniques which is primarily grouped under: (a) solid state, (b) partial solid state and (c) liquid state categories [117-119]. The selection of the processing technique is very important since the final properties depend on the resultant microstructures, and interfacial bond as discussed in chapter 2. With such a wide range of processing routes available, the appropriate choice will depend on the application and acceptable cost.

4.1.1 Solid state processing

Solid state processes are generally used to obtain the highest strength properties in MMCs, partly because segregation effects and brittle reaction product formation are at a minimum for these processes when compared to liquid state processes. The main solid state processes are: powder metallurgy, diffusion bonding and mechanical alloying. In the present study nano-grained samples were prepared using powder metallurgy and mechanical alloying methods which are explained in the following sections.

Powder Metallurgy

Powder metallurgy is the most commonly used method in solid state processing [117]. Metal powder is first blended with reinforcement particulates. A cold isostatic pressing is utilized to obtain a green compact that is then thoroughly outgassed and forged or extruded. The main advantage of the PM route is that it allows any alloy and any type of reinforcement to be used as matrix and reinforcement, respectively, the

working temperature can be adjusted to minimize reaction and high volume fraction of reinforcement can be achieved. The disadvantages include handling the powder, removal of process control agent which act as contamination and high cost of the method.

Mechanical alloying

In this method a high energy impact mill is used to continuously fragment and reweld powder particles as fresh internal surfaces are exposed. Frictional heating at the particle interface causes local melting and consolidation and rapid heat extraction by the cooler particle interior causes rapid solidification. Hence composites produced by this method are often strong due to high dislocation density and homogenous due to the thorough mixing of the constituents. The main disadvantage of this process is the reduced ductility of its products and the contamination that come from the steel balls. This method has been successful in preparing nano-grained powders of pure metals such as Cu and Ni [120].

4.1.2 Liquid Spray Processing

Liquid state processes can be classified by the method used to physically combine the matrix and reinforcement. They can be divided into four major categories: (a) dispersion (b) infiltration (c) spraying and (d) in-situ fabrication [118].

Vortex Method

In this method, the metallic matrix is superheated in the molten range and the reinforcement is subsequently incorporated in loose form. Most metal-reinforcement

exhibit poor wetting so mechanical agitation is required to combine the 2 phases. The challenges include settling of reinforcement particulates and the limited volume fraction of reinforcement that can be incorporated. Settling of reinforcement results due to density difference between reinforcement particulates and the matrix melt, for example, SiC has a density of 3.2 g/cc while molten Al and Mg has a density of 2.7 g/cc and 1.7 g/cc, respectively. The volume fraction of reinforcement is limited as the viscosity of the melt increases with particle incorporation and becomes non-newtonian [117]. As a result, the power requirements necessary for mixing limits the amount of reinforcement that can be incorporated.

Disintegrated Melt Deposition Method

In the present study a new innovative method was used which is based on utilizing the best features of vortex mixing, casting and spray processing. The benefits of microstructural refinement, reduced segregation and minimal interfacial reactions give it great potential as a fabrication technique for MMCs. This method is popularly known as Disintegrated Melt Deposition (DMD) technique [121]. It involves incorporating the ceramic particulates by vortex mixing. The resulting slurry is then disintegrated by jets of inert gas and subsequently deposited on a metallic substrate. Unlike conventional spray processes, the DMD technique employs higher superheat temperatures and lower impinging gas jet velocity. This process produces only bulk composite material and avoids the formation of over-spray powders. It offers both the features of finer grain size and low segregation of spray processes, and the simplicity and cost effectiveness of

conventional foundry processes. This technique was thus chosen as the primary process in the present study to fabricate the composites.

4.2 Microstructure Characterization

Microstructural characterization was conducted on the extruded composite samples in the metallographically polished condition in order to determine the presence of micropores, interfacial integrity between the reinforcement and the matrix, and the constitutional characteristics of the metallic matrix. Initially, the samples were polished and were examined using optical microscopy technique to determine the grain size and grain morphology of the MMCs. JEOL JSM-T330A scanning electron microscope (SEM) equipped with energy dispersive spectroscopy (EDS) was used for the microstructure analysis of the monolithic and composite samples. Scanning Electron Microscope (SEM) was used to investigate: (i) the distribution of particulates (ii) the interfacial bonding, and (iii) the presence of porosity.

4.3 Density and Porosity Measurement

The densities of the extruded composite samples were measured by Archimedes' principle. The specimens were weighed in air and in distilled water using an A & D ER-182A electronic balance to an accuracy of ± 0.0001g. The porosity was then calculated from the measured composite density, theoretically computed rule of mixture density and the reinforcement weight fractions [122-123].

4.4 Thermo-Mechanical Testing

The thermo-mechanical study was intended to measure the coefficient of thermal expansion (CTE). The test was carried out using the Setaram 92 TMA 16-18 machine that uses a spherical ended, 5mm-diameter alumina probe. The top and bottom surfaces of test specimen were ground using a 300 grit SiC abrasive paper to ensure that the specimens'surfaces were flat. A test sequence of temperature range from 20^{o}C to 400^{o}C was used for each of the extruded specimen. The temperature was measured by a K-type, coaxial thermocouple and the test was carried out in an inert environment of argon gas. The data was obtained in the form of curves of dimension changes versus temperature and time. The Setaram software was used to calculate the average coefficient of thermal expansion.

4.5 Tensile Testing and Fractography

Tensile testing of the extruded samples was conducted in accordance with the ASTM E8M-96 standard [124] on round tension test specimens of diameter 5mm and gauge length 25mm using an automated servo-hydraulic testing machine (Instron 8501), with cross head speed set at 0.254 mm.min^{-1}. An initial strain rate of 1.69x10^{-4} s^{-1} was used. Fractographic studies using SEM studies were also conducted on the tensile fractured surfaces of the extruded composite samples in order to provide insight into their failure mechanisms.

4.6 Hardness measurement

The micro-hardness measurements were conducted on the monolithic and

reinforced samples using a digital micro-hardness tester (Matsuzawa model MXT50). Microhardness measurements were carried out using a pyramidal diamond indenter with a facing angle of 136^{o} employing an indenting load of 25gf and a dwell time of 15 seconds [125]. In the composite specimens, the microhardness measurements were made on the following regions: the aluminium matrix, the reinforcement wire, and the interfacial zone.

4.7 Suspended Beam Dynamic Testing

The most popular flexural mounting method is Free-Free beam method (see Fig. 3.3). Based on the ASTM C1259-98 standard [126], the beam is suspended at its nodes by two nylon strings whose inertia is very low so as to minimize the energy dissipated through the strings. Under a resonance condition, nodes and anti-nodes are the locations in the beam that would undergo minimum and maximum vibration amplitude, respectively, and can be detected from the mode shape (see chapter 3).

The experiment was performed with the accelerometer placed at the anti-nodal position [110], viz., at the centre of the beam length so as to capture the first mode of flexural vibration, which would be similar to a half sine wave. Initially a preliminary analysis was performed to find the nodal points of the bending mode. The strings were placed at this position to minimize the energy loss passed into the strings. The nodal points for beams of uniform section in a free-free suspension are at distances from the free ends of approximately 0.224L and 0.776L, where L is the length of the beam [110, 111]. Very little exciting energy is required, even for very large specimens, because the

measurement is performed at very low strain amplitude. Hence only a very light tap is sufficient to initiate the measurement.

The excitations were provided using a modally tuned hammer equipped with load sensor at the tip. The tip material can be changed from nylon to steel so as to change the impulse duration when the excitation is applied [115]. Following excitation, first mode of flexural vibrations was captured by accelerometer and the frequency response function thus obtained was used to determine natural frequency and damping factor using circle-fit method. Thus, the damping factor η_{free} can be expressed using the angles shown in Fig. 3.6, as follows [11]:

$$\eta_{free} = \frac{\omega_a^2 - \omega_b^2}{\omega_r^2} \frac{1}{\tan(\Delta\theta_a) + \tan(\Delta\theta_b)} \tag{4.1}$$

It may be noted that under low damping conditions such as in metallic specimens, equation (2) can be used to relate the loss factor η to the other damping measures, where, ψ is the ratio between the energy dissipated during each loading cycle, ΔW, and the maximum energy stored during the cycle, W, ζ is the damping ratio, δ is the logarithmic decrement, ϕ is the phase angle between the applied stress and the resultant strain, Q^{-1} is the inverse quality factor, $A(t_1)$ and $A(t_2)$ are the displacements at times t_1 and t_2, respectively, and f_r is the resonant frequency [7].

$$\psi = \Delta W / W = 4\pi\zeta = 2\delta = 2\pi \tan\phi = 2\pi\eta = 2\pi Q^{-1} = \frac{2\ln\left(A(t_1)/A(t_2)\right)}{f_r\left[t_2 - t_1\right]} \tag{4.2}$$

Based on the ASTM standard C1259-98 [10], the dynamic elastic modulus is expressed as equation (4.3), in terms of fundamental natural frequency, in rad/sec, mass of the bar (m), in grams, and the beam dimensions, viz., diameter (d) and length (L), in

mm. The error due to finite diameter of the bar and the Poisson's ratio of the material is accounted by the correction factor C. For bars with slenderness ratio (k = L/d) greater than 20, it is given by $(1+4.939/k^2)$.

$$E = 0.04069\left(\frac{L^3}{d^4}\right)C\left(m\omega_n^2\right) \tag{4.3}$$

The impulse excitation technique performed on the suspended beam is exceptionally simple and fast and has many advantages. It was found to be highly repeatable to provide FRF data and the method is non-destructive. It uses low cost instrumentation and can accommodate a wide variety of specimen configurations and sizes. Moreover, the present experimental method was designed to minimize the support energy dissipation due to strings and the aerodynamic drag on the specimen surface. The circle-fit approach was also found to be feasible in determining the damping factor from the suspended beam's FRF data in the case of pure polycrystalline Al and Mg specimens and metal matrix composite samples [8, 9].

Chapter 5

Ceramic Particulates Reinforced Metal Matrix Composites

5.0 Introduction

Stiffer materials with high damping property are actively sought for dynamic mechanical systems such as in spacecrafts, semiconductor equipments and robotics. Particulate reinforced metal matrix composites (PRMMCs) are becoming popular among the various types of MMCs in terms of usage. These materials exhibit isotropic material behaviour with enhanced stiffness and strength compared to their parent material conditions. Particulate type reinforcement is found to be cost effective compared to fiber/whisker type reinforcement condition. Magnesium and aluminium are the well known light weight metals that have the capability to exhibit good ductility to act as the matrix material and exhibits enhanced mechanical properties when it is unified with ceramic particulates such as Alumina and SiC [95, 129-130]. In related studies, it has been shown that the addition of SiC particulates to the magnesium matrix assists in improving physical properties and elastic and plastic response of magnesium matrix [122]. The results of the literature search, however, reveal that no attempt is made to investigate the effect of particulate size and volume fraction on the room temperature damping behavior of pure monolithic metals (Al and Mg). In addition, the damping characterization using the methodology of impact-based measurement coupled with the unique circle-fit approach is also never attempted.

Accordingly, the primary objective of this investigation was to characterize the damping behavior of monolithic and reinforced Al and Mg matrix using the new methodology involving suspended beam method coupled with circle-fit approach. Particular emphasis was placed to study the effect of SiC volume fraction on the energy dissipation of the Al and Mg-based composite formulations.

5.1 Materials and Processes

In this study, two different sets of material were investigated to understand the effect of metallic matrix, particulate weight percentage and particulate size on the overall damping capacity of the composite sample. The details of the materials sets are as follows:

Case A: Magnesium based composites with matrix of 99.8% initial purity magnesium containing 7.6, 14.9 and 26.0 weight percentages of SiC particulates were processed using molten metal based technique and hot extruded at 350^{o}C [122].

Case B: Aluminium based composites with matrix of 99.8% initial purity aluminium containing 5.2, 13.9 and 17.7 weight percentages of SiC particulates were processed using conventional casting method (CCM) and hot extruded at 350^{o}C [123].

5.2 Results

Microstructure Characterization

The results of the microstructural studies conducted on the monolithic and MMC specimens are listed in Table 5.1. The grain morphology of the extruded specimens was observed using an optical microscope and representative micrographs are shown in Figs. 5.1 and 5.2. The grain morphology of the matrix was found to be equiaxed. Tables 5.1 and 5.2 show a decrease in average grain size with an increase in weight percentage of SiC.

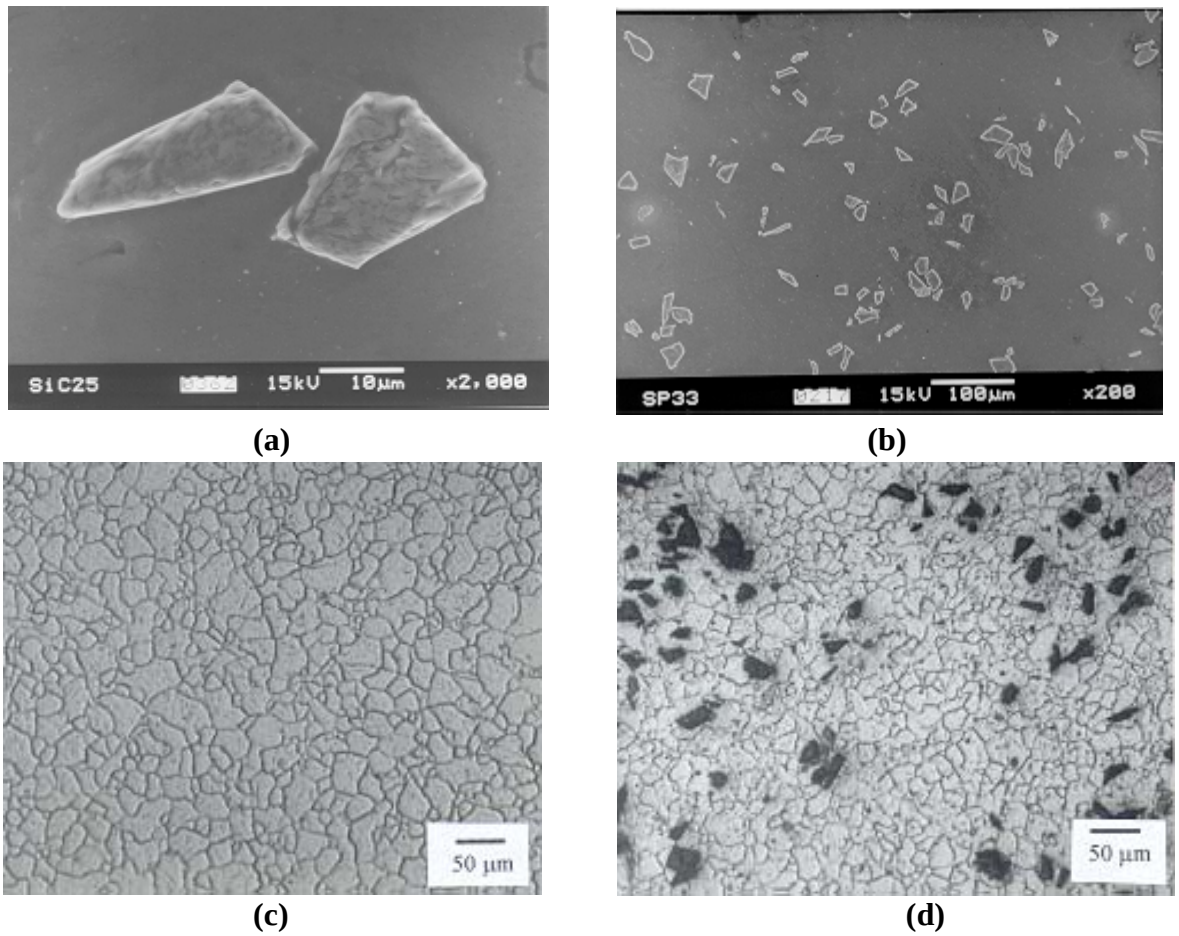

(a) **(b)**

(c) **(d)**

Fig. 5.1 (a) SEM micrograph showing the particulate/matrix interface in Mg/20µm SiC sample. (b) SEM micrograph showing the distribution of SiC particulate in Mg/20µm SiC sample. (e) Optical micrograph showing equiaxed grain morphology of pure magnesium sample. (f) Optical micrograph showing equiaxed grain morphology of Mg/20µm SiC sample.

Figures 5.1 and 5.2 are SEM and optical micrographs showing the microstructural characteristics of the composite and the monolithic samples. Uniform distribution of SiC was found with some presence of clustering and porosity in all the three different sample sets. Close inspection of the SiC particulate at high magnification in all the three material cases, shown in Figs. 5.1 (a) for case A and Figs. 5.2 (d) for case B, illustrates that the interfacial bonding (assessed in terms of voids and debonded regions) is good.

Table 5.1 Results of microstructural studies conducted on Case A monolithic Mg and Mg-SiC composite samples.

SiC Weight %	Density (g/cm^3)	Porosity (%)	Metal matrix grain Size (μm)	Grain aspect ratio	SiC size (μm)	SiC aspect ratio
0.0	1.74	0.00	27.7	1.4	-	-
7.6	1.78	0.84	24.5	1.4	22.8	1.64
14.9	1.85	1.14	21.5	1.4	22.8	1.62
26.0	1.96	0.91	19.4	1.5	23.0	1.56

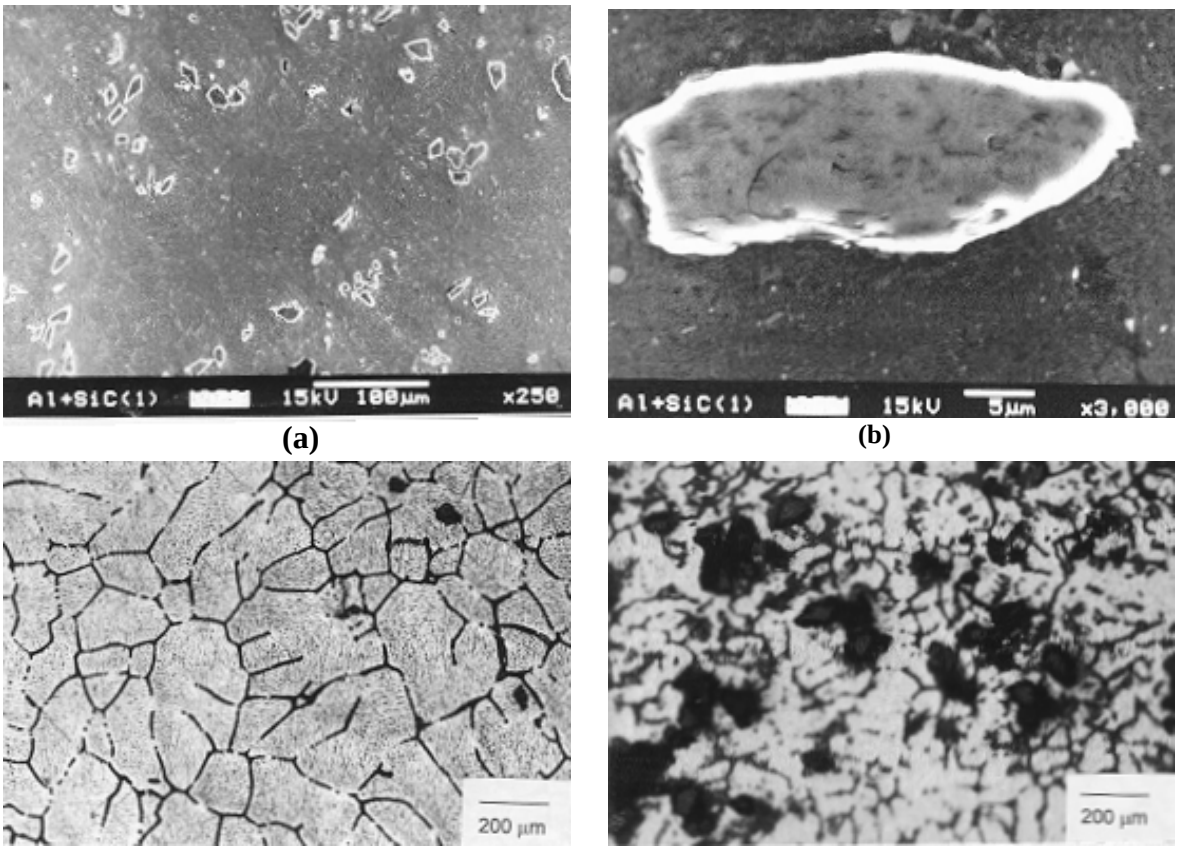

(a) **(b)**

(e) **(f)**

Fig. 5.2 (a) SEM micrograph showing the distribution of SiC particulate in Al-5.2 wt.% SiC sample. (d) SEM micrograph showing the particulate/matrix interface in Al-5.2 wt.% SiC sample. (e) Optical micrograph showing equiaxed grain morphology of pure aluminium sample. (f) Optical micrograph showing equiaxed grain morphology Al-17.7 wt.% SiC sample.

Table 5.2 Results of microstructural studies conducted on Case B monolithic Al and Al-SiC composite samples.

SiC Weight %	Density (g/cm^3)	Porosity (%)	Metal matrix grain Size (μm)	Grain aspect ratio	SiC size (μm)	SiC aspect ratio
-	2.697	0.12	55.40	1.53	-	-
5.2	2.713	0.26	47.87	1.54	15.58	1.65
13.9	2.732	0.77	42.84	1.54	14.10	1.54
17.7	2.741	0.95	35.69	1.48	12.51	1.48

Density and Porosity Measurement

The results of the experimental density values are listed in Tables 5.1 and 5.2. The volume fraction of porosity, which is computed from the determined density values and the results of the chemical dissolution, is also included.

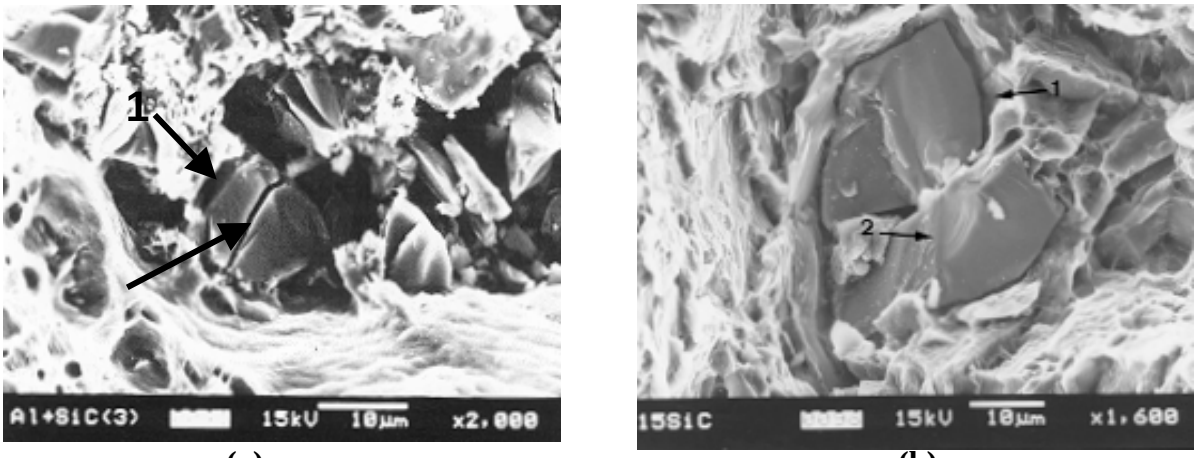

(a) **(b)**

Fig. 5.3 SEM micrograph of tensile fractured specimens of: (a) Al/17.7 wt. % SiC sample and (b) Mg/14.9 wt. % SiC sample, which is denoted with (1) interfacial debonding of SiC particulate and the metallic matrix and (2) SiC particulate breakage.

Thermo-Mechanical Testing

The thermo-mechanical study for the MMC samples was conducted and the average coefficients of thermal expansion (CTE) of the composite samples were determined and are listed in Tables 5.3 and 5.4. Results show that the CTE of the metallic matrix (Al and Mg) decreases with an increase in SiC weight percentage.

Table 5.3 Theoretical and experimental results of Case A monolithic and MMC samples.

SiC Weight (%)	**Interparticle spacing (µm)**	**Volume percentage of plastic zone (%)**	**Estimated dislocation density (m^{-2})**	**C.T.E α_{exp} ($x10^{-6}/^{o}C$)**	**Free-Free Loss factor η_{free}**	**ROM Loss factor η_{ROM}**
0.0	-	-	-	29.354	0.0047	0.0047
7.6	140.3	15.3	6.1E+11	28.045	0.0074	0.0045
14.9	98.6	30.9	1.3E+12	24.325	0.0124	0.0043
26.0	72.7	56.8	2.6E+12	23.377	0.0168	0.0040

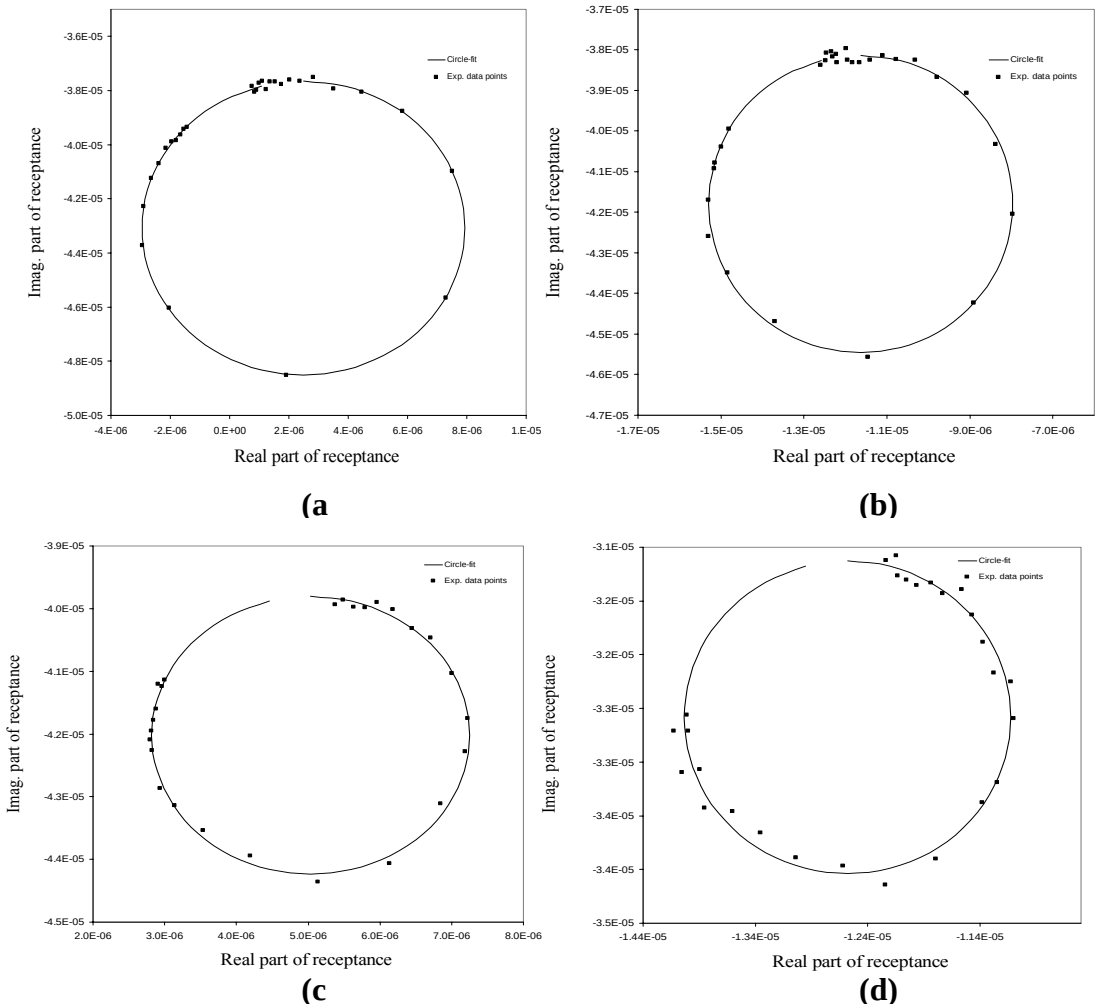

Fig. 5.4 Typical receptance frequency response function (FRF) showing actual FRF data of: (a) pure magenisium (b) Mg/7.6 wt.% SiC (c) Mg/14.9 wt.% SiC (d) Mg/26.0 wt.% SiC.

Tensile Testing and Fractography

Figure 5.3 shows typical interfacial debonding and particulate breakage observed in the fracture surface of both aluminium and magnesium based composite sample containing SiC particulate. The results of the fracture surface analysis conducted on the tensile tested specimens revealed a cleavage type fracture in both Al and Mg based samples for monolithic and composite samples. In all the composite samples, particle

fracture and particle/matrix interfacial debonding as the reinforcement associated fracture mechanisms were observed (see Fig. 5.3).

Table 5.4 Theoretical and experimental results of Case B monolithic and MMC samples.

SiC Weight (%)	Inter-particle spacing (μm)	Volume percent of plastic zone (%)	Estimated dislocation density (m^{-2})	Coef. of thermal expansion α_{exp} ($x10^{-6}/^{o}C$)	Free-Free Loss factor η_{free}	ROM Loss factor η_{ROM}
-	-	-	-	25.892	0.0029	0.0029
5.2	90.90	29.33	9.9E+11	24.566	0.0034	0.0028
13.9	51.75	76.90	3.0E+12	23.213	0.0045	0.0026
17.7	38.10	98.40	4.7E+12	22.555	0.0058	0.0025

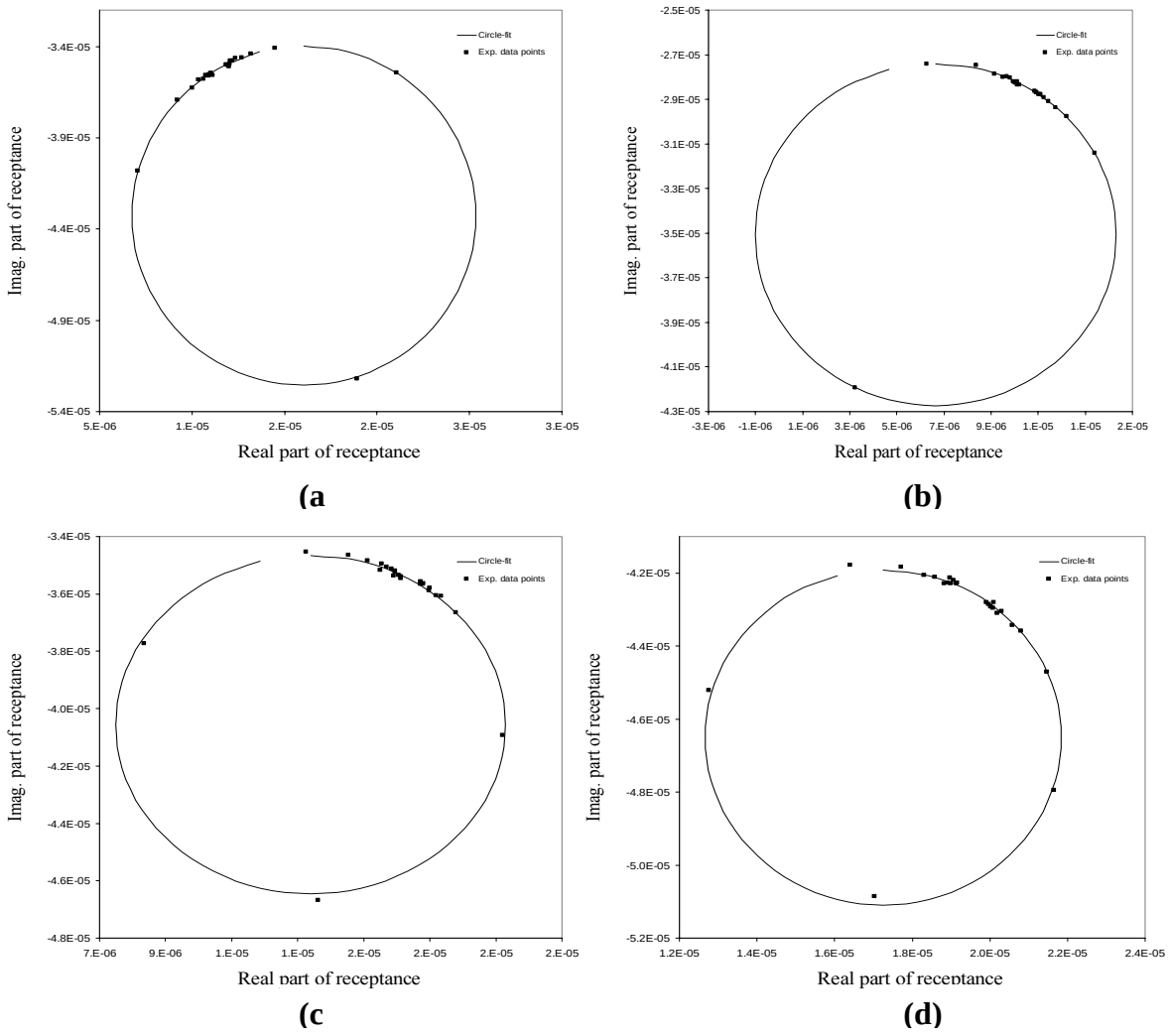

Fig. 5.5 Typical receptance frequency response function (FRF) showing actual FRF data of: (a) pure aluminium (b) Al/5.2 wt.% SiC (c) Al/13.9 wt.% SiC (d) Al/17.7 wt.% SiC.

Suspended Beam Vibration Testing

Suspended beam vibration testing was used in the present study to study the dynamic characteristics of the composite sample. Figs. 5.4 and 5.5 shows typical receptance frequency response function (FRF) showing actual FRF data of the composite samples which were used to compute the damping loss factor. The damping loss factor η_{free} results were benchmarked against respective monolithic sample and are listed in Tables 5.3 and 5.4.

5.3 Discussion

The impulse excitation technique performed on the suspended beam was found to be highly repeatable and has many advantages. The method is non-destructive, uses low cost instrumentation and can accommodate a wide variety of specimen configurations and sizes. The impulse excitation technique is exceptionally simple and fast and was seen to provide repeated FRF data of the suspended beam.

The circle-fit approach was found to be efficient in determining the damping factor from the suspended beam's FRF data. Using this approach, the damping factor of pure magnesium (case A) was found to be 0.0047, which can be compared with the logarithmic decrement based damping measurements of Trojanova et al. [45] which ranges from 0.001 to 0.004. The damping factor of pure aluminium for case B was found to be 0.00293, which can be compared with axial damping measurements of Lazan which range from 0.0003 to 0.006 [4]. In general, the results varied with a standard deviation of 300ppm. The discrepancy in the measured values against published results for these monolithic materials can be attributed to the difference in the operational frequency and

strain amplitude [23, 131] as well as due to the difference in the material processing method which results in different microstructure in terms of grain size and shape [132].

Tables 5.3 to 5.4 lists the experimentally determined loss factor variation with increase in weight percentage of SiC in the composite samples. The damping capacity of the metal matrix composite is directly related to the damping capacity of each of its constituents. Rule of mixture can be taken as a simplistic approach that may be utilized to rationalize the resultant damping capacity in particulate reinforced MMCs. Thus the overall damping capacity η_{ROM}, listed in Tables 5.3 and 5.4, would be proportional to the damping capacities of the reinforcement, η_r, and the metal matrix, η_m, multiplied by their respective volume fractions, f and (1-f), as follows:

$$\eta_{ROM} = \eta_r f + \eta_m (1 - f) \tag{5.1}$$

SiC has lower loss factor of the order of 0.0001 (refer Fig. 2.6(b)) as compared to magnesium and aluminium, which has an order of 0.0047 and 0.00293, respectively (based on the present study). From Tables 5.3 and 5.4, damping factor η_{ROM} calculated using rule of mixtures for different weight percentage of SiC in Mg/Al matrix, it is clear that addition of SiC in the Mg/Al matrix would result in the decrease in damping capacity of the resultant composite. This discrepancy between the experimental results and ROM prediction can be accounted to the intrinsic and extrinsic damping mechanisms working simultaneously.

It is interesting to note that for both good and bad interfacial bonding condition between the ceramic particle and the metal matrix, the overall damping characteristics increases in a MMC due to different damping mechanisms. In the present study, fracture surface of the tensile test specimens for the MMC sample sets (A) and (B) showed in

general, fracture path passing through the particle, confirming a reasonably good interfacial bond at the matrix-reinforcement interface. Under this situation, a semi-coherent or incoherent interface exists at the atomistic level [133] and explained previously in section 2.8.3. Thus in the present study, the increased damping can be seen as a result of the presence of plastic zone, increase in dislocation density and due to other damping sources such as ETD damping and grain boundary sliding mechanisms which would be critically analyzed for its validity in the following paragraphs.

In PRMMCs inclusion of the hard ceramic particulates causes high residual stresses around the particulates in the form of an annular plastic zone due to large difference in the coefficient of thermal expansion of metallic matrix and ceramic reinforcement, which are responsible for the generation of plastic zone at the particulate/matrix interface. The CTE for SiC is 4.3 ppm/^{o}C [23] and for Mg and Al is 28 ppm/^{o}C and 25.8 ppm/^{o}C, respectively, from the present study (refer Tables 5.3 and 5.4). Based on the works of Dunand and Mortensen [134] with an assumption of elastic-perfectly plastic material behavior, the size of the plastic zone C_s can be estimated as:

$$C_s = r_s\left(\frac{\Delta\alpha E\Delta T}{(1-\nu)\sigma_y}\right) \tag{5.2}$$

where $\Delta\alpha$ is the difference between the CTEs of metallic matrix and reinforcement, ΔT is the temperature difference which is around 327^{o} C, E and ν are the matrix elastic modulus and Poisson's ratio, σ_y is the matrix yield stress and r_s is the particulate radius. Thus for the present experiment samples containing SiC particulates, the plastic zone radius is calculated with a basic assumption of spherical particle shape using equation (5.2), and the corresponding volume fraction is listed in Tables 5.3 and 5.4. Recently

based on mechanical spectroscopic studies, Carreno-Morelli, Urreta and Schaller [135] proposed a simplistic model to determine the damping due to plastic zone as follows:

$$\tan\phi \approx \frac{f_{zp} G_c \oint \sigma d\varepsilon}{\pi \sigma_o^2} \tag{5.3}$$

where f_{zp} is the plastic zone volume fraction, G_c is the shear modulus of the composite sample, σ_o is the alternating shear stress amplitude and ε is the corresponding strain acting on the specimen. Thus it is clear from equation (5.3) that the damping depends directly on the volume fraction of the plastic zone and the strain amplitude. Also it is clear that the overlapping of plastic zones can occur for situations when the plastic zone is larger with smaller inter-particulate distance which is possible as the weight percentage increases. Tables 5.3 and 5.4 list the predicted inter-particulate distance for the experiment samples based on the model of Nardone and Prewo [136] described as follows:

$$\lambda = \left[\frac{lt}{V_f} \right]^{0.5} \tag{5.4}$$

where λ is the inter-particulate spacing, t, l and V_f are the thickness, length and volume fraction of the SiC particulate, respectively. Thus presence of clusters can be expected to change the plastic zones and thereby influence the overall damping capacity. The influence of the SiC reinforcement on the elastic-plastic behavior of the metallic matrix was also investigated by modelling the two-phase composite as a cell model using finite element method (FEM) and is explained in a separate chapter in this thesis.

Another contributing damping mechanism arises due to an increase in dislocation density in the metallic matrix due to the presence of the hard and brittle reinforcing particulates. These dislocations are generated due to thermal mismatch strain caused due

to the difference in coefficient of thermal expansion values between the metal matrix and hard brittle reinforcing phase. As mentioned previously, the CTE difference between SiC and metallic matrix, viz., Mg and Al which is around 28 ppm/^{o}C and 25.8 ppm/^{o}C, respectively, from the present study. Thus the dislocation density generated can be quite significant at the interface and can be predicted using the model based on prismatic punching of dislocations at a ceramic particulate [137]. Thus it can be shown in the form of equation (5.5) that the dislocation density ρ depends on the thermal mismatch strain, ε, (the product of temperature change, ΔT, during solidification of MMCs and CTE difference, Δα, between reinforcement and matrix), the volume fraction of the ceramic reinforcement, f, the Burgers vector, b, the particulate size, t, and the particulate aspect ratio, s. B is a geometric constant that depends on the aspect ratio (it varies between 12 for equiaxed particulate and 4 for whisker-like particulate) [137]. For both Al-SiC and Mg-SiC, the thermal mismatch strain during cooling is found to be typically 0.7% during cooling from 350^{o}C to room temperature. Based on equation (5.5) the dislocation density for the different experiment samples were calculated and are listed in Table 5.4 to 5.6 using the SiC particulates' microstructural measurements listed in Tables 5.1 and 5.2 and with an assumption for the burgers vector of 0.3nm for Mg and 0.32nm for Al [138].

$$\rho = \frac{B\varepsilon V_f}{bt(1 - V_f)} \tag{5.5}$$

Granato-Lucke mechanism is a well-accepted theory that explains the damping mechanism by dislocations [29]. When a dislocation is pinned by two obstacles such as the impurity atoms, ceramic particulates or antiplane dislocations, it behaves like an elastic vibrating string. Under low amplitude of the applied cyclic load the string vibrates to dissipate energy. Thus at low strain amplitude the damping is independent of the strain

amplitude and is dependent only on the frequency while at high strain amplitude the damping nature increases tremendously due to breakaway of the dislocations from their pinned positions due to excessive bowing [29, 101].

In the present experimental setup, the strain amplitude induced in the specimen is of the order of 10^{-6} at which the dislocation-based damping is mainly due to frequency dependent part and is expressed as follows:

$$Q_f^{-1} \approx \frac{a_o B \Lambda L^4 \omega^2}{\pi^2 C b^2} \tag{5.6}$$

where a_o is a numerical factor of order 1, B is the damping constant, ω is the operating frequency, L is the effective dislocation loop length which depends on the pinning distance, C is the dislocation line tension ($\approx 0.5Gb^2$), G is the shear modulus, b is burgers vector and Λ is the total dislocation density. This shows that the damping depends on the dislocation density, frequency of cyclic stress and burgers vector b of the bulk material [101, 139]. Thus increased density of dislocation due to presence of SiC particulates in the magnesium matrix contributes towards increased dislocation-based damping characteristics in the MMC. It may also be noted that the dislocation density increases with SiC weight percentage (equation (5.5)) and thus an increase in damping of the magnesium matrix was expected due to increase in SiC weight percentage. The experimental results listed in Table 5.3 and 5.4 conform to this hypothesis.

Based on the Al/SiC and Mg/SiC samples the following observations can be made from the damping results in Table 5.3 for Mg-SiC composites (Case A) and Table 5.4 for Al-SiC composites (Case B), it is clear that the damping capacity of the composite sample increases with SiC weight percentage. This increase in the damping capacity can be explained due to the increase in plastic zones and dislocation density listed in Table

5.3 and Table 5.4 for the respective samples based on equation (5.2) and equation (5.5), respectively.

In addition, the higher damping can be attributed to the presence of voids based on the damping studies of Zhang, Gungor and Lavernia [140] on Al alloy, which showed that the presence of voids in the metallic matrix also provides additional damping to the composite. It may be noted that under the applied cyclic load, high stresses can result near the voids due to stress concentration [141] and this can contribute to the overall energy dissipation as described by equation (5.4).

Apart from particle's contribution, the intrinsic damping nature of the metal matrix can improve just by the presence of the particle, through the grain refinement of the metal matrix. Tables 5.1 and 5.2 show that the average grain diameter of the Al and Mg matrix decreases with an increase in weight percentage of SiC. Kê's damping study on single crystal versus polycrystalline aluminium showed clearly that increased presence of grains increases the damping tremendously [22], shown in Fig. 2.30 (a), only at high temperature around 200-300^{o}C. Hence in the present study, due to room temperature experimental conditions, the contribution from grain boundary based damping mechanism can be considered minimum. But it can be presumed that the SiC reinforced Al and Mg can damp better at higher temperature (200^{o} to 300^{o} C) due to the increased grain refinement as seen in the present study (refer Table 5.1 to 5.2) [21, 26] and shown in Fig. 2.28 and Fig. 2.30 (a).

In addition to the above mentioned intrinsic damping mechanisms elasto-thermodynamic (ETD) damping can arise in a composite sample [142, 143]. This is based on Zener's research which showed that when a material is stressed in a reversible

adiabatic process, thermal gradient is induced in accordance with the Thomson effect [15, 142]. Heat conducts from the high temperature regions to the low-temperature regions and as a consequence of the second law of thermodynamics, entropy is produced which is manifested as a conversion of useful mechanical energy into heat. This phenomenon is known as the elasto-thermodynamic damping Further research by Kinra and his co-workers [142] showed that ETD is one of the contributing damping mechanisms in the MMCs. In the case of flexural vibration of beams, the ETD arises due to irreversible heat transfer from the hotter region where compressive stress prevails to the cooler region where tensile stress exists. Zener's solution of the ETD damping for a beam configuration is given by [142]:

$$\Psi_{ETD} = \Psi_o \frac{\omega\tau}{1+(\omega\tau)^2} \tag{5.7}$$

$$\Psi_o = \frac{2\pi\alpha^2 E_R T_o}{\gamma c} \tag{5.8}$$

$$\tau = \frac{\gamma c h^2}{\pi^2 k} \tag{5.9}$$

where ω is the circular frequency, τ is the characteristic time of the beam, Ψ_o is the characteristic damping of the beam, α is the coefficient of thermal expansion, E_R is the relaxed modulus of elasticity, T_o is the absolute temperature, γ is the mass per unit volume, c is the specific heat per unit mass, k is the isotropic thermal conductivity of the material and h is the beam thickness. The ETD damping mechanism is frequency dependent and reaches a maximum when the time constant of vibration reaches the characteristic time of the beam [15] given by equation (5.9). In another separate research, Bishop and Kinra [142] showed using a concentric sphere model, the maximum ETD

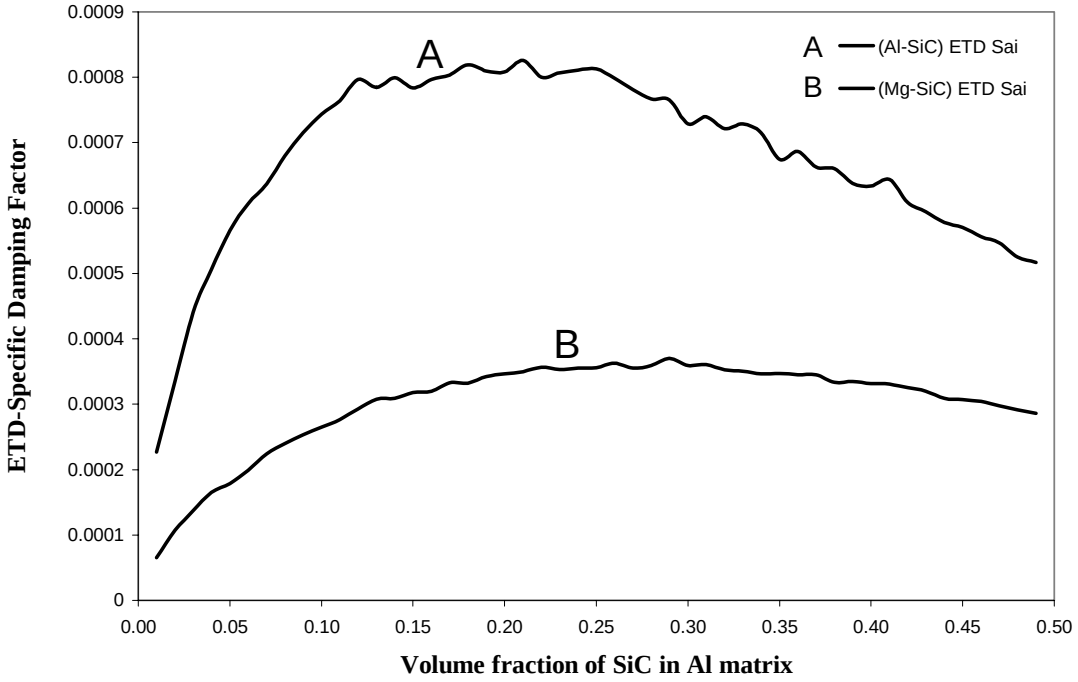

Fig. 5.6 Predicted variation of ETD damping with SiC volume fraction in Al-SiC and Mg-SiC type particulate MMC samples using closed form analytical prediction (at 1000Hz and 23^{o}C) (Note: *Noise due to numerical error*).

damping achievable for Al-SiC and Mg-SiC particulate system are 0.0024 and 0.0068, respectively, for a composition containing 46 weight percentage SiC reinforcement. Presently a software is written based on the model of Bishop and Kinra [142] to predict the ETD damping of particulate reinforced metal matrix composites for a given volume fraction and operational frequency and temperature. Fig. 5.6 shows the predicted variation of ETD damping factor (at 1000 Hz vibration frequency and at room temperature) with respect to SiC volume fraction in a Al-SiC and a Mg-SiC particulate MMC. Note the amount of numerical error that gives rise to noise in the graphs. In the present study, using finite element method a unit cell model has been developed to understand how heat transfer takes place which give rise to the energy loss; this is explained in a following chapter in this thesis.

In the present study, for the thermo-mechanical properties of the three different composite compositions, the magnitude of the ETD at a specimen level (using equation 5.7 to 5.9) is found to be of the order of 10^{-4} due to the beam dimensions, which does not seem to be significant to explain the experimental observation. But from a micro-thermoelasticity mechanism, (see Fig. 5.6) damping loss factor for the present sample composition is around $8x10^{-4}$ and $3.5x10^{-4}$ for Al-SiC and Mg-SiC samples, which when compared to monolithic condition turns out to be 27 % and 7 %, respectively. In chapter 10, more detailed explanation using a numerical model is made regarding thermoelastic damping.

The results of the present study, in essence, reveal that the circle-fit approach when combined with the impact-based measurement of the free-free type suspended beam is capable of measuring damping loss factor of the metal matrix composites. Hence it was motivating to further pursue the research work on other composite formulations to further strengthen the viability of this approach.

5.4 Summary

Following conclusions may be drawn from this part of the research study:

1. The free-free beam type flexural resonance method can successfully be used with circle-fit approach to measure the damping characteristics of the unreinforced and the reinforced aluminium and magnesium samples.
2. In general, the damping of the pure magnesium and pure aluminium matrix increases as a result of presence of SiC particulates.

3. An increase in damping with an increase in the weight/volume percentage of SiC particulates can be attributed to a progressive increase in the energy dissipation. The energy dissipation can primarily be attributed to the simultaneous influence of increase in volume percentage of plastic zone and increase in dislocation density.
4. In the present study, there was no significant macro-ETD damping at a specimen level due to chosen specimen dimension and operational frequency, as well as no grain boundary damping due to room temperature operation conditions.

Related Publications:

[1] N. Srikanth, and M. Gupta: *Materials Research Bulletin*, Vol. 37 (2002), pp. 1149-1162.

[2] N. Srikanth, and M. Gupta: *Scripta Materialia*, Vol. 45 (2001), pp. 1031-1037.

[3] N. Srikanth, S. C. V. Lim, M. Gupta: *J. of Comp. Mat.*, Vol. 36 (2002) 2339-2355.

[4] N. Srikanth, and M. Gupta: *Physica Status Solidi (a)*, Vol. 193, no. 2, (2002) 236-245.

[5] N. Srikanth, and M. Gupta: *Key Engineering Materials*, Vol. 227 (2002) 211-216.

[5] N. Srikanth, and M. Gupta, *Materials Technology*, Vol. 17, no.4 (2002) 231-234 – Special invited review paper .

[6] N. Srikanth, and M. Gupta: *Composite Science & Technology*, Vol. 63 (2003) 559-568.

[7] N. Srikanth, D. Saravanaranganathan, M. Gupta, *Mat. Sci. and Tech.*, Vol. 20 (2004) 1389-1396.

Chapter 6

Metal Particulates Reinforced Metal Matrix Composites

6.0 Introduction

Results from the first part of this research gave an encouragement that the addition of ceramic particulates resulted in high specific stiffness and strength and increased damping capability. Investigation related to machinability of MMCs has shown that the presence of hard ceramic phase decreases the tool life of cutting tools drastically [144]. Hence the idea of dis-continuous stiffer metallic phase in a ductile metallic phase adopted in the present study may enhance the machinability of this new MMC. The results of the literature search, however, reveal that no attempt has been made to investigate such metallic reinforcements addition on the damping behavior of aluminium.

Previous studies of Gupta et al. [145] has shown that titanium dissolves in aluminium at high temperatures and forms intermetallics with Al following solidification. The synthesis and processing of such material is extremely challenging due to the ability of Ti to raise the melting temperature of Al and extreme reactive nature of molten Al-Ti mixture. In order to avoid these limitations, Ti was subjected to surface modification so that it stays as elemental-Ti, mostly, following solidification. In addition, titanium being a stiffer material with a elastic modulus of 120 GPa, has a higher melting point of 1667^{o} C, and a hardness of 90 HV, and hence when left un-dissolved in molten aluminum matrix by proper surface modification on the particle surface, it can result in reinforcing the ductile Al matrix, which has a melting point of 660.3^{o} C, elastic modulus of 72.2 GPa and a hardness of 15 HV [147]. But, in terms of density, Ti is heavier than Al by 1.6 times which can make the composite heavier, but when added in smaller volume fraction this effect may not be a significant factor in the design. Hence the primary objective of this investigation was to investigate the energy dissipation of aluminium containing variable

amounts of pure Ti phase. In chapter 9, the theoretical predictions are made using a finite element method (FEM) based unit-cell model (UCM) that uses a rate-dependent based plasticity model so as to validate the experimental results.

6.1 Materials and Processes

In this study, pure Al (purity > 99.7 %) was the base metal and titanium powders with an average size of 19 ± 9 μm were used as the starting materials. To prevent Ti dissolution in Al, the Ti particle's surface was modified by preheating at 400 ^{o}C for an hour in a ceramic container to produce a surface oxide layer and then added to the molten aluminum melt (750 ^{o}C) and mechanically stirred using a zirtex-coated stirrer. The resultant slurry was allowed to flow out of the crucible and was atomized using argon gas jets positioned at a distance of ~ 215 mm from the pouring point and deposited into a metallic substrate 500 mm from the disintegrating point.

6.2 Results

Fig. 6.1(a) shows the typical SEM micrograph of the Ti particulates used as reinforcement. The processing parameters were controlled so as to allow only partial reaction of titanium with the metallic melt. Three composite ingots with 3.3, 6 and 7.5 equivalent of titanium in weight percentage were extruded. Scanning electron microscopy and energy dispersive spectrometer (EDS) studies were conducted to establish the characterization of the MMC specimens obtained using image analysis and the density measurements are listed in Table 6.1. Figs. 6.1 (b) to (d) show typical SEM micrographs, which illustrates the microstructural and fracture characteristics of various MMC samples.

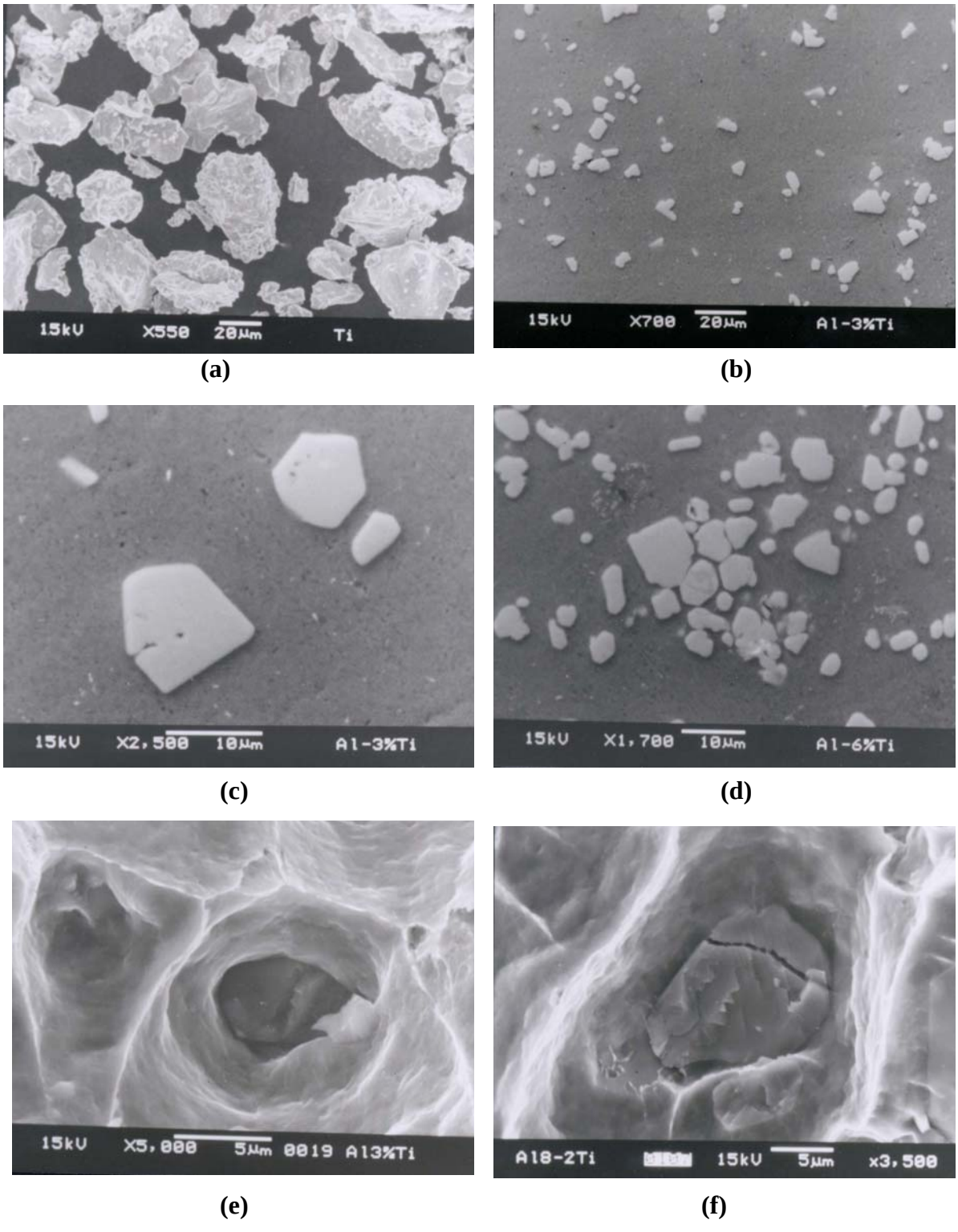

Fig. 6.1 SEM micrographs showing: (a) pure Ti particulates, (b) reinforcement distribution in Al-3.3%Ti, (c) good interfacial integrity of the reinforcement exhibited in Al-3.3%Ti, (d) typical clustering of particles in Al-6%Ti, (e) fractograph exhibiting particulate debonding in Al-3.3% Ti and (f) fractograph exhibiting particulate breakage in Al-7.5% Ti.

Table 6.1 Results of the microstructural and thermo-mechanical characterization.

Ti Weight %	Density (g/cm^3)	Ti particulate size (μm)	Ti particulate aspect ratio	Exp. mean CTE ($10^{-6}/^oC$)	Matrix * hardness (HV)	Interface * hardness (HV)
0.0	2.701	-	-	25.246	31.9± 0.52	-
3.3	2.732	4.7 ± 2.2	1.2 ± 0.3	25.260	34.0± 0.60	40.4± 0.92
6	2.756	3.3 ± 1.4	1.2 ± 0.3	23.065	43.4± 2.04	49.9± 0.83
7.5	2.767	5.6 ± 2.9	1.2 ± 0.3	22.651	39.6± 0.93	49.7± 0.36

* denotes average value of three Vickers microhardness test results

Table 6.2 X-ray diffraction results obtained from the preheated Ti powder and the extruded specimens.

Material	Number of matching Peaks			
	Ti (400 ^OC)	Al-3.3 % Ti	Al- 6 % Ti	Al- 7.5% Ti
Ti	8	1	1	1
Ti_2O_3	1	0	0	0
TiO	0	0	1	1
TiO_2	0	1	1	1
Al	0	4	4	4
Al_3Ti	0	1	2	1
Total number of peaks	9	7	9	8

X-ray diffraction was conducted to verify the presence of the reinforcement and also to detect the presence of any reaction phases that might have formed during the casting process. The lattice d-spacing corresponding to the different Bragg angles obtained from scanning each sample were matched with the standard values. Table 6.2 lists the X-ray diffraction results confirming the presence of elemental Ti along with other Al-Ti and Ti-O related phases.

The coefficient of thermal expansion of extruded composite samples was determined using thermal-mechanical analyzer and the results are listed in Table 6.1. The micro-hardness measurements were conducted on the monolithic and reinforced samples using a digital micro-hardness tester. In the composite specimens, the microhardness measurements were made on the aluminium matrix and the interfacial zone, which are

listed in Table 6.1. It may be noted that interfacial zone refers to the annular region around the reinforcement characterized by high dislocation density originating due to the difference in coefficient of thermal expansion of the matrix and reinforcement. It may be noted that the average values of microhardness of the samples increased up to 6% Ti sample and marginally reduced for 7.5% Ti sample. The results also revealed that the interface hardness in all the three composite samples was higher when compared to the matrix hardness and its value also follows the similar trend as that of the matrix hardness.

Fractographic studies using scanning electron microscopy (SEM) were also conducted on the tensile fractured surfaces of monolithic aluminum and its composite samples to provide an insight into the various possible fracture mechanisms operating during the tensile loading of the samples. Figures 6.1(e) and (f) shows the typical particle fracture and debonding failure observed in the various tensile fractured surfaces of the composite samples.

Table 6.3 Results of theoretical predictions of microstructural characteristics and of experimental damping measurement.

Ti Weight %	Ti Volume %	Interparticle spacing (μm)	Estimated plastic zone vol. fraction (%)	Estimated dislocation density (m^{-2})	Exp. damping loss factor η_{free}	Damping Increase^{+} (%)	Dynamic Modulus (GPa)
0.0	0	-	0.00	-	0.00322	-	68.39
3.3	1.8	38.46	8.61	7.9E+11	0.00341	6	74.75
6	3.7	19.32	17.70	2.3E+12	0.00376	17	78.01
7.5	5	27.86	23.92	1.9E+12	0.00397	24	79.26

+ when compared to that of the monolithic sample.

Suspended beam results in the form of circle-fit plots are shown in Fig. 6.2, from which damping loss factor and dynamic modulus were determined and are listed in Table 6.3. Results show that there is a systematic increase in damping and dynamic modulus with increase in Ti volume fraction in aluminium matrix.

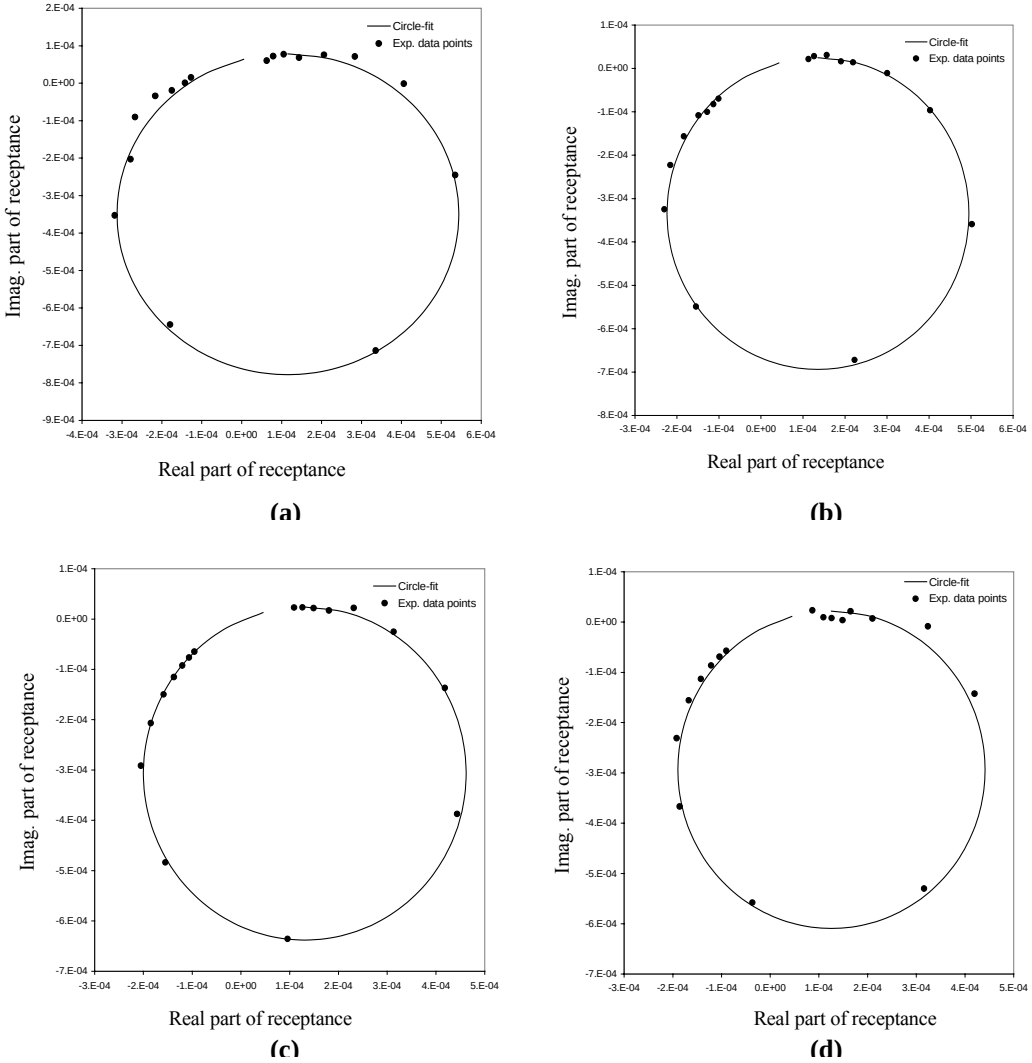

Fig.6.2 Circle-fit plot of FRF data of: (a) the pure Al sample, (b) the Al-3.3%Ti sample, (c) the Al-6%Ti sample and (d) the Al-7.5%Ti sample.

6.3 Discussion

Al alloys containing Ti as primary alloying element have proven to be a suitable for high temperature and high stress conditions. Such addition results in increase in melting temperature of aluminium (for example additon of 10 wt. % of Ti raises the melting point from ~ 660 ^{o}C to ~ 1200 ^{o}C), increases chemical reactivity of the molten mixture and forms many phases, among which three types of phases (viz., Ti_3Al, TiAl

and Al_3Ti) are seen to be ordered intermetallic phases [148]. Under equilibrium conditions the upper bound of Ti that can be completely dissolved in molten Al at 750 ^oC should not exceed 0.33 wt. %. Hence Gupta et al. [149] devised a new generation Al-Ti material by preseving the elemental Ti in the Al matrix. This was done by controlling the residency time of Ti in molten Al and by modifying the surface characteristics of Ti powders with a heat treatment that produces an additional oxide layer on the particle surface. Such a surface modification method was adopted in the present study.Computation of the gibbs free energy of formation (ΔG_f), corresponding to a temperature of 750 ^oC, using the published results of reference [150] shows that for Ti_3Al, TiAl and Al_3Ti the ΔG_f magnitudes are -22.77 KJ/mol, -20.26 KJ/mol and -29.75 KJ/mol, respectively. Hence growth of Al_3Ti is found to be more favorable than the other phases. At temperatures below melting point of aluminium (660^oC), Al diffuses predominantly and the growth of Al_3Ti intermetallic occurs exclusively on Ti-rich side through a peritectic reaction [150]. In the present study, XRD results (see Table 6.2) confirms the presence of Al_3Ti for the present material process condition in all the composite samples. Close inspection of the particle-matrix interface at high magnification in all the three different composites investigated, showed good Ti-Al interfacial bonding with limited interfacial reaction (see Fig. 6.1 (c)). The particle-matrix interfacial integrity assessed in terms of interfacial debonding and presence of voids was found to be good in the composite sample. XRD results listed in Table 6.2 confirm the metastable nature of Al-Ti materials using DMD method with the presence of titanium as elemental Ti.

In general, uniform distribution of Ti particulates and its intermetallic phases in the metal matrix was seen in all the composite samples (see Fig. 6.1(b)). Thus an isotropic material behavior can be expected in all the composite samples, from a global perspective. Occasional particulate clustering was also seen from the cross-sectional study (see Fig. 6.1(d)). In the present study, fracture surface of the tensile test specimens for the three different MMC samples showed fracture path passing through the Ti particle, confirming a reasonably good interfacial bond at the matrix-reinforcement interface (see Fig. 6.1 (e) and (f)). Under this situation, a semi-coherent or incoherent interface exists at the atomistic level.

It is interesting to note that for both good and bad interfacial bonding condition between the Ti particle and the metal matrix, the overall damping characteristics increases in a MMC due to different damping mechanisms. As explained in section 2.1, one can conclude that stiffness and damping capacity of a material are interrelated and hence it is a challenge to improve both in a composite material. Table 6.3 lists the damping loss factor and the elastic modulus of the monolithic sample and the three Al-Ti samples. The suspended beam experimental method couple with the circle-fit approach was found to be efficient in determining the damping factor from the FRF data. For example, the damping factor of pure aluminium was found to be 0.00322±0.0005, which is similar to the previous pure Al sample studied in chapter 5. Comparison against the monolithic material condition shows that addition of Ti in the Al matrix increases the overall damping capacity as well as stiffness of the composite. In addition, this improvement steadily increases with Ti weight percentage. Hence it is convincing that

the idea of stiffer metallic reinforcements in a ductile matrix serves a two pronged advantage when it is tailored for vibration suppression application.

This increase in the elastic modulus with increase in weight percentage of reinforcement can be attributed to the higher elastic modulus of Ti, which is reported to be about 120 GPa [147] as compared to the monolithic Al sample's elastic modulus value of 68.39 GPa, based on the present study (see Table 6.3). In addition, presence of brittle Al-Ti based intermetallic phases and the oxide phases in the metallic matrix are expected to increase the overall composite's stiffness, due to their higher stiffness compared to the parent materials. In a previous study [122, 130] the authors have used various theoretical models such as the Shear Lag model, Halpin-Tsai model and the Eshelby model to explain such an increase in the MMC's stiffness with reinforcement.

In general, the overall damping capacity of the metal matrix composite is directly related to the damping capacity of each of its constituents. Based on the literature review, Ti can exhibit a maximum loss factor of 0.003 [18] in the same range as that of aluminium, which is around 0.0032, based on the present work. Hence it can be expected that addition of Ti in the Al matrix would not result in any increase of the composite's damping capacity. Thus, the damping improvement observed from the experiment results has to be attributed primarily to the interface between reinforcement and the metallic matrix. As discussed in the previous chapter, the damping capacity arises due to intrinsic dissipation of strain energy due to mechanisms at the crystal level. The most significant role comes from point defect relaxation, microplasticity, dislocation motion, grain boundary sliding, inclusion-matrix friction, magnetoelastic effects, and elastothermodynamic effects. Similar to metal-ceramic interface, regular damping

mechanisms in the metallic matrix due to a high residual stress in the matrix and due to high dislocation density at the particulate/matrix interface can be expected. The high residual stresses and the dislocation density are caused due to large difference in the coefficient of thermal expansion between the phases (such as the CTE for Ti is 8.41 ppm/^{o}C [17], and for Al is 25.2 ppm/^{o}C, refer Table 6.1). In addition, transformation of Ti to Al-Ti intermetallics can enhance this residual stresses and dislocation density since the coefficient of thermal expansion of intermetallics can be expected to be much lower than the parent metals. This will increase the overall CTE mismatch when compared to a pure Ti condition. To obtain a lower bound of this increase in dislocation density and residual stress at the particulate-matrix interface, the particulate can be considered to be pure Ti, as described in the forthcoming paragraphs. This increase in plasticity can be suspected to be one of the reasons behind the increase in microhardness value at the interface compared to the bulk matrix, listed in Table 6.1, as a result of strain hardening effect. This correlation of plastic zone to the microhardness is confirmed in reference [151] using X-diffraction analysis for a particulate reinforced Al composite.

Similar to the discussion made in the previous chapter for metal-ceramic MMCs, equation (5.2) was used to predict the plastic zone radius and plastic zone volume fraction were determined that are listed in Table 6.3. Secondly, the inter-particulate distance for the composite samples based on the model of Nardone and Prewo described as equation (5.4) are listed in Table 6.3 for the Al/Ti samples. This is important since presence of clusters which is a random phenomena can result in over-lapping of thermal-mismatch induced plastic zones and thus alter the overall plastic zone within the sample. Secondly, the overall stiffness or the elastic modulus of the composite decreases due to

the presence of clusters and hence the maximum strain energy per unit volume that the composite can sustain also decreases. In addition presence of porosity within a cluster may further affect the cluster's dynamic rigidity and damping capacity.

Another major source of damping can be due to the high dislocation density ρ_{th} at the particle-matrix interface, which is listed in Table 6.3. These were computed using the prismatic dislocation-punching model of Arsenault and Shi model expressed as equation (5.5) using a Burgers vector magnitude of 0.3nm for Al matrix [108]. According to Granato-Lucke dislocation model [29], the dislocation behaves like an elastic string pinned between both sides due to any hard particulates such as precipitates, reinforcement particulate or antiplane dislocations and under a low strain amplitude (below 10^{-4}) type cyclic load it bows, which introduces increased relative atomic movement in a crystalline lattice thus interfering with homogenous deformation of the bulk material. In the present experimental setup the strain magnitude induced in the specimen is of the order of 10^{-6} and hence the frequency dependent dislocation damping is applicable. Thus increased density of dislocation (see Table 6.3) due to presence of Ti and its intermetallics in the Al matrix contributes to increased dislocation-based damping characteristics in the MMC. Experiment results in Table 6.3 show an increase in damping factor when the particulate weight percentage increases which confirms this hypothesis.

Furthermore, from Table 6.1 it is clear that the hardness of the Ti reinforced samples is in general higher than that of unreinforced material. Table 6.1 also shows increased hardness at the interface than in the metallic matrix at a location away from the interface in any Ti containing composite, which can partly be attributed to the accumulation of residual plastic zone due to thermal mismatch at the particulate-matrix

interface, dislocation density and reduction in grain size. XRD results performed at the particle-matrix interface shows the presence of Al-Ti intermetallics as well as oxides. Their presence at the particulate-matrix interface can be expected to result in increased plastic zone radius due to increased CTE mismatch, since intermetallics and oxides are expected to have lower CTE compared to their parent materials.

Other damping mechanisms such as grain boundary sliding and elasto-thermodynamic damping can be seen to be insignificant in the present experimental study due to room temperature operation conditions, sample dimensions and frequency magnitude as explained in the previous chapter. Thus from the above discussions, it is encouraging to note that addition of stiffer metallic phase in the form of particulates in a metallic matrix increases both modulus and damping reasonably.

6.4 Summary

The following inferences can be made from the analysis:

1. The free-free beam type flexural resonance method can successfully be used with circle-fit approach to measure the stiffness and damping characteristics of the Al-Ti metastable composites.
2. Addition of stiffer Ti particulates in a ductile metallic matrix enhances energy dissipation due to the various intrinsic damping mechanisms acting parallel.
3. Experiment results show that damping of Al increases with an increase in Ti weight percentage. This can be explained due to increase in dislocation density and plastic zone radius.

Related Publications:

[1] N. Srikanth, L. K. Hoong and M. Gupta, *J. Materials Science,* 40, 2005, pp.1-7.

[2] N. Srikanth, C. H. Gaofeng, and M. Gupta, *J. of Alloys and Compounds*, vol. 352, 2003, pp. 106-110.

Chapter 7

Interconnected Metal Reinforced Metal Matrix Composites

7.0 Introduction

Studies using metal particulate reinforcement as an alternative to ceramic particulates gave a assurance that the stiffer metals in a ductile metallic matrix could contribute to the enhancement of damping and stiffness. Studies of Ganesh et al. [152] showed that the results of tensile property characterization indicated that Rule-of Mixtures (ROM) elastic modulus can be exceeded in the case of metallic matrix reinforced with interconnected fibrous preforms. The results of the literature search, however, reveal that no study is made to investigate the effect of interconnected reinforcement, refer Fig. 7.1, on the room temperature damping behavior of pure aluminium. Accordingly, the primary objective of this investigation was to characterize the damping behavior of monolithic and reinforced aluminium matrix using the innovative methodology involving suspended beam method coupled with circle-fit approach. Particular emphasis was placed to study the effect of inter-connected reinforcement weight percentage on the overall damping characteristics of the aluminium matrix.

7.1 Materials and Processes

In the present work, a non-heat treatable aluminum alloy, AA1050 (99.5 wt.% Al) was used as the matrix material. Three preforms were made with 2, 4 and 6 lobe shaped structures, shown in Fig. 7.1, using 0.9mm diameter galvanized iron wire (AISI 1008) with 10.8-volume percentage zinc in the form of coating and with a Vickers hardness of 217 ±3 HV. Using conventional casting, the aluminium based composites containing 1.6, 3.1 and 4.7 volume percentage of inter-connected reinforcement were synthesized to

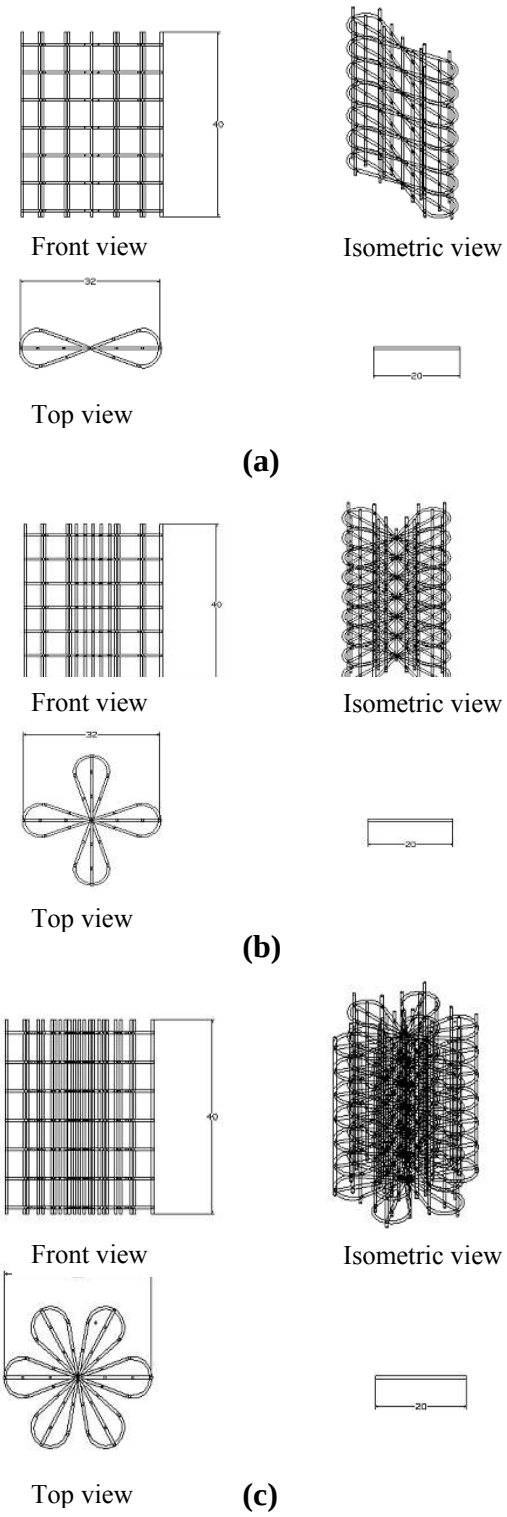

Fig. 7.1 Schematic diagram of the inter-connected reinforcement preforms with: (a) 2 lobes, (b) 4 lobes, and (c) 6 lobes geometries.

understand the variation of damping with volume fraction of reinforcement. They were subsequently hot extruded at 350^{o}C into 10 mm rods at an extrusion ratio of 13:1.

Table 7.1 Results of the microstructural, CTE, tensile properties and damping characterization.

	Sample A	**Sample B**	**Sample C**	**Sample D**
Reinforcement volume fraction (%)	-	1.6	3.1	4.7
Density (g/cm^3)	2.705	2.78	2.81	2.87
Porosity (%)	0.43	0.06	2.13	2.71
Matrix micro hardness (HV)	43.26	46.50	47.40	53.84
Interfacial micro hardness (HV)	-	489.12	570.2	543.44
Reinforcement micro hardness (HV)	-	165.67	157.60	175.35
Exp. mean CTE (10^{-6}/^{o}C)	26.6	26.3	25.3	24.9
Elastic modulus (GPa)	67.9	74.3	77.4	80.4
0.2 % yield strength (MPa)	134.8	154.9	184.9	195.0
Ultimate tensile strength (MPa)	116.5	133.7	164.7	170
Elongation (%)	23.8	7.96	2.98	0.69
Exp. damping loss factor η_{free}	0.0023	0.0027	0.0031	0.0038
Damping improvement (%)*	-	17	34.7	65
Total plastic-zone volume fraction (%)	-	2.34	4.53	6.87

* when compared to that of the monolithic sample.

7.2 Results

Macrostructure

The results of macrostructural characterization conducted on the as-deposited composites did not reveal presence of macropores in the matrix or at the interface between the matrix and reinforcement.

Density and Porosity Measurement

The results of the density measurements and volume percentage porosity computations are shown in Table 7.1. The results indicate that near dense monolithic and composites can be obtained using the fabrication methodology adopted in the present study.

Microstructural Characterization

Scanning electron microscopy conducted on the composite specimens showed good interfacial integrity (assessed in terms of interfacial debonding or presence of cracks) between the reinforcement wire and the matrix. X-ray diffraction was conductd to verify the presence of any process induced reaction phases at the Al-Fe interface (Fig. 7.2 (a)). Evidences of extremely limited interfacial reaction were observed at the reinforcement wire fringe (see Fig. 7.3).

Thermo-Mechanical Testing

The results of coefficient of thermal expansion measurements for the monolithic and composite samples are listed in Table 7.1. Results show that the coefficient of thermal expansion of the aluminium matrix decreases with the incorporation and increasing presence of interconnected fibrous reinforcement.

Hardness Testing

The results of hardness measurements carried out on the monolithic and composite samples are summarized in Table 7.1. It may be noted that the average values of the matrix microhardness of the sample increased with an addition and increasing presence of the interconnected wire mesh reinforcement in the metallic matrix. The results also revealed that the interface hardness was significantly higher when compared to the matrix hardness in all the composite samples.

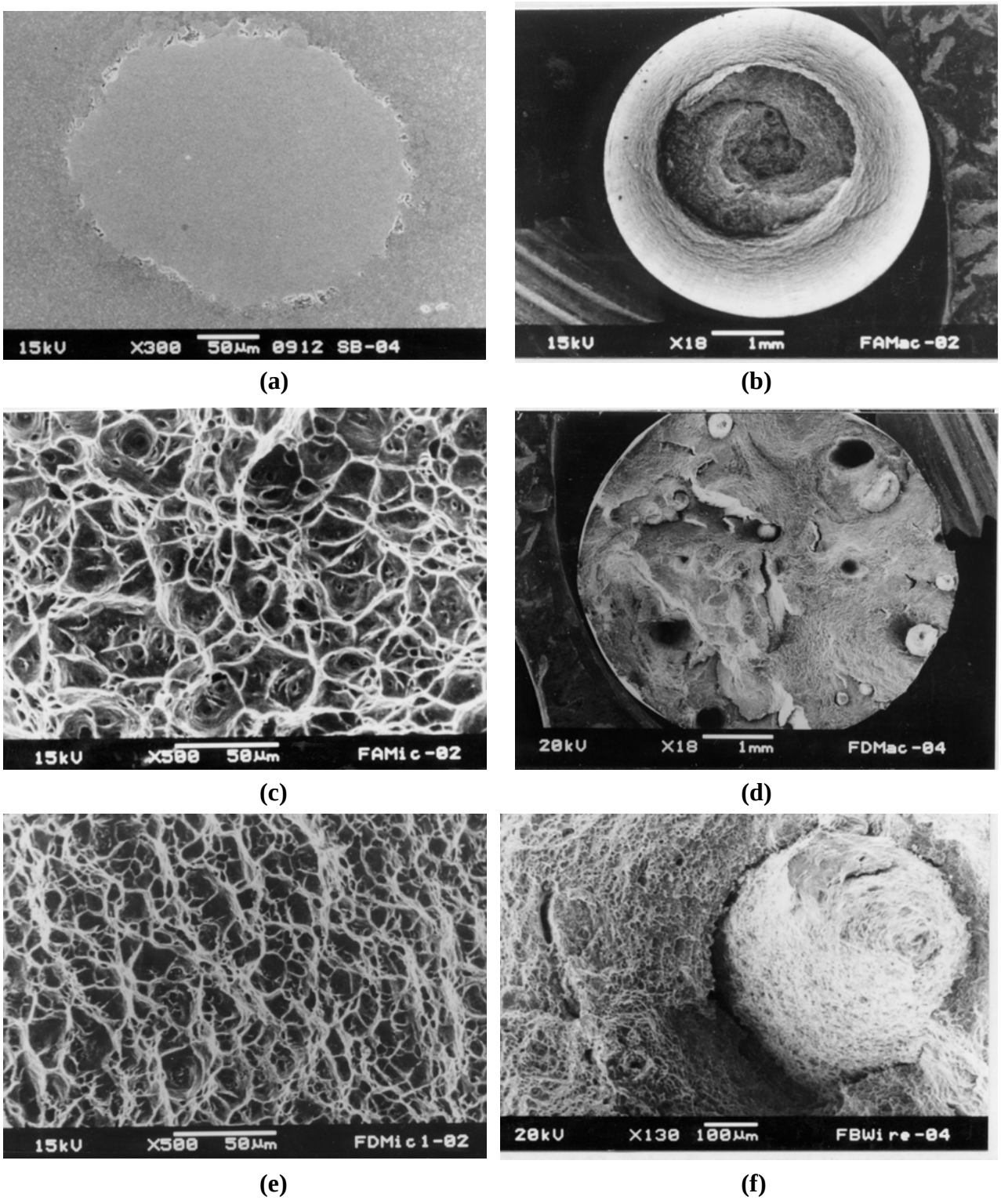

(a) **(b)**

(c) **(d)**

(e) **(f)**

Fig. 7.2 Representative SEM micrographs showing: (a) the interfacial integrity between the matrix and reinforcement wire of Sample B, (b) tensile fracture surface of monolithic aluminium, (c) magnified image of dimpled fracture surface of monolithic aluminium, (d) typical tensile fractured surface of Sample B, (e) magnified image of dimpled fracture surface of Sample B and (f) interfacial debonding of matrix and the reinforcement wire and wire breakage in the tensile fracture surface of Sample B.

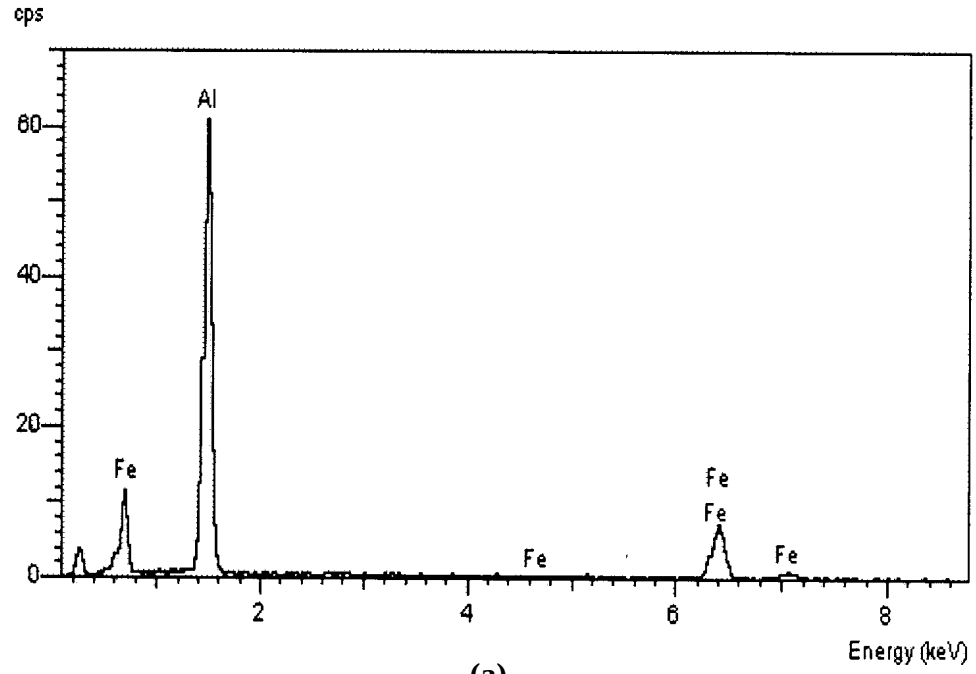

(a)

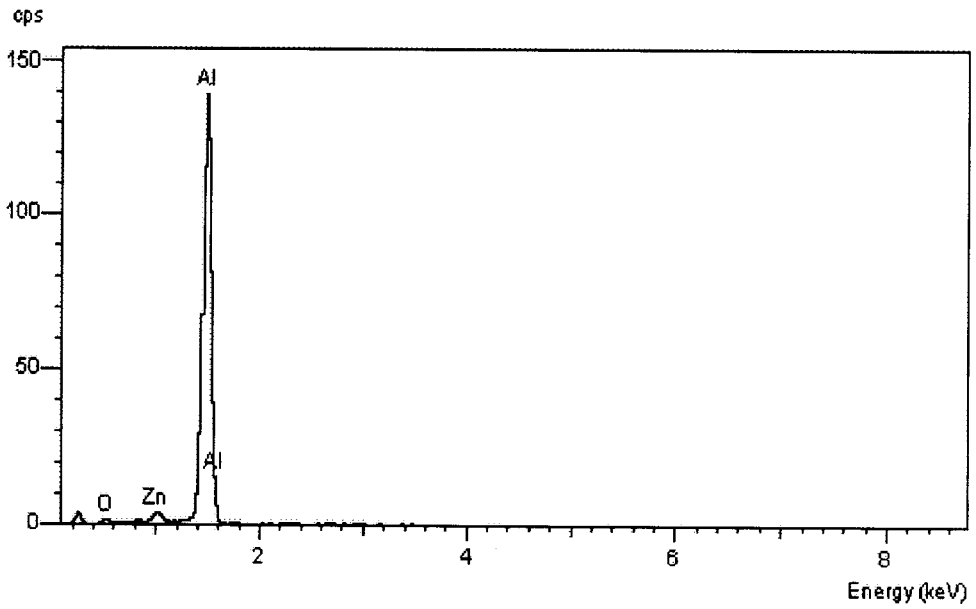

(b)

Fig. 7.3 Representative EDX graphs showing the composition at: (a) interfacial reaction zone and (b) the matrix of the composite materials.

Tensile Testing and Fractography

The results of the ambient temperature tensile testing of the composite samples, refer Table 7.1, showed that the incorporation of interconnected reinforcement lead to an increase in elastic modulus, 0.2% yield strength and ultimate tensile strength (UTS) of the aluminium alloy matrix while the ductility got adversely affected.

Figure 7.2 shows the tensile fracture surface of the monolithic aluminium and composite samples. The results show cup and cone type of fracture with dimpled surface indicative of ductile mode of fracture in the case of monolithic aluminium alloy. The composite material exhibited a mixed mode of fracture involving fiber breakage and pull-out. Composite matrix region, in general, showed a ductile dimpled surface with brittle characteristics near the wire and the pullout cavities.

Suspended Beam Vibration Testing

Suspended beam vibration testing was used in the present study to compute the damping loss factor and Fig. 7.4 shows the typical circle-fit plots for the various samples. The results obtained from the composite samples were benchmarked against the monolithic aluminium sample. Table 7.1 lists the damping loss factor η_{free} for the monolithic and composite samples.

7.3 Discussion

The impulse excitation technique performed on the suspended beam is exceptionally simple and fast and has many advantages. It was found to be highly repeatable to provide FRF data and the method is non-destructive, uses low cost

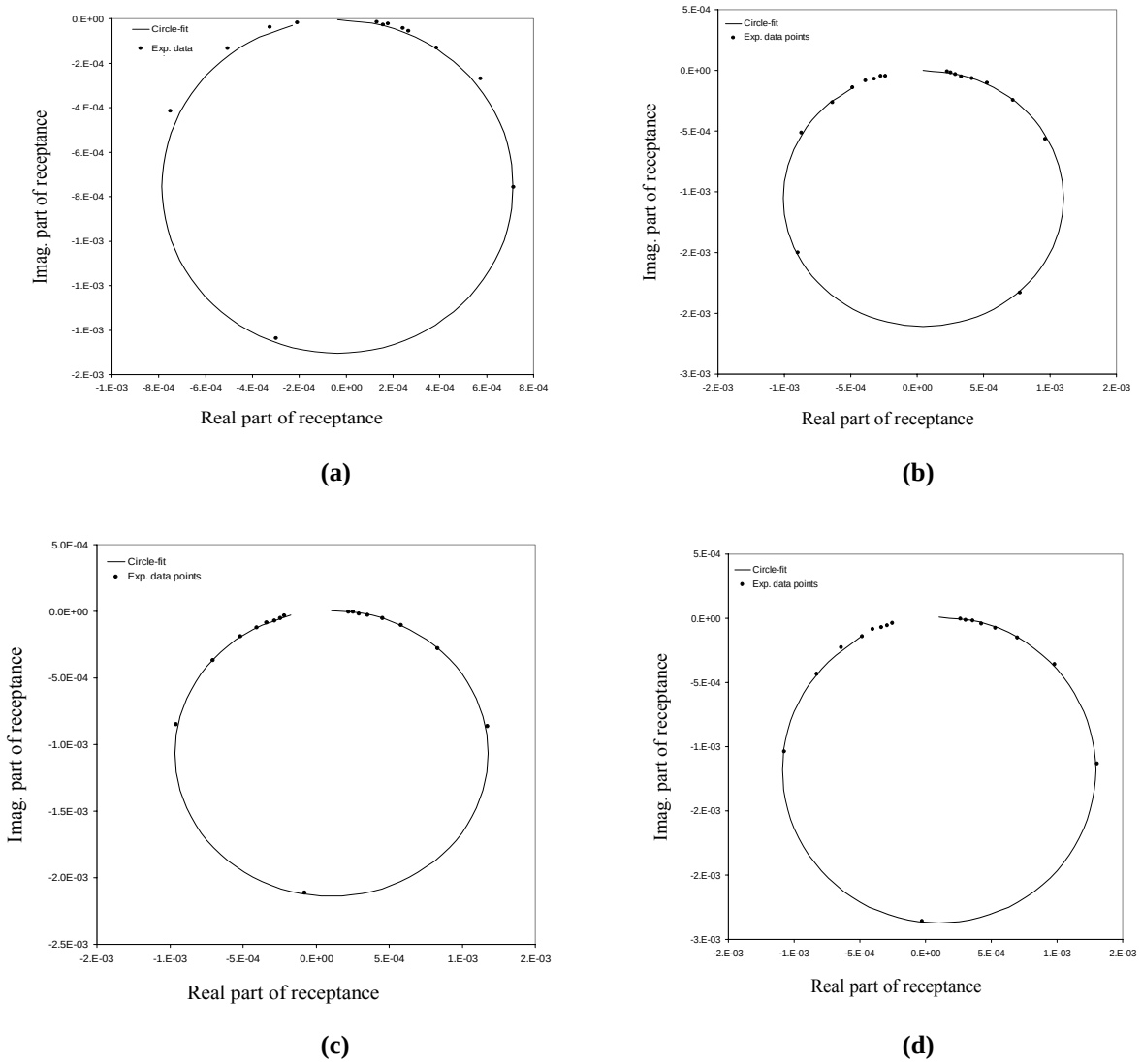

Fig. 7.4 Actual FRF data of sample corresponding to: (a) pure Al (b) Al with1.6vol.% iron mesh reinforcement (c) Al with 3.1vol.% iron mesh reinforcement and (d) Al with 4.7vol.% iron mesh reinforcement .

instrumentation and can accommodate a wide variety of specimen configurations and sizes.

Extremely limited interfacial reaction was observed in the interface between the reinforcement wire and the matrix (see Fig.7.1 (a)). Wire-matrix interfacial integrity assessed in terms of interfacial debonding and presence of voids was found to be good in the composite sample.

Table 7.1 lists the damping factor of the monolithic sample and the composite samples. Comparison shows that addition of interconnected iron wire reinforcement in the Al matrix increases the overall damping capacity and this damping improvement increases with reinforcement volume percentage.

The overall damping capacity of the metal matrix composite is directly related to the damping capacity of each of its constituents. Based on the damping studies of Thirumalai et al. [153], iron fibers has slightly lower loss factor of the order of 0.0009 as compared to aluminium, which has an loss order of 0.0023, based on the present work. Hence the addition of the interconnected fibers of galvanized iron in the Al matrix would be expected to decrease the overall damping capacity of the composite. Thus the experiment results have to be attributed primarily to the interface between reinforcement and the metallic matrix in addition to the intrinsic dissipation of strain energy due to mechanisms at the crystal level. The most significant role comes from point defect relaxation, dislocation motion, grain boundary sliding, inclusion-matrix friction, magnetoelastic effects, and elasto-thermodynamic (ETD) effects.

Continuous fiber reinforced metal matrix composites have additional mechanisms apart from the regular damping mechanisms in the metallic matrix, which improve their damping capacity. These mechanisms arise due to the inclusion of the stiffer reinforcement phase causing high residual stresses due to a large difference in the coefficient of thermal expansion of matrix (aluminium) and reinforcement (iron fibers) which are responsible for the production of plastic zone at the reinforcement/matrix interface.

In a macroscopic ideal composite sample of volume V in which different phases

are present such that f_i is the volume fraction of phase I ($\sum f_i=1$) and G_i is elastic shear modulus [154]. If the interface boundaries transmit stresses perfectly and do not dissipate energy, and these phases are homogenous, the internal friction of the composite becomes:

$$\eta = \frac{\sum_i \Delta w_i f_i}{2\pi \sum_i \frac{\sigma_i^2 f_i}{2G_i}} \tag{7.1}$$

where Δw_i and σ_i are the energy dissipated in a unit volume and the mean stress in the phase i, respectively. Three different phases are considered in the composite sample: the reinforcing fibers (R), the plastic zone around the fibers (zp) and the normal matrix (M), far from the fibers. Thus the total damping of the composite can be expressed as:

$$\eta_{pred} = \eta_M + \eta_R + \frac{f_{zp} \oint \sigma d\varepsilon}{\left(\pi \sigma_o^2 / G_{mmc}\right)} \tag{7.2}$$

where f_{zp} is the volume fraction of plastic zone, G_{mmc} is the elastic shear modulus of the composite, σ_o is the maximum amplitude of the sinusoidally varying stress σ, and ε is the corresponding varying strain.

The annular plastic zone induced around the reinforcement fiber is due to thermal mismatch caused due to difference in coefficient of themal expansion between the Al and reinforcement phases. The CTE for iron is 12 ppm/^{o}C and for Al is 26 ppm/^{o}C [5]. Based on the works of Dunand and Mortensen [134], the size of the plastic zone C_s can be estimated as follows:

$$C_s = r_f \left(\frac{4\Delta\alpha E \Delta T}{(5-4\nu)\sigma_y} \right)^{1/2} \tag{7.3}$$

where $\Delta\alpha$ is the difference between the CTEs of Al and iron, ΔT is the temperature difference which is around 327^{o} C, E and ν are the matrix elastic modulus and Poisson's ratio, σ_y is the matrix yield stress and r_f is the wire radius.

The volume fraction of plastic zone can be expressed in terms of the plastic zone size, fiber radius and reinforcement volume fraction f, as follows:

$$f_{zp} = f\frac{\left(C_s{}^2 - r_f^2\right)}{r_f^2} \tag{7.4}$$

Thus, equation (7.4) indicates that the internal friction in the composite sample depends on fiber content and on the matrix strength. When σ_y increases say by precipitation hardening, plastic relaxation may be inhibited.

Using the thermo-physical properties into equation (7.4) the plastic zone volume fraction for the three samples were calculated based on a assumption of 138μm and are listed in Table 7.1. It is clear that the plastic zone increases with reinforcement volume percentage. This increase in plasticity can be suspected to be reason behind the increase in microhardness value at the interface compared to the bulk matrix and reinforcement values, listed in Table 7.1, as a result of strain hardening effect. This correlation of plastic zone to the microhardness is confirmed in reference [151] using X-diffraction analysis for a particulate reinforced Al composite.

Another parallel damping mechanism occurs due to high density of dislocations at the matrix-reinforcement interface [137]. The energy dissipation arises due to increased relative atomic movement by the dislocations in a crystalline lattice, which interfere with homogenous deformation of the bulk material under the applied stress [29]. Thus the induced strain lags behind the stress causing increased damping characteristics. Based on

a prismatic dislocation-punching model of Arsenault and Shi [137], the dislocation density ρ at the interface is given as follows:

$$\rho = \frac{B\varepsilon V_f}{bt(1 - V_f)} \tag{7.5}$$

The thermal mismatch strain ε is given by the difference in thermal expansion times the temperature difference. V_f is the volume fraction of the ceramic reinforcement, b the Burgers vector, t the smallest dimension of the reinforcement which is the wire diameter (equals 0.25 mm after extrusion in this experimental study, see Fig. 7.2 (a)) and B the geometric constant (equals 4 for continuous fiber reinforcement [137]). In the present study, the wire diameter in the extruded composite sample denoted as t is of the order of 0.25 mm, refer Fig. 7.2 (a), which is very large compared to the reinforcement size in conventional particulate reinforced metal matrix composites. For Al-iron interface, the thermal mismatch strain during cooling is found to be typically 0.45% during cooling from 350^{o}C to room temperature, which can produce a dislocation density of the order of 10^{10} m^{-2} for a typical iron volume fraction range of 0.05 when the burgers vector is assumed to be 0.32 nm [137]. This is far below the dislocation density value of 10^{11}-10^{12} m^{-2} experienced in the SiC reinforced Al based composites system [26]. Hence the dislocation based damping mechanism is expected to be minimum in the present study.

In addition, the higher damping can be attributed to the presence of voids based on the damping studies of Zhang, Gungor and Lavernia [140] on Al alloy, which showed that the presence of voids in the metallic matrix also provides additional damping to the composite. It may be noted that under the applied cyclic load, high stresses can result

near the voids due to stress concentration [141] and this can contribute to the overall energy dissipation as described by the following equation.

$$\Delta W \approx \oint \sigma d\varepsilon \tag{7.6}$$

It may be noted that the volume percentage of porosity in the composite sample C and D is higher compared to that of monolithic aluminium sample and hence is expected to contribute positively to enhance damping in the case of the composite samples.

In addition, the intrinsic damping nature of the metal matrix can improve by the reinforcement associated grain refinement of the metal matrix. Studies shown in chapter 5 confirmed that the average grain diameter of the Al matrix decreases with an addition of SiC reinforcement, which can also be expected in this study due to the presence of the iron-wire reinforcement in the Al matrix. Kê's damping study on single crystal versus polycrystalline aluminium showed clearly that increased presence of grains increases the damping tremendously [22] only at high temperature around 200-300^{o}C. Hence in the present study, due to room temperature experimental conditions, the contribution from grain boundary based damping mechanism can be considered minimum. Presently, experimental work is in progress to understand the grain boundary based damping mechanisms in aluminium under room temperature conditions.

In addition to the above mentioned intrinsic damping mechanisms elasto-thermodynamic (ETD) damping can arise in a composite sample [23]. In the present study, using proper prediction models for the thermo-mechanical properties of the composite specimen, the magnitude of the macro-ETD is found to be of the order of 10^{-4} due to the beam dimensions, which does not seem to be significant to explain the experimental observation.

Thus the results of the present study, in essence, reveal that the circle-fit approach when combined with the impact-based measurement of the suspended beam is capable of measuring damping loss factor and the dynamic stiffness of the iron-fiber reinforced Al samples. Additionally it is encouraging to find that the interconnected nature of reinforcement enhanced damping and stiffness of the metallic matrix.

7.4 Summary

Following conclusions may be drawn from the present study:

1. The free-free beam type flexural resonance method can be successfully used with circle-fit approach to measure the damping characteristics of the Al based composites.
2. The damping of the pure aluminium matrix increases as a result of presence of interconnected galvanised iron fibre reinforcement.
3. An increase in damping with an increase in the volume percentage of interconnected galvanised iron fibre reinforcement can be attributed to a progressive increase in the energy dissipation. The energy dissipation can primarily be attributed to the influence of increase in volume percentage of plastic zone around the reinforcement.

Related Publications:

[1] N. Srikanth, V. V. Ganesh, and M. Gupta: *Mat. Sci. and Tech.*, Vol. 19 (2003) 1-7.

[2] N. Srikanth, L. A. Kurniawan, and M. Gupta, *Composites Science and Technology*, Vol. 63 (2003) 839-849.

Chapter 8

Hybrid Composites

8.0 Introduction

Thus far the results from damping studies on metal based (Al or Mg) composites reinforced with ceramic, metal and the shape (viz., discontinuous versus inter-connected) gave a promising trend that in general damping capacity of the matrix metal is enhanced by the presence of a reinforcement. Secondly the maximum volume fraction of a reinforcement in a composite depends on the shape and size of the reinforcement. Thirdly their effectiveness in damping also depends on the type of interface metal-metal versus metal-ceramic, etc. Hence interest arose in studying the interaction of these reinforcement by making hybrid composites. Literature review shows most of the researchers studied composites with single type reinforcement. In this part of the work, the systematic study on few combinations of hybrid composites to explain the effectiveness of such reinforcement selection was carried out.

8.1 Materials and Processes

The composite samples were prepared using the disintegrated deposition method (DMD) [4]. They were subsequently hot extruded at 350^{o} C into 10mm rods at an extrusion ratio of 13:1. The combination of materials is listed bellow:

Case A: This set of samples aimed for comparing the effectiveness of sub-micron sized SiC versus micron sized SiC particles with a combination of Ti particulates. The matrix used was elemental magnesium turnings of 99.9 % purity (supplied by ACROS organics, New Jersey, USA) as the base material. The submicron sized silicon carbide particulates (provided by SIKA Tech, Saint-Gobain, France) had a average size of 0.6 μm, while Ti particles were 120 μm in size. Three composites with different volume fractions of the

sub-micron sized SiC_p (i.e.: 2.7 %, 5.8 % and 9.0 %) were made. Additionally to study the influence of Ti particles, three composites having different SiC volume fractions (i.e.: 2.8 %, 5.7 % and 8.8 %) but with a similar volume fraction of the Ti particulates, i.e. 1.1 vol. %, were processed by the technique of disintegrated melt deposition (DMD).

Case B: In this set of samples, the matrix used was 99.5% initial purity aluminium. The silicon carbide particulate size used in the present study (Amet P600 D-series) was around 25 μm and the wire mesh consisted of galvanized iron wire (see Fig. 8.1). Three composite rods with different reinforcements were prepared viz., sample-BC1 contained 2.03 vol. % of Iron wire mesh, sample-BC2 contained 4.83 vol. % of SiC and sample-BC3 contained 2.05 vol. % of Iron wire mesh along with 0.53 vol. % of SiC. In addition a monolithic Al sample was prepared which is denoted as sample-BM using the same processing route.

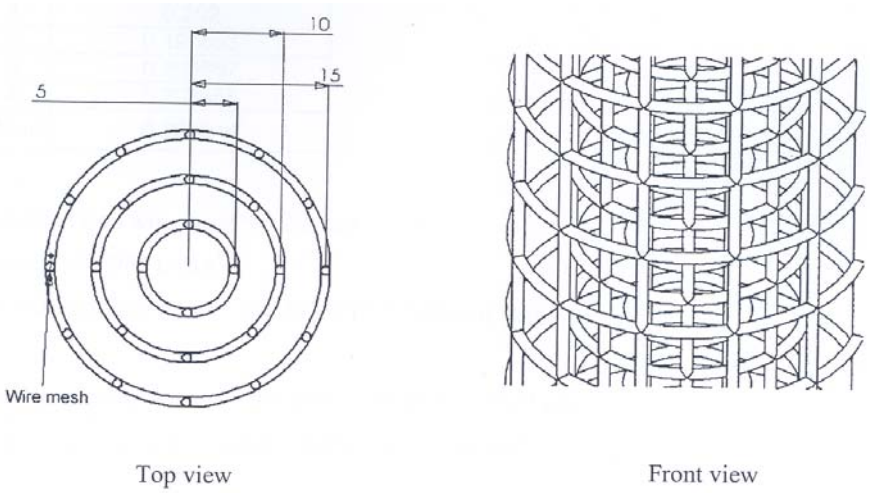

Fig. 8.1 Schematic diagram of the inter-connected reinforcement performs used in the ingot.

Case C: To understand the novel idea of semiconductor like Ge reinforcement in Al matrix, a composite rod with 1.9 volume percentage of Ge with a particulate size of 17

μm was prepared using the DMD approach. Similarly, three composite rods with different silicon carbide particulate volume fraction, viz., 2.9 %, 3.2 % and 8.2 %, with a particulate size close to 25 μm along with additional presence of Ge particulates were synthesized.

Table 8.1 Results of acid dissolution, density, porosity, chemical analysis and grain size measurements of the Case A samples.

Material	Reinforcement (wt. %)		Reinforcement (vol. %)		ρ (g/cm^3)	P vol. %	Grains details		SiC details		Ti details	
	SiC	Ti	SiC	Ti			Size (μm)	AR	Size (μm)	AR	Size (μm)	AR
Mg	-	-	-	-	1.738	0.12	21	1.8	-	-	-	-
Mg/SiC	4.8	-	2.7	-	1.769	0.12	18	1.9	0.57	1.2	-	-
Mg/SiC	10.2	-	5.8	-	1.793	0.53	17	1.8	0.58	1.1	-	-
Mg/SiC	15.4	-	9.0	-	1.835	1.75	12	1.4	0.58	1.1	-	-
Mg/SiC/Ti	5.0	2.7	2.8	1.1	1.797	0.69	20	1.9	N.A	N.A	17	2.4
Mg/SiC/Ti	9.9	2.7	5.7	1.1	1.818	1.90	17	14	N.A	N.A	16	1.9
Mg/SiC/Ti	14.9	2.7	8.8	1.1	1.879	1.03	15	1.5	N.A	N.A	16	2.1

Note: AR denotes aspect ratio, ρ denotes experimental density, P denotes porosity, N.A denotes not available.

8.2 Results

Microstructure Characterization

The results of microstructural studies conducted on both the monolithic and reinforced specimens for case A, B and C are listed in Table 8.1, Table 8.2 and Table 8.3, respectively. Microstructural characterization conducted on the as deposited composite and monolithic ingots revealed: (a) no evidence of blowholes and macro pores, (b) presence of trace amounts of porosity in the solidified oxide of the sludge. No evidence of gravity settling of the reinforcing particulates was observed in the composite samples. In general, a decrease in the average grain size with an increase in weight percentage of the reinforcing particulates is observed in the composite samples. The grain morphology

of the extruded specimens was observed in an optical microscope using standard bright field illumination technique and was found to be equiaxed.

Table 8.2 Results of the microstructural and thermomechanical properties of Case B samples.

	Sample BM	**Sample BC1**	**Sample BC2**	**Sample BC3**
SiC vol. (%)	-	-	4.83	0.53
Iron mesh vol. (%)	-	2.03	-	2.05
Density (g/cm^3)	2.71± 0.02	2.85± 0.02	2.71± 0.01	**2.89± 0.03**
Porosity (%)	0	1.29	1.58	1.19
Grain size (μm)	13.8 ± 0.8	6.5 ± 0.5	10.0 ± 1.9	**8.7 ± 1.2**
Grain aspect ratio	1.8 ± 0.5	1.6 ± 0.3	1.8 ± 0.6	1.9 ± 0.4
Matrix micro hardness (HV)	45 ± 2	50 ± 1.6	44 ± 3	47 ± 1.8
Al-Fe Interfacial hardness (HV)	-	48 ± 1.4	-	57 ± 7
Al-SiC Interfacial hardness (HV)		-	72 ± 4	141 ± 17
Fe Reinf. micro hardness (HV)	-	181 ± 9	-	188 ± 9
SiC Reinf. micro hardness (HV)	-	-	1749 ± 75	1778 ± 192
Macro hardness (HR15T)	57 ± 0.5	55 ± 0.8	54.5 ± 1.1	57.7 ± 1.9
Exp. mean CTE ($10^{-6}/^{o}C$)	27.35 ± 0.8	24.81 ± 0.4	26.02 ± 0.9	24.57 ± 1.2
Elastic modulus (GPa)	70.73	76.70	73.91	75.17
0.2 % yield strength (MPa)	142 ± 4	151 ± 32	148 ± 30	191 ± 23
Ultimate tensile strength (MPa)	165 ± 4	167 ± 35	172 ± 27	213 ± 21
Ductility (%)	17.5 ± 2.1	4 ± 3.3	9.8 ± 1.4	3.3 ± 0.9
Interparticle spacing of SiC (μm)	-	-	113	343
Estimated plastic zone vol. (%)	-	2.7	14.9	4.8
Estimated dislocation density (m^{-2})	-	4.71e9	6.41e11	6.73e10
Exp. damping loss factor η_{free}	0.0051	0.0059	0.0058	0.0064
% Improvement in damping	-	15%	15%	25%

Figures 8.2 (a) and (b) are scanning electron micrographs for Case A samples showing the distribution of the reinforcing SiC and Ti particulates in the magnesium matrix. The SiC particulates were seen both at grain boundaries and within the grain interior. A uniform distribution of the reinforcing SiC particulates was found with some evidence of clustering or particulate agglomeration and porosity in all of the composite

Table 8.3 Microstructural results of the various composite samples of Case C.

Material	Reinforcement		Exp. density (g/cm^3)	Porosity (%)	Grain size (μm)	CTE ($x10^{-6}/^oK$)
	Ge (Vol. %)	SiC (Vol. %)				
Al	-	-	2.71	0.68	20.29	29.15
Al-1.9Ge	1.9	-	2.76	20±4.8	16.96	27.88
Al-1.8Ge/2.9SiC	1.8	2.88	2.77	17±4.5	12.22	28.31
Al-2.1Ge/3.2SiC	2.1	3.24	2.78	12±4.2	12.13	27.79
Al-1.9Ge/8.2SiC	1.9	8.15	2.80	10±4.2	9.76	27.35

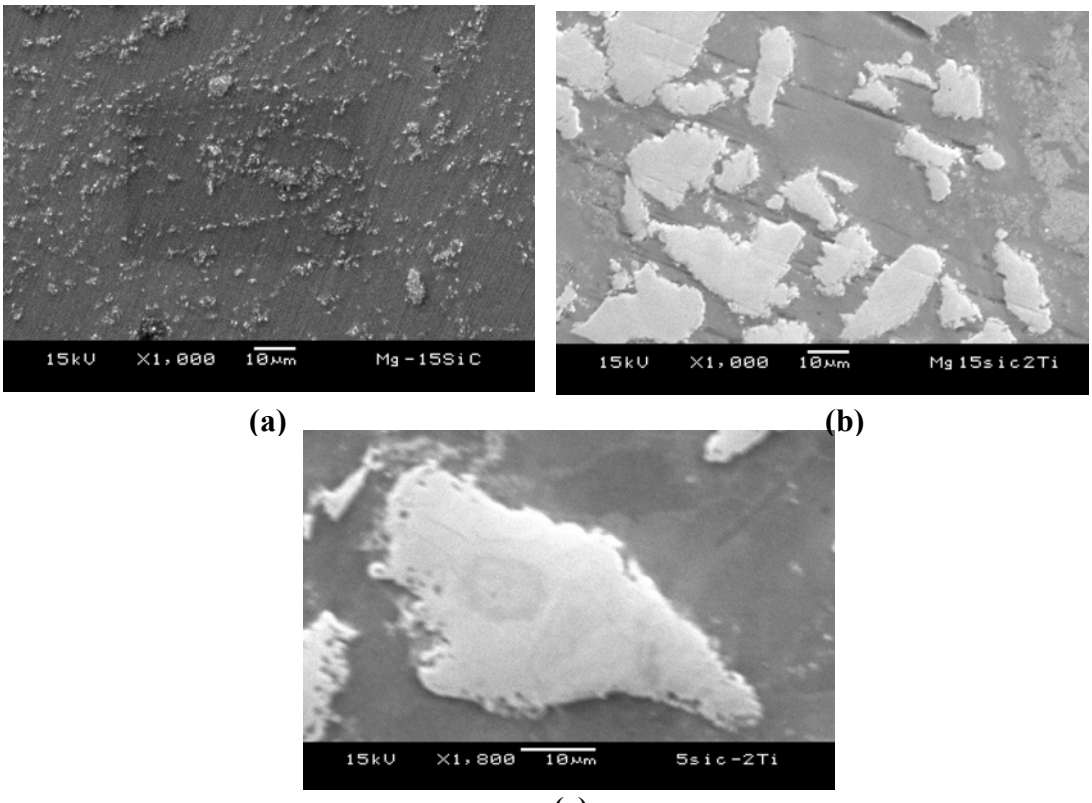

(a) **(b)**

(c)

Fig. 8.2 SEM micrographs of case A samples showing: (a) the distribution of SiC particulate in Mg/ 9 vol. % SiC sample, (b) the distribution of Ti particulate in Mg/ 8.8 vol. % SiC/1.1 vol. % Ti sample and (c) the particulate/matrix interface of Ti in Mg/ 5.7 vol. % SiC/1.1 vol. % Ti sample.

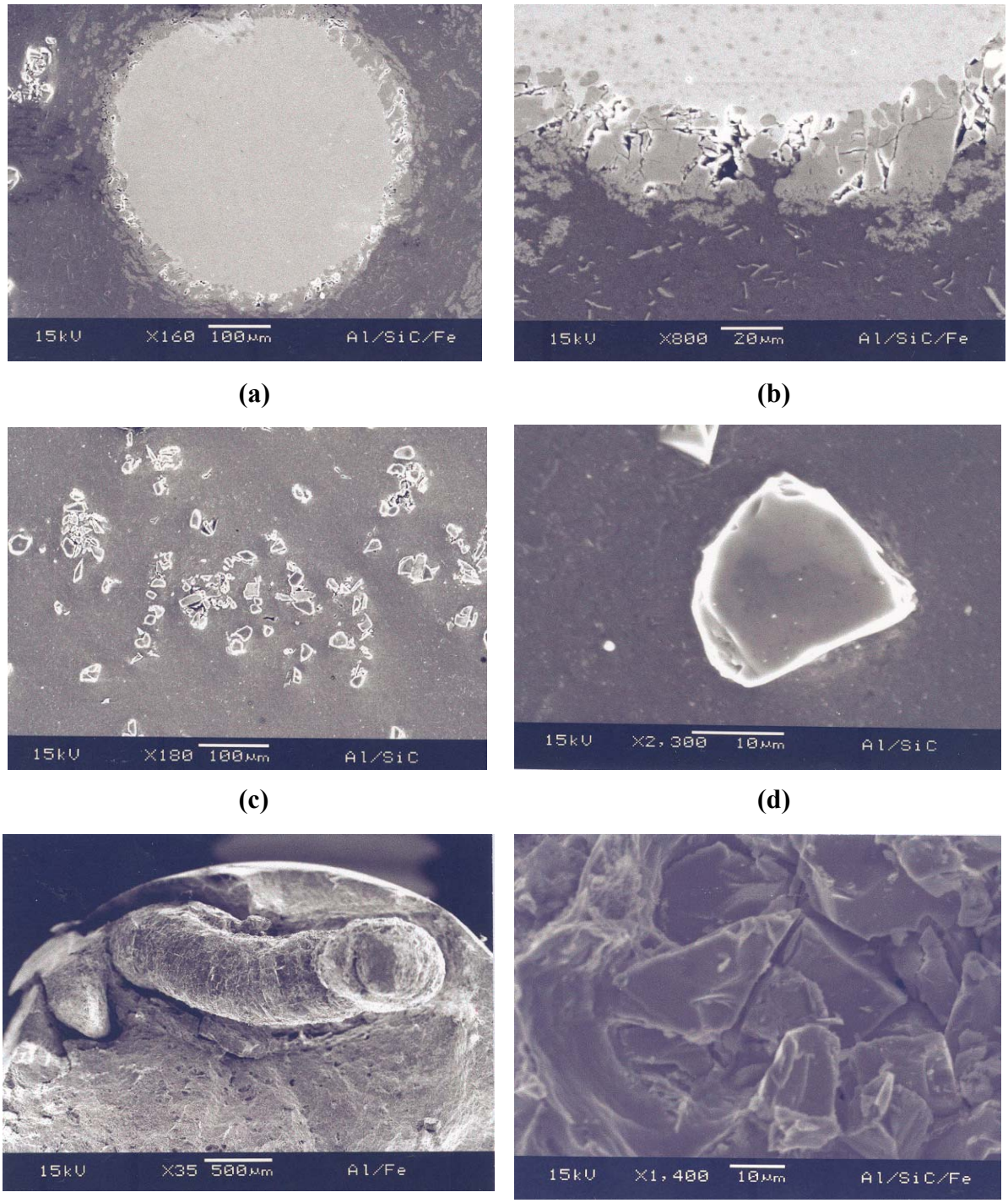

Fig. 8.3 Representative SEM micrographs of case B samples showing: (a) & (b) the interfacial integrity between the matrix and reinforcement wire of sample BC1 at low and high magnification, respectively, (c) typical SiC distribution in the sample BC2 (d) typical interfacial integrity of the SiC particulate with the matrix in the sample BC2 (e) typical interfacial debonding of matrix and the reinforcement wire and wire breakage in the tensile fracture surface of Sample BC1 (f) typical SiC failure in sample BC3 exhibiting interfacial debonding and particulate breakage.

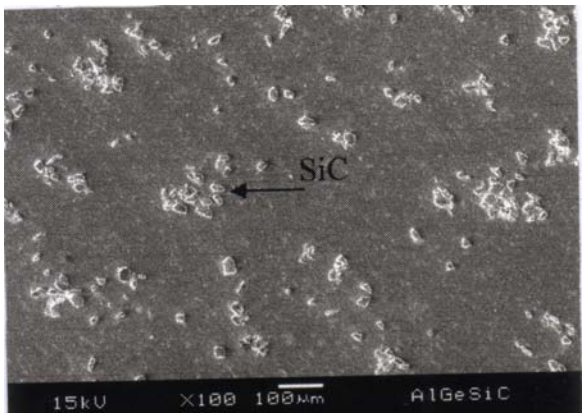

(a)

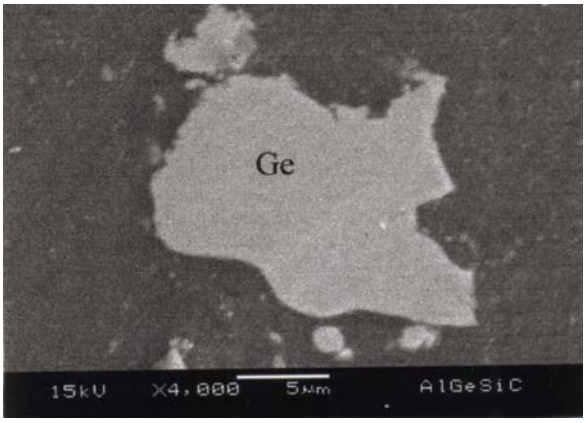

(b)

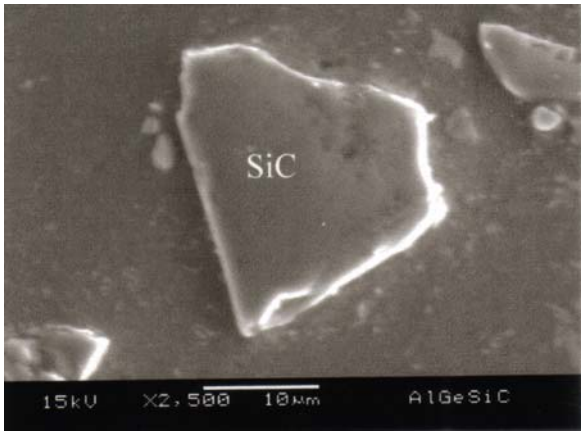

(c)

Fig. 8.4 SEM micrographs of case C samples showing: (a) the distribution of Ge and SiC particulate in Al-1.8Ge/2.9SiC sample, (b) the particulate/matrix interface of Ge in Al-1.8Ge/2.9SiC sample and (c) the particulate/matrix interface of SiC in Al-1.8Ge/2.9SiC sample.

samples. A close inspection of the reinforcing Ti particulate at higher magnifications (Fig. 8.2 (c)) confirms the interfacial bonding (assessed in terms of voids and debonded regions) to be good. Similarly, SEM studies of Case B samples showed that the distribution and interface quality of SiC and the iron wire mesh in the Al matrix was good, see Fig 8.3. Again, for Case C samples, SEM micrographs shown in Fig. 8.4 (a) shows that the SiC and Ge particle distribution are uniform in the Al/Ge/SiC samples while Fig. 8.4 (b) and (c) shows that the interface between Al-SiC and Al-Ge is good.

Table 8.4 Results of X-ray diffractometry studies conducted on extruded MMC samples of Case A.

Phases	Number of matching peaks in each case.						
	Mg	Mg/4.8 SiC	Mg/10.2 SiC	Mg/15.4 SiC	Mg/1.1Ti_P /2.8SiC_P	Mg/1.1Ti_P /5.7SiC_P	Mg/1.1Ti_P /8.8SiC_P
Mg	9[3]*	8[3][a]	7[3]	7[3]	7[3]	7[3]	8[3]
SiC	--	4[3]	4[3]	4[3]	4[3]	4[3]	3[3]
Mg_2Si	--	3[1]	3[2]	3[3]	3[1]	3[1]	3[2]
Ti	--	--	--	--	2[1]	3[1]	3[2]

* The value in the square brackets indicates the number of strongest peaks matched.

Table 8.5 X-Ray diffraction results of Case C samples.

Material	**Al**	**Al-1.9Ge**	**Al-1.8Ge/2.9SiC**	**Al-2.1Ge /3.2 SiC**	**Al-1.9Ge /8.2 SiC**
Al	4[3]	5[3]	4[3]	5[3]	6[3]
Ge	-	-	1	1	-
SiC	-	-	-	1	3

Density and Porosity Measurement

The results of the experimental density values for cases A, B and C are summarized in Table 8.1, Table 8.2 and Table 8.3, respectively. The volume fraction of porosity, which is computed from the determined density values and the results of chemical dissolution, is

also included in these respective tables.

X-Ray Diffraction Studies

The X-ray diffraction results corresponding to Case A: (a) Mg, (b) Mg/SiC, and (c) Mg/SiC/Ti samples were carefully analyzed. The lattice spacing [d] values were compared with the values of magnesium, SiC, Mg_2Si and other phases of the Mg-O system. The phase analysis results are summarized in Table 8.4.

X-ray diffraction studies were performed for Case B composites samples to study the presence of any interfacial compounds such as oxides, carbides and intermetallics

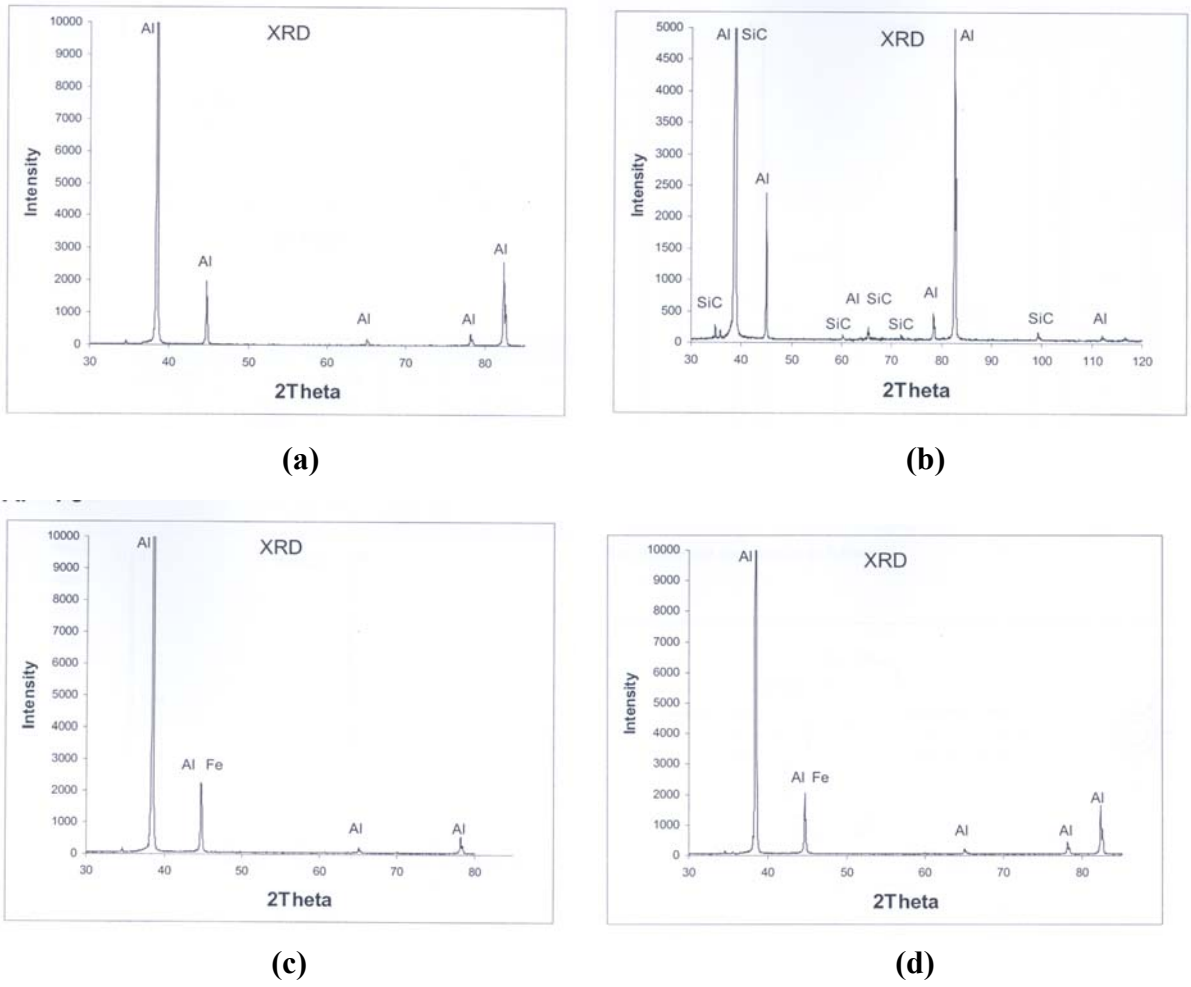

Fig. 8.5 Representative XRD graph performed on: (a) monolithic Al sample-BM (b) sample-BC1 (c) sample-BC2 (d) sample-BC3.

(see Fig. 8.5). Similarly, Table 8.5 lists the X-ray diffraction studies for Case C samples that list the presence of various phases.

Thermo-Mechanical Testing

The thermo-mechanical study on monolithic and reinforced samples were conducted and the average coefficient of thermal expansion of case A, B, C are listed in Table 8.6, Table 8.2 and Table 8.3, respectively. Test results reveal the coefficient of thermal expansion of the magnesium matrix to decrease with an increase in particulate reinforcement (SiC and Ti) content in terms of weight percentage.

Hardness Testing

The results of hardness measurements performed on both the monolithic and composite samples are summarized in Table 8.6 for Case A samples. It is noted that the average value of the interfacial hardness at the Mg-Ti interfaces in the Mg/SiC/Ti composite sample is significantly higher than hardness of the bulk matrix. However, for the SiC particulates such measurements could not be carried out due to their sub-micron size.

Table 8.2 lists the hardness results of Case B samples containing Al/Fe/SiC phases. The matrix and the reinforcement hardness were measured for the various phases present and the interfacial hardness of matrix-reinforcement viz., Al-Fe and Al-SiC were also measured using micro-hardness method. Comparison of the results shows that the metal-ceramic interface hardness is higher than the metal-metal interface.

Table 8.6 Results of hardness and thermal expansion properties of Case A samples.

Material	Micro hardness (HV)			Macro-hardness (HR15T)	CTE($x10^{-6}$)
	Matrix	SiC_P Interface	Ti_P Interface		
Pure Mg	41±1	--	--	47±1	28.0
Mg/4.8SiC	53±1	--	--	58±1	23.8
Mg/10.2SiC	55±1	--	--	59±1	21.2
Mg/15.4SiC	56±2	--	--	63±1	21.0
$Mg/1.1Ti_P/2.8SiC_P$	48±1	--	54±2	48±2	23.4
$Mg/1.1Ti_P/5.7SiC_P$	49±1	--	55±2	52±1	22.8
$Mg/1.1Ti_P/8.8SiC_P$	66±1	--	71±3	65±1	19.9

Table 8.7 Experimental values of various thermo-mechanical properties of the various composite samples of Case C.

Material	Micro-Hardness			Macro-hardness (HR15T)	Dyn, Modulus (GPa)	0.2 % Yield stress (MPa)	Ult. Tensile Stress (MPa)	Ductility (%)
	Matrix (HV)	SiC (HV)	Interface zone (HV)					
Al	43±2.2	-	-	42±1.7	71.6	115.44	135.3	20.3
Al-1.9Ge	45±2.2	-	-	52±0.6	68.5	109.55	165.8	22.5
Al-1.8Ge/2.9SiC	49±2.2	79±18	55±3	54±2.0	71.3	113.62	173.1	19.6
Al-2.1Ge/3.2SiC	49±1.3	70±13	58±3	54±0.5	71.2	116.19	179.8	18.9
Al-1.9Ge/8.2SiC	49±1.9	81±36	60±4	55±1.0	70.6	123.44	176.5	9.0

Table 8.8 Results of room temperature tensile properties of Case A samples.

Material	Dynamic Modulus (GPa)	0.2% YS (MPa)	UTS (MPa)	Ductility (%)
Pure Mg	39.82	153±8	207±4	9.2±1.4
Mg/4.8SiC	45.60	182±2	219±2	2.1±0.9
Mg/10.2SiC	47.22	171±3	221±14	1.5±0.2
Mg/15.4SiC	48.24	155±1	207±9	1.4± 0.1
$Mg/1.1Ti_P/2.8SiC_P$	46.76	169±8	204±17	2.7± 0.7
$Mg/1.1Ti_P/5.7SiC_P$	47.96	161±9	199±16	2.9±0.9
$Mg/1.1Ti_P/8.8SiC_P$	51.81	217±2	233±6	1.0± 0.1

Similar matrix, reinforcement and interfacial hardness measurements were performed on Case C samples which are listed in Table 8.7. Macro hardness measurements show in general that the overall hardness increases with increase in reinforcement volume fraction. Secondly, the trend holds well in the composite samples that the interface hardness is higher than ductile metallic matrix.

Tensile Testing

Tables 8.8, 8.2 and 8.7 list the 0.2% yield strength, ultimate strength and ductility of the monolithic and MMC samples. Results clearly show that the presence of particulate reinforcing phase leads to a decrease in ductility and an increase in both yield strength and tensile strength.

Table 8.9. Results of theoretical predictions and damping measurement of Case A samples.

Material	Estimated Plastic zone vol. [%]	Estimated Dislocation density [m^{-2}]	Estimated Interparticle spacing [μm]		Exp. loss factor η_{free}	Increase in damping compared to pure Mg * (%)
			SiC	Ti		
Pure Mg	-	-	-	-	0.0035	
Mg/2.7SiC_p	5.86	2.65E+13	3.7	-	0.0060	70.4%
Mg/5.8SiC_p	12.60	5.97E+13	2.5	-	0.0073	106.3%
Mg/9SiC_p	19.55	9.62E+13	2.0	-	0.0081	128.5%
Mg/1.1Ti_P /2.8SiC_P	10.55	2.82E+13	3.6	162.1	0.0068	90.8%
Mg/1.1Ti_P /5.7SiC_P	21.48	6.02E+13	2.5	152.5	0.0075	110.8%
Mg/1.1Ti_P /8.8SiC_P	33.16	9.53E+13	2.0	152.5	0.0084	137.7%

Note: * denotes damping loss factor of pure magnesium is taken as 0.0035.

In the case of Case A samples, except for the Mg/1.1Ti_p/5.7SiC_p composite a clear trend existed for the variation of strength with volume fraction of the reinforcing phase in the metal matrix. Fracture surface examination of the Mg samples revealed a brittle failure mode. Fracture surface studies performed on the Mg/SiC and Mg/SiC/Ti samples revealed a mixed-mode type of fracture with distinct evidence of limited plastic deformation of the matrix.

Similarly for Case B and Case C, the fractographic studies showed that both particle debonding and cracking takes place. This shows that the interface between the matrix and interface is good.

Table 8.10 Results of theoretical predictions and damping measurement of the various composite samples of Case C.

Material	Est. Plastic zone vol. [%]	Est. Dislocation density [m^{-2}]	Estimated Interparticle spacing [μm]		Exp. loss factor η_{free}	Increase in average damping compared to pure Al * (%)
			Ge	SiC	mean	
Al-1.9Ge	11.0	5.3E+11	35.1	-	0.0043	46
Al-1.8Ge/2.9SiC	29.7	8.8E+11	35.3	65.2	0.0054	84
Al-2.1Ge/3.2SiC	33.8	1.02E+12	32.7	61.1	0.0059	101
Al-1.9Ge/8.2SiC	64.4	1.6E+12	34.8	34.4	0.0064	118
Al #	-	-	-	-	0.0029	-
Al – 4.4 SiC #	29.3	9.9E+11	-	90.9	0.0033	14
Al – 11.8 SiC #	76.3	3.0E+12	-	51.7	0.0045	54
Al – 15 SiC #	98.9	4.7E+12	-	38.1	0.0058	97

Note: * denotes reference damping loss factor of pure aluminium is taken as 0.0029 and # indicates samples from chapter 5.

Suspended Beam Vibration Testing

Suspended beam vibration testing was used to compute the damping loss factor.

The results are benchmarked against a pure magnesium sample. The damping loss factor [η_{free}] for the monolithic and MMC samples of Case A, B and C are listed in Table 8.9, Table 8.2 and Table 8.10, respectively. Using the resonant frequency, sample dimensions, and experimental density values the dynamic modulus of the samples was determined using equation (3.3), and the values are summarized in the respective Tables.

8.3 Discussion

Case A samples

Table 8.9 lists the damping factor of case A sample set consisting of monolithic Mg and the composite samples. A comparison of the damping factor reveals that addition of sub-micron sized SiC particles to the Mg metal matrix increases the overall damping capacity when compared to the damping capacity of pure magnesium, which has a damping capacity of 0.0035. The increase or improvement in damping capacity increases with an increase in sub-micron sized SiC content (weight percentage). Based on the previous damping studies explained in chapter 5, addition of micron-sized SiC particulates to pure Mg shows a similar increase in damping (Table 5.4). Thus, addition of sub-micron SiC particulates to the magnesium metal matrix appears to be effective in dissipating energy when compared to micron-sized SiC particulates when a cyclic stress is applied.

Similarly, a comparison shows that addition of 1.1 vol. % of Ti particulates to the Mg matrix coupled with the presence of SiC particulates further increases the overall damping capacity. This improvement in damping remains similar with an increase in volume fraction of the reinforcing SiC particulates. For example:

(a) 2.8 vol. % of SiC in Mg along with the presence of 1.1 % Ti provides a damping increase of 90.8 % compared to pure Mg, and

(b) The sample containing only 2.7 vol. % SiC provided an increase in damping of 70.4 %.

Thus, a difference of ~20 % is observed due to the additional presence of titanium particulates [1.1 vol. %] in the Mg/2.7vol.%SiC/1.1vol.%Ti composite sample. Thus, it is summarized that the damping gets significantly enhanced due to the combined presence and interactive influence of titanium (Ti) and sub-micron SiC_p in the magnesium metal matrix.

SiC is relatively more stable in the magnesium matrix, which makes Mg/SiC a better choice compared to the other established material systems such as Al/SiC [155-156]. In this study, the Mg–SiC interfacial integrity assessed in terms of: (i) interfacial debonding, and (ii) presence of voids, was found to be good. No interfacial reaction products were observed when examined in the SEM. The results indicate the suitability of superheat temperature (750 ^{0}C) used in this study to synthesize Mg/SiC composites. However, results of X-ray diffraction studies conducted on the Mg/SiC samples (see Table 8.4) reveal the presence of the Mg_2Si phase besides the Mg and SiC phases. The results obtained clearly indicate that the temperature and time conditions employed during processing were sufficient for minimal reaction between molten magnesium and the reinforcing SiC particulates. Considering that SiC_p contain free silicon and are often associated with a thin layer of silicon dioxide (SiO_2) [157]; the possible reactions can be expressed as follows [158-159]:

$$2Mg + SiC == Mg_2Si + C \quad (8.1)$$

$$4Mg + SiO_2 == Mg_2Si + 2\,MgO \quad (8.2)$$

$$2Mg + Si == Mg_2Si \quad (8.3)$$

The presence of Mg_2Si, detected in this study (Reference: Table 8.4), is very much in conformance with the theoretical speculation and experimental findings of a previous investigation [159]. The inability after exhaustive examination in the SEM to detect the presence of Mg_2Si suggests that its size may be too small below the delectability limit.

Study of the phase diagram of the Mg-Ti system reveals that titanium does not react with magnesium to form an intermetallic compound [160]. Theoretically, high solid solubility is expected in the Ti-Mg material system due to satisfaction of the Hume-Rothary principles [161] such as: (1) atomic size difference being less than 10%, (2) the elements magnesium and titanium have the HCP type crystal structure, (3) electro-negativity differences being similar, yet their valence does vary (Ti = 4 and Mg = 2). Due to this notable difference in valence, the solubility of Mg in Ti has been reported to be up to 0.7 atomic % at temperatures as high as 890 ^{o}C and less than 0.2 atomic % at temperatures below 500 ^{o}C. Attempts to enhance the solid solubility of magnesium and titanium using the mechanical alloying methods have shown that only a maximum of 9 wt. % of Mg solubility in titanium has been achieved [162], which involved enhancing the free energy of the solute rich phase compared to free energy of the solvent-rich phase by additional milling. Further, titanium remains stable even up to the boiling point of magnesium (1090 ^{o}C), due essentially to its high melting point [T_M = 1668 °C] [147]. The results of this study (Fig. 8.2 (c)) reveal that Ti remains stable in a magnesium matrix and also exhibits a good interface thus convincingly confirming the existence of good diffusion bonding between the two elements.

Case B Samples

Microstructural results confirmed that good wetting of the reinforcement existed in the various samples. This can be observed in terms of the increase in the yield strength, ultimate tensile strength and hardness. Presence of stiffer reinforcement results in a decrease in the thermal expansion and ductility of the metallic matrix which follows the general characteristics of metal matrix composites as explained in previous chapters. Extremely limited interfacial reaction was observed in the interface between the reinforcement wire and the matrix (see Fig. 8.3 (a) and (b)) and was confirmed using XRD based measurements shown in Fig. 8.5. The interfacial integrity between wire and the matrix was assessed in terms of interfacial debonding and presence of voids in the composite sample. However, high magnification of the Al-Fe interface showed (Fig. 8.3 (b)) cracks and debonding to some extent. XRD conducted on the Al-Fe (Al matrix–galvanized iron wire) showed the presence of Fe and Al (see Fig. 8.5 (c) & (d)). The absence of zinc indicates either the presence of minimal and hence undetectable amount of zinc or a near-complete dissolution of zinc coating from the reinforcement wire into the matrix while processing. Based on the binary phase diagram [164] Al-Fe binary system can form intermetallics such as Fe_3Al, FeAl, $FeAl_2$, Fe_2Al_5, and $FeAl_3$, which requires a minimum temperature of 1102^{o}C for compound formation. In the present study, the process temperature did not exceed 750^{o}C and hence chances of this compound formation are remote. In addition, the present XRD results in Fig. 8.5 (c) and (d) confirm the absence of these compounds at the particle-matrix interface.

At the SiC particle interface with Al matrix good interfacial bond was observed (see Fig. 8.4 (d)) without any significant reaction products. But from published literature, three

possible reactions can be expected to occur as follows [165]:

$$\left\langle \begin{matrix} 4Al + 3SiC \rightarrow Al_4C_3 + 3Si \\ 4Al + 4SiC \rightarrow Al_4SiC_4 + 3Si \end{matrix} \right\rangle \quad (8.4)$$

Under the presence of oxide on the SiC particulate the following reaction can be predicted:

$$3SiO_2 + 4Al \rightarrow 2Al_2O_3 + 3Si \quad (8.5)$$

In the present study, XRD analysis did not show any obvious presence of oxides and carbides (see Fig. 8.5(b)).

The overall damping capacity of the metal matrix composite is directly related to the damping capacity of each of its constituents. Based on the damping studies of Thirumalai et al. [153], iron fibers has slightly lower loss factor of the order of 0.0009 as compared to aluminium, which has a loss factor of 0.0051, based on the present work. Also their studies showed that SiC has slightly lower loss factor of the order of 0.0026 as compared to aluminium matrix. In the present study, result show that the presence of ~ 2 % Fe wire in Al shows a damping capacity of 0.0059 which results in an increase of about 16 % when compared to the damping capacity of pure Al that has a damping capacity of 0.0051. Also damping results of 4.83 vol. % of SiC in pure Al shows similar increase in damping (refer Table 8.2). Thus addition of interconnected Fe wire in Al matrix appears to be more effective in dissipating energy when a cyclic stress is applied.

Similarly, comparison also shows that addition of SiC in the Al matrix with additional presence of interconnected Fe wire increases further the overall damping capacity. For example, 0.5 vol. % of SiC in Al along with the presence of 2 vol. % interconnected Fe wire provides a damping increase of 25 % compared to pure Al, while the sample containing only 2 % of interconnected Fe wire alone provided a damping increase of 15 %. Thus a difference of 10 % can be observed due to the additional

presence of 0.5 vol. % of SiC particulates. This can be equivalent to 3.2 vol. % of SiC particulates alone to produce such an increase in damping. Thus it can be summarized that the damping gets enhanced due to the combined presence of interconnected iron wire and SiC particulates in aluminium.

Case C Samples

Table 8.10 lists the damping factor of the various unreinforced and composite samples. Presence of 1.9 % Ge in Al shows a damping capacity of 0.0043 which results in an increase of about 46% when compared to the damping capacity of pure Al that has a damping capacity of 0.0029 (see Table 8.10). As explained in chapter 5, damping studies showed addition of SiC in pure Al similar increase in damping (refer Table 5.3). Comparison of the Al-Ge sample's damping capacity with Al-SiC system explained in chapter 5 shows that the addition of 1.9 vol. % of Ge particulates provides damping equal to that of ~10.2 vol. % of SiC particulates. Thus addition of Ge particulates in Al matrix appears to be more effective in dissipating energy when compared to SiC particulates when a cyclic stress is applied. The results are also consistent with the observations of Hinai et al. [166] made on Al-Ge alloy (Ge ranging from 2 to 20 wt. %) processed using casting route followed by forging, cold swaging and drawing. Their results of the damping capacity measured using a inverted torsion pendulum method showed that the rate of increase in damping was dramatic under the presence of cold working when the Ge additions was in the range of 0-10 wt. %, however, it marginally improves when Ge is in the range of 10-20 wt. %. They attributed the observed damping behavior to the viscous slip flow at the interface between the matrix of Al solid solution and the Ge

precipitates and due to the grain refinement and increased dislocation density following cold working of the samples.

Similarly, comparison of results in Table 8.10 shows that addition of SiC in the Al matrix with additional presence of Ge increases further the overall damping capacity and this damping improvement increases with SiC volume fraction. For example, 8.2 vol. % of SiC in Al along with the presence of 1.9 % Ge provides a damping increase of 118 % compared to pure Al, while the sample containing only 1.9% Ge alone provided a damping increase of 46 %. Thus a difference of 72 % can be observed due to the additional presence of 8.2 vol. % of SiC particulates. This can be further compared with Al-SiC damping studies explained in chapter 5, which showed that the addition of 8.2 vol. % of SiC particulates alone can only produce a damping increase of around 29%. Thus it can be summarized that the damping gets significantly enhanced due to the combined presence of Ge and SiC particulates in aluminium.

Reasons for damping enhancement

The overall damping capacity of the metal matrix composites is directly related to the damping capacity of its constituents. Generally stiff materials such as ceramics viz., silicon carbide (SiC) and alumina (Al_2O_3) and metals viz., iron and titanium possess a lower damping loss factor than the metallic materials such as Al and Mg (see Fig. 2.6 (b)). For example, SiC has a slightly lower loss factor, of the order of 0.0026, when compared to magnesium, which has the loss factor of the order of 0.0035. Similarly, the damping capacity of titanium is 0.003 [18], and iron fiber is 0.0009 [153], which is less than the

damping capacity of Mg and Al. Hence the observed enhancement can be attributed to various interfaces that exist between the various phases within the composite material.

The reasons for the damping enhancement discussed in chapters 5, 6 and 7, is thus applicable for the present set of samples. Fig. 8.6 shows that stiffer material has generally lower thermal expansion than the ductile metallic matrices. Thus using equation (5.2) the plastic zone volume fraction in each sample was estimated and accordingly listed in Table 8.9, 8.2 and 8.10 for case A, B, C, samples, respectively. Hence in the present tested samples high residual stresses are expected that arise due to the thermal cooling from the process temperature to room temperature. Additionally, the presence of plastic zone can be observed indirectly, by measuring the hardness at the particle-matrix interface. In the present study, microhardness measurements were conducted at the Al-SiC interface for the various composite samples and the results are listed in Tables 8.6, 8.2 and 8.7 for case A, B and C, respectively. The results revealed that the interface hardness of the composite sample was significantly higher when compared to the matrix

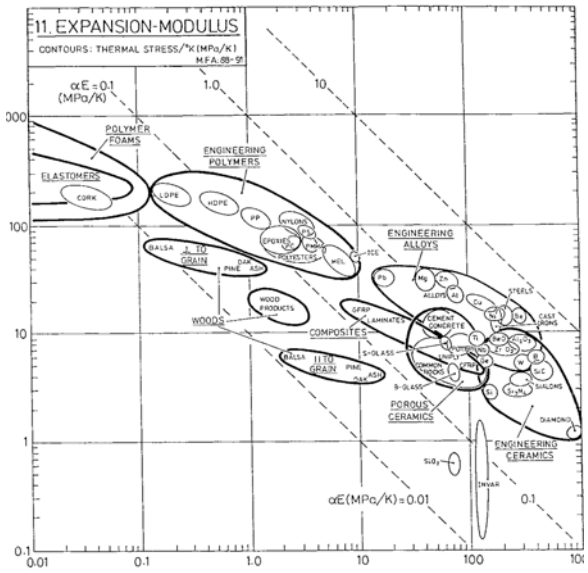

Fig. 8.6 Ashby's map showing variation of damping loss factor against the thermal expansion for various engineering materials [8].

hardness of the composite sample which indirectly confirms the presence of the plastic zone that exists around the particles and contributes in the form of strain hardening of the ductile matrix.

For Al-SiC and Al-Ge, the thermal mismatch strain during cooling is found to be typically 0.71% and 0.65%, respectively, during cooling from 350^{o}C to room temperature, which can produce a high dislocation density at the interface when the Burgers vector (b) of Al is assumed to be 0.32nm [138]. Similarly for the Mg-SiC and Mg-Ti combination, the thermal mismatch strain during cooling is found to be 0.77% and 0.63% when cooling from 350^{o}C to 27 ^{o}C which is capable to produce a high dislocation density at the interfaces (Burgers vector of Mg is ~0.3nm [138]). Thus the dislocation density is estimated and is listed in Table 8.9, 8.2 and 8.10 for case A, B, C, samples, respectively. As explained in previous chapters they are expected to enhance the internal friction based on the G-L theory's frequency dependent part, since in the present experimental setup the strain magnitude induced in the specimen is of the order of 10^{-6} at which the dislocation-based damping is mainly due to frequency dependent part [140] and is expressed as follows:

$$Q_f^{-1} = \frac{C\rho\omega^2}{b^2} \tag{8.6}$$

where C is a physical constant, ω is the vibration frequency, b is burgers vector and ρ is the dislocation density. This shows that the damping depends on the dislocation density, frequency of cyclic stress and burgers vector b of the bulk material. Thus increased density of dislocation (see Tables 8.9, 8.2 and 8.10) due to presence of SiC particulates in the aluminium matrix causes increased damping characteristics in the MMC.

Energy dissipation also occurs at the grain boundaries due to their sliding behavior in a viscous manner under a shear stress field at high temperature ranging from 200-300 ^{o}C [22]. In the present study, grain size reduction was observed (see Table 8.1, 8.2 and 8.3, respectively) due to the presence of reinforcement which can give rise to enhanced grain boundary related damping but in the present work experiments were conducted at room temperature and hence grain boundary related damping can be presumed to be insignificant [22]. The increase in the residual plastic zone, dislocation density and reduction in grain size also leads to increase in the yield strength change similar to that of the hardness increase. Thus the changes in the mechanical properties can be seen as a confirmation to the predicted microsturctural changes within the material.

8.4 Summary

Based on three sets of samples, following conclusions may be drawn:

In general, the free-free beam type flexural resonance method can successfully be used with circle-fit approach to measure the damping characteristics of the hybrid metal based composites.

Case A: The damping of pure magnesium is significantly enhanced by the presence of sub-micron size particulates of SiC alone and by the joint presence of titanium and sub-micron SiC particulates. An increase in damping with an increase in the weight/volume percentage of SiCp gets further enhanced with the presence of Ti particulates. This is attributed to an increase in energy dissipation. The energy dissipation is attributed to the concurrent and mutually interactive influences of: (a) an

increase in volume percentage of plastic zone, and (b) a local increase in dislocation density.

Case B: The damping capacity of pure aluminium can be significantly enhanced by the individual presence of interconnected iron wire and SiC particulates or by the combined presence of both types of reinforcement. The enhanced energy dissipation can primarily be attributed to the microstructural changes such as increased plastic zone and grain size reduction.

Case C: The damping of pure aluminium can be significantly enhanced by the presence of germanium alone or by the coupled presence of germanium and silicon carbide particulates. An increase in damping with an increase in the weight/volume percentage of SiC particles gets enhanced with the presence of Ge particles which can be attributed to a progressive increase in the energy dissipation. The energy dissipation can primarily be attributed to the simultaneous influence of increase in volume percentage of plastic zone and increase in dislocation density.

Related Publications:

[1] N. Srikanth, S. Ugandhar, M. Gupta, T. S. Srivatsan, *Advanced Engineering Materials*, Vol. 7, 2005, pp.735-743.

[2] S. Ugandher, N.Srikanth, M. Gupta, S.K.Sinha, *Advanced Engineering Materials*, vol. 6, 2004, pp.957-964.

[3] N. Srikanth, M. Gupta, *J. of Engineering Materials and Technology*, vol.127, 2005, pp.289-294.

Chapter 9

Numerical Modeling of Plastic Zone Induced Damping in PRMMCs

9.0 Introduction

Literature review shows finite element method is a useful numerical tool capable of predicting the thermophysical properties of metal matrix composites [167-170]. Research findings of Xu et al. [171] and Wang et al. [172] have been successful in studying the plastic energy dissipation in metal matrix composites at high strain amplitudes. Their model was based on an elastic-plastic model and did not take in to account the residual stresses in the composite. Hence their prediction at low strain amplitude showed insignificant damping capacity for the MMC which is contrary to experiment results. At high strain amplitude due to constrained behavior at the metal-particulate interface the metallic matrix yields and hence their model could predict significant damping. Hence in the present study, presence of residual stresses in the metal matrix composites, when cooling down from the extrusion temperature to room temperature, which is well established by experiments [171], have been accounted in the energy dissipation studies of the composite.

Considering the significant potential of aluminium due to its higher specific stiffness along with excellent castability and machinability, this chapter focuses on the enhancement of the damping capacity of Al due to the presence of stiff reinforcement such as SiC, Ti and Ge particulates. The theoretical predictions are made using a finite element method (FEM) based unit-cell model (UCM) that uses a rate-dependent based plasticity model. The numerical predictions were further validated using experimental results obtained from suspended beam technique coupled with circle-fit approach listed in the previous chapters. In addition, the present study also addresses the applicability of the UCM to study the effect of process-induced defects such as voids, particulate breakage

and metal-ceramic interface de-bondage on the overall damping capacity of the composite.

9.1 Finite Element Method

Finite Element Method is an efficient tool to analyze particulate dispersed metal matrix composites due to its modelling capability of the particulate. FEM is one of the tools, which has the distinct advantage to model more closely to the exact geometry. Secondly, it has the advantage to model the various material properties in the geometry as well as the anisotropy of the individual phases. Thirdly, it can model the exact fixity and the load conditions on the specimen [5].

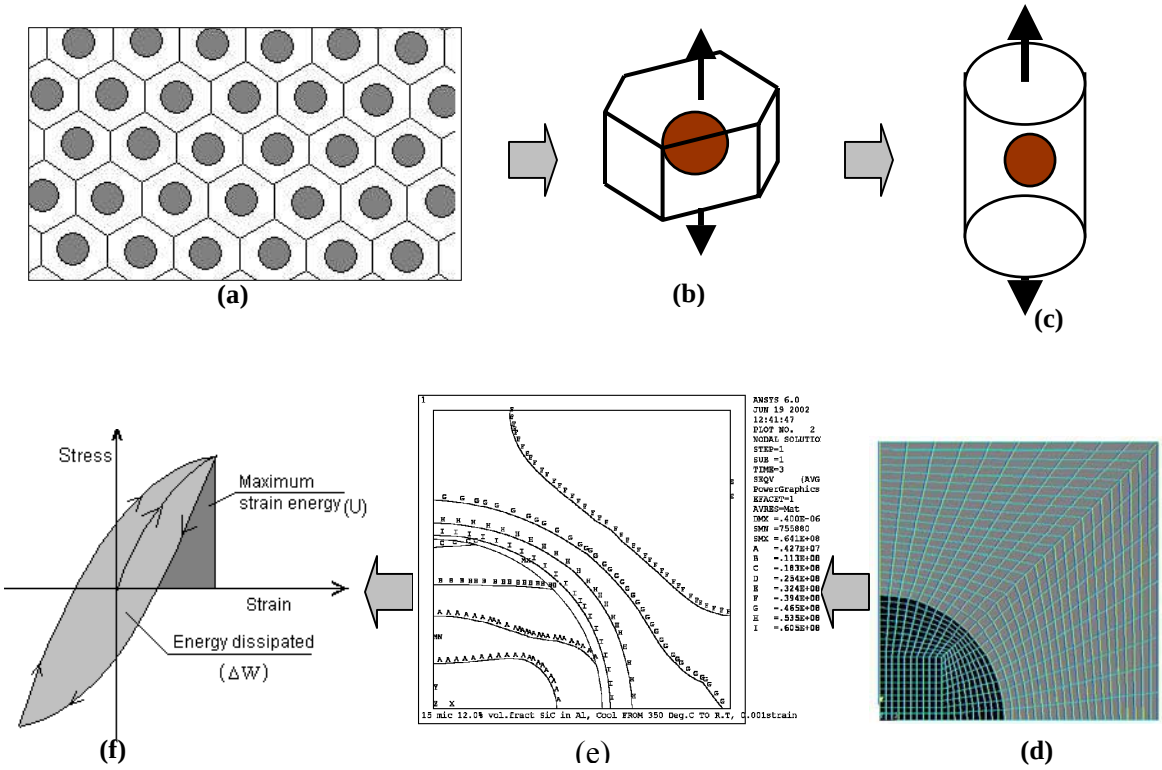

Fig. 9.1 Methodology for deducing a simplified FEM model for the PRMMC: (a) hexagonal representation of a particulate reinforced MMC, (b) unit hexagonal cell, (c) approximated cylindrical unit cell, (d) axisymmetric FEM model of the cylindrical unit cell, (e) equivalent stress contour plot and (f) hysterisis curve.

Mostly FEM has been successfully used in analyzing continuous and dis-continuous reinforced composites. In the present work, a cell model approach is adopted to study the energy dissipation capability of the particulate reinforced composites. The composite material was idealized in terms of periodic array of identical hexagonal cylindrical cells, shown in Fig. 9.1 (a), with the SiC reinforcement located in the center of each cell. Axisymmetric cylindrical cells, which can be regarded as approximations to the three-dimensional array of the hexagonal cylindrical cells [167-171], were used in the calculation (see Fig. 9.1 (c)).

9.2 Unit Cell Model

Exact micro-mechanical modelling of a two or more phase composite material is very complicated due to the geometric size and shape of the individual phases. Hence unit cell models have been designed and successfully used by a number of researchers, including Llocra et al. [167], Bao et al. [168], and Shen et al. [169] to calculate the thermo-mechanical properties of composites. These models were successfully used to predict results similar to more rigorous and computationally more intense three-dimensional models. In the present study, an axi-symmetric cell model similar to Bao et al. [168] is chosen to model a particulate reinforced metal matrix composite. This limits the particulate shape to axially symmetric in nature such as a sphere, cylinder, or an ellipsoid and provides the convenience to analyze the 3D model as a 2D axi-symmetric model, which results in high accuracy with least computer resource. The unit cell model for a spherical particulate is shown in Fig. 9.1 (d). Cylindrical coordinates are defined so that r represents the radial direction and z represents the axial direction of the cylinder. In

the present study, the particulate is assumed to be a spheroid, which occupies the region $r^2+z^2 \leq R^2$, where R is the particulate radius. The particulate is placed at the exact center of the metal matrix cylinder with a radius L and length 2L. The dimensions of the cylinder are so chosen so as to satisfy the required volume fraction of the reinforcement in the composite under study. The reinforcement volume fraction was taken as the ratio of the reinforcement volume to the cell volume. The aspect ratio of the cell, the ratio of the height of the cylinder to its diameter, was taken to be the same as that of the reinforcement. The cylindrical surface is constrained to remain cylindrical but can move in or out with zero average normal traction. The faces perpendicular to the direction of stressing also remain planar with zero shear traction and a sinusoidally varying normal stress. Before applying such a cyclic load, the UCM was subjected to thermal cooling from extrusion temperature to room temperature to account for the residual stress in the subsequent calculations.

The ANSYS^{TM} code was employed using 8-noded viscoplastic (Visco108) elements to solve the boundary value problem formulated above [173]. Fig. 9.1 (a) to (f) shows the overall modeling methodology of particulate reinforced metal matrix composites.

9.3 Constitutive Behaviour of Viscoplastic Metallic Matrix

The maximum temperature experienced by the SiC particulate, during extrusion process, is significantly below the melting temperature, hence we assume that the particulate obeys a thermoelastic material behavior. However, for the aluminium matrix the extrusion temperature corresponds to a homologous temperature equal to 0.67 during

extrusion process. In the previous study of Xu et al. [171] and Wang et al. [172], the matrix was assumed as elasto-plastic and without any process induced residual plastic strain. While in the present study, the metallic matrix is assumed to be an thermo-elasto-viscoplastic material behavior, whose state is described by a structural parameter s, in addition to the stress σ and temperature T, to account for the isotropic work-hardening and recovery [174].

To specify the constitutive equation of the metallic matrix, the rate-dependent plasticity (or viscoplasticity) is characterized by the irreversible straining that occurs in the material over time. The plastic strains are assumed to develop as a function of the strain rate. Here we present the rate-dependent model developed by Anand [174]. This rate-dependent model differs from the rate-independent model in that there is no explicit yield condition, and no loading/unloading criterion is used. Instead, plastic flow is assumed to take place at all non-zero stress values, although at low stresses the rate of plastic flow may be immeasurably small. The total strain rate tensor D is the sum of the elastic strain rate tensor D^e , thermal strain rate tensor D^{th} (which is equal to $T^{\bullet}\alpha_m(u)$, where (u) is the second-order unit tensor and T is the temperature and the dot in the superscript refer to the rate of change with time), viscoplastic strain rate tensor D^p , as follows:

$$D=D^e+D^{th}+D^p \tag{9.1}$$

The viscoplastic deformation is assumed to be isochoric process (i.e. volume is constant). Based on small strain theory [174], the evolution equation for the cauchy stress σ is given as follows:

$$\sigma^{\bullet} = 2\mu_M\left(D - D^p\right) + (K_M - 2\mu_M/3)\left(trD\right)(u) - 3K_M\alpha_M T^{\bullet}(u) \tag{9.2}$$

where μ_M and K_M are the elastic shear and bulk moduli of the metallic matrix. The viscoplastic strain rate is related to the stress deviator σ' as follows:

$$D^p = 3\sigma' d^p / 2\bar{\sigma} \tag{9.3}$$

where, d^p is the equivalent plastic strain rate and $\bar{\sigma}$ is the von-mises equivalent tensile stress in terms of deviatoric stress σ' as follows:

$$\bar{\sigma} = (\frac{3}{2}\sigma' : \sigma')^{0.5} \tag{9.4}$$

Further, the equivalent plastic strain rate, which is determined by the consistency condition in the rate-independent model, needs to be prescribed by an appropriate constitutive function. The specifics of this constitutive equation are the flow equation:

$$d^p = Ae^{-Q/R\theta}\left[\sinh\left(\bar{\sigma}\xi / s\right)\right]^{1/m} \tag{9.5}$$

where A is the pre-exponential factor, θ is the absolute temperature, R is the universal gas constant, Q is the activation energy, m is the strain rate sensitivity index, ξ is multiplier of stress, and s is the structural parameter which corresponds to the evolution of the deformation resistance and is given in the rate form $\left(s^{\bullet}\right)$ as follows:

$$s^{\bullet} = \left[h_o\left(|B|\right)^a \operatorname{sgn}\left(B\right)\right] d^p \tag{9.6}$$

where h_o is hardening constant, a is the strain-rate sensistivity index for both hardening and softening and sgn (B) refers to the sign of the parameter B which is a function of s as follows:

$$B = 1 - s / s^* \tag{9.7}$$

where s^* refers to the saturation value of deformation resistance which is expressed as follows:

$$s^* = \hat{s}\left[\frac{d^p}{A}\exp\left(Q/R\theta\right)\right]^n \tag{9.8}$$

where $\hat{s}$ is the coefficient for deformation resistance saturation value, n is the strain rate sensitivity parameter of saturation (deformation resistance) value. Equation (9.6) allows to model for both strain hardening and strain softening material behaviours. Based on the works of Brown et al.[175], for most of the common deformation the static recovery phenomena is negligible and hence neglected in the above formulation.

9.4 Numerical Implementation

Based on the above model along with a consistent stress update procedure, which is equivalent to the Euler backward scheme to enforce the consistency condition, analysis was conducted. The evolution equation (9.6) at the end of the time step and the rate-dependent and rate-independent plasticity are computed accordingly [173]. Further, the plastic work done E_e^{Pl} in each element is computed for each time step as follows:

$$E_e^{Pl} = \sum_{i=1}^{NINT}\sum_{j=1}^{NCS}\{\sigma\}^T\left\{\Delta\varepsilon^{pl}\right\}vol_i \tag{9.9}$$

where NINT and NCS refers to the number of integration points within the element and number of iterations, respectively, parameter vol_i refer to the volume of i^{th} element, $\{\sigma\}$ is the stress vector, $\left\{\varepsilon^{el}\right\}$ is the elastic strain and $\left\{\Delta\varepsilon^{pl}\right\}$ is the plastic strain increment. A program was written using Ansys Parametric Design Language (APDL) [173] to calculate the accumulated plastic energy (ΔW) in one stress cycle. The maximum strain energy was computed using the predicted values of the elastic modulus of the MMC,

E_{mmc}, and the maximum stress amplitude, σ_{max} , and the volume of the unit cell, v, as follows:

$$U = \frac{\sigma_{max}^2}{E_{mmc}} v \qquad (9.10)$$

The accumulated plastic energy and the maximum strain energy were further substituted in equation (2.5) to deduce the damping loss factor.

9.5 Results From Numerical Predictions

9.5.1 Al-SiC System

The unit cell model proved to be a proper idealization of the particulate reinforced MMC. The model assumed Al as the metallic matrix and SiC as the reinforcing particulates. The elastic modulus and thermal expansion coefficient of aluminium was taken as 69.4 GPa and 25.89×10^{-6} per.deg. C, respectively, based on the present study. The elastic modulus and thermal expansion coefficient of SiC particulates were assumed to be 410 GPa and 4.3×10^{-6} per. deg. K, respectively [171]. The Poisson's ratio of aluminium and SiC was taken to be 0.3 and 0.25, respectively [176]. The metallic matrix (Al-1100-O) was assumed to obey Anand viscoplastic material model for which the material constants were assumed as $A = 1.91 \times 10^7$ sec^{-1}, $\xi = 7.0$, $m = 0.23348$, $s_o = 18$MPa, h_o=1115.6 MPa, $Q/R_g = 21090$ K, $\alpha = 1.3$, $n = 0.07049$ and $\hat{s} = 18.9$ MPa [174].

The cooling rate adopted to predict the thermally induced residual stress was 100 deg. C/ sec [176]. The unit cell was made corresponding to a spherical particulate of size 15μm inside a cylindrical metallic matrix with an length to diameter ratio of 1 and a

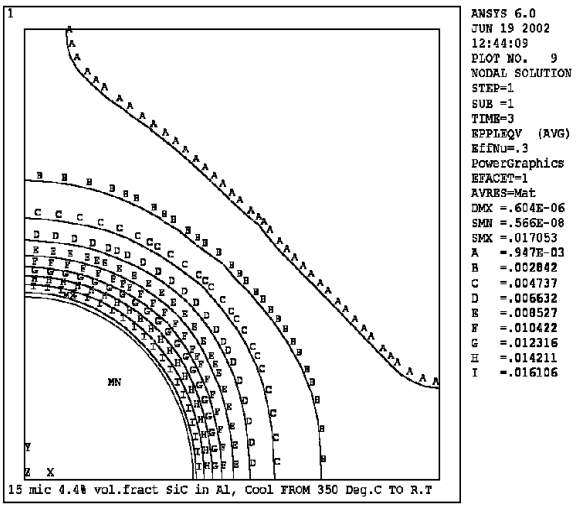

(a)

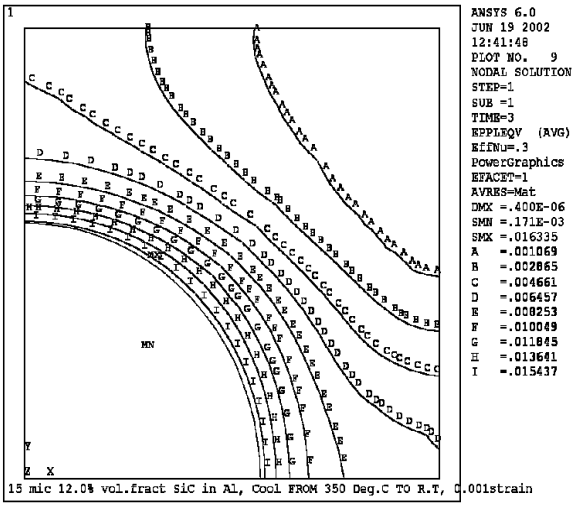

(b)

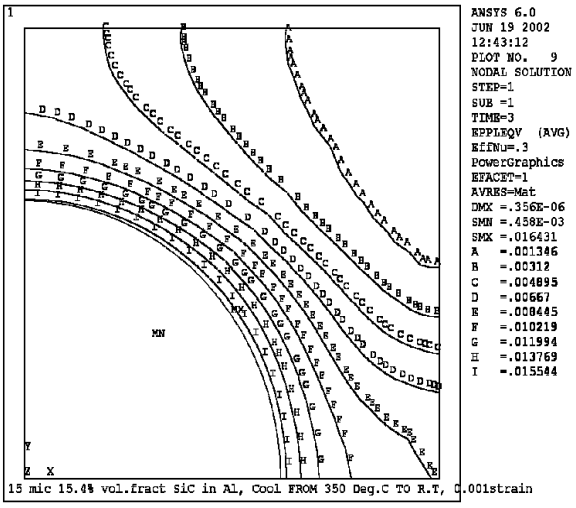

(c)

Fig. 9.2 Equivalent plastic strain plot in the unit cell model containing particulates with: (a) Al- 5.2 wt. % SiC (b) Al- 13.9 wt. % SiC and (c) Al- 17.7 wt. % SiC.

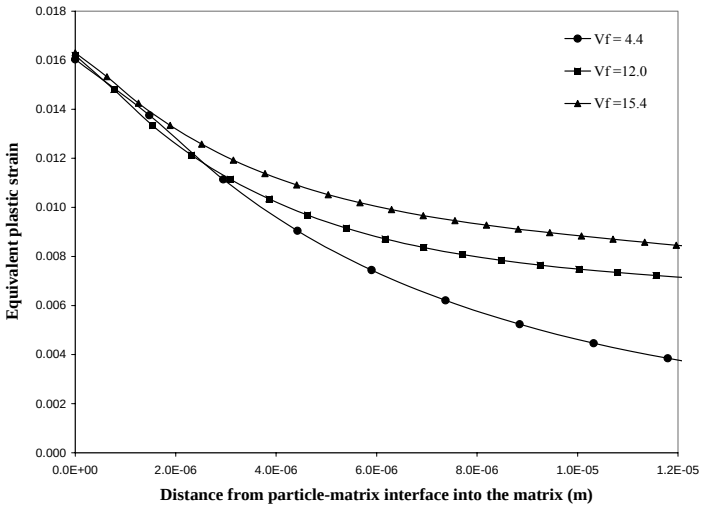

(a)

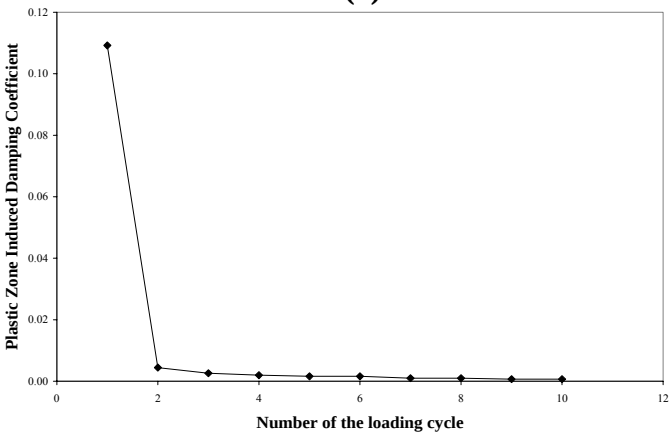

(b)

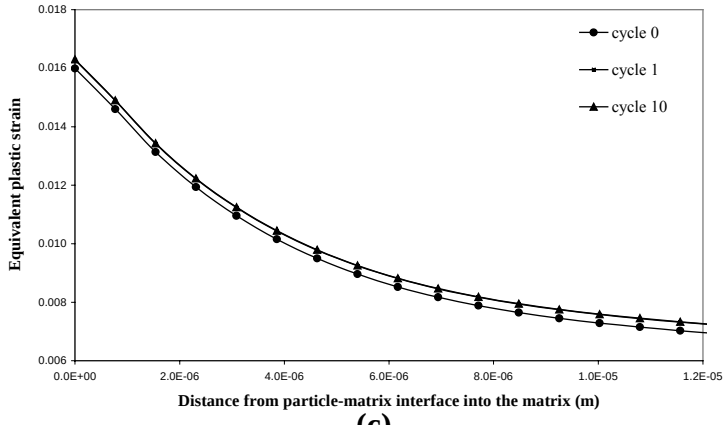

(c)

Fig. 9.3 UCM predicted results: (a) Variation of equivalent plastic strain plot along the radial direction for different volume percentage of SiC in the Al matrix, viz., 4.4 %, 12.0% and 15.4% (b) Variation of plastic zone induced damping loss factor with the number of the loading cycle in the Al- 13.9 wt. % SiC (c) Variation of equivalent plastic strain plot along the radial direction for different loading cycle in the Al- 13.9 wt. % SiC.

volume modeled such that the volume fraction of particulate to the matrix is maintained at similar to that of experimental result, shown in Fig. 9.1(d). To begin with, the model was used to predict the residual plastic zone due to cooling from extrusion temperature (which is around 350 deg.C) to room temperature. Figures 9.2 (a) to (c) are the contour plots showing the residual plastic strain present corresponding to the three experimental MMC samples. Figure 9.3 (a) plots the variation of the equivalent plastic strain along the radial distance from the metal-ceramic interface into the matrix. Next on top of the residual stress the model was subjected to a tensile cyclic load with a maximum stress amplitude of 10KPa and a time period of 1 second. From the computed results, the total energy dissipated in one cycle ΔW as well as the maximum strain energy U was deduced. Using these values, the damping loss factor was calculated using equation (2.5) and the results are shown as a bar chart in Fig. 9.4(a). Furthermore, the analysis was repeated under the absence of residual stress condition to understand the effect of thermal cooling on the energy dissipation capability, which showed negligible energy dissipation similar to the studies of Wang et al. [172].

Next to understand the effect of particulate shape, the spherical particulate was varied to an ellipsoid, cylinder, double cone and a truncated cylinder, shown in Fig. 9.5(a). Fig. 9.6 shows the plastic strain variation due to particle shape variation which helps to understand the effect of stress concentration and aspect ratio of the particle.

Finally, the unit cell model containing 12 volume percentage of SiC was used to study the different types of process induced defects individually, such as voids, particulate-matrix debond and particulate breakage, illustrated in Fig. 9.5(b), and described as follows:

- To understand the effect of particulate breakage, the spherical particulate was modelled as two broken pieces with no force transmitting capability in between.
- To understand the effect of particulate debonding the interface between the spherical particulate and the spherical cavity of the matrix is modelled with contact elements [173] with a friction coefficient of 0.3. This enables normal hydrostatic forces to be passed to the particulate from the matrix and vice-versa while the shear stress obeys the coulombs law of friction [5]. Thus the energy dissipated due to rubbing at the interface during sliding is also taken into account.
- To understand the effect of void, a spherical void of 0.0077 volume fraction was added to a 12 volume percentage of SiC. The void was placed at the axis of the unit cell model above the SiC particulate to achieve axis-symmetry in the model.

Fig. 9.7 shows the plastic strain contours due to the above defects with the unit cell. Further to understand the effect of the strain amplitude of the applied sinusoidally varying stress, the analysis was repeated on a fully bonded Al-12 vol. % SiC sample. The maximum strain energy and energy lost within one cycle were predicted and the overall damping loss factor was computed for the different strain amplitude which are plotted in Fig. 9.8.

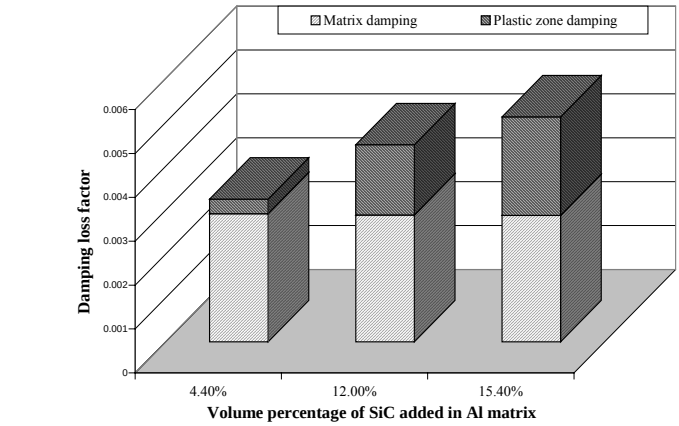

(a)

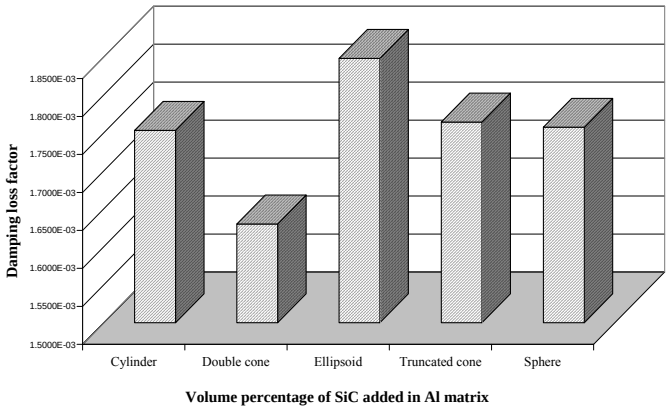

(b)

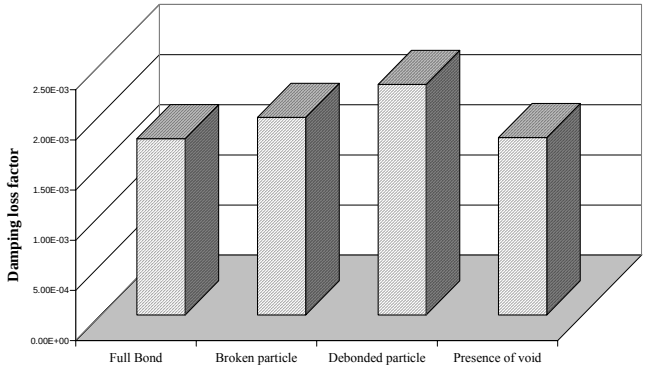

(c)

Fig. 9.4 (a) Variation of FEM predicted damping loss factor with respect to volume fraction of SiC in Al matrix. (b) Comparison of FEM predicted damping loss factor for different particulate shapes. (c) Comparison of FEM predicted damping loss factor for different process induced defects.

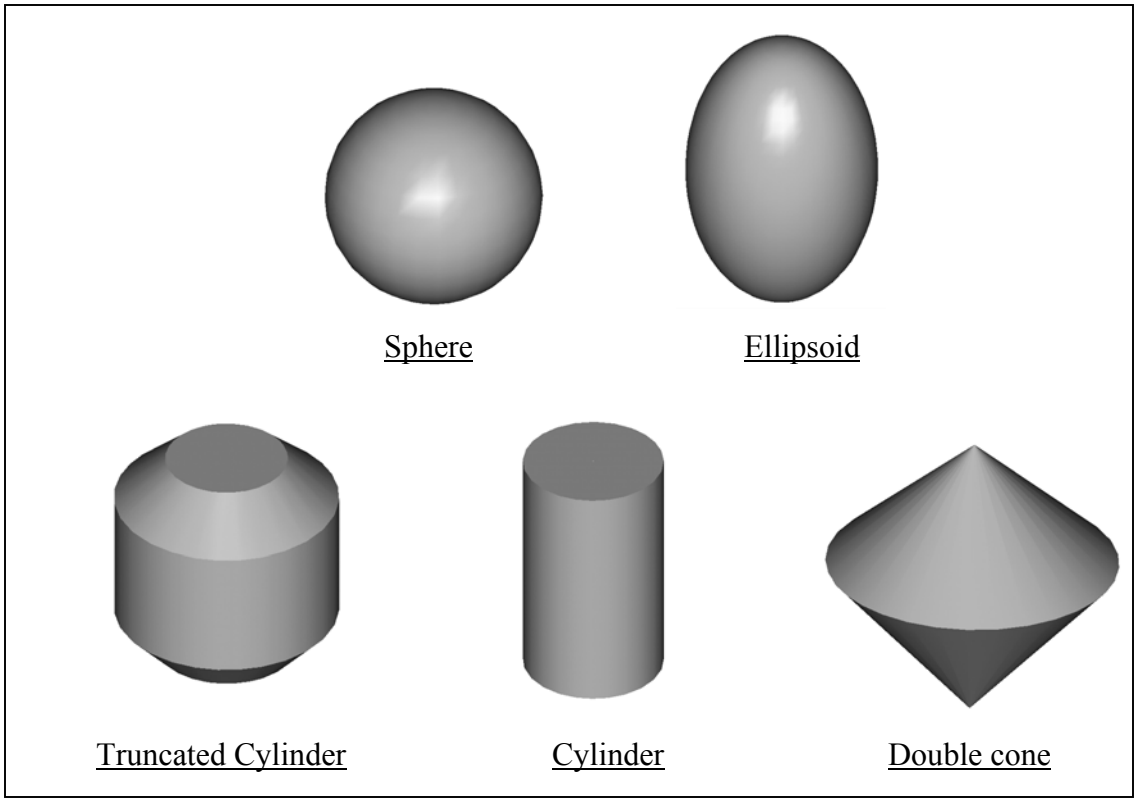

(a)

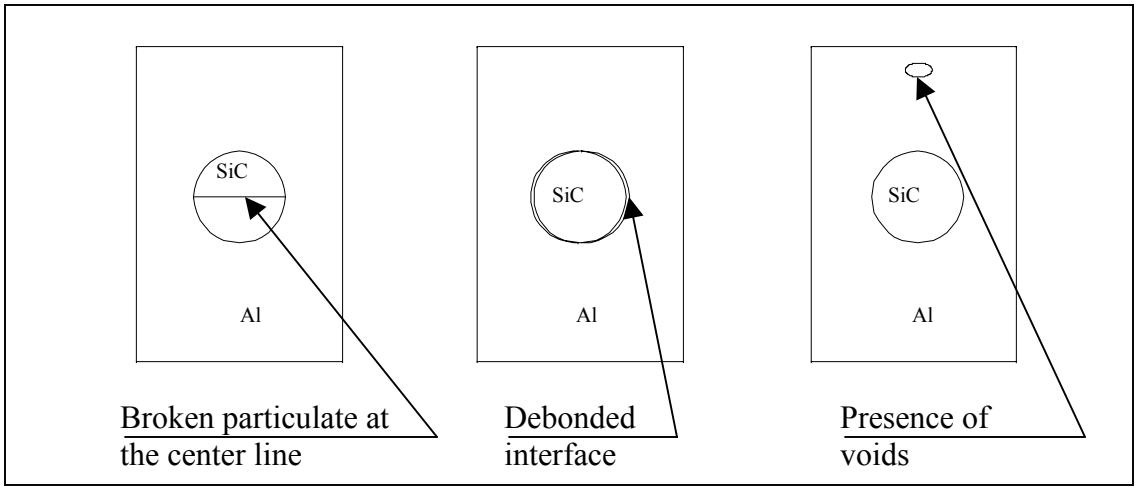

(b)

Fig. 9.5 (a) Particulates of similar volume but with different shape morphologies. (b) Process-induced defects assumed to study their effects on the overall energy dissipation.

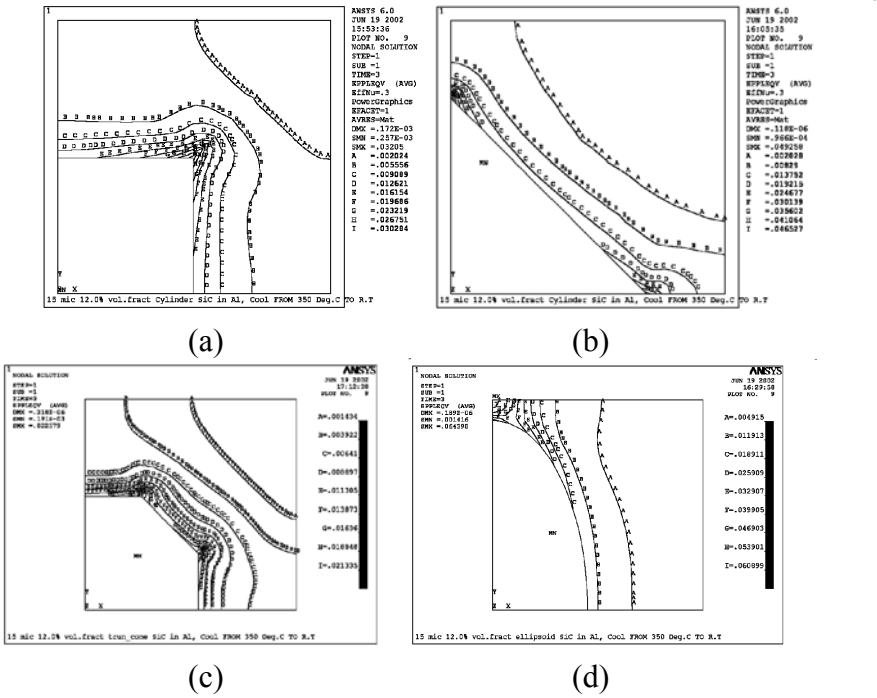

Fig. 9.6 Equivalent plastic strain plot in the unit cell model containing particulates with: (a) spherical shape (b) double cone shape (c) cylindrical shape and (d) ellipsoidal shape with an aspect ratio of 2.

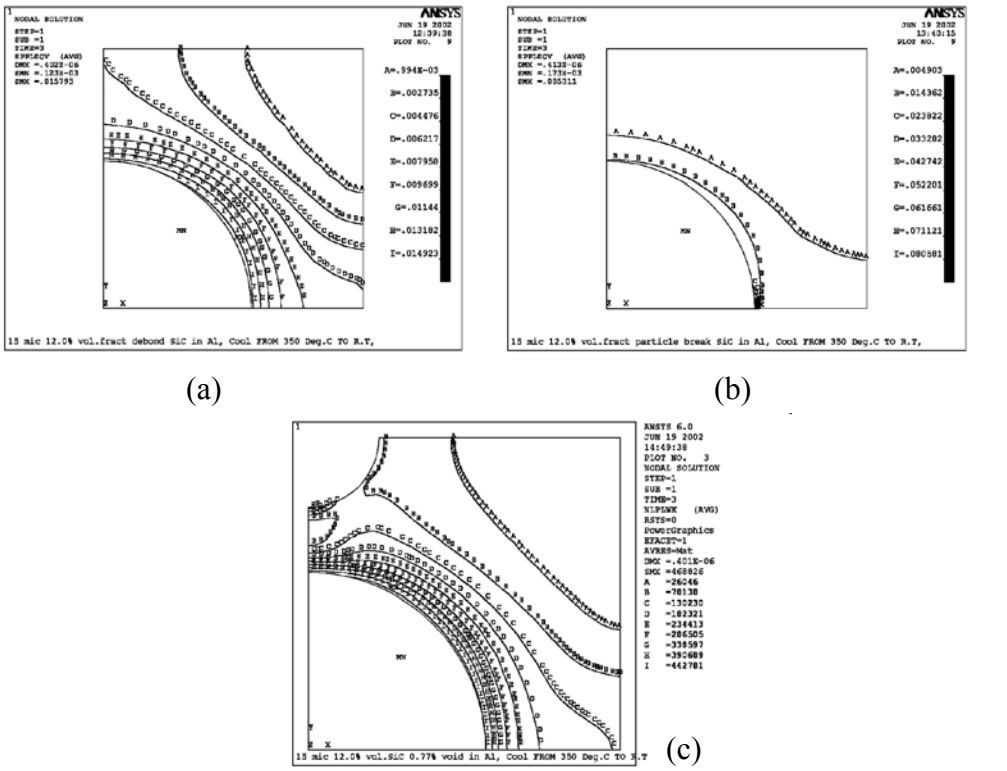

Fig. 9.7 Equivalent plastic strain plot in the unit cell model under the presence of: (a) debonded metal-particulate interface, (b) a broken particulate along the central half plane (at y=0), and (c) void of 0.77 volume percentage.

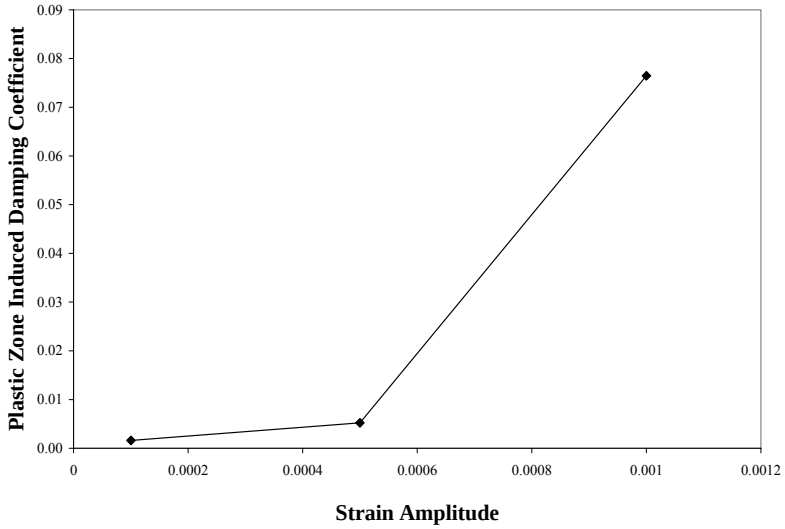

Fig. 9.8 Variation of plastic zone induced damping coefficient with strain amplitude.

9.5.2 Al-Ti System

To understand a stiff metal reinforcement in a ductile metallic matrix Al-Ti system was taken due to the encouraging results obtained in chapter 6. The unit cell model assumed Al as the metallic matrix and Ti as the reinforcing particulates. The elastic modulus and thermal expansion coefficient of aluminium and titanium were taken to be temperature dependent as shown in Fig. 9.9. The Poisson ratios of aluminium and titanium were taken to be 0.3 and 0.361, respectively [147]. The metallic matrix (Al-1100-O) was assumed to obey the Anand viscoplastic material model for which the material constants were assumed as $A = 1.91 \times 10^7$ sec^{-1}, $\xi = 7.0$, $m = 0.23348$, $s_o = 18$MPa, $h_o = 1115.6$ MPa, $Q/R_g = 21090$ K, $\alpha = 1.3$, $n = 0.07049$ and $\hat{s} = 18.9$ MPa [177]. Based on the experiment results of Lennon and Ramesh [178], the Ti particulate's stress-strain behavior under various temperatures and strain rates is modeled using a multi-linear isotropic material model [173].

The cooling rate was taken to be 100 deg. C/ sec and the unit cell was made corresponding to a spherical particulate of size 5μm inside a cylindrical metallic matrix

with a length to diameter ratio of 1 and a volume modelled such that the volume fraction of particulate to the matrix is maintained similar to that of the experimental result, shown in Fig. 9.1(d). To begin with, the model was used to predict the residual plastic zone due to cooling from extrusion temperature (which is around 350 deg.C) to room temperature. Figures 9.10 (a) to (c) are the contour plots showing the residual plastic strain present corresponding to the three experimental MMC samples. Figure 9.11(a) plots the variation of the equivalent plastic strain along the radial distance from the metal-ceramic interface into the matrix. Next on top of the residual stress the model was subjected to a tensile cyclic load with a maximum strain amplitude of 0.0001.

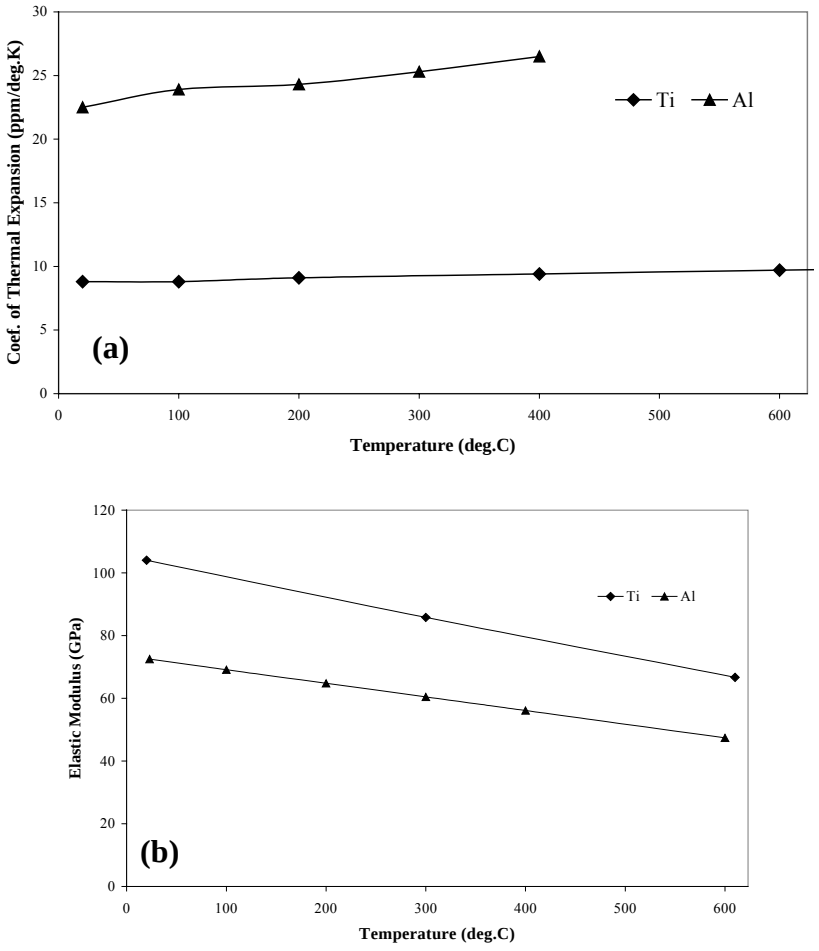

Fig. 9.9 Variation of aluminium and titanium properties with temperature: (a) coefficient of thermal expansion and (b) elastic modulus.

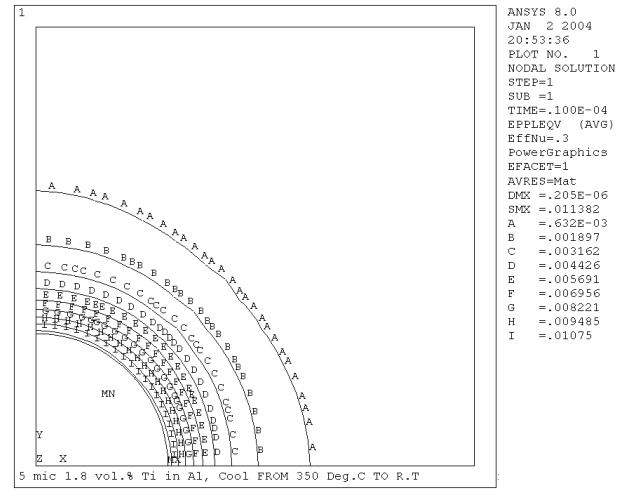

(a)

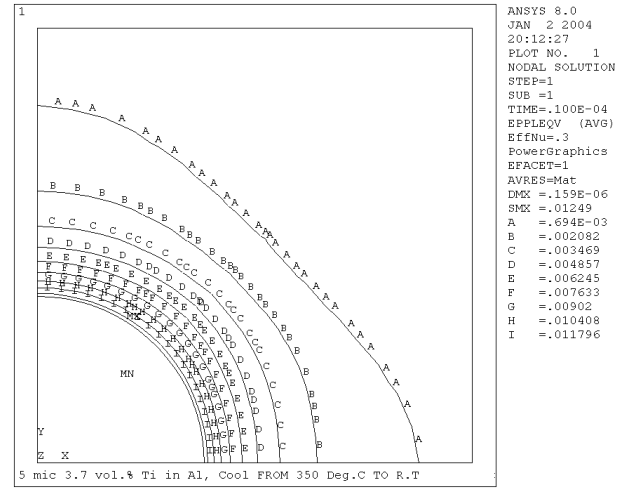

(b)

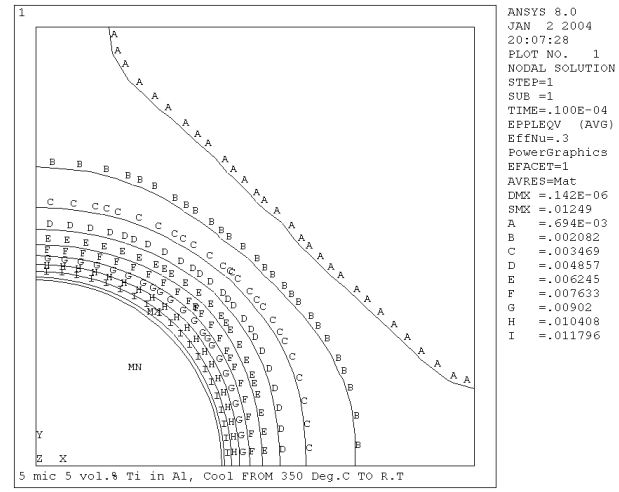

(c)

Fig. 9.10 Equivalent plastic strain plot in the unit cell model containing particulates with: (a) Al- 3.3 wt. % Ti, (b) Al- 6 wt. % Ti and (c) Al- 7.5 wt. % Ti.

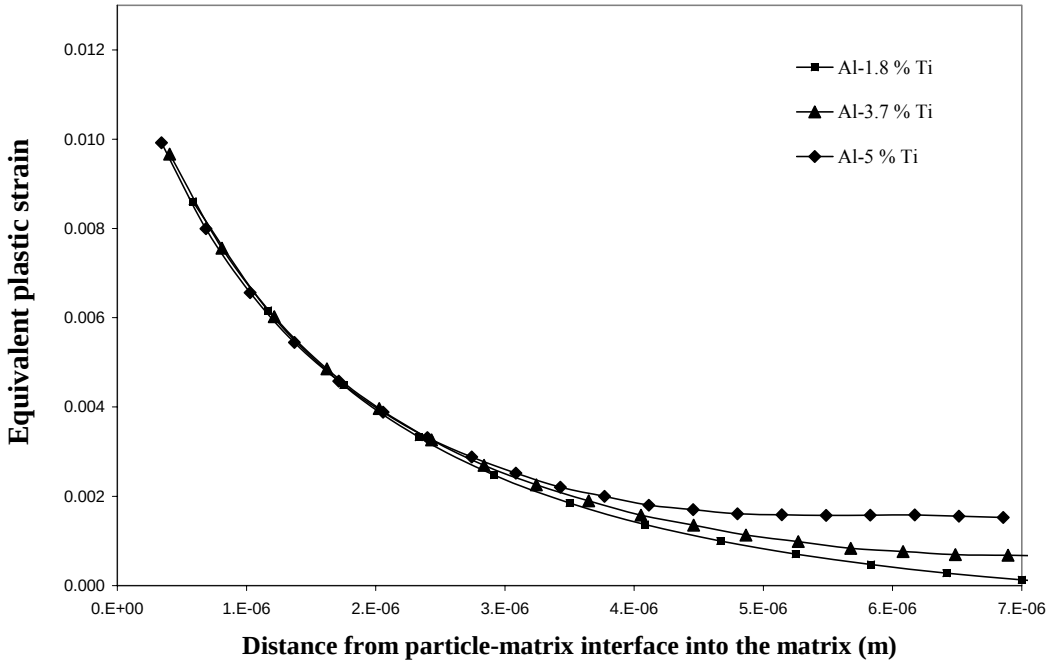

(a)

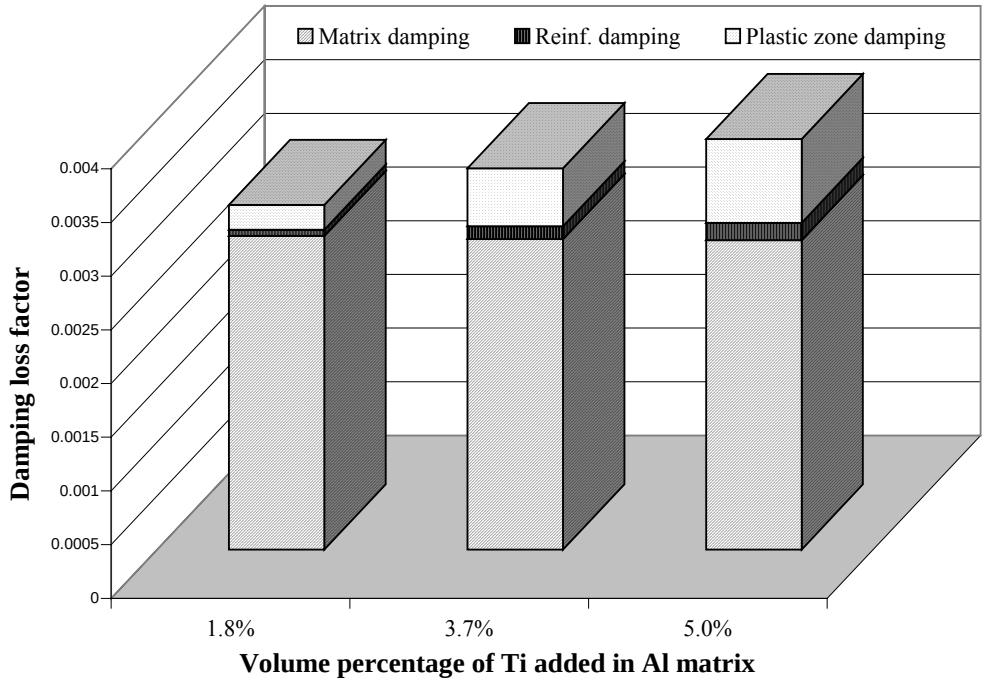

(b)

Fig. 9.11 Plots showing variation of: (a) equivalent plastic strain in the unit cell model along the radial direction and (b) computed damping loss factor for different weight percentage of Ti in the Al matrix, viz., 3.3 %, 6% and 7.5%.

9.5.3 Al-SiC-Ge System

Similar to the Al-SiC system, a unit cell was made to study the Al-SiC-Ge system. A spheroid type shape was assumed for the SiC and Ge particulate since it provides the lower bound of residual plastic zone as was observed in the Al-SiC system. Two compositions were built which corresponds to the composites viz., Al-1.9Ge and Al-1.8Ge/2.9SiC. A rate dependent viscoplastic material model was used for the Al metal matrix (melting point ~ 660^{o}C) similar to the Al-SiC and Al-Ti system to account the temperature and strain-rate dependency of flow stress and thus accurately predict the residual plastic zone at the matrix-reinforcement interface. Based on the microstructural studies of the composite samples, SiC and Ge were found to be stable due to their high melting point of 2827^{o}C and 936^{o}C, respectively, which are well above the extrusion temperature of 350 ^{o}C [151]. Hence relatively the SiC and Ge can be assumed to exhibit elastic material behavior. A spheroid type shape was assumed for the SiC and Ge particulate since it provides the lower bound of residual plastic zone. Figure 9.12 (a) and

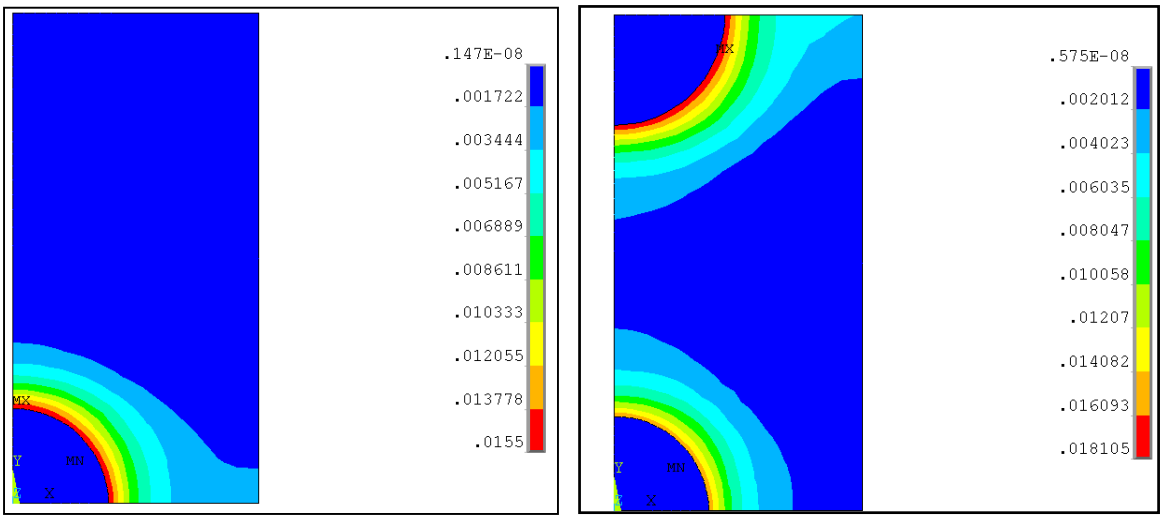

(a) **(b)**

Fig. 9.12 Equivalent plastic strain contour plot in the unit cell model containing composition equivalent to: (a) Al- 1.9 vol. % Ge (b) Al-1.8 vol. % Ge /2.9 vol. % SiC.

(b) shows the equivalent plastic strain (EQPLST) contours for the two different compositions. Next on top of the residual stress the model was subjected to a tensile cyclic load with a maximum strain amplitude of 0.0001 and a time period corresponding to the specimen resonant frequency of 2500Hz was applied. From the computed results, the total energy dissipated in one cycle ΔW as well as the maximum strain energy U was deduced. Using these values, the damping loss factor was calculated.

9.6 Discussion

Considering the MMC as a multiphase system, the mechanical loss can be written as the sum of the contributions from the particulates, the general metallic matrix far from the matrix-particulate interface and the micro-plastic zone around the reinforcement, which are denoted with the subscript r, m, and zp, respectively as follows:

$$\eta_{mmc} = \tan\phi \approx \eta_r + \eta_m + \frac{f_{zp} E_{mmc} \Delta W}{\pi \sigma_{max}^2} \tag{9.11}$$

where η_r and η_m corresponds to the damping loss factor of reinforcement and the metallic matrix, respectively, f_{zp} is the volume fraction of the microplastic zone around the reinforcement, E_{mmc} is the elastic modulus of the metal matrix composite, σ_{max} is the maximum stress amplitude and ΔW is the energy dissipated in one cycle under the presence of the micro-plastic zones. Thus it is clear from equation (9.11) that the damping loss factor increases proportionally with the plastic zone volume fraction. The FEM results from the present study can be explained by a simplistic model which is based on a elastic-perfectly plastic model [15]. The size of the plastic zone C_s predicted from the FEM can be compared against the equation (5.2).

Secondly, the deformation of essentially all metals is, to a certain extent, time-dependent. This dependence, however, becomes more pronounced at temperatures exceeding a third of the material's melting point. Hence it is termed viscoplastic material behavior, which refers to the mechanical response of solids involving time-dependent, irreversible (inelastic) strains. This can be seen as a more accurate way of predicting the energy dissipated per cycle as represented by equation (5.3). In this part of the study, ΔW was calculated using the FEM based unit-cell model which mimics a rate dependent viscoplastic model (called Anand model [16] explained in the previous section) for the aluminium matrix. In the UCM, the reinforcement such as SiC, Ti ang Ge particulates were assumed to possess a spheroid shape so as to achieve a conservative result in terms of energy dissipation and stiffness since it possess a minimum stress concentration and a unit aspect ratio. From the computed ΔW and U, the plastic zone induced damping loss factor was deduced. Fig. 9.3 (b) shows the variation of the damping loss factor due to the micro-plastic zones with the number of the loading cycle which shows that the predicted damping loss factor is significant at the first cycle and reduces significantly for the second cycle and later stabilizes for the further loading cycles. Similar observation of damping variation was seen with loading cycles in the elastic-plastic based damping studies of Xu and Schmauder [171]. This can be explained by Fig. 9.3 (c), which shows the variation of the equivalent plastic strain within the Al-SiC unit cell increases for the first cycle and strain hardens the metallic matrix, which reduces further increase in the overall plasticity with similar loading cycles.

Similarly, for Al-Ti system uniform increase in damping is observed with increase in volume fraction. Secondly, as noted earlier the Al-Ti has a lower thermal mismatch

than Al-SiC and hence the plastic zone volume fraction is less, hence the energy dissipated per cycle is less. Fig. 9.11 shows the FEM predicted damping loss factor under similar volume conditions for the three volume percentages of Ti viz., 1.8, 3.7 and 5.0. The increase in the damping loss factor with volume fraction of Ti can be explained based on equation (9.11) that the damping depends directly on the volume fraction of the plastic zone under similar loading conditions.

To study the Al/SiC/Ge two different compositions were studied as shown in Figure 9.12 (a) and (b) which describes the equivalent plastic strain (EQPLST) contours. This shows clearly that the overall plastic zone around the particulate has increased due to the combined presence of SiC and Ge particles compared to only Ge particle presence. Also the maximum value of the plastic strain at the interface has increased in the Al-1.8Ge/2.9SiC composition compared to Al-1.9Ge, from 0.0155 to 0.0181. Application of a sinusoidal load with a low strain amplitude of 10^{-6} and a frequency of 300 Hz showed that the energy dissipated in the form of plastic work by the residual plastic zone was in the order of 0.0011 and 0.0014 for Al-1.9Ge and Al-1.8Ge/2.9SiC, respectively. Thus the presence of 1.9 vol. % of Ge in Al matrix enhances energy dissipation capability compared to the monolithic Al matrix. Secondly, presence of 2.88 vol. % of SiC increases the energy dissipation capability of the Al matrix by 27% compared to the energy dissipating capacity of Al-1.9Ge composition. Thus the hybrid composite has increased energy dissipating capability than the single reinforcement type.

The drawback of the present FEM model is that it assumes a uniform inter-particulate distance, since it is based on a unit cell concept, which may not be true due to the presence of clusters in the actual experiment samples. However, the model can

account to some extent for sharp faceted particulate shapes compared to the spherical shape assumed in the previous study. Secondly in terms of the interfacial condition, the present model assumes a fully-bonded interface between the particle and the Al-matrix which may be considered as an ideal condition. However as explained in Fig. 9.5(b), it accounts for defects such as particle breakage, particle debond and partial debond etc. In reality, the experimental sample would be expected to have both bonded and debonded interfaces as well as transformation of Al to Al-SiC interfacial compounds. The later effect at the particulate-matrix interface can be expected to influence the plastic zone radius due to variation in the CTE mismatch, since the interfacial compounds (oxides, carbides, etc.) are expected to have lower CTEs compared to their parent materials. Hence the researcher can model individual defect's effect on damping and superimpose on one global model to take a overall effect on a multi-cell model. While further efforts to improve the numerical model are being made to circumvent these shortcomings, the results of the model confirms that the explanation expressed in the forms of equations (5.3) and (5.4) are able to explain the experimental observation of the various MMC samples.

9.7 Summary

Based on the systematic numerical study using the unit-cell model following conclusions can be reached:

1. The FEM based cell model used in the present study enables the determination of damping loss factor of composites due to the presence of residual plastic zones

induced due to thermal mismatch during cooling from extrusion temperature to room temperature.

2. The results matches well with experimental results obtained from impact based suspended beam experiments, which corresponds to low strain amplitude condition.
3. Numerical results also show similar increasing trend in damping loss factor with weight percentage of SiC and Ti added in the metallic matrix, consistent with the experimental observation of suspended beam experiments.
4. Effect of stress concentration due to sharp faceted particulates increases the energy dissipation capability of the metallic matrix due to the increased presence of plastic zone.
5. The present model is capable to study the effect of process induced defects such as particulate breakage, presence of void in the metallic matrix and debonding at the metal-particulate interface on the overall energy dissipation capability of the MMC. Comparison against ideally bonded condition shows that these defects increase the energy dissipation capability of the MMC.
6. An increase in damping with an increase in the weight/volume percentage of SiC particles gets enhanced with the presence of Ge particles which can be attributed to a progressive increase in the energy dissipation. The energy dissipation can primarily be attributed to the simultaneous influence of increase in volume percentage of plastic zone and increase in dislocation density.
7. The present results thus suggest that with a proper selection and combination of reinforcement material (metallic + ceramic) the overall damping capacity of the

composite can be significantly enhanced which can tailored using numerical models.

Related Publications:

[1] N. Srikanth and M. Gupta, *J. of Alloys and Compounds*, accepted, 2005.

[2] N. Srikanth, K. K. Tun and Manoj Gupta, *J. of Comp. Mat.*, Vol. 37, 2003, pp. 1385-1410.

[3] N. Srikanth, M. Gupta, J. *of Engg. Mat. and Tech.*, Vol.127, 2005, pp.289-294.

Chapter 10

Numerical Modeling of ETD in Metal Based Composites

10.0 Introduction

Engineering materials generally exhibit decreased stiffness and strength with increased damping. Also material defects induced damping results in a drop in stiffness. Compared to these phenomena, thermo-elastic damping offers several advantages viz., they are predictable and hence materials such as particulate reinforced MMCs, laminates and unidirectional composites, can be tailored to provide enhanced damping for a particular application.

Material deformation results in temperature variation with in a material. Metallic materials exhibit cooling under tensile stress and heating under compression. After the initial coupling equations were published by Nowicki in 1962 [179], Zener was the first to relate this coupling to an energy loss in vibration. His monograph in 1948 examined the various dissipation mechanisms in metals, which included the relations for thermoelastic dissipation that were derived from basic energy conservation in a material along with irreversible thermodynamic theory [15]. He postulated that a irreversible heat transfer takes place from the heat source which is the compressive stress side of a flexure beam to the heat sink which is the tensile portion of the beam where cooling exists. Thus relaxation of the thermoelastic solid is achieved through the irreversible flow of heat driven by local temperature gradients that through the coupling accompany the strain field. This process of energy dissipation, called thermoelastic damping, is a fundamental one. As long as the thermal expansion coefficient is nonzero, thermoelastic damping sets a damping capacity for any vibrating mechanical component in a dynamic system.

In this present study, a finite element based unit-cell is also introduced to visualize the heat flow and damping loss factor due to micro-thermoelasticity in a MMC

under a cyclic load. The model is also capable to study the effect of particle morphology such as sharp edges and particulate's aspect ratio on the ETD damping capacity of the MMC. Secondly, the inertial effects of the particle are taken into account compared to the pseudo static model of Milligan and Kinra [188]. Thirdly, the effect of process induced defects such as particle-matrix debonding and particle breakage as well as presence of voids and cracks in the metallic matrix on the overall ETD damping capacity of the MMC. Since Al/SiC is the most widely studied PRMMC system, such a material has been taken as the material of choice for the detailed study, however the present model can be extended to any material system.

10.1 Theoretical Consideration

Elastic as well as plastic deformation results in altering the temperature of a material. For example, in a metallic material tensile deformation results in volume increase as well as cooling, while compressive deformation results in volume decrease as well as heating. Thus under elastic loading the component material exhibits heating or cooling depending on the hydrostatic stress it experiences [180]:

$$q_e^{'} = \frac{(3\lambda + 2\mu)}{(\rho c / \alpha)} T_o \varepsilon_{kk}^{'} \tag{10.1}$$

where $q_e^{'}$ is the rate of heating or cooling, T_o is the component temperature before the load is applied, λ and μ are the Lame constants, ρ is the density, c is the specific heat, α is the thermal expansion coefficient, $\varepsilon_{kk}^{'}$ is the elastic strain rate while k ranges from 1 to 3 which indicates the material coordinates. But under plastic deformation, most of the work

done on the material is converted to heat and plastic work. The heat produced purely aims to increase the temperature and thus converts it in to a positive heat source.

$$q_p^{'} = \frac{\beta \sigma_{ij} \varepsilon_{ij}^{p}}{\rho c} \tag{10.2}$$

where $q_p^{'}$ is the heat source from the plastic deformation, β is the fraction of heat that converts to heat which is around 0.5, σ_{ij} is the applied stress and ε_{ij}^{p} is the plastic strain rate.

Thermoelastic damping arises from the coupling of the stress-strain state equation to heat flow in the material. The familiar effects of the coefficient of thermal expansion where stresses and strain can be thermally induced can be derived from the dependence of the Hemholtz free energy on both strain and temperature [15]. From this starting point, however, one finds that the temperature gradient in a material can be driven by changes in strain. The coupled (linearized) state equations for an isotropic medium is derived as follows.

The linear thermoelastic stress/strain relation for an isotropic material, also known as the Duhamel-Neuman form of Hooke's law, which in indicial notation, is expressed as [179, 107-108]:

$$\sigma_{ij} = \delta_{ij}\lambda\varepsilon_{kk} + 2\mu\varepsilon_{ij} - \delta_{ij}\left(3\lambda + 2\mu\right)\alpha\left(T - T_o\right) \tag{10.3}$$

where λ and μ are Lame's constants, T is the temperature, T_o is the temperature of a stress free reference state, α is the linear thermal expansion and δ_{ij} is the Kronecker delta. The second equation required to define the linear, coupled, thermoelastic theory is the energy equation, given by [182, 183]:

$$kT_{,mm} = \rho c_E T_{kk}^{'} + \left(3\lambda + 2\mu\right) T_o \varepsilon_{kk}^{'} \tag{10.4}$$

where k is the thermal conductivity, ρ is the density and c_E is the specific heat at constant deformation. Since ε_{kk} is time harmonic, the fluctuation of temperature is also time harmonic. For most crystalline solids the relative temperature resulting from the thermoelastic effect is very small, i.e. $\left|\Delta T / T_o\right| \approx 10^{-3}$. Hence in equation (10.4) it has been assumed that the time varying temperature can be replaced by a constant temperature T_o. Other basic assumption is that the heat conduction term in the energy equation depends on temperature difference $T\text{-}T_o$ in each orthogonal direction, instead of the Laplacian of the temperature, i.e. $T_{,mm}$. For example, Zener assumed for a beam bending, the strain, stress and temperature varies spatially with "orthogonal thermodynamic potentials" which satisfy a characteristic equation, along with appropriate boundary conditions. The characteristic equation and boundary condition for temperature are:

$$\frac{k}{\rho c_E}\left(T_{,kk}\right)+\frac{T}{\tau}=0$$
$$T_{,i}=0, \quad \text{at} \quad x_i=\pm\frac{t}{2} \tag{10.5}$$

where t is a geometric boundary condition, such as thickness of the specimen. The solutions to this equation show that the temperature varies periodically through the thickness of the beam. This assumption also implies that the temperature only varies in one direction; in this case it varies along the thickness. This changes the relation of stress and temperature from a three-dimensional temperature change, $\left(3\lambda+2\mu\right)$, to that of a single dimension, $2\mu\left(1-\nu\right)$. Use of equation (10.5), requires that the thermal conductivity k, in equation (10.4), be replaced by a constant κ which is related to the geometric boundary conditions resulting in

$$\kappa T = \rho c_E T'_{kk} + \left(2\mu\left(1-\upsilon\right)\right) T_o \varepsilon'_{kk} \tag{10.6}$$

where the geometry related constant for a beam of thickness t in transverse bending is

$$\kappa = \frac{k\pi^2}{t^2} \tag{10.7}$$

Thermoelastic damping occurs only in deformations that cause volumetric change (e.g. bending and tension/compression) [179] hence in equation 10.3, there is no thermal coupling for the case $i \neq j$. In the case of pure shear deformation no volumetric change occurs and hence no contribution towards thermoelastic damping. Solving above equations for temperature and its first derivative and then solving for stress, gives the energy equation in stress, strain and their first derivatives:

$$\sigma_{ij} = \lambda\varepsilon_{kk} + 2\mu\varepsilon_{ij} + \left(\frac{\rho c_E}{\kappa}\sigma'_{ij} - \frac{2\mu\rho c_E}{\kappa}\varepsilon'_{ij} - \varepsilon'_{kk}\left(\frac{\rho c_E \lambda}{\kappa} + \frac{\left(\alpha 2\mu\left(1-\upsilon\right)\right)^2 T_o}{\kappa} \right) \right) \tag{10.8}$$

The first two terms of the above equation denotes the isotropic elastic relation. The third bracketed term contains the damping effect, similar to viscosity, from thermo elastic dissipative sources.

Zener showed that under certain assumptions about the specimen geometry, the thermoelastic dissipation can be related to an equivalent viscoelastic material's constitutive equation which he termed as standard linear solid and is described mathematically as follows [184]:

$$\sigma + \tau_\varepsilon \dot{\sigma} = M_R\left(\varepsilon + \tau_\sigma \dot{\varepsilon}\right) \tag{10.9}$$

where σ is stress, ε is strain, τ_ε is the time constant of relaxation of stress under constant strain, τ_σ is the time constant of relaxation of strain under constant stress and M_R is the relaxed elastic modulus. Thus his intent was to show that the damping behavior can be

approximated by a single relaxation peak with a characteristic relaxation time which corresponds to the thermal diffusion time across the width 'b' of the beam, which is proportional to b^2/χ, where χ is the thermal diffusivity of the material.

Under sinusoidal vibration with a frequency ω the stress and strain are given by:

$$\varepsilon = \varepsilon_o e^{i\omega t} \qquad \sigma = \sigma_o e^{i\omega t} \tag{10.10}$$

A complex elastic modulus relates the stress to the strain, where the ratio of the real to the imaginary part of the complex quantity provides a measure of the dissipation or internal friction of the material as follows [15, 184]:

$$Q = \Delta_m \frac{\omega\tau}{1+(\omega\tau)^2} \tag{10.11}$$

where $\tau = \sqrt{\tau_\sigma \tau_\varepsilon}$ and $\Delta_m = \dfrac{M_U - M_R}{\sqrt{M_R M_U}}$ is a dimensionless quantity called the relaxation strength of the modulus.

10.2 Macro thermo elasticity: Flexural vibrations of beams

As discussed previously, in a isotropic, homogenous, thermoelastic, Bernoulli-Euler beam of constant rectangular cross section with height h and undergoing time-harmonic bending vibrations in the x-y plane, the curvature of the beam varies with time $\kappa = \kappa_o e^{i\omega t}$ where ω is the circular frequency in rad/sec. The stresses in the beam can be expressed in terms of curvature ($\varepsilon_{xx} = -\kappa y$ and $\varepsilon_{xx} = \varepsilon_{zz} = -\nu\varepsilon_{xx}$). Thus the variation in the curvature during bending results in fluctuation of the hydrostatic stress (ε_{kk}) as follows:

$$\varepsilon_{kk} = -(1-2\nu)\kappa_o y e^{i\omega t} \tag{10.12}$$

Thus the stressed material experiences a temperature change as it experiences a reversible adiabatic (isentropic) process which can be predicted using the first and second laws of thermodynamics. For an isotropic material, the change in temperature due to change in hydrostatic stress (σ_{kk}) can be predicted as follows [142]:

where s is the entropy which is to be constant in an isentropic process. Thus shear

$$\left(\frac{\partial T}{\partial \sigma_{kk}}\right)_S = -\frac{\alpha T}{\rho c} \tag{10.13}$$

stresses are not expected to produce heat. Using the above principle Zener's solution of the ETD damping for a beam configuration is given by [15]:

$$\Psi_{\text{ETD}} = \Psi_o \frac{\omega\tau}{1+(\omega\tau)^2} \tag{10.14}$$

$$\Psi_o = \frac{2\pi\alpha^2 E_R T_o}{\gamma c} \tag{10.15}$$

$$\tau = \frac{\gamma c h^2}{\pi^2 k} \tag{10.16}$$

where ω is the circular frequency, τ is the characteristic time of the beam, Ψ_o is the characteristic damping of the beam, α is the coefficient of thermal expansion, E_R is the relaxed modulus of elasticity, T_o is the absolute temperature, γ is the mass per unit volume, c is the specific heat per unit mass, k is the isotropic thermal conductivity of the material and h is the beam thickness. The ETD damping mechanism is frequency dependent and reaches a maximum when the time constant of vibration reaches the characteristic time of the beam [1, 26] given by equation (10.16). Shieh had extended this thermoelastic damping study to timoshenko type beams [186, 187]. In the present study the samples were 10mm in diameter and 300 mm in length, hence they essentially satisfied Euler's beam conditions. Using the thermomechanical properties of the matrix

material, viz., Al and Mg the damping loss factor due to the macro-thermoelasticity of the beam was found to be 10^{-5}, which is presumed to be insignificant. But to understand the micro-thermoelasticity at the reinforcement particulate level the method summarized in the following section was adopted.

10.3 Micro Thermoelastic Damping: PRMMCs

Presence of stress raisers such as reinforcements, precipitates, voids, cracks would alter the hydrostatic stress distribution causing enhanced heat dissipation. In this section the effect of the presence of spherical reinforcement as an individual stress raiser is discussed.

A complete set of field equations required for calculating the elastothermodynamic damping was presented by Kinra and Milligan [188]. They presented elegantly for isotropic composite material and further extended to: (a) a single linear inclusion in an unbounded matrix [188], (b) bending of a laminate beam [188], (c) a multi-layered metal-matrix composite [189] and finally (d) to an imperfect thermal interface in a fiber reinforced metal matrix composite [190].

For conciseness, the basic equations that are needed for the present work are reproduced. The isothermal isotropic Hooke's law is [179]:

$$\varepsilon_{lm} = \frac{1}{E}\left(\sigma_{lm}\left(1+\upsilon\right) - \upsilon\sigma_{kk}\delta_{lm}\right) \tag{10.17}$$

where σ_{kk} is the stress tensor, E is the Young's modulus, δ_{lm} is the Kronecker delta and υ is the poisson's ratio. The one-way coupled heat conduction equation in spherical coordinates is [119, 120]:

$$\frac{1}{r^2}\frac{\partial}{\partial r}\left(r^2\frac{\partial T}{\partial r}\right) - \frac{C}{k}\frac{\partial T}{\partial r} = \frac{\alpha}{k}T_o\frac{\partial \sigma_{kk}}{\partial r} \tag{10.18}$$

where r is the radial coordinate, T is absolute temperature, T_o is the thermodynamic equilibrium temperature and also the reference temperature at which all the material properties are taken, t is time, α is the linear coefficient of thermal expansion, k is the thermal conductivity, and C is specific heat per unit volume. In the case of a spherical coordinate, the heat conduction equation involves only the radial coordinate and hence the problem can be seen as spherically symmetric. The term on the right of equation (10.15) is due to the thermoelastic effect, given by equation (10.1). Solving the above equation we get the temperature distribution from which the thermal gradient is obtained. The rate of entropy produced per unit volume $\dot{s}_p$ due to irreversible heat conduction is given as follows [119]:

$$\dot{s}_p = \frac{k}{T_o^{\,2}}\left(\frac{\partial T}{\partial r}\right)^2 \tag{10.19}$$

where the dot over a symbol represents partial differentiation with respect to time. It is important to recognize that the entropy produced is proportional to the square of the temperature gradient at that point.

Under a cyclic load with frequency ω (which is the circular frequency), the maximum elastic stored energy per unit volume is given by [188-190]

$$W = \frac{\sigma_{lm}\varepsilon_{lm}}{2} = \frac{1}{2E}\left[(1+\upsilon)\sigma_{lm}\sigma_{lm} - \upsilon\sigma_{kk}^{\,2}\right] \tag{10.20}$$

The entropy produced per unit volume during one cycle of vibration is given by [188-190]:

$$\Delta S = \oint \dot{s}_p dt \tag{10.21}$$

The entropy produced can also be represented in terms of temperature variation that is also time harmonic (described as $T^*(r,t) = T_o + V^* e^{i\omega t}$). The superscript * denotes a

complex number and thus the temperature is theoretically a complex quantity with a phase difference compared to the applied harmonic stress field σ_{kk}. The entropy increase is given by:

$$\Delta s = \frac{k}{T_o}\frac{\pi}{\omega}\mathrm{Re}\left(\frac{\partial V^*}{\partial r}\frac{\partial \overline{V}^*}{\partial r}\right) \tag{10.22}$$

where the overbar $\left(\overline{V}\right)$ denotes the complex conjugate.

The mechanical energy dissipated (converted into heat), ΔW, in the continuum of volume V, during one cycle of vibration is given by:

$$\Delta W = T_o \int_V \Delta s dt \tag{10.23}$$

This equation gives the correspondence between entropy produce in the composite during a cycle of vibration and the elastic energy that has been made unavailable for work by turning it into heat. The specific damping capacity is defined as the energy dissipated through the composite in one cycle normalized by the maximum elastic energy stored during that cycle, as follows:

$$\psi = \frac{\Delta W}{\int_V W dV} \tag{10.24}$$

By this method the damping characteristics of SiC reinforced Al matrix was studied and Fig. 10.1 shows the variation of the specific damping with volume fraction of reinforcement and cyclic frequency. Here the frequency is represented in normalized form of using the characteristic time of heat conduction in the inclusion (τ), similar to the practice of Kinra et al. [107] $\left(\Omega = \omega\tau\right)$ where τ for the inclusion depends on its diameter (a), thermal conductivity (k) and specific heat (C) as follows:

$$\tau = \left(\frac{C}{k}\right)a^2 \tag{10.25}$$

10.4 Finite element implementation of Micro-thermoelasticity

The above formulation of Kinra et al. [190] has been attempted to be implemented in a finite element form with full coupling between the heat transfer equation and force transfer equation within in the UCM under a cyclic load. In a three dimensional condition, the dependence of the total strain on the stress vector $\{\sigma\}$ and temperature rise ΔT can be represented as follows [173, 191]:

$$\{\varepsilon\} = [D]^{-1}\{\sigma\} + \{\alpha\}\Delta T \tag{10.26}$$

where [D] is the stiffness matrix, $\{\alpha\}$ is the vector of thermal expansion coefficient, ΔT is temperature rise ($T\text{-}T_o$). Since stresses vary with time under cyclic load, for example in the case of cyclic bending, heat flows from the hot region to cold region with a characteristic time constant which depends on the thermophysical properties and hence lags behind the stress cycle. According to second law of thermodynamics, entropy (S) is generated $(Q = ST_o)$ due to this irreversible heat conduction (Q) that can be determined as follows [190]:

$$S = \{\alpha\}^T\{\sigma\} + \frac{\rho C_p}{T_o}\Delta T \tag{10.27}$$

where T_o is reference temperature and C_p is the specific heat at constant pressure that is related to specific heat at constant volume (C_v) as follows [192]:

$$C_V = C_P - \frac{T_o}{\rho}\{\alpha\}^T[D]\{\alpha\} \tag{10.28}$$

Taking strain $\{\varepsilon\}$ and ΔT as independent variables, the coupled equations (10.26) and (10.27) can be expressed as follows:

$$\{\sigma\} = [D]\{\varepsilon\} - [D]\{\alpha\}\Delta T \tag{10.29}$$

$$Q = T_o\left[[D]\{\alpha\}\right]^T\{\varepsilon\} - \rho C_V \Delta T \tag{10.30}$$

Expressing in terms of heat transfer, the rate of heat generation is given by [193]:

$$\frac{\partial Q}{\partial t} = T_o \left[[D]\{\alpha\} \right]^T \frac{\partial \{\varepsilon\}}{\partial t} + \rho C_V \frac{\partial \Delta T}{\partial t} - [K]\nabla^2 T \qquad (10.31)$$

where [K] is the thermal conductivity matrix and ∇ is the Laplacian operator. Thus under dynamic condition the finite element model's force and heat balance is expressed by the following set of equations which can be solved by numerical methods [173]:

$$[M]\{u^{''}\} + [K]\{u\} + [K_{Te}]\{u\} \qquad (10.32)$$

$$[C_{ETD}]\{T^{'}\} + [C_T]\{T^{'}\} + [K_T]\{T\} = \{Q\} \qquad (10.33)$$

where each dash on the superscript denotes a differentiation with time, $[M]$ and $[K]$ are the mass and stiffness matrices, respectively, $\{u\}$ is the displacement vector, $[K_t]$ is thermal diffusion conductivity matrix, $[C_t]$ is the specific heat matrix, $[K_{Te}]$ is thermoelastic stiffness matrix which is computed as follows:

$$[K_{Te}] = -\int_{vol} \left([B]^T \{[D]\{\alpha\}\} \left(\nabla \{N\}^T \right) \right) dv \qquad (10.34)$$

where $[B]$ is the strain-displacement matrix, $\{N\}$ is the shape function matrix, $[C_{ETD}]$ is the ETD damping matrix which is derived as follows:

$$[C_{ETD}] = -T_o [K_{Te}]^T \qquad (10.35)$$

Thus; when the material is subjected to vibration, stresses vary sinusoidally and the induced strain due to the coupling of thermal and mechanical energy lags behind the

$$\sigma(t) = \sigma_o \sin(\omega t) \quad \& \quad \varepsilon(t) = \varepsilon_o \sin(\omega t - \delta) \qquad (10.36)$$

applied stress by a phase angle 'δ' as follows [194]:

Denoting $\{\varepsilon\}^*$ as the complex conjugate of total strain, the time averaged total strain energy U_t becomes a complex number and is determined as follows:

$$U_t = 0.25\int_V \{\sigma\}^T \{\varepsilon\}^* \, dV \tag{10.37}$$

where the real part of U_t represents stored energy and imaginary part represents the dissipated energy due to the thermoelastic damping. The ratio of the imaginary to the real part provides the loss factor (η), which is equal to the inverse of quality factor (Q) which is given by [173]:

$$\eta_{etd} = Q^{-1} = \frac{\sum_{n=1}^{tot} \mathrm{Im}(U_t)}{\sum_{n=1}^{tot} \mathrm{Re}(U_t)} \tag{10.38}$$

where 'tot' denotes the total number of elements in the finite element model.

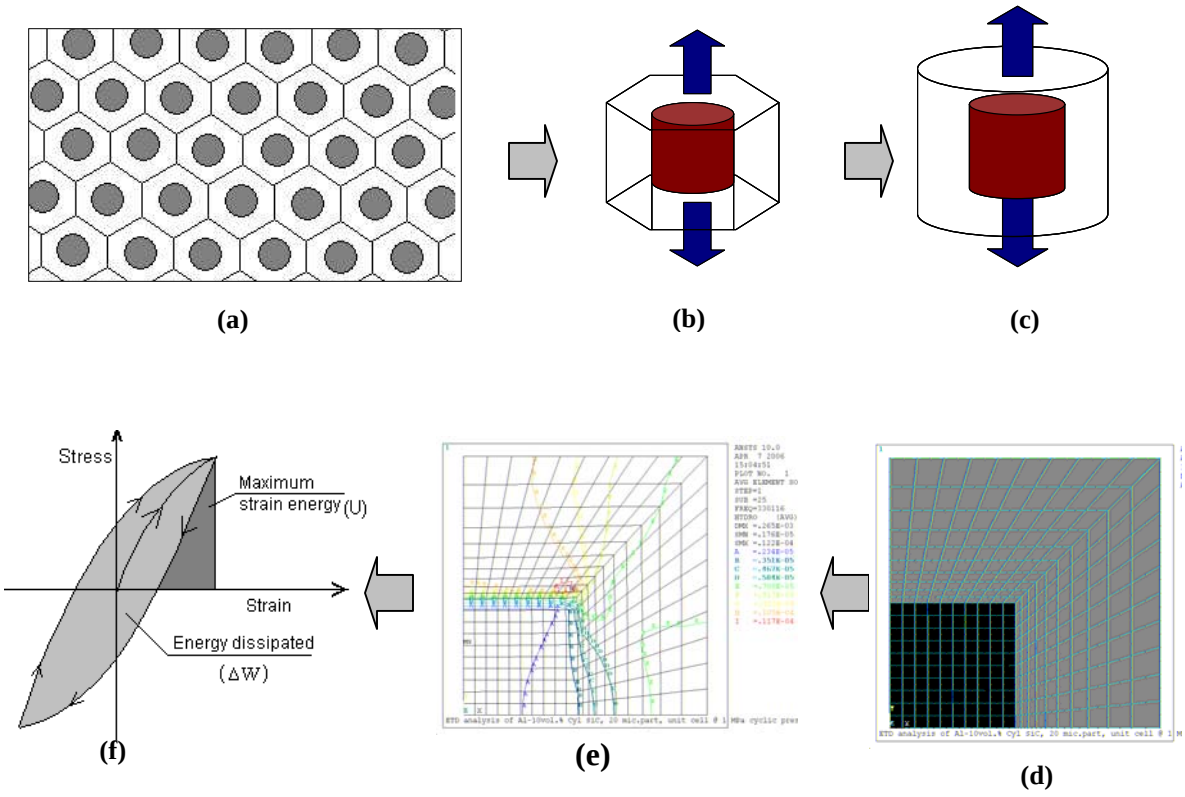

Fig. 10.1 Methodology for deducing a simplified FEM model for the PRMMC: (a) hexagonal representation of a particulate reinforced MMC, (b) unit hexagonal cell, (c) approximated cylindrical unit cell, (d) axisymmetric FEM model of the cylindrical unit cell, (e) equivalent stress contour plot and (f) hysterisis curve.

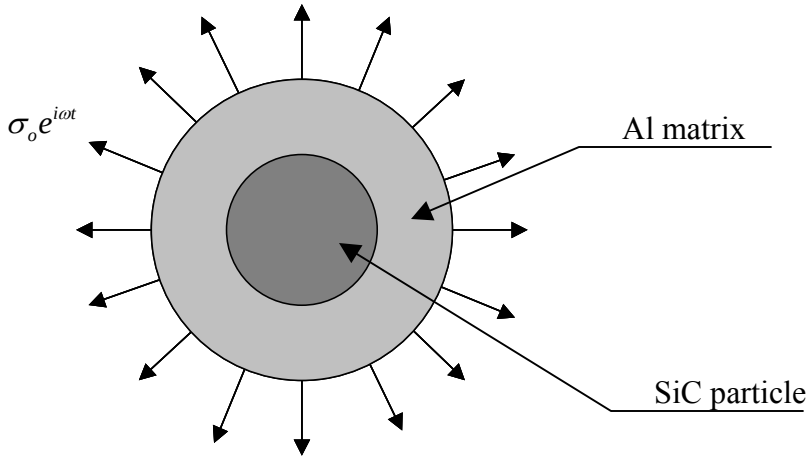

(a)

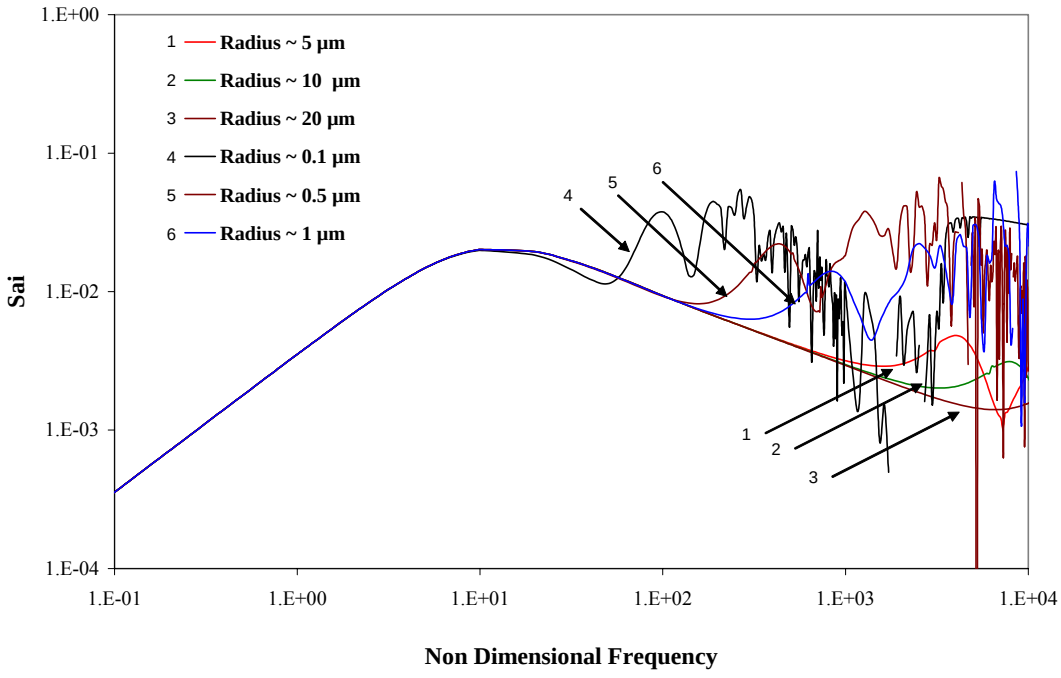

(b)

Fig. 10.2 (a) FEM based axisymmetric model similar to that of Kinra et al. [7] having a spherical matrix and particle (b) Corresponding damping characteristics result of Al – 10 vol. % SiC for different spherical particle radius ranging from 0.1 to 20 micron.

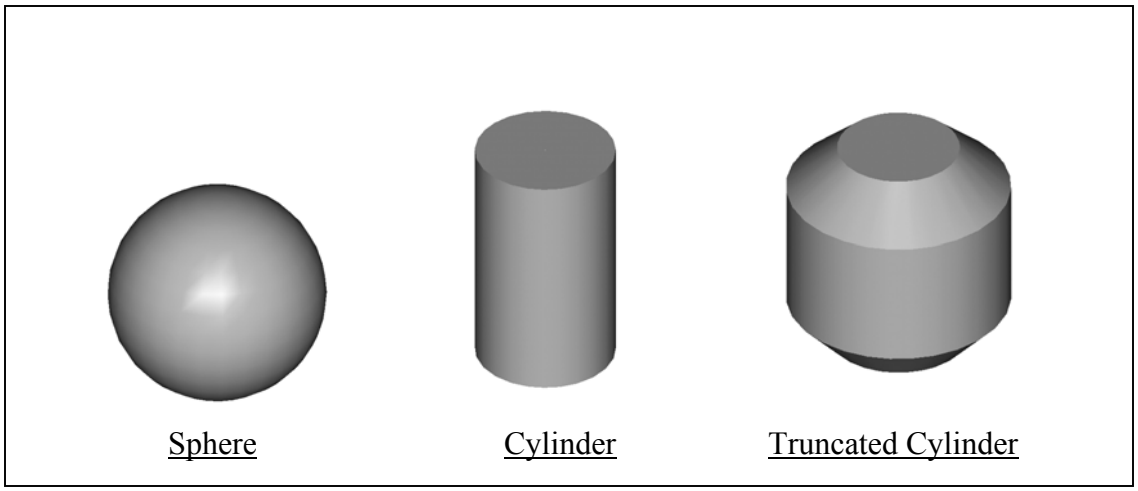

Fig. 10.3 Particulates of similar volume but with different shape morphologies.

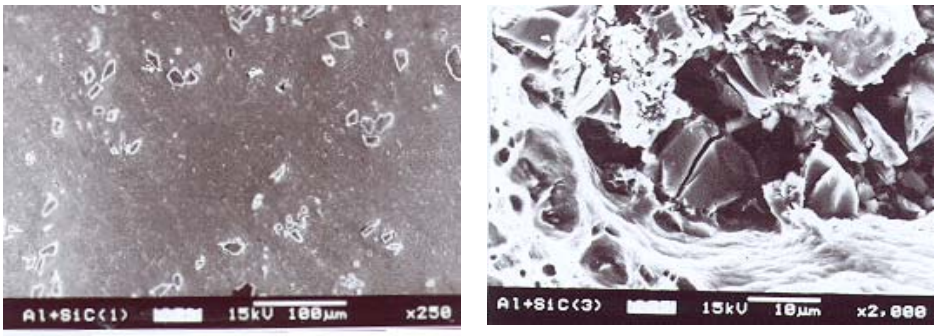

(a) **(b)**

Fig. 10.4 (a) Typical SiC particle distribution and shape in an Al containing 5 volume percentage of SiC (b) Typical particle cracking and debond

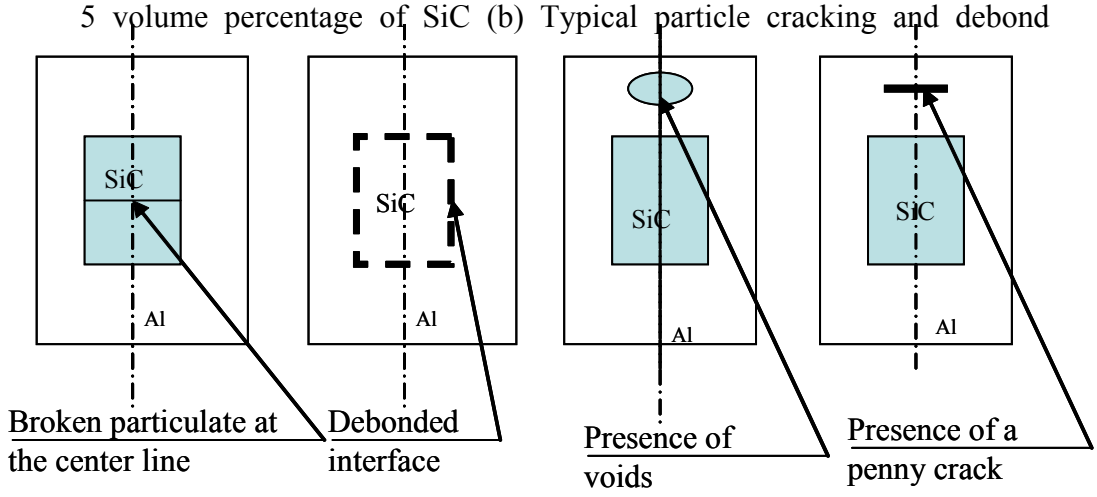

(a) **(b)** **(c)** **(d)**

Fig. 10.5 UCM models with different defects (a) broken particle (b) particle-matrix debonding (c) presence of voids in matrix and (d) presence of cracks in matrix.

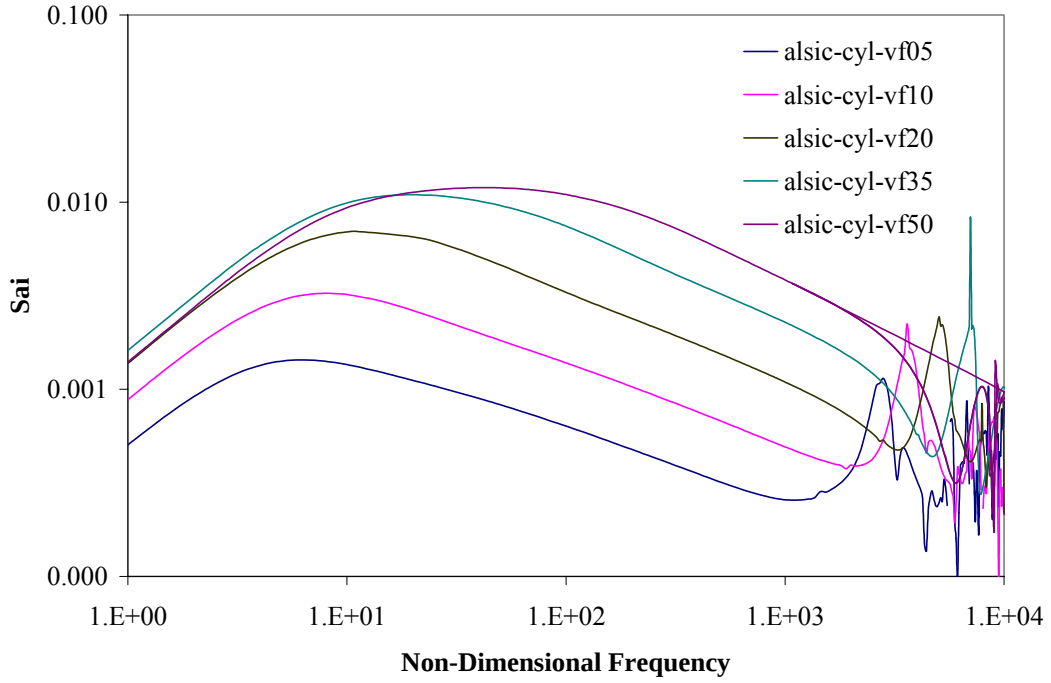

Fig. 10.6 Damping characteristics of Aluminium with cylindrical SiC particle and volume fraction ranging from 5 to 50 percentage.

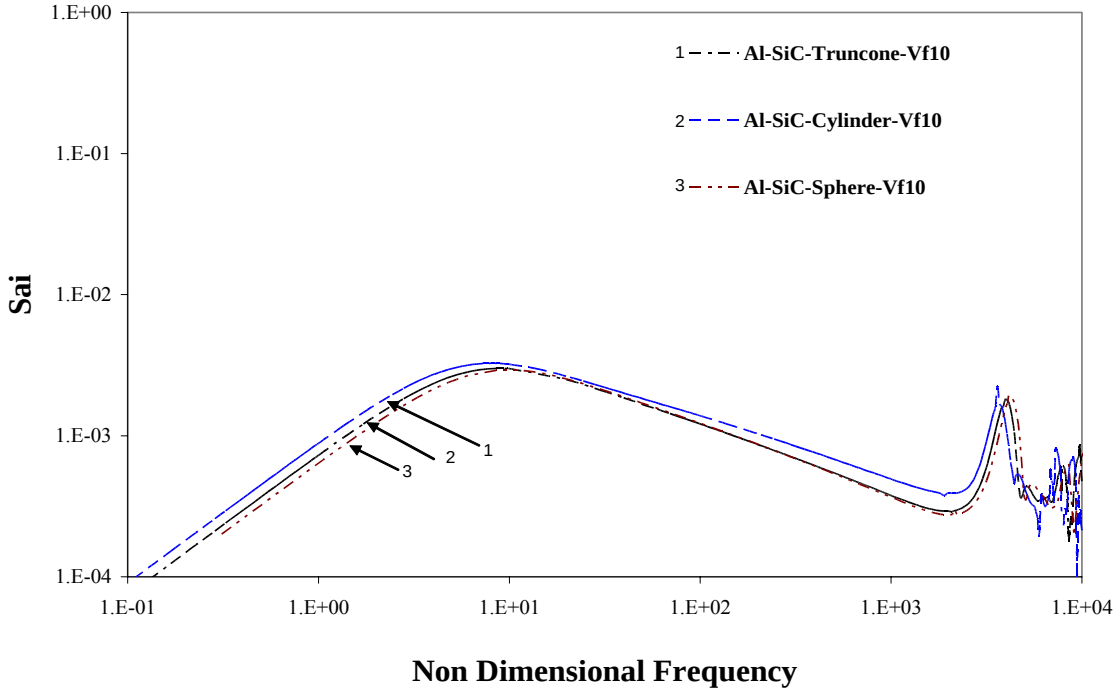

Fig. 10.7 Variation of damping characteristics of Al containing 10 volume percentage of SiC with particle shapes of cylinder, sphere and truncated cone.

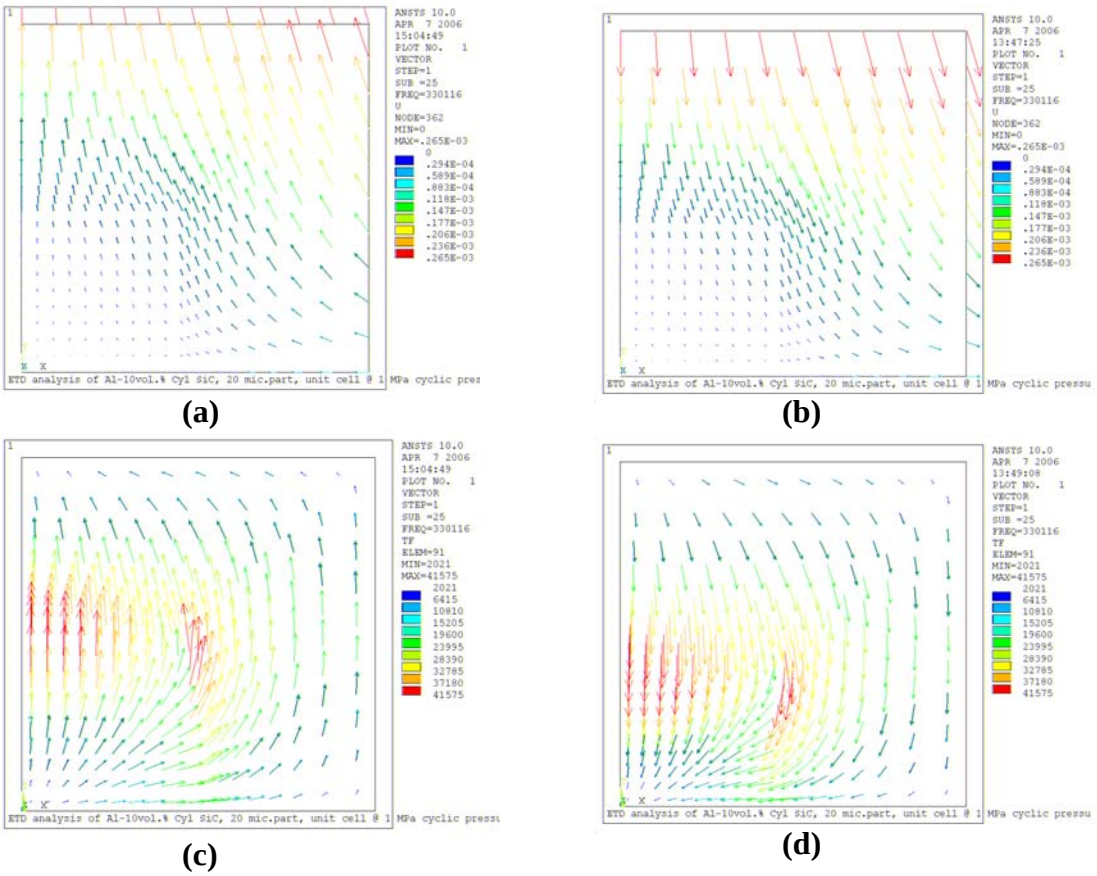

Fig. 10.8 Material deformation under (a) tensile part and (b) compressive part of the cyclic load at a non-dimensional frequency of Ω~10. Corresponding temperature flux pattern in the unit cell under the same instance of (c) tensile direction (d) compressive direction of the cyclic load.

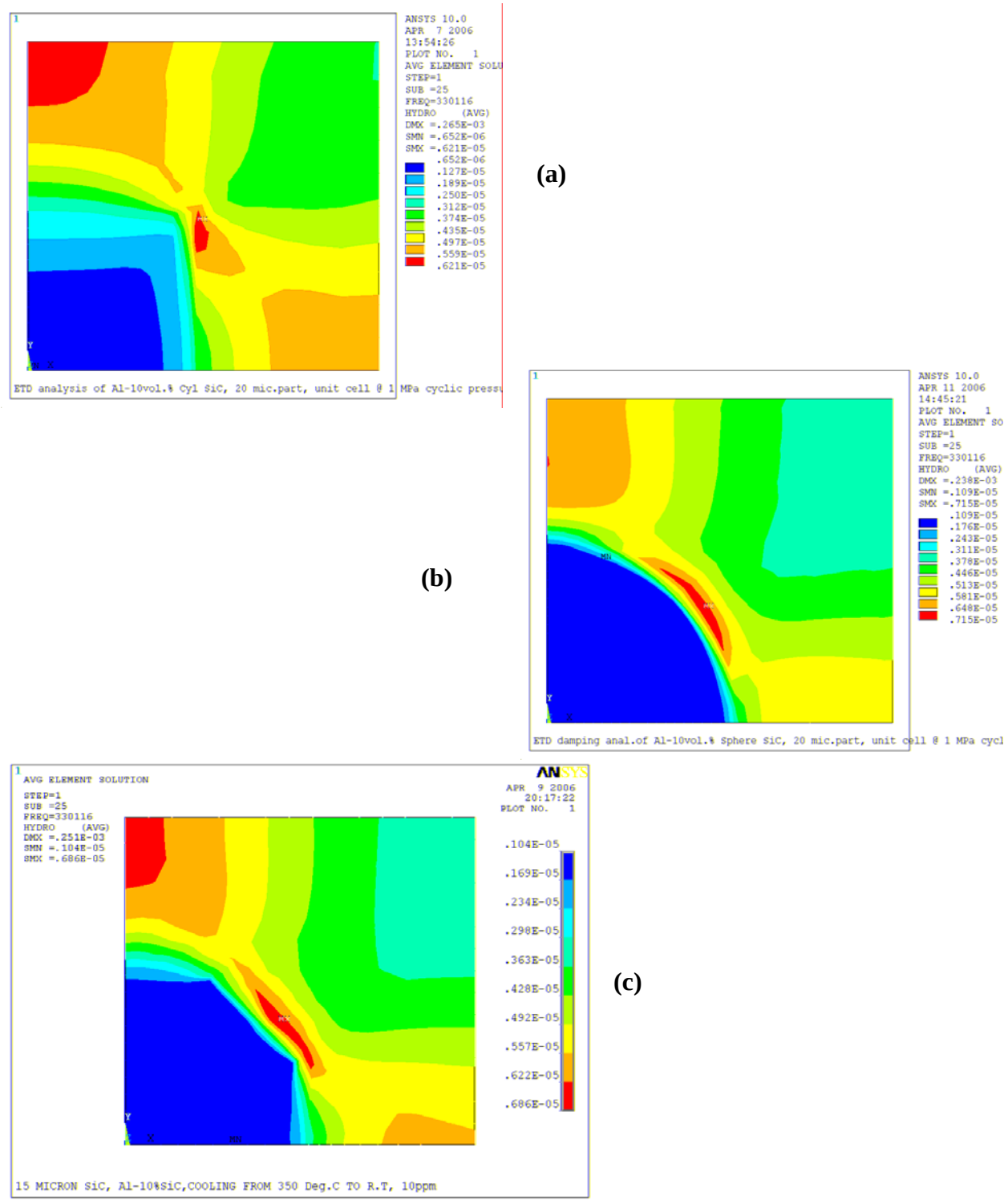

Fig. 10.9 Typical hydrostatic stress distribution under the compressive part of the load cycle at non-dimensional frequency of Ω~10 for a particle shape of (a) cylinder (b) sphere (c) truncated cone.

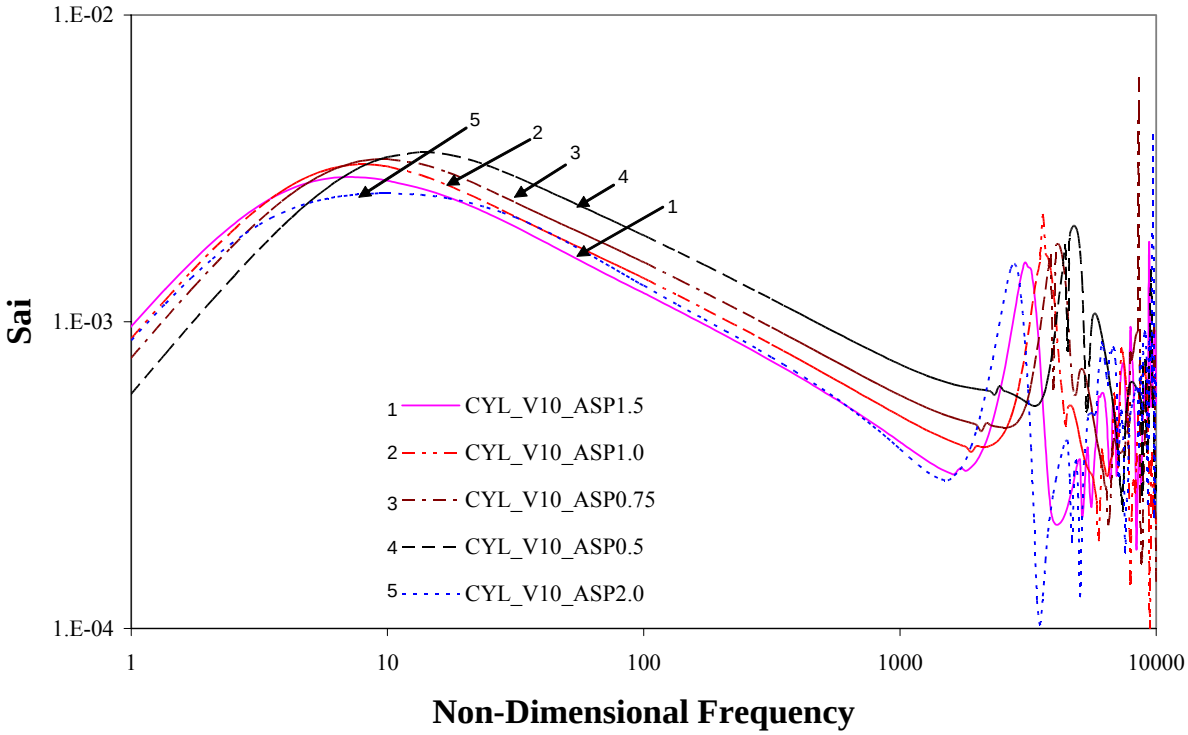

Fig. 10.10 Damping characteristics of Aluminium containing 10 volume percentage of cylindrical SiC particle with aspect ratio ranging from 0.5 to 2.0.

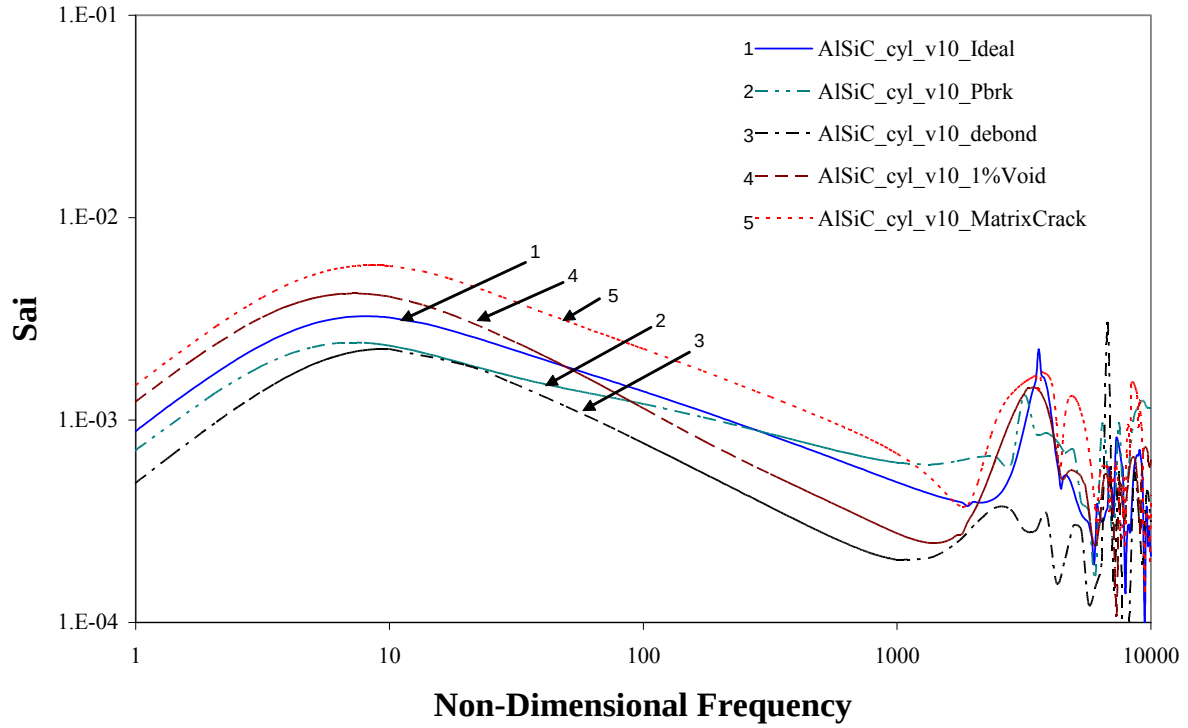

Fig. 10.11 Effect of process-induced defects on the ETD damping characteristics of a Al matrix containing 10 volume percentage of cylinder shaped particle.

10.5 UCM for Micro-thermoelasticity

Using the finite element methodology described in previous section a unit cell model was made to extend the analytical method developed by Kinra and his co-workers [120]. The drawback of their analytical method is that the particles are assumed to be spherical and are placed in a hollow metallic matrix sphere. Composing a global MMC using such matrix spheres is not practical as it leads to voids in between the spheres. Secondly, particles are non-spherical in reality and have sharp corners. Presence of stress concentrations such as aspect ratio of particles, overall particle shape and sharp corners results in non-uniform hydrostatic stresses which alters the heat generation and thus the energy dissipated during the vibration.

As explained in chapter 9, the particles can be assumed to be uniformly distributed based on general observation of isotropic behavior of the PRMMCs. These particles are assumed to be placed at the center of hexagonal metal matrix cells. Further to cut down the computation time, the hexagonal cells are simplified to circular cylinders so as to convert the three-dimensional model to an equivalent two-dimensional one.

The composite material was idealized in terms of periodic array of identical hexagonal cylindrical cells, shown in Fig. 10.1 (a), with the SiC reinforcement located in the center of each cell. Axisymmetric cylindrical cells, which can be regarded as approximations to the three-dimensional array of the hexagonal cylindrical cells [167-172], were used in the calculation (see Fig. 10.1 (c)).

Exact micro-mechanical modeling of a two or more phase composite material is very complicated due to the geometric size and shape of the individual phases. Hence unit cell models have been designed and successfully used by a number of researchers,

including Llocra et al. [167], Bao et al. [168], and Shen et al. [169] to calculate the thermo-mechanical properties of composites. These models were successfully used to predict results similar to more rigorous and computationally more intense three-dimensional models. In the present study, an axi-symmetric cell model similar to Bao et al. [168] is chosen to model a particulate reinforced metal matrix composite. This limits the particulate shape to axially symmetric in nature such as a sphere, cylinder, or an ellipsoid and provides the convenience to analyze the 3D model as a 2D axi-symmetric model, which results in high accuracy with least computer resource. The unit cell model for a cylindrical particulate is shown in Fig. 10.1 (d). Cylindrical coordinates are defined so that 'r' represents the radial direction and 'z' represents the axial direction of the cylinder. In the present study, the particulate is assumed to be a cylinder with a particle radius R with an aspect ratio ranging from 0.5 to 2. The dimensions of the cylinder are so chosen so as to satisfy the required volume fraction of the reinforcement in the composite under study. The reinforcement volume fraction was taken as the ratio of the reinforcement volume to the cell volume. The particulate is placed at the exact center of the metal matrix cylinder with a radius L and length 2L. Thus the aspect ratio of the cell, the ratio of the height of the cylinder to its diameter, was maintained to be unity. The cylindrical surface is constrained to remain cylindrical but can move in or out with zero average normal traction. The faces perpendicular to the direction of stressing also remain planar with zero shear traction and a sinusoidally varying normal stress. Before applying such a cyclic load, the UCM was subjected to thermal cooling from extrusion temperature to room temperature to account for the residual stress in the subsequent calculations.

The ANSYS^{TM} (version 10) code was employed using a mid-noded coupled field element (Plane 221) to solve the boundary value problem that was explained systematically in the previous section [173]. Fig. 10.1 (a) to (f) shows the overall modeling methodology of particulate reinforced metal matrix composites.

The unit cell model proved to be a proper idealization of the particulate reinforced MMC. The model assumed Al as the metallic matrix and SiC as the reinforcing particulate. Table 1 lists the material properties assumed in the present study. The unit cell was made corresponding to a cylindrical particulate of size 20 μm inside a cylindrical metallic matrix with an length to diameter ratio of 1 and a volume modeled such that the volume fraction of particulate to the matrix is maintained at different values ranging from 5 to 50 vol. %, as shown in Fig. 10.1(d). The model was subjected to a tensile cyclic load with maximum stress amplitude of 1Pa. The cyclic frequency range extended to an additional decade compared to the studies of Kinra [189, 190] so as to easily compare with their pseudo-static model and study the dynamic effects. The results were expressed in terms of the non-dimensional frequency (Ω), which is defined as the product of the operating frequency and the thermal time constant [189, 190, 196], and thus Ω was varied from 0.1 to 10,000. From the computed strain energy results, the real and imaginary portion was deduced for each element and was summed for the complete model based on equation (10.38).

To confirm that the present FEM methodology works well, a spherical model similar to that of Kinra et al. [190] and Srivatsava et al. [196-197] (see Fig. 10.2 (a)) was built which comprised a spherical particle inside a spherical matrix sphere and was subjected to a pulsating hydrostatic pressure on the matrix surface. The results shown in

Figure 10.2 (b) matches well with the published results of Kinra et al. [190] and Srivatsava et al. [196].

Based on the confidence gained from the above exercise the FEM based unit-cell as explained in Fig. 10.1 was built. The loads were assumed to be uniaxial loading such that each cell in a composite is subjected to tensile/compressive loading when the sample is subjected to a flexing condition. As explained in the previous paragraph, to extend the use of FEM, the particle was assumed to have a cylinder shape (see Fig. 10.3) such that it is symmetric, yet having enough stress concentration features similar to actual SiC particle's morphology (see Fig. 10.4 (a)). Further, to understand the effect of particle shape, the cylindrical particulate was compared against a sphere and a truncated-cylinder type particle shape, as shown in Fig. 10.3. Also to understand the effect of particle aspect ratio, the UCM with a cylindrical particle shape was studied by varying the aspect ratio from 0.5 to 2.0. The results from such shape variation studies help to understand the effect of particulate morphology on the ETD damping characteristics of the composite.

Finally, the unit cell model containing 10 volume percentage of SiC was used to study the different types of process induced defects individually, such as voids and cracks in the metallic matrix, particulate-matrix debonding and particulate breakage, illustrated in Fig. 10.5, and described as follows:

- To understand the effect of particulate breakage, the cylindrical particulate was modeled as two broken pieces with no force transmitting capability in between.
- To understand the effect of particulate debonding, the interface between the cylindrical particulate and the cylindrical cavity of the matrix is modeled with contact elements [198] with a friction coefficient of 0.3. This enables normal

hydrostatic forces to be passed to the particulate from the matrix and vice-versa while the shear stress obeys coulombs law of friction [173]. Thus, the energy dissipated due to rubbing at the interface during sliding is also taken into account.

- To understand the effect of voids, a spherical void of 1 volume fraction was added to an Al containing 10 volume percentage of SiC composite. The void was placed at the axis of the unit cell model above the SiC particulate to achieve axis-symmetry in the model.
- To understand the effect of the presence of a crack close to a particle in the metallic matrix, a penny shaped crack with a radius of 20% of the particle size was analyzed with its axis matching with the unit cell's axis. The composition of the unit cell was maintained to be Al with 10 volume percentage of SiC.

10.6 Discussion of UCM Predicted Micro-ETD Effects

The analytical model of Kinra et al. [190] and Srivatsava et al. [196] assumed a spherical particulate inside a spherical matrix with a harmonic hydrostatic pressure loading as shown in Fig. 10.2(a). Such assumptions impose several restrictions in modeling the actual geometry, load and other boundary conditions. The finite element based UCM model developed in the present study was found to be exceptionally simple and fast to run in a PC platform (Windows XP^{TM}). To demonstrate its accuracy, similar model conditions as that of Kinra [190] were performed for the Al/ 20 vol. % SiC PRMMC system. At low frequency range of $(\Omega \sim 10)$ it is clear from Fig. 10.2 (b) that a damping peak similar to Kinra's model [190] is observed, which matches with the characteristic thermal time constant that is expressed as follows:

$$\tau_t = a^2 \rho C / k \tag{10.39}$$

where C is specific heat, ρ is density, a is particle size and k is thermal conductivity. Studies of Srivatsava et al. [196] showed that the inertial load become important in the force balance equation at high frequencies $(\Omega > 1000)$, in terms of the dynamic effects of the particle mass with respect to the frequency. In the present study, similar to their studies the particle radius in a MMC containing 20 vol. % was varied viz., 0.1 μm, 0.5 μm, 1 μm, 5 μm, 10 μm and 20 μm and the frequency dependent damping characteristics are compared in Fig. 10.2 (b). A dominant damping peak arises above $\Omega > 1000$ for a 10 μm particle size similar to results of Srivatsava et al. [196] which matches the time constant for the mechanical resonance of the particle, which is given as follows [199]:

$$\tau_m = a\sqrt{\left(\rho / \left(\lambda + 2\mu\right)\right)} \tag{10.40}$$

where 'a' is the particle radius, ρ is the reinforcement density, λ and μ are the Lame constants. For submicron particle size (a < 1 μm) it is clear from Fig. 10.2 (b) that the dominant mechanical resonance peak reduces in terms of frequency and approaches the $\Omega \sim 10$ peak. Thus it is encouraging that as the particle size reduces, enhanced damping in terms of increased number of damping peaks can be observed, which encourages researchers to move towards sub-micron or nano-particle type composites. Such increased damping due to particle size reduction has been observed in the present research which is explained in detail in chapter 11.

Fig. 10.6 shows the variation in the damping loss factor for different volume fraction of the SiC in the Al matrix. This shows clearly that the increase in volume fractions increases the overall ETD damping capacity of the composite. Experimental results listed in chapter 5 also showed such increased damping loss factor of Al matrix

for increase in SiC volume fraction viz., 4.4, 12.0 and 15.4 which increased the damping capacity by an order of 27%, 61% and 71%, respectively, when compared against the monolithic aluminium sample. This was explained based on the damping relation to the volume fraction of the plastic zone under similar loading condition. However, the present study shows ETD mechanism can also contribute to composite's overall damping capacity since various damping mechanisms in a composite material can act in tandem.

In reality, SiC particulates in the MMC as seen in Fig. 10.6, possess shapes similar to a polyhedron with multiple sharp edges leading to stress concentrations. In the present model, enhancement has been made compared to the model of Kinra [190] and Srivatsava [196] in terms of modeling the particle with a cylindrical shape to account the effect of sharp edges so as to invoke the stress concentration. Further to compare the effect of particle shape, separate models were prepared with truncated cone and spheroid shape, as shown in Fig. 10.3. Fig. 10.7 shows the variation of the damping loss factor against the normalized frequency for a 10 vol. % of SiC in an Al matrix which shows that the presence of stress concentration features of the particulate's shape such as sharp edges results in enhanced ETD damping compared to the spheroid particle shape. For example at $\Omega \sim 10$ peak it is clear that a cylindrical particle provides higher damping of 9.6 percentage than the spherical particulate. This can be hypothesized that as the particle shape has sharp edges, the force distribution is non-uniform and concentrates more at the stress-raising corners and hence the hydrostatic stress distribution differs at the tensile and compression part of the load cycle. Fig. 10.8 compares the material deformation direction and the heat flow direction within the UCM during the tensile and compressive part of a load cycle. Hence variation in the particle shape distorts the hydrostatic stress

contours (see Figs. 10.9 (a)-(c))within the UCM containing different particle shapes with unit aspect ratio viz., cylinder, sphere and truncated cone, as shown in Fig. 10.3. Similarly, results from UCM models with same particle radius of 10 μm but with different aspect ratio of cylindrical particle viz., 0.5, 0.75, 1.0, 1.5 and 2.0 shows that the ETD damping capacity (see Fig. 10.10) is higher for smaller aspect ratios which may be due to the reduction in the particle mass.

To identify the presence of microstructural defects in the composites, the stiffness or the elastic modulus is a good parameter especially at low strain amplitude, similar to the present experiment. Experiment results show in general that the PRMMCs do not reach the upper bound of stiffness that is predicted using the rule of mixture. This was mainly attributed to the process induced defects such as presence of debonding at the metal-ceramic interface, presence of broken particulates in the MMC as well as due to the presence of voids [200] (see Fig. 10.4 (b)). Also results mentioned in chapter 5 showed that the particle size reduces as the MMC undergoes secondary processes such as extrusion. Thus particle debonding due to poor wettability and particle breakage due to the secondary processes can be expected to exist in a MMC and can play a key role in the damping characteristics of an MMC. From a damping perspective, it is interesting to note that for both good and bad interfacial bonding condition between the ceramic particulate and the metal matrix, the overall damping characteristics increases in an MMC due to different damping mechanisms. In the present study, the effect of debonding on the overall ETD damping characteristics of the MMC along with the interface damping was computed by investigating the energy dissipated in the unit-cell model under a debonded metal-particulate interface condition with a cylindrical particulate morphology. Analysis

was performed for a friction coefficient of 0.3, which showed that the damping loss factor of the Al containing 10 volume percentage of SiC, see Fig. 10.11. Such results when compared against a fully bonded interfacial condition, shows clearly that the ETD damping loss factor is decreased which is due to poor stress transfer and poor thermal heat transfer across the debonded interface. However, experimental studies of Zhang et al. [201] showed that the debonded interface results in enhanced damping. This can be explained in terms of the frictional energy loss during cyclic loading at the particulate-matrix interface which can be analytically described as follows [201]:

$$\eta_{debond} = \frac{3\pi}{2}\gamma\mu k f \tag{10.41}$$

where μ is the coefficient of friction between the SiC on an Al surface, k is the stress concentration factor at an interface between a soft particulate and the metal matrix, γ is a correction factor and f is the volume fraction of SiC added. Hence η_{debond} depends directly on the friction coefficient, stress concentration and the volume fraction of debonded particulates. Similarly, analysis for a broken particulate condition (see Fig. 10.11) shows a similar reduction in ETD damping loss factor compared to a fully bonded particulate condition, due to lack of force and heat transfer through the particulate during the tensile and compressive part of the cyclic loading.

Investigation of the presence of a void and a crack in the metallic matrix close to a SiC particulate in an Al matrix shows increased damping capacity as compared to the ideal UCM model with no matrix defects, see Fig. 10.11. According to Fougere et al. [202] the elastic moduli 'E_p' of porous materials depend on the porosity percentage 'p' by an exponential function, $E_p = E_o \exp(-\beta p)$, where β is a material constant which ranges between 2 and 4 and E_o is Young's modulus under no porosity condition. Thus the force

distribution is altered in the metallic matrix and similarly results in reduction in strain energy and an increase in dissipated energy and hence an overall increase in ETD damping capacity. This matches well with analytically predicted results of Panteliou et al. [203], where they showed that the presence of voids of few volume percentage and cracks in the metallic matrix result in increased ETD damping capacities which were verified experimentally.

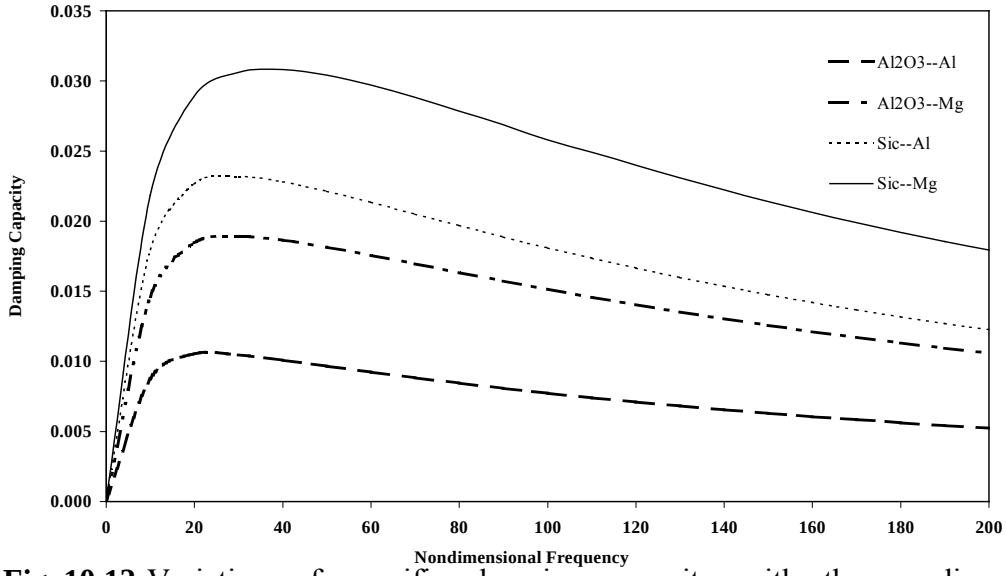

Fig. 10.12 Variation of specific damping capacity with the nondimensional frequency for different matrix-reinforcement combinations for a similar volume fraction of 0.5.

In summary, the present UCM model built using generalized FEM methodology, forms an elegant tool in predicting the ETD damping capability of a particulate type composite using the common thermo-physical properties of the parent materials used in the composite. But it assumes a uniform inter-particulate distance, since it is based on a unit cell concept, which may not be true due to the presence of clusters observed in the SEM micrograph, shown in Fig. 10.4(a). Based on the study of Zhou et al. [205], the presence of clusters leads to unequal load sharing and overlapping of the thermally induced plastic zones which is presently being studied. However, the model can account

to some extent for sharp faceted particulate shapes and the particle's aspect ratio compared to a spherically shaped particulate assumed in the previous studies [190, 196]. Further in terms of interfacial condition, both fully-bonded and a fully-debonded interface between the SiC-particle and the Al-matrix can be modelled using the present UCM methodology which may be considered as the two extremes of the real situation. While further efforts are made to closely mimic the actual composite, the result of the present study shows clearly that the present UCM model described in this section can be a useful design tool to predict the elasto-thermodynamic damping capacity of a particle reinforced composite in terms of particle size, shape, volume fraction, material type and also account for the effect of process induced defects, for a given dynamic design application. Thus the model is capable to predict for different material combinations for a given strain amplitude, frequency and temperature as shown in Fig. 10.12 and 10.13.

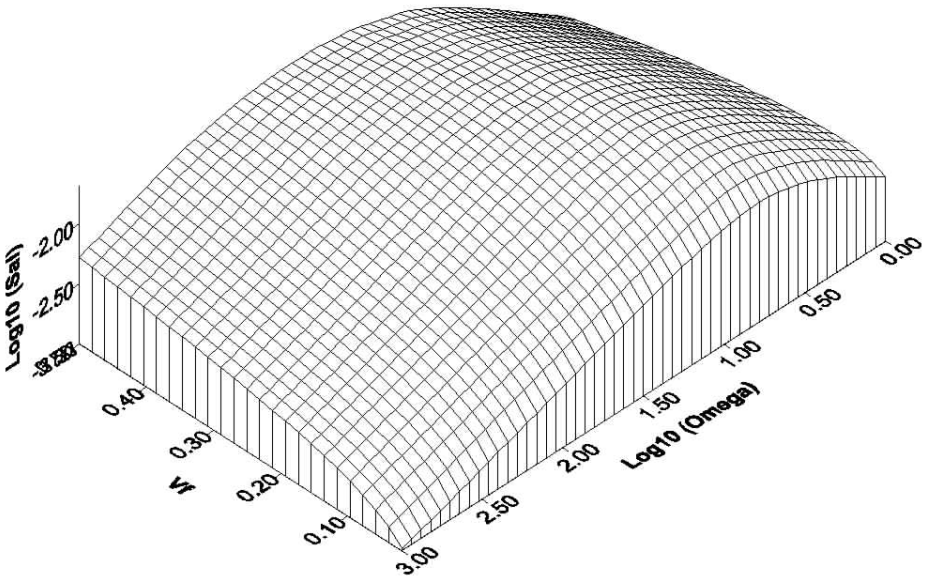

Fig. 10.13 Surface plot of specific damping capacity variation of Al matrix with various volume fraction of SiC reinforcement and subjected to different frequency. Kindly note that the normalized frequency and the damping capacity are denoted in log scale.

10.7 Summary

Based on the present study about ETD damping following conclusions can be reached:

1. ETD damping is purely a thermo-mechanical phenomenon which is purely non-destructive in nature compared to microplastic damping. It can be tailored for a given application whose vibration parameter such as amplitude and frequency are known.
2. ETD-damping becomes dominant at higher frequencies (ultrasonic frequencies) yet they seem to contribute up to 25% of the total enhancement in overall damping capacity of Al based composites, for example.
3. The unit-cell model seems to be viable choice to visualize the stress pattern and heat flow pattern in and around the matrix-reinforcement interface.
4. The FEM based cell model used in the present study enables the determination of damping loss factor of composites due to the elasto thermodynamic phenomenon that arises due to the cyclic variation in the hydrostatic strain distribution within the composite.
5. The UCM model is capable to account the inertial loads and thus predict the effect of particle size. Results show a decrease in particle size increases the damping loss factor that arises due to the ETD effect. Hence it is encouraging from a ETD damping standpoint to move towards a micro or a nano sized particle.
6. Results also show similar increasing trend in damping loss factor with volume percentage of SiC added in the metallic matrix.

7. Effect of stress concentration features of particulates increases the ETD contribution to the energy dissipation capability of the metallic matrix due to non-uniform force transfer between the matrix and reinforcement. For example, use of cylindrical particle enhances the damping capacity by 9.6 % than a spherical particulate at a non-dimensional frequency of Ω~10.
8. The present model is capable to study the effect of process induced defects such as particulate breakage, presence of void in the metallic matrix and debonding at the metal-particulate interface on the overall energy dissipation capability of the MMC. Comparison against ideally bonded condition shows that these defects decrease the energy dissipation capability of the MMC due to poor force and heat transfer.
9. Presence of matrix defects like voids and cracks, adjacent to a reinforcement results in increased damping capacity than an ideal MMC condition.

Chapter 11

Effects of Nano Particle Reinforcement on MMC Damping

11.0 Introduction

Studies on micron sized SiC particle reinforcement in a ductile matrix such as Al exhibit good improvement in damping capacity. Another widely used ceramic reinforcement is Al_2O_3 that is more inert than SiC in Al and is resistant towards oxidation. Research findings also reveal that when the microstuctural features such as reinforcement dimension approaches less than 100 nm, the material exhibits novel behavior, which has grown into a special field of materials called Nano-Materials (NM) [205, 206]. The results of the literature search, however, reveal that no attempt is made to investigate the effect of particle size on the damping behavior of a ductile metallic matrix. Hence in this part of the study, damping capacity that indirectly signifies internal friction of a material is investigated for Al based metallic matrix as a function of length scale of alumina reinforcement. The work was further extended to Mg matrix so as to confirm the findings.

11.1 Materials and Processes

Case A: Three composite ingots with different alumina particle size viz., 10 μm, 0.3 μm and 50 nm (obtained from Baikowski, Japan) were prepared using the disintegrated deposition method (DMD) [2] and corresponding to volume percentage of 10.13, 1.47 and 0.94, respectively were hot extruded. The matrix used was pure Al (99.9% pure) and in order to overcome the problem of poor wettability of Al_2O_3 by Al, either the matrix is alloyed or the reinforcement is surface coated. Study shows presence of MgO on the surfaces of Al_2O_3 improves wettability [207], hence Mg is added ~ 4 wt.% to improve wettability of alumina to the pure Al matrix in the present study. A monolithic Al sample

containing same amount of Mg was also prepared for comparison through the same process route.

Table 11.1 Results of the case A monolithic and composite samples.

Specimen	A	B	C	D
Material description	Al-Mg	Al-Mg-0.05μm Al_2O_3	Al-Mg-0.3μm Al_2O_3	Al-Mg-10μm Al_2O_3
Al_2O_3 Vol. (%)	-	0.94	1.47	10.13
Al_2O_3 Wt. (%)	-	1.4	2.18	14.46
Mg Content (wt.%)	3.79	3.42	3.97	4.07
Grain Size (μm)	0.8 ± 0.1	0.4 ± 0.1	0.5 ± 0.1	0.7 ± 0.1
Grain Aspect ratio	1.3 ± 0.2	1.3 ± 0.2	1.4 ± 0.3	1.3 ± 0.2
Al_2O_3 Particle Size (μm)	-	0.05 ± 0.02	0.30 ± 0.15	8.03 ± 1.22
Al_2O_3 Particle Aspect ratio	-	1.6 ± 0.5	1.5 ± 0.3	1.4 ± 0.2
Density (g/cm^3)	2.641	2.662	2.646	2.657
Porosity (%)	0.056	0.114	0.041	1.033
Micro-hardness (HV)	68 ± 2.8	78 ± 1.5	74 ± 3.1	71 ± 4.2
Macro-hardness (HV)	67 ± 1.1	73 ± 1.5	69 ± 1.1	63 ± 2.7
Experimental mean CTE ($10^{-6}/^oC$)	27.6 ± 1.4	25.4 ± 0.9	26.8 ± 0.3	24.2 ± 0.4
Dyn. Modulus (GPa)	70	75	73	70
0.2 % Yield Str. (MPa)	219 ± 8	302 ± 3	233 ± 4	229 ±13
Ult. Tens. Str. (MPa)	320 ± 9	363 ± 25	342 ± 7	298 ± 7
Failure Strain (%)	11.8 ± 0.8	6.6 ± 0.6	11.1 ± 1	5.2 ± 1.0
Est. Inter particle distance (μm)	-	0.7	12.0	29.8
Est. disl. density (m^{-2}) per unit vol. fraction of alumina filler	-	2.63E13	1.21E12	1.64E11
Exp. Damp. loss factor η_{free}	0.0057	0.0088	0.0082	0.0075
% increase in damping per unit vol. fraction of Al_2O_3	-	58 %	30 %	3 %

Table 11.2 Results of density, CTE and hardness measurement of Mg and Mg/Al_2O_3 composites.

Wt. % of Al_2O_3	Vol. % of Al_2O_3	Density (g/cm^3)	Grain Size (micron)	CTE ($x10^{-6}/°C$)	Microhardness (HV)
-	0.000	1.7397	49 ± 8	28.4 ± 0.3	40 ± 0
0.5	0.224	1.7523	-	27.5 ± 0.1	51 ± 1
1.5	0.677	1.7470	-	ND*	56 ± 1
2.5	1.134	1.7623	14 ± 2	25.1 ± 0.3	66 ± 1

* ND: Not Determined.

Case B: Similarly, DMD technique was used to synthesize Mg (99.9% pure) reinforced with 0.5, 1.5 and 2.5-weight percentages of 50-nm sized Al_2O_3 particulates. For comparison, monolithic magnesium was synthesized using similar steps except that no reinforcement particulates were added.

Table 11.3 Results of damping measurement and prediction in the case of Mg and Mg/Al_2O_3 samples.

Wt. % of Al_2O_3	**Inter-particle spacing (μm)**	**Estimated plastic zone volume (%)**	**Estimated dislocation density (m^{-2})**	**Dynamic modulus (GPa) E_{dyn}**	**Exp. damping loss factor η_{free}**	**Increase in damping (%)**
-	-	-	-	42.77	0.011	-
0.5	1.06	0.3	7.74E+10	44.42	0.013	18
1.5	0.61	1.0	2.33E+11	45.14	0.014	27
2.5	0.47	1.7	3.91E+11	52.52	0.018	64

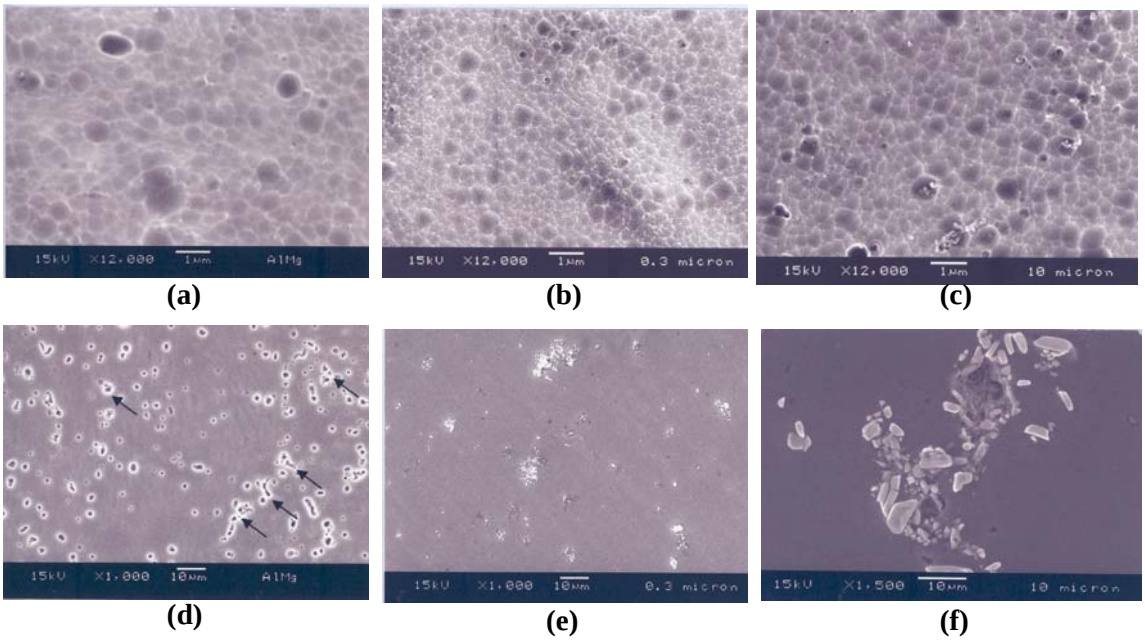

(a) **(b)** **(c)**

(d) **(e)** **(f)**

Fig. 11.1 Representative SEM micrographs showing: grain morphology of: (a) Al-Mg (b) Al-Mg-0.3 μm Al_2O_3 and (c) Al-Mg-10 μm Al_2O_3 and distribution of: (d) $Al_{12}Mg_{17}$ precipitates in Al-Mg matrix and typical clusters in (e) Al-Mg-0.3 Al_2O_3 and (f) Al-Mg-10 Al_2O_3.

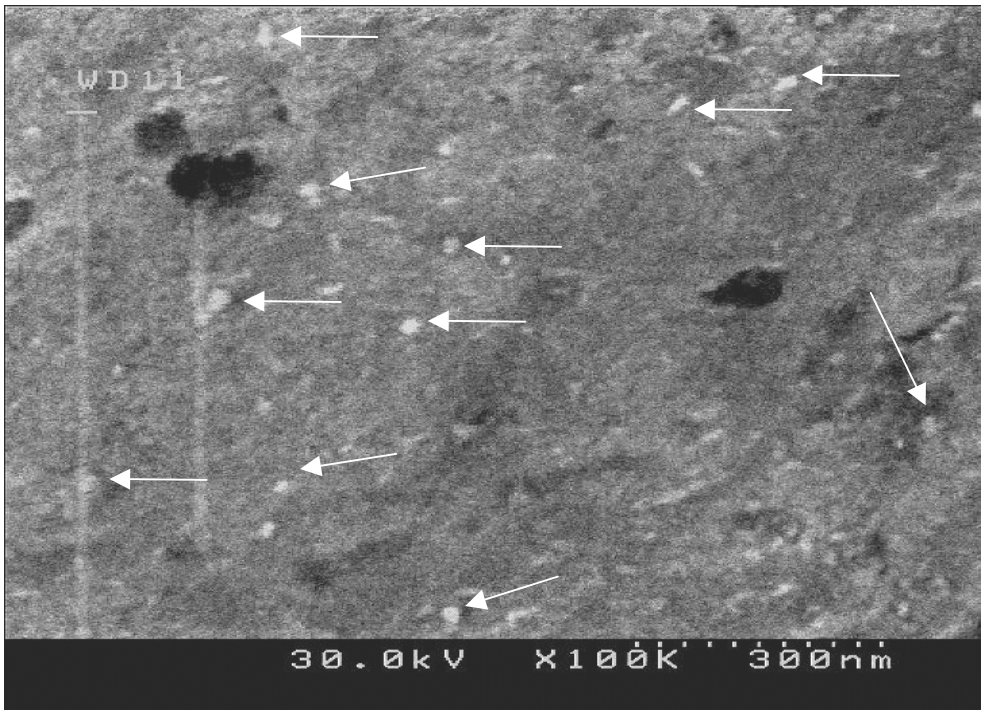

Fig. 11.2 Typical FESEM image showing nano-size Al_2O_3 particulate distribution in a Mg/2.5 vol.%Al_2O_3 sample.

11.2 Results

The results of the density measurements of the case A and B specimens obtained using Archimedes' principle [4] are listed in Table 11.1 and Table 11.2. The samples were polished and were examined using optical microscopy technique to determine the grain size. The coefficient of thermal expansion of the monolithic sample was determined on extruded samples using thermal-mechanical analyzer and the Vickers hardness (HV) was obtained using a digital micro-hardness tester (Matsuzawa model MXT50) [4]. Table 11.1 and 11.2 lists the hardness values of various specimen, which shows that a steady increase in hardness with decrease in particle size in the case of Al-Mg/Al_2O_3 sample, while with the increase in volume fraction the hardness increases in the case of Mg/Al_2O_3 samples. Tensile test results show for Case A samples, the decrease in particle size shows

a systematic increase in yield strength, tensile strength. Hence it is encouraging to observe the effect of particle dimension and particle volume fraction on the overall MMCs' thermo-mechanical properties.

Damping loss factor and elastic modulus were estimated using the impact-based "Free-Free" or "Suspended" beam method in accordance with ASTM C1259-98 standard [126]. Description of the experimental setup can be found in chapter 4, section 4.7. Table 11.1 lists the variation in damping loss factor with reduction in particle size, which clearly shows that as the particle approaches the nano-size from micron-size the damping capacity of the composite increases. Similarly, Table 11.2 shows the variation of damping loss factor with increase in volume fraction of alumina in Mg matrix, which confirms that there is a systematic increase in damping capacity of the composite with reinforcement volume fraction.

Field emission scanning electron microscope (FESEM) was used to study the nano-size Al_2O_3 particulate distribution in the metallic matrix. Fig. 11.1 shows the grain morphology, particle and precipitate distribution in the case A samples. Similarly, Fig. 11.2 shows a typical particulate distribution in an Mg/2.5 vol.%Al_2O_3.

11.3 Discussion

Close inspection of the alumina particle at high magnification illustrated good particle-matrix interfacial bonding in all the three composites investigated in the present study. In case A samples, this can be partly attributed to the efficacy of adding the elemental Mg in the Al matrix, which can be confirmed in terms of increased strength and stiffness (see Table 11.1). Uniform distribution of alumina particles with minimal

clustering was seen in all the composite samples and thus a isotropic behavior from a global perspective can be assumed.

Table 11.1 shows that the damping capacity of the case A composite samples increases due to the presence of alumina particles compared to the monolithic sample. Additionally, variation in η_{free} is seen to increase with decrease in alumina particle size. This can be expected due to high dislocation density at the particle-matrix interface, which can be observed in terms of increased hardness and yield strength due to work hardening of the metallic matrix [8], and can be estimated using a prismatic dislocation-punch model described as equation 5.5 (and are listed in Table 11.1). According to Granato-Lucke dislocation model, the dislocation behaves like an elastic string pinned between both sides due to any hard particles such as $Al_{12}Mg_{17}$ intermetallic precipitates, alumina particles or antiplane dislocations [29, 101] and under a low strain amplitude (below 10^{-4}) type cyclic load it bows, which introduces increased relative atomic movement in a crystalline lattice thus interfering with homogenous deformation of the bulk material. In the present experimental setup the strain magnitude induced in the specimen is of the order of 10^{-6} and hence the frequency dependent damping is applicable and is as follows [9]:

$$Q_f^{-1} \approx k\Lambda L^4 \qquad (11.1)$$

where k is a material constant, L is the effective dislocation loop length which depends on the inter-particle spacing and Λ is the total dislocation density which increases with decrease in alumina particle size (as shown in Table 11.1) thus contributes to increased dislocation-based damping characteristics in the composite samples. However, presence of clusters (see Fig. 11.1(e)) adversely affects the overall damping capacity [1].

Similarly for case B samples, the average sizes of alumina particulates was 50-nm. In general, uniform distribution of alumina particulates was observed in all the MMC samples and was confirmed based on the isotropic material behavior observed in terms of the elastic modulus in all the composite samples, from a global perspective. Table 11.3 lists the experimentally determined loss factor variation with an increase in weight percentage of Al_2O_3 in the magnesium matrix. It may be noted that the increase in damping of Mg is realised as a result of presence and increasing weight percentage of Al_2O_3 irrespective of the fact that Al_2O_3 has lower loss factor of the order of 0.0009 [12] as compared to magnesium, which has loss factor of the order of 0.011. Such an increase in the loss factor due to the addition of Al_2O_3 can be attributed to the Al_2O_3 associated intrinsic and extrinsic damping mechanisms as described in the forthcoming paragraphs. Table 11.3 lists the predicted increase in dislocation density with volume fraction that clearly shows there is a steady increase in dislocation density with increase in reinforcement volume fraction as observed in Chapter 5 for micron-sized reinforcement. This can be observed with the steady increase in hardness of the metallic matrix due to the work hardening during material processing, which is listed in Table 11.2. Based on equation (11.1) such an increase in dislocation will give rise to increased energy dissipation within the metallic matrix. The experiment results list in Table 11.3 confirms this hypothesis.

Another parallel damping mechanism occurs at the grain boundaries due to their sliding behavior in a viscous manner under a shear stress field. This process manifests itself in anelastic deformation and internal friction. Damping study on aluminium by $K\hat{e}$ [22] showed that polycrystalline microstructure had increased energy dissipation due to

increased presence of grain boundaries as compared to single crystal. During thermomechanical processing, the presence of alumina particles in the metal matrix stimulates grain nucleation. For micro-sized ceramic particulates grain refinement has been observed during thermomechanical processing (see Chapter 5). Based on the assumption of one grain per particle, the grain diameter D_{gb} is predicted for the conventional micron-sized ceramic particulates, as follows [208]:

$$D_{gb} = d\left(\left(1 - V_f\right)/V_f\right)^{1/3} \tag{11.2}$$

where d is the particle diameter and V_f is the volume fraction of reinforcement. With an assumption of 1.134 volume percentage of alumina and 50-nm particle diameter the final grain size can be estimated to be 0.22-μm. But based on experiment results listed in Table 11.3, grain size reduction is seen but not to that extent predicted by equation (11.2), in the composite sample containing 1.134-vol. percentage of alumina (14 μm) compared to the monolithic Mg sample (49 μm). Yet this grain size reduction (~ 71%) is significant and thus can enhance anelastic energy dissipation during a cyclic motion. Similar discussion hold good for Al-Mg/Alumina samples (case A) due to systematic decrease in grain size with particle dimension (see Table 11.1). Additional details on the effect of nano-grain size is discussed in the following chapter.

In addition, presence of voids in the metallic matrix also provides additional damping to the overall composite damping capability based on the studies of Zhang et al. [25]. Other damping mechanisms such as macro-elasto-thermodynamic damping can be seen to be insignificant in the present experimental study due to room temperature operation conditions, sample dimensions and frequency magnitude. But as shown in Fig. 10.1 as the particle dimension reduces additional ETD-damping at particle level increases

giving rise additional maxima with frequency and hence it is rewarding to use nano-sized particles as reinforcement.

The increase in the elastic modulus for case B samples with increase in weight percentage of reinforcement can be attributed to the higher elastic modulus of Al_2O_3, which is reported to be about 420 GPa [23] as compared to the monolithic Mg sample's elastic modulus value of 42.77 GPa, based on the present study (see Table 11.3). In addition, any presence of brittle oxide phases of magnesium in the metallic matrix are also expected to increase the overall composite's stiffness, due to their higher stiffness compared to the parent materials. In a previous study, Srikanth et al. [122] showed that various theoretical models such as the Shear Lag model, Halpin-Tsai model and the Eshelby model can be used to explain such an increase in the MMC's stiffness with reinforcement.

Studies of Trajanova et al. [209] have shown that 1 vol. % alumina with a particle diameter of 20 μm showed surprisingly lesser damping than the monolithic magnesium. However they did not discuss the reasons for this decrease in damping. Based on their material process description it is clear that they adopted a powder metallurgy route, which may have not provided enough chemical bonding between the matrix and the reinforcement. Solidification processing approach was thus used in the present study to enhance the chemical integrity of the Al_2O_3/Mg interface. In general, reduction of particulate diameter results in a significant increase in surface energy [210]. Hence in the present study nano size spherical particle was chosen as the reinforcement morphology so as to achieve increased surface energy so as to achieve better chemical bonding between the matrix and the reinforcement. The results of the studies of the various samples have

confirmed this hypothesis. Thus from the above discussions, it is encouraging to note that addition of hard nano-size alumina particulates improves the metallic matrix stiffness and damping properties significantly. Fig. 11.3 explains such an increase in damping loss factor (e.g. case B) help in achieving faster settling of the vibration in a structural system such as a beam with cantilever like support system (e.g. a satellite's antenna structure) and subjected to a initial unit deformation followed by free oscillations.

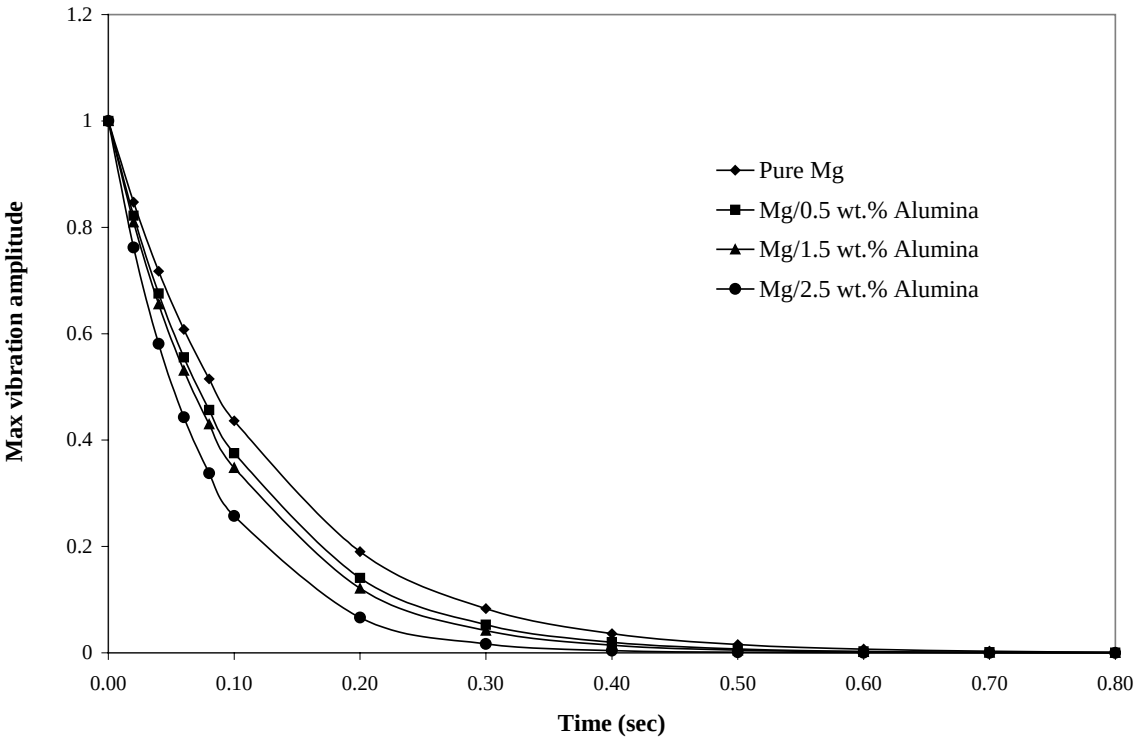

Fig. 11.3 Decay of vibration amplitude with time under different damping loss factor in a cantilever when subjected to a unit starting deformation.

11.5 Summary

Based on the present study following conclusions can be drawn:

1. The free-free beam type flexural resonance method can be successfully used with circle-fit approach to measure the damping characteristics of the magnesium

containing different volume fraction of nano-size alumina particulates.

2. Presence of alumina particles in Al matrix enhances energy dissipation irrespective of their size due to the various intrinsic damping mechanisms acting parallel.
3. The damping of Al increases with a decrease in alumina particle size for a fixed amount of alumina reinforcement. This can primarily be explained due to increase in dislocation density arising from an increase in surface area with a decrease in particle size.
4. An increase in damping of Mg with an increase in the weight/volume percentage of Al_2O_3 particulates can be attributed to a progressive increase in the energy dissipation due to simultaneous influence of various intrinsic and extrinsic damping mechanisms.
5. The hardness, elastic modulus and damping capacity of the pure magnesium matrix increased as a result of the increasing presence of Al_2O_3 particulates.

Related Publications:

[1] N. Srikanth, S. F. Hassan, M. Gupta, *J. of Comp. Mat.,* vol.38, Nov.2004, pp.2037 - 2047.

[2] N. Srikanth, X. L. Zhong, M. Gupta, Materials Letters, accepted, 2005.

[3] N. Srikanth, H. K. F. Calvin and M. Gupta, *Mat. Sci. Engg. A*, accepted, 2005.

Chapter 12

Effect of Nano Grain Size on Damping Capacity of Metallic Materials

12.0 Introduction

The potential of nanomaterials (NMs) to exhibit unusual combination of properties has been instrumental in fuelling extensive research activities across the world. More particularly, these materials have thrilled the material community due to the unconventional behavior in terms of mechanical, physical and chemical properties compared to a coarse-grain sized counterpart viz., higher hardness, higher strength and higher diffusivity [205, 206, 211]. Research shows that normal coarse-microcrystalline material behavior is approached when the grain size exceeds 100-nm [212].

As discussed in previous chapters damping property of a material reflects the ability of a material to dissipate mechanical energy. The dissipation of the mechanical energy takes place through the means of different energy transformation such as mechanical energy to caloric energy. In macro-grained metallic specimens presence of crystalline defects, elastothermodynamic and magnetoelastic effects contribute to the total damping. In addition to these mechanisms, in a NM, increased presence of microstructural defects, such as dislocations, grain boundaries, triple junctions, pores, etc., has been observed, compared to a micro-crystalline material (CM) [205]. Thus the damping study would help to understand the damping sources present and thereby describe the microstructure of the material indirectly.

Among different metallic materials, copper remains as one of the interesting material for the material community. The results of literature search have indicated that damping behavior of microcrystalline copper has been investigated [18] and the damping capacity depends on frequency, temperature and strain amplitude [14, 23]. No information, however, is available on the energy dissipation capability of nanocrystalline

bulk copper synthesized using the technique of mechanical milling (MM) coupled with hot extrusion. As mechanical milling remains one of the most industrially adaptable synthesis technique of high performance metallic materials, it is expected that the properties (such as stiffness and damping properties) of the NMs synthesized using mechanical milling will be of paramount importance to a design engineer especially for designing dynamic systems.

Accordingly, the variation in the microstructure of a NM type pure copper is studied in terms of damping capacity. The pure Cu based NM sample was prepared using the methodology of mechanical milling coupled with hot extrusion excluding sintering step. The room temperature damping behaviour was determined using a free-free type suspended beam technique utilizing frequency domain based circle-fit approach. The damping loss factor, η thus computed for a NM was further compared with that of the micro-grain size copper samples.

12.1 Materials and Processes

In the present work, Copper particles of 99 percent purity and less than 50 micron size (supplied by Goodfellow, England) and stearic acid (> 99.5% purity, supplied by Sigma-Aldrich, Switzerland) were used as the starting materials. The primary processing consisted of mechanical milling (MM) 50 grams of copper powder and 1 wt. % of stearic acid together at room temperature using a FRITSCH Pulverisette 5 planetary ball mill at 250 rpm for 10 hours (denoted as 10h-MMed samples). Next, the mechanically milled (MMed) powder was loaded into the 35mm-diameter compaction die lubricated by dry graphite lubricant and were subsequently cold-pressed uniaxially at 70 tons using a

hydraulic press. The secondary processing consisted of hot extrusion of the cold-compacted sample at an extrusion ratio of 12.25:1 to form a 10-mm diameter extruded rod. Further, for comparison, samples without MM were made (denoted as 0h-MMed samples) by cold compaction of the elemental powder without performing mechanical milling. The extrusion pressures of 0h-MMed samples and 10h-MMed samples were maintained close to ~70 tons and ~80 tons, respectively. The extrusion die temperature was maintained at 400°C throughout the extrusion process. The powder compact was soaked at 700°C for 0h-MMed sample and 600°C for 10h-MMed sample prior to extrusion. The different temperatures were used to maintain the average grain size in nanometer range and to avoid surface cracks. For comparison, a micro-grain size Cu sample (from Goodfellow^{TM}, England) of high purity (99.99%) under as-drawn condition was also tested.

12.2 Results

Grain Size Estimation

The microstructural characterization of the elemental powder, mechanically milled powder and the extruded samples was performed using Shimadzu Lab-XRD-6000 X-ray diffractometer with Cu-Kα radiation operated at 40 kV and 30mA, and at a scan speed of 2°C/min. Fig. 12.1 shows the X-ray diffraction spectra of the initial powder and final extruded nano-Cu samples. Based on these XRD data, the crystalline size of the nano-Cu samples were calculated using Sherrer equation [213]. The estimated results of the grain size are listed in Table 12.1. Grain size of the micro-grain sized Cu sample was measured using standard metallographic methods.

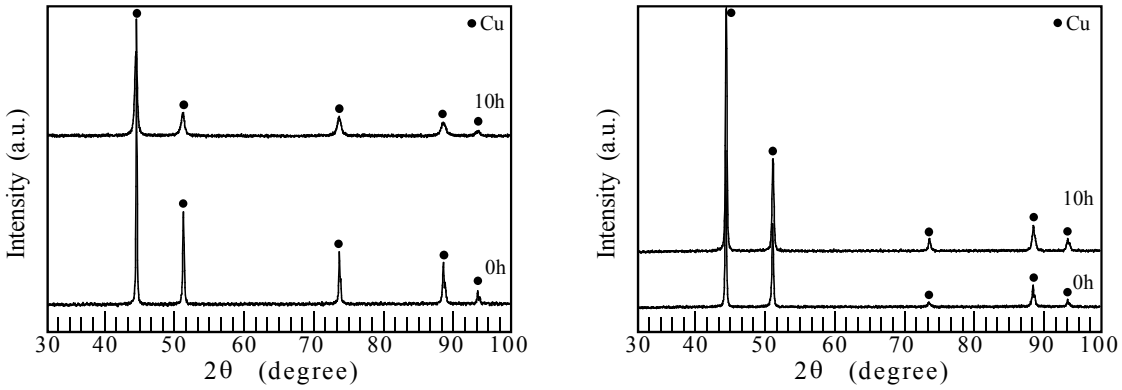

Fig 12.1 X-ray diffraction spectra of: (a) MMed pure Cu powder and (b) MMed extruded Cu at different milling durations.

Density Measurement

The results of the experimental density values measured using Archimedes' principle are listed in Table 12.1.

Hardness Testing

The results of microhardness measurements carried out on the NM and CM samples are summarized in Table 12.1. It may be noted that the 10 hr milling leads to an increase in the average value of hardness by ~ 186 % when compared to 0h-MMed sample. The corresponding grain size reduction was ~ 33 %.

Coefficient of thermal expansion

The results of CTE measurements in the temperature range of 50-600^{o}C (refer Table 12.1) revealed that milling does not affect the CTE of the bulk-extruded copper even when the grain size difference is about 36-nm. The results are in accordance with the grain size-CTE trend predicted by researchers elsewhere [206].

Table 12.1 Results of microstructural and damping studies of nano-Cu samples.

Sample details	Milling duration (hr)	Density (g/cm^3)	MMed powder size	Grain size after extrusion	Hardness (HV)	CTE (ppm/ ^oC)	Dyn. elastic mod. E_d (GPa)	Damp. loss factor η_{free}
Nano-Cu-0hrMMed	0	8.8547	156 nm	99 nm	53±1	21.23±0.41	128.1	0.0020
Nano-Cu-10hrMMed	10	8.2208	25 nm	63 nm	152±2	21.19±0.17	109.7	0.0074
Micro-Cu	-	8.96 *	-	20.6 μm	109±2	17.0 *	117	0.0068

* denotes from reference [214].

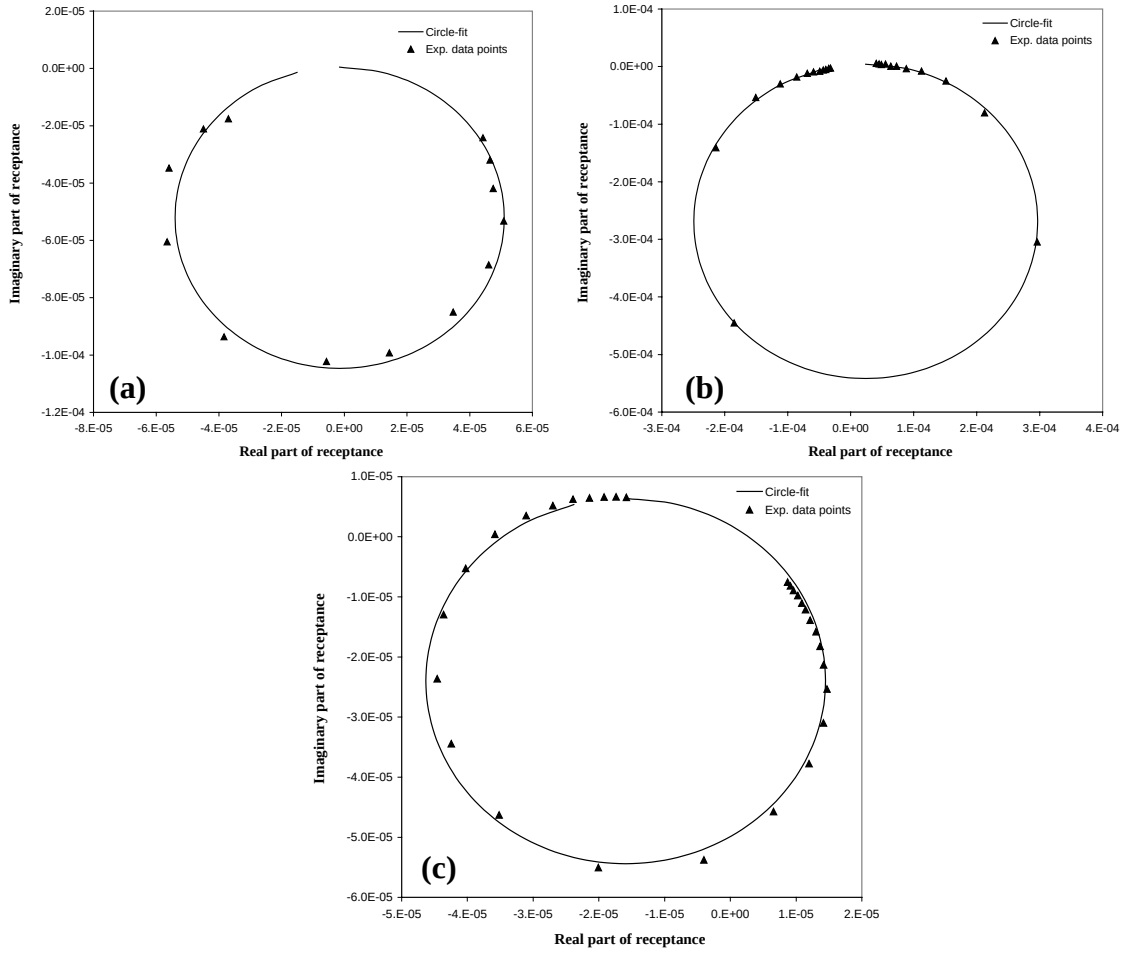

Fig. 12.2 Typical receptance frequency response function (FRF) showing: (a) Actual FRF data for the 0-h MMed sample. (b) Actual FRF data for the 10-h MMed sample. (c) Actual FRF data for the micro-grain Cu sample.

Suspended Beam Vibration Testing

Suspended beam vibration testing was used in the present study and Fig. 12.2 shows the typical circle fit plots for the various samples used in this study. The damping loss factor η_{free} and the dynamic elastic modulus E_d for NM and CM Cu-samples corresponding to both 0 hr and 10 hr mechanical milling condition and are listed in Table 12.1.

12.3 Discussion

Table 12.1 lists the damping loss factor of the 0 hour and 10 hours mechanically milled nano-Cu samples. Comparison shows that the additional milling process results in the increase of the damping loss factor and a subsequent decrease in dynamic elastic modulus. The results can be explained based on the presence of residual stress induced due to the milling process as described in the forthcoming paragraphs.

As explained in chapter 2, metallic materials possess different forms of damping sources which exists in parallel due to various relaxation processes, such as, point defect relaxation, dislocation motion, grain boundary sliding, inclusion-matrix friction, magnetoelastic effects, and elasto-thermodynamic effects. In addition to these mechanisms, a nano-crystalline metallic material have increased presence of interfacial defects such as grain boundaries, triple junctions, and elastically distorted layers, compared to the conventional coarse-crystalline material [205, 206, 211]. In a NM, dislocations are said to be present in a lesser quantity and are expected to be sessile (immovable) in configuration. This is based on the theory that the existence of image forces in finite atomic ensembles tends to pull the mobile dislocations out of the grains.

But TEM based deformation studies of Youngdahl et al. [215] on nanocrystalline Cu samples with grain size ~100-nm shows that the dislocation activity is quite dominant and is active up to a grain size of ~ 30-nm. In the present study, the additional milling process provided to the 10hr-MMed sample is expected to have contributed high density of sessile dislocations in the microstructure compared to the 0hr-MMed sample. Studies of Le Brun et al. [216] shows that the ball milling of Cu powders results in inhomogeneous deformation that can be observed as deformation substructures (like striations) in the grains using SEM and TEM. Thus their study showed that the mechanical milling of the powders increases the microhardness by a factor of 2.5 as a result of work hardening and due to the reduction in the grain size. Similar increase in the hardness, by a factor of ~3 (from 53 Hv to 152 Hv) has been observed in the present study (see Table 1) with a simultaneous reduction in grain size by a factor of one-third. The effect of grain size reduction on the hardness H_v can be deduced using the Hall-Petch relationship for nanocrystalline Cu up to a grain size of 5-nm [202].

$$H_v = H_o + kd^{-0.5} \tag{12.1}$$

where H_o and k are the material constants and d is the grain size diameter. For nano-Cu, the Hall-Petch constants are found to be viz., H_o and k are ~0.4 GPa and ~9, respectively [217]. Hence in the present study, the grain size reduction from 99-nm to 63-nm can attribute to an increase in hardness by a factor of only ~ 18 % which does not explain the experimental results of hardness showing an increase of 186 %. This clearly shows that work hardening is prominent due to high density of micro-plastic zones in the form of sessile dislocations that has accumulated in the microstructure. High resolution electron microscopy (HREM) studies of Ganapathi and Rigney [218] on nano-Cu samples have

confirmed that cells bounded by cell-walls are formed due to severe deformation under sliding condition. The cell walls are full of dislocations, which arrange themselves so as to minimize energy. Thus from the above discussions, increased hardness can be seen as increased micro-plastic zones.

In the present study, the damping characteristics of the micro-grain sized sample also shows a damping loss factor of 0.0068 which is comparatively higher than that of an annealed Cu sample which possess a damping loss factor of 0.0011 [219]. This significant increase in the damping is also due to the presence of presence of residual stress which can be seen in terms of increased hardness of 109 Hv compared to an annealed Cu sample which has a hardness of 47 HB (~52 Hv) for a grain size of 0.07 mm. Based on reference [220], the increase in hardness is mainly due to work hardening in micro-grain sized copper samples which is the well known mechanism for increasing the strength. Thus the increased energy dissipation due to the presence of process induced residual stress in nano-grain sized copper samples agrees well with the observation of micro-grain sized copper samples.

Studies of other researchers on metallic materials have clearly shown the dependencies of η on temperature, frequency and strain amplitude, which provide a large amount of important information on the mechanisms of micro-plasticity on the relaxation behavior of the metallic materials [14, 16, 18]. Mulyukov et al. [221] have shown that the severely deformed sub-micron-grained copper samples exhibit exponentially varying damping capacity with an increase in strain amplitude. Their study shows that the damping loss factor of the cold worked sample was around 0.00238. Furthermore, carrying out an annealing process above the temperature of 250 ^{o}C, on these severely

deformed samples, drastically reduced the overall damping capacity by a factor of 5. This clearly shows that the accumulation of the residual stress in the form of the micro-plastic zones contributes significantly to the intrinsic damping capacity of the material.

Based on the Granto-Lucke theory, the sessile dislocations with pinned configuration by any two obstacles such as the impurity atoms or antiplane dislocations can also be seen to aid the overall energy dissipation capability. They behave like an elastic vibrating string in an electron and phonon environment [29]. Under low strain amplitude the damping depends on the dislocation density, frequency of cyclic stress and burgers vector b of the bulk material as follows:

$$Q_f^{-1} \approx k\Lambda L^4 \tag{12.2}$$

where k is a material constant, L is the effective dislocation loop length which depends on the inter-particle spacing and Λ is the total dislocation density.

Based on the theory of anelasticity, presence of the internal dislocations can also be inferred in the form of a decrement in the elastic modulus, which can be expressed as follows:

$$\frac{\Delta E}{E} = A\Lambda L^2 \tag{12.3}$$

where A is a material constant. From Table 12.1, a decrement of 14% between the 0h-MMed sample and 10h-MMed sample can be observed in terms of elastic modulus, which indirectly confirms the presence of high dislocation density. This is similar to the decrease in the elastic modulus of a micro-grain size sample that has an elastic modulus of 117 GPa (see Table 12.1), which is less than the elastic modulus of an annealed copper sample (125 GPa [220]) by 6.4%.

In addition to the above discussions on dislocation density, grain boundaries in a metallic material are also considered as defects since they are not in a perfect crystalline condition and lack long-range periodicity found in a typical crystal [206]. Based on a spherical or a cubical grain shape assumption, the volume fraction of nanocrystalline materials associated with the boundaries 'V' can be calculated [205]:

$$V = 3\lambda / d \qquad (12.4)$$

where λ is the average grain boundary thickness and d is the average grain diameter. Generally in a nano-material the grain boundary thickness varies from 0.5-1 nm [222]. Hence compared to a polycrystalline sample containing 10-μm grain size, a 60-nm nano-sample can contain as much as 5% of atoms in the grain boundary region while the polycrystalline sample is expected to contain only 0.03% of atoms. Such non-crystalline nature are synonymous to amorphous condition under definition, and are condensed phases that are not in thermodynamic equilibrium [223]. These solids, behave similar to the polymeric materials that are known to exhibit viscoelastic material behaviour. Experiments have been conducted on pure amorphous metallic materials which exhibit clear glassy state, evidenced by a discontinuous change in the thermo-physical properties, such as, the shear modulus, heat capacity, coefficient of expansion thermal, etc [223]. In the NM, such a frequency dependent behavior can be seen based on the mechanical spectroscopic studies of Bonneti et al.[224]. The anelasticitiy due to grain boundaries in metals is because of viscous nature, which transforms the mechanical energy in to caloric energy [14]. Kê's damping study on single crystal versus polycrystalline aluminium clearly shows that increased presence of grains increases the damping tremendously at high temperature around 200-300^{o} C [22]. In the present study, the experiments are

performed at room temperature and hence the grain boundary sliding can be presumed to be insignificant based on a coarse polycrystalline material model. But according to Siegel [225], grain boundary diffusion and grain boundary sliding are enhanced in a NM and hence the validity of Ke's studies may need to be investigated further for a nano-crystalline microstructure. Literature review shows that the damping measurement results of copper with coarse-crystalline microstructure and single-crystal microstructure are 0.0011 [153] and 0.0003 [18], respectively. In the present study, the 0h-MMed sample, which is expected to have relatively lesser residual stresses compared to 10h-MMed sample and belongs to a class of NM, exhibits a damping loss factor of 0.0020. But care should be taken to account the increased presence of nano-pores in the grain boundaries in a NM material [211], on the damping capacity of the matrix [140]. To understand the effect of grain boundary on mechanical properties, the coefficient of thermal expansion (CTE) can be taken for investigation. The CTE exhibits the combined expansion behavior of the grains and the grain boundaries in a metallic material. In the present study, the thermal expansion of both 0hr and 10hr MMed samples exhibits similar CTE results of 21.2×10^{-6} K^{-1} and are higher than the CTE results of both single-crystalline Cu sample and coarse-crystalline Cu sample which are around 16×10^{-6} K^{-1} [226] and 17×10^{-6} K^{-1} [227], respectively. Thus the presence of increased volume fraction of grain boundary in the NM sample can be seen in increasing the damping loss factor and thermal expansion behavior on a relative scale.

In addition to the above damping mechanisms, extrinsic damping sources exist under a cyclic load in a metallic material. Zener's research showed that when a material is stressed in a reversible adiabatic process, thermal gradient is induced in accordance

with the Thomson effect [15]. Heat conducts from the high temperature regions to the low-temperature regions. However small this temperature increase, this is viewed as a loss of energy and is known as elasto-thermodynamic damping (ETD) [15]. In the present study, using the thermo-mechanical properties of copper the magnitude of the macro-thermoelastic damping was predicted using the appropriate ETD model explained in chapter 10 and was found to be of the order of 10^{-5} due to the beam dimensions (diameter ~10mm) and the resonant frequency magnitude (which was around 700 Hz), that does not seem to be significant to explain the experimental observation. But nano-pores can give rise inhomogenity and cause hydrostatic stress to arise which may result in micro-thermoelastic damping that can be determined using the analytical and numerical models explained in chapter 10.

12.4 Summary

Based on the present study, following conclusions may be drawn:

1. The free-free beam type flexural resonance method can successfully be used with circle-fit approach to measure the damping characteristics of microcrystalline and bulk nanostructured copper samples.
2. Addition of the mechanical milling process step during the synthesis of the NM alters the microstructure and thereby increases the damping capacity and reduces the dynamic modulus of copper.
3. An increase in the overall energy dissipation and reduction in dynamic modulus in the case of 10h-MMed Cu sample when compared to the 0h-MMed Cu sample can

primarily be attributed to the increase in the process induced micro-plastic zones which matches well with the dynamic property of a micro-grain size Cu sample.

Related Publications:

[1] N. Srikanth, M. A. Thien and M. Gupta: *Mat. Sci. and Engg. A.*, Vol. 366 (2004) 38-44.

Overall Conclusions

Following conclusions may be drawn from the present study:

1. The free-free beam type flexural resonance method can successfully be used with circle-fit approach to measure the damping characteristics of the unreinforced and the reinforced metallic samples. This method can be extended to study bulk nano materials also.
2. In general, the damping of the pure magnesium and pure aluminium matrix increases as a result of presence of SiC particulates.
3. An increase in damping with an increase in the weight/volume percentage of micron sized SiC particulates can be attributed to a progressive increase in the energy dissipation. This is confirmed in both Al and Mg based matrix. The energy dissipation can primarily be attributed to the simultaneous influence of increase in volume percentage of plastic zone and increase in dislocation density.
4. Use of stiff metal particulates, such as Ti, seems to be a viable choice to enhance damping. Progressive increase in damping was observed with an increase in volume fraction of reinforcement.
5. Interestingly, when the reinforcement is inter-connected it provides further enhancement in damping similar to the enhanced stiffness it provides.
6. Further, use of a hybrid combination of two different reinforcements also shows enhanced damping within the metallic samples. This observation was confirmed in three different case studies with different formulation Mg/Ti/SiC, Al/Fe/SiC, and Al/Ge/SiC.
7. The FEM based cell model used in the present study enables the determination of damping loss factor of composites due to the presence of residual plastic zones

induced due to thermal mismatch during cooling from extrusion temperature to room temperature. The results matches well with experimental results obtained from impact based suspended beam experiments, which corresponds to low strain amplitude condition. Numerical results also show similar increasing trend in damping loss factor with weight percentage of SiC and Ti added in the metallic matrix, consistent with the experimental observation of suspended beam experiments. Also the model can be used to study hybrid composites such as Al/SiC/Ge which micmics similar to the experiment results. Effect of stress concentration due to sharp faceted particulates increases the energy dissipation capability of the metallic matrix due to the increased presence of plastic zone.

8. The present model is capable to study the effect of process induced defects such as particulate breakage, presence of void in the metallic matrix and debonding at the metal-particulate interface on the overall energy dissipation capability of the MMC. Comparison against ideally bonded condition shows that these defects increase the energy dissipation capability of the MMC.

9. In the present study, there was no significant macro-ETD damping due to chosen specimen dimension and operational frequency, as well as no grain boundary damping due to room temperature operation conditions. ETD damping is purely a thermo-mechanical phenomenon which is non-destructive in nature compared to microplastic damping. It can be tailored for a given application whose vibration parameter such as amplitude and frequency are known. ETD-damping becomes dominant at higher frequencies (ultrasonic frequencies) yet they seem to contribute up to 25% of the total enhancement in overall damping capacity of Al

based composites, for example. Secondly, in this study the unit-cell model seems to be viable choice to visualize the stress pattern and heat flow pattern in and around the matrix-reinforcement interface.

10. Presence of alumina particles in Al matrix enhances energy dissipation irrespective of their size due to the various intrinsic damping mechanisms acting parallel. The damping of Al increases with a decrease in alumina particle size (from micron size to nano size) for a fixed amount of alumina reinforcement. This can primarily be explained due to increase in dislocation density arising from an increase in surface area with a decrease in particle size.

11. Similarly, an increase in damping of Mg with an increase in the weight/volume percentage of Al_2O_3 particulates can be attributed to a progressive increase in the energy dissipation due to simultaneous influence of various intrinsic and extrinsic damping mechanisms. The hardness, elastic modulus and damping capacity of the pure magnesium matrix increased as a result of the increasing presence of Al_2O_3 particulates.

12. An increase in the overall energy dissipation and reduction in dynamic modulus in the case of 10h-MMed Cu sample when compared to the 0h-MMed Cu sample can primarily be attributed to the increase in the process induced micro-plastic zones which matches well with the dynamic property of a micro-grain size Cu sample. Addition of the mechanical milling process step during the synthesis of the NM alters the microstructure and thereby increases the damping capacity and reduces the dynamic modulus of copper.

Future Recommended Work

Following topics can be aimed for further work to extend the present study:

1. The free-free beam type flexural resonance method can be modified to account variation in temperature. Secondly it can be modified with a forced vibration source through a string at a anti-node of the specimen. Hence a sine-sweep can be performed to determine the damping at different frequencies. Also the applied force amplitude can be modified to vary the strain amplitude in the specimen.
2. Further research can aim to segregate the overall damping capacity to individual damping mechanisms such as grain boundary effects, dislocations, residual stresses, etc. This can be achieved by performing damping studies under pure shear, flexural and axial conditions as well as different experimental conditions such as temperature (Room temp to 500 ^{o}C) , strain amplitude (10^{-6} to 10^{-1}) and frequency (1 Hz to MHz range), so as to understand the contribution of each mechanisms.
3. Numerical models should be designed using Molecular Dynamics (MD) and Monte Carlo (MC) methods to study the energy dissipation at the interface under higher surface energy and thus extend this work to study damping effects in nano-materials.

References

[1] Cyril M. Harris, *Shock and Vibration Handbook*, 3rd edition, McGraw Hill Book Company, San Francisco, 1987.

[2] Eugene L. Rivin, *Stiffness and Damping in Mechanical Design*, Marcel Dekker Inc., New York, 1999.

[3] Denys J. Mead, *Passive Vibration Control*, John wiley and sons, New York, 1999.

[4] Anton Puskar, *Internal Friction of Materials*, Cambridge International Science Publishing, Cambridge, 2001.

[5] R. D. Cook, D. S. Malkus and M. E. Plesha, Concepts and applications of finite element analysis, third edition, John Wiley and Sons, New York, 1989.

[6] Details of Tacoma Bridge published in: http://www.vibrationdata.com/Tacoma.

[7] Details of Canadram Robot published in: http://www.space.com/news/hubble.

[8] M. F. Ashby, *Materials selection in mechanical design*, Boston, Butterworth-Heinemann, 1999.

[9] C. T. Sun, and Y. P. Lu, *Vibration Damping of Structural Elements*, Prentice Hall , Englewood Cliffs, New Jersey, 1995.

[10] P. A. Zinoviev, Y. N. Ermakov, *Energy dissipation in composite materials*,, Technomic Publication Company, Lancaster, PA, 1994.

[11] B. Terry and G. Jones, *Metal Matrix Composites – 'Current developments and future trends in industrial research and applications*, Elsevier science publishers, Oxford, England, 1990.

[12] T. W. Clyne and P. J. Withers, *An introduction to metal matrix composites*, Cambridge university Press, Australia, 1993.

[13] M. D. Huda, M. S. J. Hashmi and M. A. El-Baradie, *Key engineering materials*, 104-107 (1995) 37-64.

[14] A. Nowick, and B. Berry, *Anelastic Relaxation in Crystalline Solids*, Academic press, New York, 1972.

[15] C. Zener, *Elasticity and Inelasticity of Metals*, University of Chicago Press, Chicago, 1948.

[16] R. D. Batist, *Internal friction of structural defets in crystalline solids*, American Elsevier Publishing Company, NewYork, 1972.

[17] A. M. Freudential, *The inelastic behavior of Engineering Materials and Structures*, John Wiley and Sons, New York, 1950.

[18] B. J. Lazan, *Damping of Materials and Members in Structural Mechanics*, Newyork, Pergamon Press, 1968.

[19] A. D. Nashif, D.I.G. Jones, J. P. Henderson, *Vibration damping*, Wiley, New York, 1985.

[20] Eds. A. Rivere, V. Pelsoin, and P. Gadaud, *Internal Friction and Ultrasonic Attenuation in Solids*, Presented in Eleventh Internal Conference of ICIFUAS 11, Journal De Physique IV, Poistiers, France, 1996.

[21] . J. Lavernia, R. J. Perez, and J. Zhang, *Metallurgical and Materials Transactions* A, vol. 26A (1995) pp. 2803-2818.

[22] T. S. K$\hat{e}$, *Physical Review*, 71 (1947) 533-546.

[23] V. K. Kinra, and A. Wolfenden, *M^3D: Mechanics and Mechanisms of Material Damping*, ASTM STP. 1169, American Society of Testing Materials, Philadelphia, 1993.

[24] D. Hull and D. J. Bacon, *Introduction to Dislocations*, Fourth Edition, Butterworth Heinemann, Boston, 2001.

[25] A. R. Rosenfield, G. T. Hahn, A. L. Bernent, R. I. Jaffee, *Dislocation Dynamics*, McGraw Hill Book Company, 1968.

[26] E. J. Lavernia, J. Zhang, and R. J. Perez, *Key Engineering Materials*, 104-107 (1995) 691-728.

[27] Z. Xiaonong, Z. Di, W. Renjie, Z. Zhenggang and W. Can, *Scrita Materialia*, 37(11) (1997) 1631-1635.

[28] R. J. Perez, J. Zhang, E. J. Lavernia, *Scripta Materialia*, 27 (1002) pp. 1111-1114.

[29] A. Granato, and K. Lucke, *Journal of Applied Physics*, 27 (1956) 583-593.

[30] B. M. DeKoven, A. J. Gellman, R. Rosenberg, *Interfaces between polymers, metals, and ceramics*, Materials Research Society, California, U.S.A. , 1989.

[31] D. Wolf and S. Yip, *Materials interfaces, atomic-level structure and properties* Chapman & Hall, London, 1992.

[32] J. M. Howe, *Inter. Mater. Rev.*, 38 (1993) 257.

[33] K. A. Mauritz, E. Baer and A. J. Hopfinger, *J. Polymer Sci.*, Macromol. Rev., 13 (1978) 1.

[34] D. E. Luzzi, *Ultramicroscopy*, 30 (1989) 132.

[35] I. Kaur, Y. Mishin, W. Gust, *Fundamentals of grain and interphase boundary diffusion*, John Wiley , New York, 1995.

[36] B. Gruber, *Theory of crystal defects*, Academic Press, New York, 1966.

[37] J. M.Howe and R. Gronsky, in *Proceedings of the 44 th Annual Meeting of the electron Microscopy Soceity of America,* G. W. Baiely, Ed., Scan Francrisco Press, CA (1986) p. 552.

[38] A. Ourmazd, D. W. Taylor, M. Bode and Y. Kim, *Science,* 246 (1989) 1571.

[39] J. W. Cahn and J. E. Hilliard, *J. Chem. Phys.*, 28 (1958) 258.

[40] J. M. Howe, in Proceedings of the I*nternational Conference on Martensitic Trnasformations* (ICOMAT-92) C M. Wayman and J. Perkins, Eds., Monterey Institute of Advanced Studies, Carmel, CA (1993) p. 185.

[41] R.Becker, *Ann. Phys.*, 32 (1938) 128.

[42] G. Rao, J. M. Howe and P. Wynblatt, *Acta Metall. Mater.*, (in press)

[43] A.F. Schwatzmann, in *High Resolution Electron Microscopy of Defects in Materials*, R. Sinclair, D. J. Smith and U .Dahmen, Eds., *Materials Research Soceity Symposium Proceedings*, vol. 183, Materials Research Society, Pittsburgh, PA (1990) p.161.

[44] D. Turnball, in *Impurities and Imperfections,* American Society for Metals, Metals Park, OH (1955) p. 121.

[45] F. C. Frank and J. H. Van der Merwe, *Proc. Roy. Soc.* 198A (205) (1949) 216.

[46] J. H. Vander Merwe, *Proc. Phys. Soc.*, 63A (1950) 616.

[47] U. Dahmen, Microsc. *Soc. Am. Bull.*, 24, 341 (1994).

[48] G. Z. Voyiadjis, P. I. Kattan, *Damage mechanics*, Taylor & Francis publishers, Boca Raton, 2005.

[49] V. Bermudez, *Appl.Phys. Letters*, 42 (1983) 70.

[50] B. K. Rao and P. Jena, *Appl. Phys. Letters*, 57 (1990) 2308-2310.

[51] S. Ranganathan, *Interfaces: structure and properties*, Trans Tech Pub, Aedemannsdorf, Switzerland, 1993.

[52] A. Kostka, J. Lelatko, M. Gigla, H. Morawiec and A. Janas, *Mat. Chem. And Physics*, 81 (2003) 323-325.

[53] S. Li, R. J. Arsenault and P. Jena, *J. Appl. Physics*, 64 (1988) 6246.

[54] S. S. Kistler, *J. Am. Ceram. Soc*. 45(1962) 59-68.

[55] R. Raj, A. Saha, L. An, D. P. H. Hasselman, P. Ernst, *Acta Materialia*, 50 (2002) 1165-1176.

[56] A. M. Stoneham and P. W. Tasker, *J. Phys.*, 49 (1988) 99-113.

[57] C. Kruse, M. W. Finnis, V. Y. Milman, C. Payman, A. D. Vita, M. J. Gillman, J. *Am. Cer. Soc.*, 77 (1994) 431.

[58] J. C. Romero, L. Wang and R. J. Arsenault, Mat. Sci. and Engg. A, 212 (1996) 1-5.

[59] I.L. Singer, S. Fayeulle, P. D. Ehni and R. G. Vardiman, *Appl. Phys. Lett.* 65 (1994) 3191-3193.

[60] T. Sritharan, L. S. Chan, L. K. Tan, N. P. Hung, *Materials Characterization*, 47 (2000) 75-77.

[61] J. Lloyd, I. Jin, *Metall. Trans A.* 19A (1988) 3107-3109.

[62] T. Fan, Z. Shi, D. Zhang, R. Wu, *Mater. Sci. Eng.* A257 (1998) 281-6.

[63] L. M. Tham, M. Gupta, L. Cheng, *Mater. Sci. Eng.* A354 (2003) 369-376.

[64] H. Du, Z. Yang, M. Libera, D. C. Jacobson, Y. C. Wang, and R. F. Davis, *J. Am. Ceramic Soc.,* 76 (1993) 330.

[65] R. D. Evans and J. D. Boyd, *Scripta Materialia,* 49 (2003) 59-63.

[66] P L. Ratnaparki and J. M. Howe, *Acta Metall. Mater.* 42 (1994) 81.

[67] J. Sun, *Int. J. Fracture* 44 (1990) 51.

[68] V. P. Carey, *Liquid Vapour Phase Change Phenomena,* Hemisphere Publishing Corporation, Washington, 1992.

[69] A.G.Evans, M.Ruhle, B.J.Dalgleish and P.G.Charlambides, *Materials Science And Engineering* A126 (1990) 53-64.

[70] R. Warren, C. H. Anderson, *Silicon carbide fibers and their potential for use in composite materials,* Part II, *Composite*s, April 1984, pp. 101-111.

[71] W. Kohler, *Aluminum* 51 (1975) 443-447.

[72] D. C. Haverson, A. J. Pyzik, I. A. Aksay, *Processing and micro structural characterization of B_4C/Al cermet, in: Proceedings of the ceramic Engineering and Science,* American Ceramic Society, July-August 1985, pp. 736-744.

[72] S. M. Wolf, A. P. Levitt, J. Brown, *Chem. Eng. Prog.* 62 (1966) 74-78.

[73] M. Kobashi, T. Choh, *J. Mater. Sci* 28 (1993) 684.

[74] V. Agarwala, D. Dixit, Trans. *Japan, Inst. Met.* 22 (1981) 521-526.

[75] H. Ribes, R.Dasilva, M.Suery, T. Breteau, *Mater. Sci. Tech.* 6 (1990) 621.

[76] L. N. Thanh, M. Suery, *Scripta Metall*. 25 (1991) 2781.

[77] T. W. Clyne, *Proceedings of ICCM-VI* and ECCM-2, vol. 2, Elsevier, Amsterdam, 1987, pp. 275-286.

[78] T. Nami, Y. Osawa, M. Kikuchi, IMONO, *J. Japan Foundryman's Soc.* 56 (1984).604-609.

[79] R. Lingon, *Rech. Aerospat*, 1 (1974) 49.

[80] T. Young, *Trans. R. Soc.* 95 (1805) 65.

[81] V. Laurent, D. Chatain, N. Eustathopoulos, *Mater. Sci. Eng.* A 135 (1991) pp.9-94.

[82] F. Delannay, L. Froyen, A. Deruyttere, *J. Mater. Sci.* 22 (1987) 1-16.

[83] T. W. Chou, A. Kelly, A. Okura, *Composites* 16 (1985) 187.

[84] H. Landis, J. Unnam, S.V.N. Naidu, W. Brewer, *Sampe Quaterly*, July 1981, p. 19.

[85] T. Ishikawa, J. Tanaka, H. Teranishi, T. Okamuara, T. Hayase, *US patent, 440-571*, 1981.

[86] D. M. Goddard, *Met. Prog.* 125 (1984) 49.

[87] B. C. Pai, P. K. Rohatgi, *Mater. Sci. Eng.* 21 (1975) 161.

[88] M. F. Amateau, *J. Comp,* 10 (1976) 279.

[89] L. Aggour, E. Fitzer, M. Heym, *Thin solid Films,* 40 (1977) 97.

[90] R. Warren, C. H. Anderson, *Silicon carbide fibers and their potential for use in composite materials*, Part II, Composites, April 1984, pp. 101-111.

[91] D. C. Haverson, A. J. Pyzik, I. A. Aksay, *Processing and micro structural characterization of B_4C/Al cermet*, in: *Proceedings of the ceramic Engineering and Science,* American Ceramic Society, July-August 1985, pp. 736-744.

[92] J.J. Brennan, J. A. Pask, *J. Am. Ceram. Soc*. 51 (1968) 569-573.

[93] A. Wolfenden, M. R. Harmouche and S. V. Hayes, in *Testing Technology of Metal Matrix Composites,* ASTM STP 964, edited by P.R. DiGiovanni and N. R.Adsit, ASTM, Philadelphia, PA, 1988, pp. 207-215.

[94] J. K. Kim and Y.W. Mai, *Interfaces in Composites*, in *Materials science and technology – A comprehensive treatment*, edited by R. W. Cahn, P. Haasen, E. J. Kramer , volume 13, VCH press, p. 121-179, Weinheim, Germany, 1993.

[95] Ed. S. Suresh, A. Mortensen and A. Needleman, *Fundamentals of metal-matrix composites*, Butterworth - Heinemann publisher, Oxford, 1993.

[96] A. Wolfenden and J. M. Wolla, *Dynamic mechanical properties*, in *Metal Matrix Composites: Mechanisms and Propertie*s, Ed. R. K. Everett and R. J. Arsenault, Academic press, pp. 287-328, Boston, USA, 1991.

[97] J. T. Hartman, K. H. Keene, R. J. Armstrong, and A. Wolfenden, *J. Metals*, 38 (4), 1986, pp. 33.

[98] P. J. Withers, W. M. Stobbs, and O. B. Pedersen, *Acta Metall. Mater*. Vol. 37, 1989, p. 3061.

[99] C. Y. Barlow and N. Hansen, *Acta Metall. Mater.* 39 (1991) 1971.

[100] M. F. Ashby, *Phil. Mag.,* 21 (1970) 399.

[101] M. Manoharan and M. Gupta, *Composites Part B*, 30 (1999) 107-112.

[102] J. Zhang, R. J. Perez, and E. J. Lavernia, *Journal of Materials Science*, 28 (1993) 835-846.

[103] C. Wang and Z. Zhu, *Scripta Materialia*, 38 (12) (1998) 1739-1745.

[104] S. E. Urreta, R. Schaller, E. Carreflo-Morelli and L. Gabella, *Journal de Physicque IV*, Colloque C8, *Supplement au Journal de Physique III*, 6 (1996) 747-750.

[105] W. S. Miller and F. J. Humphreys, *Fundamental Relationships between Microstructure and Mechanical Properties of Metal Matrix Composites*, eds. M. N. Gungor, and P. K. Liaw, TMS Warrendale, 1989, p. 517.

[106] C. Zener, J. H. Holloman, *J. App. Physics*, 15 (1944) 22.

[107] J. E. Bishop and V. K. Kinra, *Metallurgical and Materials Transactions,* 26A (1995) 2773-2783.

[108] S. K. Srivastava, B. K. Mishra and S. C. Jain, *Transactions of ASME*, 121 (1999) 476-481.

[109] G. G. Wren and V. K. Kinra, *Modeling and measurement of axial and flexural damping in metal matrix composites*, in: V.K. Kinra, A. Wolfenden (Editors), *M^3D: Mechanics and Mechanisms of Material Damping*, ASTM STP. 1169, American Society of Testing Materials, Philadelphia, 1993, pp. 282-316.

[110] W. T. Thomson, *Theory of Vibration with Applications*, 4th edition, Chapman and Hall, New York, 1993.

[111] A. Dimarogonas, *Vibration for engineers*, second edition, Prentice hall International Inc., New Jersey, 1996.

[112] D. J. Inman, *Engineering Vibration*, Second edition, Prentice Hall, New Jersey, 2001.

[113] E. Oran Brigham, *The Fast Fourier transform*, Prentice-Hall, Englewood Cliffs, N.J.,1974.

[114] C. C. Kennedy, C. D. Pancu, *J. Aeronaut. Science*, 14 (1947) 41-56.

[115] D.J. Ewins, *Modal Testing: Theory and Practice*, Research Studies Press, New York, 1984.

[116] K. P. Menard, *Dynamic mechanical analysis: a practical introduction,* CRC Press Boca Raton, 1999.

[117] D. J. Lloyd, *International Materials Reviews*, 39(1) (1994) 1-23.

[118] C. Suryanarayana, *Non-equilibrium Processing of Materials*, Pergamon Press, Amsterdam, The Netherlands, 1999.

[119] S. Suresh, A. Mortensen, and A. Needleman, *Fundamentals of Metal Matrix Composites*, Butterworth-Heinemann, Boston, 1993, pp. 23-41.

[120] L. Lu and M.O. Lai, *Mechanical alloying*, Kluwer Academic Publishers, Boston, 1998.

[121] M. Gupta, M. O. Lai, C. Y. Soo, *Material Research Bulletin*, 30 (1995) 1525-1534.

[122] N. Srikanth, D. Saravanaranganathan, M. Gupta, *Materials Science and Technology*, 16 (2000) 309-314.

[123] L.M. Tham, L. Su, L. Cheng, M. Gupta, *Materials Research Bulletin*, 34 (1998) 71-76.

[124] ASTM E8M-96: 'S*tandard Test Methods of Tension Testing of Metallic Materials*', Annual Book of ASTM Standards, 1996, Philadelphia, American Society for Testing and Materials.

[125] H. E. Boyer, *Hardness testing, ASM Committee on Hardness Testing,* ASM International, Metals Park, Ohio, 1987.

[126] ASTM C1259-98: '*Dynamic Young's Modulus, Shear modulus, and Poisson's Ratio for Advanced Ceramics by Impulse Excitation of Vibration*', Annual Book of ASTM Standards, 1998, Philadelphia, American Society for Testing and Materials.

[127] L. C. V. Samuel, *Characterization of Magnesium Based Composites Synthesized Using the Liquid Phase Process,* Master's dissertation, National University of Singapore, 1999.

[128] K. K. Tun, *Synthesis and Characterization of Al-Based Composites Using Mechanical Disintegration Method,* Master's dissertation, National University of Singapore, 1999.

[129] N. Srikanth, L. M. Tham and M. Gupta, '*Regarding the determination and prediction of elastic modulus of Al-based metal matrix composites using impact-based methods*', published in '*National symposium on progress in materials research*', held on 27 March 98 at National Univeristy of Singapore, pp. 376-379.

[130] N. Srikanth, L.-M. Tham and M. Gupta, *Aluminium Transactions,* pp. 11-17, 1999.

[131] K. Sugimoto, K. Niiya, T. Okamoto, and K. Kishitake, *Trans. JIM*, 18 (1977) 277-288.

[132] H. M. Ledbetter and S. K. Datta, *Material Science and Engineering*, 67 (1984) 25-30.

[133] G. Schoeck, *Phys. Stat. Sol.*, 32 (1969) 651-658.

[134] D. Dunand, and A. Mortensen, *Materials Science and Engineering*, A135 (1991) 179-184.

[135] E. Carreno-Morelli, S. E. Urreta, and R. Schaller, *Acta Mater*., 48 (2000) 4725-4733.

[136] V. C. Nardone, and K. W. Prewo, *Scr. Metall*. 20 (1986) 43-47.

[137] T. Minoro, and R. J. Arsenault, *Metal Matrix Composites – Thermomechanical Behavior*, Pergamon publishers, New York, U.S.A, 1989.

[138] H. J. Frost, and M. F. Ashby, *Deformation-Mechanism Maps, the Plasticity and Creep of Metals and Ceramics*, Pergamon Press, Oxford, New York, 1982.

[139] R. D. Batist, *Mechanical Spectroscopy*, chapter 12, in '*Characterization of Materials*', Eds. R.W. Cahn, P. Haasen and E. J. Kramer, Vol. 2B, Materials Science and Technology – A comprehensive Treatment, VCH publishers, New York, 1994, pp. 161-214.

[140] J. Zhang, M. N. Gungor, and E. J. Lavernia, *J. Material Sci*., vol. 28 (1993) 1515-1520.

[141] W. D. Pilkey, *Peterson's Stress Concentration Factors*, John Wiley and Sons, New York, 1997.

[142] J. E. Bishop, and V. K. Kinra, *Metallurgical and Materials Transactions A*, 1995, 26A (1995) 2773-2783.

[143] S. K. Srivastava, B. K. Mishra and S. C. Jain, *Transactions of the ASME*, Vol. 121, (1999). 476-481.

[144] A. Manna and B. Battacharayya, *Journal of Materials Processing Technology*, 140 (2003) 711-716.

[145] M. Gupta, J. Juarez-Islas, W. E. Frazier, F. A. Mohamed, E. J. Lavernia, *Metall. Trans.* B, 23 (1992) 719.

[147] A. Buch, *Pure Metals Properties – A Scientific Technical Handbook*, ASM International, Materials park, Ohio, USA, 1999.

[148] Z. Zhang, SL Chen, YA Chang, UR Kattner, *Intermetallics*, 5 (1997) 471-482.

[149] M. Gupta, F. Y. Chung, T. S. Srivatsan, *Materials and Manufacturing Processes*, 18(6) (2003) 891-902.

[150] L. M Peng, J. H. Wang, H. Li, J. H. Zhao, L. H. He, *Scripta Materialia*, 52 (2004) 243-248.

[151] S. K. Shee, S. K. Pradhan, M. De. *Materials Chemistry and Physics*, 52 (1998) 228-235.

[152] V. V. Ganesh, P. K.Tan, and M. Gupta: *Journal of Alloys and Compounds*, 315 (2001) 203-209.

[153] R Thirumalai, R.Gibson, *Characterisation of dynamic extensional modulus and damping of reinforcing fibers for advanced composites at elevated temperatures* in: *Damping of Multiphase Inorganic Materials*: Proceedings of the Damping of

Multiphase Inorganic Materials Symposium, Chicago, Illinois, USA: ASM International, 1993. pp. 37-44.

[154] C. Morelli, S. E. Urreta, R. Schaller. *Acta Materialia* 48 (2000) 4725-4733.

[155] J. Lloyd, I. Jin, *Metall. Trans. A.*, 19A (1988) 3107-3109.

[156] T. Fan, Z. Shi, D. Zhang, R. Wu, *Mater. Sci. Eng. A,* A257 (1998) 281-286.

[157] L. Salvo, G. L. Esperance, M. Suery and J. G. Legoux, *Mater. Sci. Eng.*, A177 (1994) 173-183.

[158] M. Gupta, I. A. Ibrahim, F. A. Mohamed, E. J. Lavernia, *Journal of Materials Science*, 26 (1991) 6673.

[159] B. Inem, G. Pollard, *Journal of Materials Science*, 28 (1993) 4427.

[160] J. L. Murray, Ti-Mg (Titanium-Magnesium), in *Binary Alloy Phase Diagrams*, ASM, Metals Park, Ohio, 1987, pp. 1554-1556.

[161] A. H. Cottrell, *Theoretical structural metallurgy*, Edward Arnold Publisher, London, 1954, pp.125-138.

[162] E. Zhou, C. Suryanarayana, F. H. Froes, *Materials Letters*, 23 (1995) pp. 27-31.

[163] M. Gupta, M. O. Lai and C. Y. Soo, *Materials Science and Engineering* A, Vol. 210 (1996), p.114.

[164] H. Okamoto, *Phase diagrams for Binary Alloys*, ASM International, Materials Park, Ohio, p.31.

[165] J. Romero, L. Wang, R. Arsenault, *Mater. Sci. Engg.* A, 212 (1996) 1-5.

[166] M. Hinai, S. Sawaya and H. Masumoto, *Vibration Damping Characteristics Of Al-Ge Alloys*, Mater. Trans., JIM, 32 (1991) 957-960.

[167] J. Llorca, *Acta Metall. Mater.*, 42 (1995) 151-162.

[168] G. Bao, *Acta Metal. Mater.*, 40(1992) 2547-2555.

[169] Y. L. Shen, M. Finot, A. Needleman and S. Suresh,. *Acta Metall. Mater.*, 43 (1995) 1701-1722.

[170] L. Farrissey, S. Schamauder, M Dong, E.Soppa, M. H.Poech and P. McHugh, *Computational Materials Science*, 15 (1999) 1-10.

[171] D. Xu, , and S. Schmauder,. *Computational Materials Science*, 15 (1999) 96-100.

[172] J. Wang, Z. Zhang and G.Yang,. *Computational Materials Science* 18 (2000) 205-211.

[173] *ANSYS Reference-Theory Manual*, (2005). version 10, Swanson analysis systems publications, Houston, U.S.A.

[174] L. Anand, *Int. J. Plasticity* 1 (1995) 213-251.

[175] S. B. Brown, K.H. Kim and L. Anand,. *Int. J. Plasticity* 5 (1989) 95-130.

[176] F. Teixeira-Dias, and L.F. Menezes *Computational Materials Science* 21 (2001) 26-36.

[177] M. Surey, C. Teodosiu, L. F. Menezes, *Mater. Sci. Eng.*, A167 (1993) 97-105.

[178] A. M. Lennon, K.T. Ramesh, *Int. Journal of Plasticity*, 20 (2004) 269-290.

[179] W. Nowacki, *Thermoelasticity*, Pergamon Press, Oxford, 1986.

[180] K. N.Pandey and S. Chand, *Int. J. Pressure Vessels and Piping*, 80 (200) 673-687.

[181] J. Alblas, *J. of Thermal Stresses*, 4 (1981) 333-355.

[182] B. A. Boley and J. H. Weiner *Theory of thermal stresses*, John Wiley and Sons, New York, 1960, pp. 49-53.

[183] A. Bejan, *Advanced Engineering Thermodynamics*, John Wiley and Sons, New York, 1988.

[184] C. Zener, *Physical Review,* 53 (1938) 90-99.

[185] B, D. Collean and W. Noll, *Foundations of Linear Viscoelasticity*, Review of Modern Physics, 33 (1961) 239-249.

[186] R. C. Shieh, *ASME Journal of Applied Mechanics*, 42 (1975) 405-410.

[187] R. C. Shieh, *ASME Journal of Applied Mechanics*, 46 (1979) 169-174.

[188] V. K. Kinra and K. B. Milligan, *Journal of Applied Mechanics,* 61(6) (1994) 71-76.

[189] K. B. Milligan and V. K. Kinra, *Journal of Applied Mechanic*s, 62(2) (1995) 441-449.

[190] K. B. Milligan and V. K. Kinra, *Metallurgical and Materials Transactions* A, 26A (1995) 2773-2783.

[191] O.C. Zienkiewicz, R.L. Taylor, *The Finite Element Method*, 6th Edition, Elsevier Butterworth-Heinemann, Oxford, Burlington, MA, 2005.

192] M. Zemansky and R. Dittman, *Heat and Thermodynamics*, 6th edition, McGraw Hill, 1981, NewYork, pp. 224-225.

[193] M. Özisik, *Heat Conduction*, John Wiley and Sons, New York, NY, 1980.

[194] V. K. Kinra, and A. Wolfenden: *M3D: Mechanics and Mechanisms of Material Damping*, (ASTM STP. 1169, ASTM, Philadelphia, 1993).

[195] M.J. Owen, V. Middleton, and I.A. Jones, *Integrated design and manufacture using fibre-reinforced polymeric composites*, CRC Press, Boca Raton, 2000.

[196] S. K. Srivatsava, B. K. Mishra and S.C. Jain, *ASME Transactions: Journal of Vibration and Acoustics*, Vol. 121, 1999, 476-481.

[197] S. K. Srivastava, B. K. Mishra and S. C. Jain, *Journal Of Reinforced Plastics And Composites*, vol. 20 (18): (2001) pp. 1601-1616.

[198] Cook, R. D., Malkus, D. S., and Plesha, M. E. (1989). *Concepts and Applications of Finite Element Analysis*, third edition, John Wiley and Sons, New York.

[199] B.. A. Boley and J. H Weiner, *Theory of Thermal Stresses*, John Wiley and Sons, 1960, pp. 49-53.

[200] L. Farrissey, S. Schamauder, M. Dong, E. Soppa, M. H. Poech, and P. McHugh, *Computational Materials Science*, 15 (1999) 1-10.

[201] J. Zhang, R. J. Perez and E. J. Lavernia, *Acta Metall. Mater.* 42(2) (1994) 395-409.

[202] G. E. Fougere, J. R. Weertman, R. W. Siegel, and S. K. Kim, *Scripta Matellurgica et Materialia* 26 (1992) 1879.

[203] S. D. Panteliou and A. D. Dimarogonas, *Theoretical and Applied Fracture Mechanics*, 34 (2000) 217-223.

[204] Y. C. Zhou, S. G. Long, Z. P. Duan, and T. Hashida, *Journal of Engineering Materials and Technology* 123 (2001) 251-260.

[205] C. Suryanarayana, *International Materials Review* 40 (1995) 41-64.

[206] H. Gleiter, *Acta Materialia* 48 (2000) 1-29.

[207] R. K. Rohatgi, R. Asthana and S. Das, *Int. Mat. Review*, 31(1986) 115.

[208] W. S. Miller, F. J. Humphreys, *Scripta Materialia*, 25 (1991) 33-38.

[209] Z. Trajanova, P. Lukac, H. Ferkel, B. L. Mordike, W. Riehemann, *Materials Science and Engineering* A, 234-236 (1997) 798-801.

[210] Y.Waseda, A. Muramatsu, *Morphology Control of Materials and Nanoparticles – Advanced Materials Processing and Characterization*, Springer publications, Germany, 2004.

[211] J. Weissmuller, in: D. L. Bourell (Ed.) *Nanocrystalline Materials - an Overview, Synthesis and Processing of Nanocrystalline powder*, The Minerals, Metals and Materials Soceity, USA, 1996, pp. 3-19.

[212] R. A. Andrievski and A. M. Glezer, *Scripta Mater*. 44 (2001) 1621-1624.

[213] P. Le Brun, E. Gaffet, L. Froyen, L. Delaey, *Scripta Matellurgica et Materialia* 26 (1992) 1743.

[214] Goodfellow^{TM} – *Metals, Alloys, Compounds, Ceramics, Polymers, Composites*, Catalogue 1996, Cambridge, England, p. 18.

[215] C. J. Youngdahl, J. R. Weetman, R. C. Hugo, and H. H. Kung, *Scripta Mater.* 44 (2001) 1475.

[216] P. Le Brun, E. Gaffet, L. Froyen, L. Delaey, S*cripta Matellurgica et Materialia* 26 (1992) 1743.

[217] S. Takeuchi, *Scripta Mater*. 44 (2001) 1483.

[218] S. K. Ganapathi, and D. A. Rigney, *Scripta Metallurgica et Materialia* 24 (1990) 1675.

[219] R. Thirumalai and R. Gibson, in: R. B. Bhagat (Ed.) *Damping of Multiphase Inorganic Materials*, ASM International, Materials Park, Ohio, 1993, pp. 37-46.

[220] J. R. Davis, *ASM Speciality Handbook – Copper and Copper Alloys*, ASM International, Materials Park, Ohio, 2001, p. 451.

[221] R. R. Mulyukov, N. A. Akhmadeev and R. Z. Valiev, *Materials Science and Engineering* A171 (1993) 143.

[222] R. A. Andrievski and A. M. Glezer, *Scripta Mater*, 44 (2001) 1621-1624.

[223] J. Malek and J. Shanelova, in: M. F. Thorpe and L. Tichy (Eds.) *Properties and Applications of Amorphous Materials*, Klumer Academic Publishers, London, 2001, pp. 35-44.

[224] E. Bonneti, E. G. Campari, L. Del Bianco, L. Pasquini and E. Sampaolesi, Nanostructured Materials, 11 (1999) 709.

[225] R. W. Siegel, in: C. Suryanarayana, J. Singh, and F. H. Froes (Eds.) *Processing and Properties of Nanocrystalline Materials* Eds. et al., The Minerals, Metals and Materials Society USA, 1996, pp. 3-10.

[226] R. Birringer, *Mat. Sci. Eng. A*117 (1989) 33-43.

[227] P. Robinson, in: R. L. Steven (Ed.) *Properties and Selection: Non ferrous Alloys and Special-Purpose Materials*, ASM Handbook, Vol. 2, ASM International, Materials park, Ohio, 1990, p. 265.

Appendix

Appendix A

Disintegrated Melt Deposition Method:

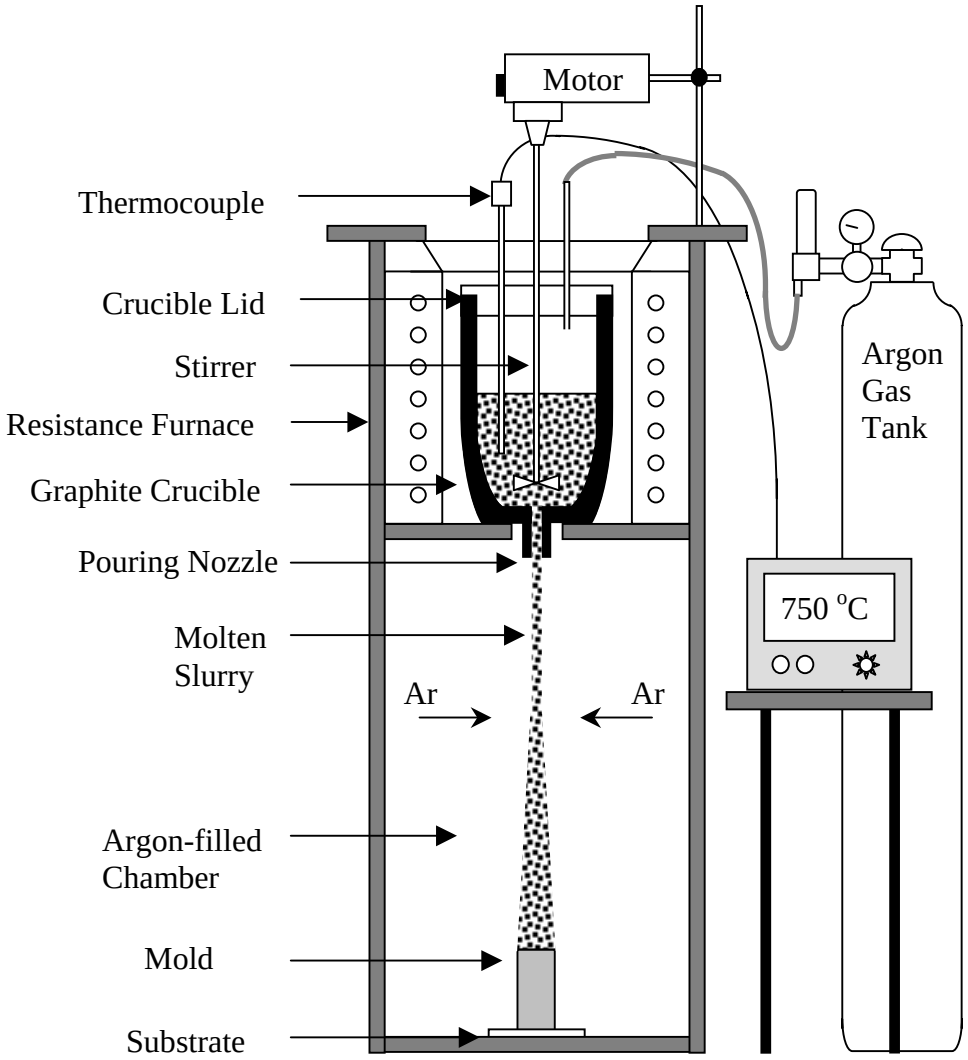

Appendix B

Flow chart illustrating the whole work flow: